

学位論文

Measurements of di-electron production in
Au+Au collisions at $\sqrt{s_{NN}} = 200$ GeV
核子対あたり重心系エネルギー200GeVでの金・金
衝突における電子対測定

平成25年12月博士（理学）
申請

東京大学大学院理学系研究科
物理学専攻

渡辺 陽介

Abstract

High-energy heavy ion collisions provide the unique opportunity to study strongly interacting matter at extreme conditions of temperature and/or density in the laboratory. Di-electron measurement is a powerful tool to diagnose the matter formed in high-energy heavy ion collisions. Since di-electrons are not subject to the final state interaction, they carry information about the properties of the matter at the time of their production.

The hot/dense matter formed in heavy-ion collisions affects the di-electron spectra in various ways. The shape of the low mass region (Below ρ mass) is expected to be modified due to the in-medium modification of low mass vector mesons, in particular ρ meson. In addition, theory predicts that the intermediate mass region (Between ϕ and J/ψ masses) is the most appropriate window to observe the thermal radiation from the QGP.

Previous di-electron measurements suffer from a large number of background electrons originating from π^0 Dalitz decays and γ conversions. A new detector, Hadron Blind Detector (HBD), is developed to reject those background electrons by exploiting the fact that the opening angle of such pairs is very small compared to the opening angle of other sources like the light vector mesons.

The HBD is a new Čerenkov detector consisting of a 50 cm long radiator operated with pure CF_4 and directly coupled to a triple Gas Electron Multiplier (GEM) photon detection element. The HBD was installed in PHENIX for 2010 $Au + Au$ runs (Run-10) and successfully operated. This manuscript presents the results of the first di-electron measurement at mid-rapidity using the HBD in $Au + Au$ collisions at $\sqrt{s_{NN}} = 200$ GeV. As a result, the consistent results with the previous PHENIX measurement were obtained for all the mass regions. This fact demonstrates the proof-of-principle of the HBD.

Contents

Abstract	iii
List of Figures	ix
List of Tables	xvii
1 Introduction	1
1.1 High energy heavy ion collisions	1
1.2 Di-electron measurements	4
1.2.1 Overview	4
1.2.2 Low mass region	7
1.2.3 Intermediate mass region	12
1.2.4 Charmonium J/ψ	14
1.3 Purpose and organization of this thesis	15
1.4 Major contributions	15
2 Experimental setup	17
2.1 Accelerator complex	17
2.2 PHENIX overview	18
2.3 PHENIX Central Arm Magnet	22
2.4 Event Characterization	23
2.4.1 Beam-beam counter (BBC)	23
2.4.2 Zero degree calorimeter (ZDC)	24
2.4.3 Reaction Plane Detector (RXNP)	25
2.5 Charged Particle Tracking	26
2.5.1 Drift Chamber (DC)	26
2.5.2 Pad Chamber (PC)	26
2.6 Electron identification	28
2.6.1 Ring Imaging Čerenkov Counter	28
2.6.2 Electromagnetic Calorimeter	29
2.6.3 East arm Time of Flight Detector	30
2.7 Hadron Blind Detector (HBD)	33
2.8 Trigger	36
2.9 Data Acquisition	36
3 HBD calibration and performance	39
3.1 Gain calibration	39

3.1.1	Gain determination	39
3.1.2	Pad-to-pad gain equilibration	42
3.2	Quantum Efficiency (QE) correction	46
3.3	Alignment	48
3.4	Scintillation background subtraction	50
3.5	Pattern recognition	52
3.5.1	Standalone algorithm	53
3.5.2	Non-standalone algorithm	53
3.6	Performance	54
4	Data analysis	57
4.1	Analysis overview	57
4.2	Collision geometry and centrality determination	60
4.3	Charged track reconstruction and momentum determination	62
4.4	Electron identification variables	65
4.4.1	RICH	65
4.4.2	EMCal and TOFE	66
4.4.3	HBD	68
4.4.4	Summary of eID variables	68
4.5	Detector simulations	68
4.6	Event cuts	71
4.7	Run selection	71
4.8	Fiducial cuts	73
4.8.1	HBD projection cut	73
4.8.2	HBD support structure conversion cuts	74
4.8.3	Drift chamber fiducial cuts	75
4.8.4	Other fiducial cuts	75
4.9	HBD double hit rejection	77
4.10	Electron Identification	78
4.10.1	Neural Network training	79
4.10.2	Step 0: Loose eID cuts	82
4.10.3	Step 1: PMT erasing	82
4.10.4	Step2a, Step2b and HBD S/D: Cut optimization	83
4.11	Pair ghost cut	85
4.11.1	RICH cut	86
4.11.2	EMCal cut	88
4.11.3	PC1 cut	89
4.11.4	HBD cut	91
4.11.5	The affected mass regions	91
4.12	Background subtraction	92
4.12.1	Combinatorial pairs	92
4.12.2	Cross pairs	98
4.12.3	Jet pairs	99
4.12.4	Electron-hadron pairs	103
4.12.5	Normalization	103
4.13	Hadronic cocktail	109
4.13.1	Neutral pion	109

4.13.2 Other mesons	110
4.13.3 Open heavy flavor	110
4.13.4 J/ψ	112
4.13.5 Systematic uncertainties on cocktail	112
4.13.6 The Au+Au Run-10 cocktail	112
4.13.7 Acceptance and efficiency correction	115
4.13.8 Bin shift correction	118
4.14 J/ψ yield	119
4.15 Summary of systematic uncertainty	119
5 Results and discussion	121
5.1 Invariant mass spectra and acceptance corrected p_T spectra	121
5.2 Control samples: π^0 and J/ψ region	124
5.3 Comparison with PHENIX Run-4 data points	125
5.4 Comparison with cocktail	127
5.4.1 Invariant mass spectra	127
5.4.2 Acceptance corrected p_T spectra	132
5.5 Comparison with direct photon measurements	135
5.6 Comparison with models	137
5.6.1 ρ modification	137
5.6.2 QGP radiation	139
6 Conclusion and outlook	141
6.1 Conclusion	141
6.2 Outlook	142
Acknowledgements	145
A Non-standalone pattern recognition algorithm of HBD	147
A.1 Cluster size optimization	147
A.2 Definition of <code>hbdid</code> variable	149
B DC fiducial cuts	155
C Weighting factor to introduce “flow” into mixed background	157
Bibliography	161

List of Figures

1.1	Lattice QCD results of energy density scaled with T^{-4} as a function of the temperature T in units of the critical temperature T_c [5].	3
1.2	Space-time evolution of a nucleus-nucleus collision. The times and temperatures for the different phases are taken from [17].	3
1.3	Expected sources of dielectron production as a function of invariant mass.	5
1.4	Schematic view of possible spectral modifications.	6
1.5	Di-electron invariant mass spectra in $p + p$ collisions at $\sqrt{s_{NN}} = 200$ GeV measured by PHENIX in the 2009 run [20, 21].	7
1.6	CERES results [31]. Left Panel: The mass spectrum on top of known hadron decays. Right panel: The mass spectrum after hadronic decay component subtraction. The spectrum is compared to the dropping mass scenario and broadening scenario.	9
1.7	NA60 results [32]. The mass spectrum after hadronic decay component subtraction. The spectrum is compared to the dropping mass scenario and broadening scenario.	9
1.8	PHENIX results [35]. Left panel: The measured mass spectrum compared to the cocktail of known hadron decays including the open charm contribution. Right panel: The mass spectrum compared to several ρ meson spectral shape modification scenarios.	10
1.9	PHENIX results [35]. Di-electron yield per participating nucleon pair ($N_{part}/2$) as function of N_{part} for two different mass ranges ((a): $0.15 < m_{ee} < 0.75$ GeV/ c^2 , (b): $0 < m_{ee} < 0.1$ GeV/ c^2) compared to the expected yield from the hadronic cocktail.	11
1.10	STAR preliminary results [37]. Di-electron mass spectra for different beam energies. The comparison with the broadening scenario is also shown in the plots.	11
1.11	PHENIX results [35]: Di-electron yield in the IMR scaled with N_{coll} vs N_{part}	13
1.12	STAR preliminary results [37]: Data/cocktail ratio for each centrality bin. The $c\bar{c}$ contribution in the cocktail is based on PYTHIA simulation scaled by N_{coll}	13
1.13	STAR and PHENIX results [52, 53]: The nuclear modification factor as a function of N_{part} measured by both experiments at mid-rapidity.	14
2.1	RHIC accelerator complex.	18
2.2	PHENIX configuration in 2010. The top panel shows the central arm from the beam view. The bottom panel shows the muon arms from the east side view.	20
2.3	PHENIX coordinate system.	21

2.4	Magnetic field lines in the “+−” field configuration [58].	22
2.5	Magnetic field strength as a function of the distance from the beam axis [58].	23
2.6	(a) Single Beam Beam counter consisting of one-inch mesh dynode photomultiplier tube mounted on a 3 cm quartz radiator. (b) A BBC array comprising 64 BBC elements. (c) The BBC is shown mounted on the PHENIX detector. The beam pipe is seen in the middle of the picture. The BBC is installed on a mounting structure just behind the central spectrometer magnet [59].	24
2.7	A plan view of the collision region showing the location of the ZDCs [61].	25
2.8	Schematic view of the arrangement of the scintillators in one RXNP arm. The length of each scintillator side is shown in centimeters [62].	25
2.9	The layout of wire position within one sector and inside the anode plane (left). A schematic view of the stereo wire orientation (right) [66].	27
2.10	The pad and pixel geometry (left). A cell defined by three adjacent pixels is at the center of the right picture. The numbers shown in the figure are for PC1 [66].	28
2.11	A cutaway view of the PHENIX RICH detector [68].	29
2.12	A schematic view of a PbSc module [71].	31
2.13	A schematic view of a PbGl supermodule [71].	31
2.14	Picture of the TOFE mounted on the East arm [70].	32
2.15	Schematic view of one TOFE panel [70].	32
2.16	Triple GEM stack operated in the standard forward bias mode (left) and reverse bias mode (right) [74].	33
2.17	Absolute quantum efficiency of CsI in vacuum and CF ₄ over the bandwidth 6.2-10.3 eV [75].	34
2.18	The 3D view of the two arm HBD. (left) Exploded view of one HBD arm. (right) [74].	34
2.19	HBD response to single electrons (left) and to unresolved double hits (right) [74].	36
2.20	Schematic diagram of the data acquisition system [76].	37
3.1	Pulse height distribution in one detector. The ordinate is normalized to represent the number of hits per event.	40
3.2	Gain versus run number.	41
3.3	Gain versus time for two detector modules. The data are from a few runs taken at the end of the 200 GeV part of Run 10.	42
3.4	An example for pad gain determination, by fitting the exponential. Shown are four pads from WN2 module.	43
3.5	The distribution of pad gains in two modules WS1 and WN1. Top: before the equilibration, bottom: after the equilibration.	44
3.6	Stability of the pad-to-pad gain equilibration throughout the 200 GeV portion of Run-10 for the ES modules (1-5 from top to bottom). Blue (red) points are before (after) the gain equilibration.	45
3.7	HBD cluster charge distribution associated with central arm electrons (Black). Contribution from scintillation light is estimated with track swapping (Red) and subtracted to obtain the Čerenkov response (Blue).	47
3.8	Charge scaling factor λ_t of different run groups for ES4 module of the east arm.	47

3.9	Peak of “double” charge distribution before and after the quantum efficiency correction for ES4 module.	48
3.10	“Double” charge distribution before and after the quantum efficiency correction for five modules of the east arm.	48
3.11	The schematic drawing depicting the HBD arm rotation around the x-axis (PHENIX coordinates). On the left is the view of one HBD arm from x-direction and on the right is a zoomed drawing of one HBD sector, containing two modules.	49
3.12	The HBD module offsets after applied correction.	50
3.13	Photon yield for various scintillating gases excited by ^{16}O ions of $E_{kin} = 80 \text{ MeV}$ [79]. Intensities are normalized with respect to constant energy loss.	51
3.14	Cell charge per unit area ($Q_{\text{cell}}/a_{\text{cell}}$) for different centrality ranges. The displayed data are for module WN2.	51
3.15	Schematic drawing of HBD readout hexagonal pads. One pad is divided into 4 mm triangles in the clustering algorithm described in the text.	54
3.16	The effective signal (left) and the signal-to-background ratio (right) for three types of cuts and for each centrality bin. Those values for the central arm cuts are normalized to be one. HBD(S) refers to the HBD single cut, $\text{hbdid} \geq 10$, and HBD(D) refers to the HBD double cut, $\text{hbdcharge} < 30$	55
4.1	Analysis flow.	58
4.2	Collision geometry in 2D (Top) and 3D (Bottom) view.	61
4.3	Distribution of the BBC total charge for the events with $0 < z_{vtx} < 5 \text{ cm}$. Each slice corresponds to a 10% centrality bin.	62
4.4	Left: Schematic view of a track in the DC r - ϕ plane. Right: Schematic view of a track in the DC r - z plane [77].	64
4.5	Schematic description of the variables which characterize a RICH ring. A track projection vector and five PMTs with correlated hits are also shown.	66
4.6	The r_{cor} distribution from single electron simulation. The shaded area shows the r_{cor} region between 3.4 cm and 8.4 cm.	66
4.7	Charge over momentum (Q/mom) vs ToF for PbSc(left) and TOFE(right) in the 0-10% centrality bin.	67
4.8	The comparison of major eID variables in data (Black) and in the detector simulation (Red) using the open Dalitz pairs in the 60-92% centrality bin. The comparisons of neural network outputs described in Section 4.9 and 4.10 are also shown in the lowest panels.	71
4.9	Vertex distribution for a run taken with a $\pm 30 \text{ cm}$ vertex trigger (left) and a run taken with a $\pm 20 \text{ cm}$ vertex trigger (right).	72
4.10	Electron-tracks per event distributions as function of the vertex position for a run with wide vertex trigger (left) and narrow vertex trigger (right).	72
4.11	$\langle \text{disp} \rangle$ as a function of run number. The runs inside the shadowed band are accepted as good runs.	73
4.12	Track projections onto the HBD in the $\phi - z$ plane. The black points represent the tracks before applying the HBD projection cut and the blue points are the tracks accepted by the projection cut. Minimum bias data.	74

4.13 The ϕ_0 distribution of all tracks (black) and the tracks accepted by the cut (red) that removes conversions from the HBD support structure. Minimum bias data.	75
4.14 α vs board number for e^\pm yield without fiducial cut (left column) and with fiducial cut(right column) for all the four sectors in Run Group 01.	76
4.15 Correlation between $\cos(\theta_0)$ and b_{bcz} . The left panel shows the raw correlation map and the right panel shows the correlation map after applying the fiducial cut that removes the tracks around $z \sim 0$	76
4.16 The input variables for the neural network (top panels and bottom left). The red lines correspond to single hits (signal) and the blue lines to double hits (background). The black is the sum of the two. The resulting neural network output is shown in the bottom right panel. This is an example for centrality 30-40% and HBDSIZE=2 from the Monte-Carlo simulation.	78
4.17 nnout0 distribution in the 20-40% centrality bin. The red line corresponds to signal hits and the blue line corresponds to background hits.	81
4.18 nnout2a distribution in the 20-40% centrality bin. The red line corresponds to signal hits and the blue line corresponds to background hits.	81
4.19 nnout2b distribution in the 20-40% centrality bin. The red line corresponds to signal hits and the blue line corresponds to background hits.	82
4.20 Scatter plots of the effective signal versus the signal-to-background. The point shown with the yellow square is the setup selected for the analysis.	84
4.21 Left panel: like-sign foreground, mixed background, and the subtracted spectra. On can see a large correlation at low masses. Right panel: unlike-sign foreground and mixed background and the subtracted yield , where a clear correlation peak is visible at $0.25 \text{ GeV}/c^2$. The plots are for 0-10% centrality.	86
4.22 The $\Delta\phi - \Delta z$ distributions in RICH. The left panels show unlike-sign foreground (top), like-sign foreground ++ (middle) and like-sign foreground -- (bottom). The right panels show unlike-sign mixed background (top), like-sign mixed background ++ (middle) and like-sign mixed background -- (bottom).	87
4.23 The corrected yield vs. the ring sharing cut value. The right plot is a zoom of the y-axis. The data are for 0-10% central events.	88
4.24 The $\Delta y - \Delta z$ distributions in EMCAL. The left panels show unlike-sign foreground (top), like-sign foreground ++ (middle) and like-sign foreground -- (bottom). The right panels show unlike-sign mixed background (top), like-sign mixed background ++ (middle) and like-sign mixed background -- (bottom).	89
4.25 The corrected yield vs. the EMCAL cut value. The data are for 0-10% central events.	90
4.26 The $\Delta_\phi - \Delta_z$ in PC1, unlike-sign foreground (left), unlike-sign mixed background (right). The red ellipse marks the region with extra yield in the foreground and the magenta ellipse marks the region with missing yield in the foreground.	90
4.27 PC1 $\Delta\phi$ distribution to see the effect of the PHENIX track reconstruction algorithm on the proximity hits in PC1. This $\Delta\phi$ distribution is obtained with the ellipse cut shown in Fig 4.26.	91
4.28 Like-sign pair's opening angle distribution. The plot is for 0-10% centrality bin.	92

4.29	Like-sign (left) and unlike-sign (right) foreground spectra without any pair cuts (Black) and with RICH, EMCAL and PC1 pair cuts (Blue). The plots are for the 0-10% centrality bin.	92
4.30	The ratio between the foreground mass spectrum and the simple mixed background without flow effect for the 20-40% centrality bin.	94
4.31	2D flow cartoon.	95
4.32	The inclusive single electron yield as a function of the angle relative to the reaction plane for $0.7 < p_T < 0.8 \text{ GeV}/c$ in the 20-30 % centrality bin.	95
4.33	The ratio between foreground and mixed background mass spectra in ToyMC with and without flow effect in the mixed background. Black: simple mixed-event technique. Red: weighting method.	96
4.34	Reaction plane resolution as a function of centrality [86].	97
4.35	Inclusive single electron v_2	97
4.36	PYTHIA like-sign foreground spectrum scaled by $1/3.9 \cdot \langle N_{coll} \rangle \cdot R_{AA}(p_{T1}) \cdot R_{AA}(p_{T2})$ of 20-40% centrality bin. The normalized and scaled mixed background is also shown in the figure.	101
4.37	R_{AA} of neutral pion as a function of p_T from [92].	102
4.38	R_{AA} of charged pion as a function of p_T from [93].	102
4.39	Illustration of the a possible electron hadron correlation.	104
4.40	Foreground pairs and normalized background sources in each centrality bin.	106
4.41	Unlike-sign pairs after background subtraction. Only statistical errors are shown in the figure.	107
4.42	Like-sign residual yield divided by the mixed background yield as a function of mass for each centrality bin. The grey shadowed bands represent the normalization error of the mixed background. The green bands represent the systematic error due to the like-sign residual yields.	108
4.43	Ideal acceptance of the PHENIX detector in the $+-$ magnetic field configuration. The Y axis is charge/ p_T and the X axis is the DC ϕ_0 variable. The red lines are the parametrization used in EXODUS to define the ideal acceptance.	113
4.44	Deviation in reconstructed momentum (left), theta (middle) and phi (right) in the 600-700 MeV/c momentum bin. The momentum deviation is fitted with a Gaussian and an exponential function to account for the radiative tail. The θ and ϕ deviations are very well fitted by a Gaussian function only.	114
4.45	Run10 dielectron cocktail for minimum bias events. The mesonic contributions are obtained from EXODUS. The correlated e^+e^- pair yield form the semileptonic decays of heavy flavor mesons is from MC@NLO. The J/ψ decay into e^+e^- is taken from Run-9 $p + p$ collisions after scaling with N_{coll} . The systematic uncertainties in the cocktail are shown as the yellow band and discussed in Section 4.13.5.	114
4.46	Acceptance and efficiency correction for the pair p_T range between 0.8 and 1.0 GeV/c for each centrality bin.	118
5.1	Invariant mass spectra of e^+e^- pairs in the PHENIX acceptance for different centrality bins. The invariant mass spectrum for the minimum bias events is also shown. Statistical and systematic errors are included.	122
5.2	Acceptance corrected p_T spectra of e^+e^- pairs for $0.3 < m_{ee} < 0.5 \text{ GeV}/c^2$	123
5.3	Acceptance corrected p_T spectra of e^+e^- pairs for $0.5 < m_{ee} < 0.75 \text{ GeV}/c^2$	123

5.4	Data/cocktail ratio in the mass region $0.0\text{-}0.1 \text{ GeV}/c^2$. The shadowed band represents the systematic error on the cocktail.	124
5.5	$J/\psi R_{AA}$ as a function of N_{part} in Run-10 and Run-4 [52].	125
5.6	Acceptance corrected p_T spectra of e^+e^- pairs for $0.3 < m_{ee} < 0.5 \text{ GeV}/c^2$ in Run-4 [35] and in the present analysis of Run-10.	126
5.7	Acceptance corrected p_T spectra of e^+e^- pairs for $0.5 < m_{ee} < 0.75 \text{ GeV}/c^2$ in Run-4 [35] and in the present analysis of Run-10.	126
5.8	Invariant mass spectra of e^+e^- pairs in the PHENIX acceptance for different centrality bins. The experimental results are compared to the expected yield from the cocktail of light hadron decays, correlated heavy flavor decays and J/ψ decays. Statistical and systematic errors both on data and the cocktail are included.	129
5.9	Invariant mass spectra of e^+e^- pairs in the PHENIX acceptance for minimum bias events. The experimental results are compared to the expected yield from the cocktail of light hadron decays, correlated heavy flavor decays and J/ψ decays. Statistical and systematic errors both on data and the cocktail are included.	130
5.10	Invariant mass spectrum of e^+e^- pairs in the PHENIX acceptance in minimum-bias $Au + Au$ collisions compared to the Run-4 cocktail [35].	130
5.11	Data/cocktail ratio in the mass region $0.15\text{-}0.75 \text{ GeV}/c^2$. The shadowed band represents the systematic error on cocktail.	131
5.12	Data/cocktail ratio in the mass region $1.2\text{-}2.8 \text{ GeV}/c^2$. The shadowed band represents the systematic error on the cocktail.	131
5.13	The ratio of the acceptances in Run-10 and Run-4 to the enhancement component observed in Run-4.	132
5.14	Acceptance corrected p_T spectra of e^+e^- pairs for $0.3 < m_{ee} < 0.5 \text{ GeV}/c^2$	133
5.15	Acceptance corrected p_T spectra of e^+e^- pairs for $0.5 < m_{ee} < 0.75 \text{ GeV}/c^2$	133
5.16	The m_T spectrum for the mass range $0.5 < m_{ee} < 0.75 \text{ GeV}/c^2$ after subtracting the hadronic cocktail without the ρ meson contribution. The fit to the sum of two exponentials is also shown.	134
5.17	Acceptance corrected p_T spectra of e^+e^- pairs for $0.3 < m_{ee} < 0.5 \text{ GeV}/c^2$. The cocktail with the direct photon yield estimated in [35] is also shown in the figure.	136
5.18	Acceptance corrected p_T spectra of e^+e^- pairs for $0.5 < m_{ee} < 0.75 \text{ GeV}/c^2$. The cocktail with the direct photon yield estimated in [35] is also shown in the figure.	136
5.19	Invariant mass spectrum of e^+e^- pairs in the minimum bias collisions for the low p_T region, $0 < p_T < 0.5 \text{ GeV}/c$. The ρ meson contribution, including in-medium effects, calculated by R. Rapp and van Hees [35, 107, 108] is added to cocktail without the ρ and shown in the figure by the dashed line. The HMBT(Hadron Many Body Theory) refers to the broadening scenario and the PY refers to the partonic yield from $q\bar{q}$ annihilation.	138
A.1	Charge distribution of 1 pad (pad0), 2 pad (pad0 \oplus pad1)and 3 pad (pad0 \oplus pad1 \oplus pad2) clusters for genuine electrons (black) and fake electrons (red) pointing to the triangle 0 in Fig. 3.15.	148

A.2	Electron efficiency as a function of triangle number (Fig. 3.15) when 90 % of fake hits are rejected. The points with different colors show the efficiency of different cluster sizes.	149
A.3	Schematic drawing of the HBD readout plane.	150
A.4	Charge threshold of a cluster consisting of one hexagonal pad in each HBD module of the east arm at $\sqrt{s_{NN}} = 200$ GeV for a rejection of backplane conversion by a factor of 10.	151
A.5	Electron efficiency and the remaining fraction of backplane-conversion electrons as a function of <code>hbdid</code> . See the text for the definition of <code>hbdid</code>	152
A.6	Electron efficiency as a function of p_T for the case of $\text{hbdid} \geq 10$. See the text for the definition of <code>hbdid</code>	153
B.1	α vs board number for e^\pm yield without fiducial cut (left column) and with fiducial cut(right column) for all the four sectors in Run Group 1.	155
B.2	α vs board number for e^\pm yield without fiducial cut (left column) and with fiducial cut(right column) for all the four sectors in Run Group 2.	155
B.3	α vs board number for e^\pm yield without fiducial cut (left column) and with fiducial cut(right column) for all the four sectors in Run Group 3.	156
B.4	α vs board number for e^\pm yield without fiducial cut (left column) and with fiducial cut(right column) for all the four sectors in Run Group 4.	156
B.5	α vs board number for e^\pm yield without fiducial cut (left column) and with fiducial cut(right column) for all the four sectors in Run Group 5.	156

List of Tables

1.1	Summary of dilepton (e^+e^- or $\mu^+\mu^-$) measurements in heavy ion collisions [19]. The energy is quoted in GeV per nucleon in the lab. system with the exception of PHENIX and STAR where the energy per nucleon pair is in the c.m.s.	7
2.1	Collision species and their energy delivered by RHIC from 2000 to 2013.	19
2.2	Pseudo-rapidity $\Delta\eta$ and azimuthal $\Delta\phi$ coverage of each detector (Run-10 setup).	21
2.3	The performance of PC1, PC2 and PC3.	28
4.1	Average N_{part} and N_{coll} of each centrality bin in $Au + Au$ collisions at $\sqrt{s_{NN}} = 200$ GeV.	61
4.2	Variables used for the electron identification in the analysis.	69
4.3	Signal and background definition for the neural network trainings	80
4.4	Input parameters of each neural network	80
4.5	S/D cuts threshold used as a reference.	85
4.6	Optimized <code>nnout</code> threshold. The <code>nnoutsd</code> thresholds are shown as the shifts relative to the values listed in Table 4.5.	85
4.7	Branching ratio (BR) used in the jet simulation.	101
4.8	Normalization window for each centrality bin. The number of like-sign pairs in the window is also shown in the table.	105
4.9	Fit parameters derived from the π^0 and charged pion p_T distributions for different centralities using the modified Hagedorn function [94, 95, 96].	110
4.10	p_T integrated yield of π^0 s and the other light mesons in different centralities. For the 60-92% bin, the value from this analysis is used.	111
4.11	Acceptance filter parameters in the $+ -$ magnetic field configuration.	113
4.12	Efficiency loss due to detector occupancy for the centrality bins used in the analysis.	117
4.13	Efficiency loss due to the eID step 1 discussed in Section 4.10.3 for the centrality bins used in this analysis.	117
5.1	The enhanced yields in Run-10 and Run-4 for the minimum bias events. The Run-4 yields are corrected to the yields in the Run-10 acceptance.	132
5.2	The excess from the cocktail in PHENIX acceptance calculated by the different models for the range $0.5 < m_{ee} < 0.75$ GeV/ c^2 and $0.0 < p_T < 0.5$ GeV/ c . The excess in the data is also shown.	138
5.3	Thermal radiation calculations for $1.2 < m_{ee} < 2.8$ GeV/ c^2 are added to the cocktail and then divided by the cocktail. The data divided by cocktail is also shown.	139

Chapter 1

Introduction

1.1 High energy heavy ion collisions

High-energy heavy ion collisions provide the unique opportunity to study strongly interacting matter at extreme conditions of temperature and/or density in the laboratory. At such conditions, quarks and gluons are no longer confined inside hadrons. They are free to move over distances which are large compared to the hadron size and they are the relevant degrees of freedom [1, 2, 3]. Therefore, the formed matter is often referred to as “Quark Gluon Plasma (QGP)” [4].

Quantitative calculations are performed using lattice QCD. Figure 1.1 shows the evolution of energy density with the temperature [5]. The step-like behavior, which is a characteristic feature of a phase transition, is due to the change in the number of degrees of freedom when the transition between hadron gas and QGP occurs. The energy density does not reach the Stefan-Boltzmann limit ε_{SB}/T^4 which corresponds to the ideal gas due to strong interactions in the QGP.

Lattice QCD also predicts the transition into a chirally symmetric phase occurring at the same time as the transition into the deconfined phase [6]. The chiral symmetry is spontaneously broken in normal matter [7, 8, 9]. The breaking occurs due to a non-vanishing ground state expectation value of the quark condensate $\langle\bar{q}q\rangle$ and is responsible for the fact that the constituent quark mass ($\sim 300 \text{ MeV}/c^2$) is much heavier than the current quark mass ($\sim 5 \text{ MeV}/c^2$) [10]. In the limit of high temperature and high baryon density, the quark condensate vanishes ($\langle\bar{q}q\rangle \rightarrow 0$) and the chiral symmetry is expected to be restored.

Figure 1.2 shows the space-time evolution of the matter produced in heavy ion collisions [11]. Immediately after the collision, a huge amount of energy is released in a tiny volume

and free partons are produced. Once equilibrium is achieved, common thermodynamic quantities, such as temperature and pressure, can be used to describe the system and the evolution from this point on is modeled by relativistic hydrodynamics [12, 13, 14, 15, 16]. As the matter expands, the temperature drops and crosses the transition temperature T_c , where hadronization of partons occurs. If the transition is first-order, the system passes through a mixed-phase consisting of quarks, gluons and hadrons. Eventually the inelastic scattering of hadrons ceases. The temperature is called the chemical freeze-out temperature. Then the elastic scattering of hadrons ceases. The temperature is called the kinetic freeze-out temperature. After the kinetic freeze-out, the particles stream freely to the detectors.

The production of particles in heavy ion collisions strongly depends on collision geometry. (See Section 4.2 for detail.) The perpendicular distance between the paths of the two nuclei is referred to as impact parameter. Collisions with small impact parameter are called “central collisions (events)” and collisions with large impact parameter are called “peripheral collisions (events)”. Collisions without any selection of impact parameter are called “minimum bias collisions (events)”. Instead of using the impact parameter, the following variables directly related to the impact parameter are often used :

- N_{coll} : A variable related to the number of binary nucleon-nucleon collisions. The particle production at initial stages of collisions is roughly proportional to N_{coll} .
- N_{part} : A variable related to the reaction volume. The particle production at later stages of collisions is roughly proportional to N_{part} .

Since the impact parameter, N_{coll} and N_{part} are not experimental observables, an experimental quantity called “centrality” is defined and related to those variables via the Glauber model calculation. Small centrality corresponds to the small impact parameter and vice versa.

The study described in this manuscript aims at measuring the properties of hadron gas and partonic matter formed in heavy ion collisions using di-electron channel.

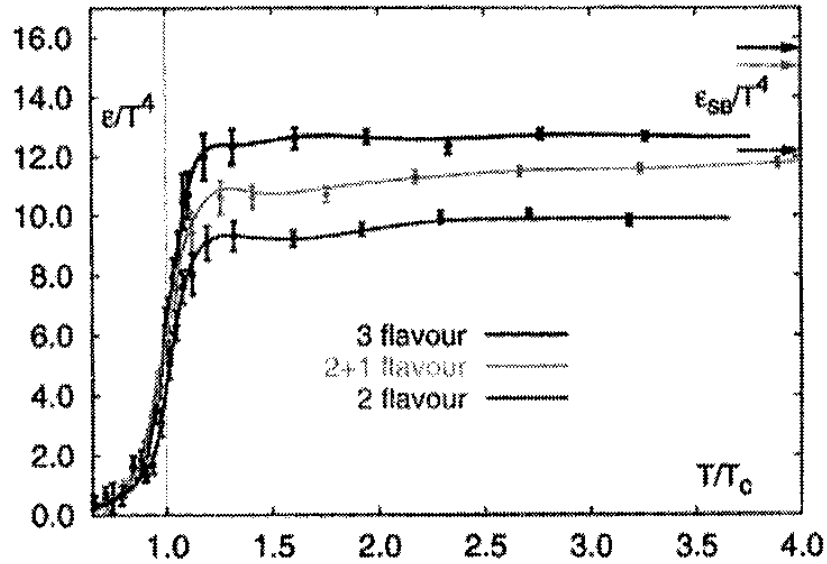


FIGURE 1.1: Lattice QCD results of energy density scaled with T^{-4} as a function of the temperature T in units of the critical temperature T_c [5].

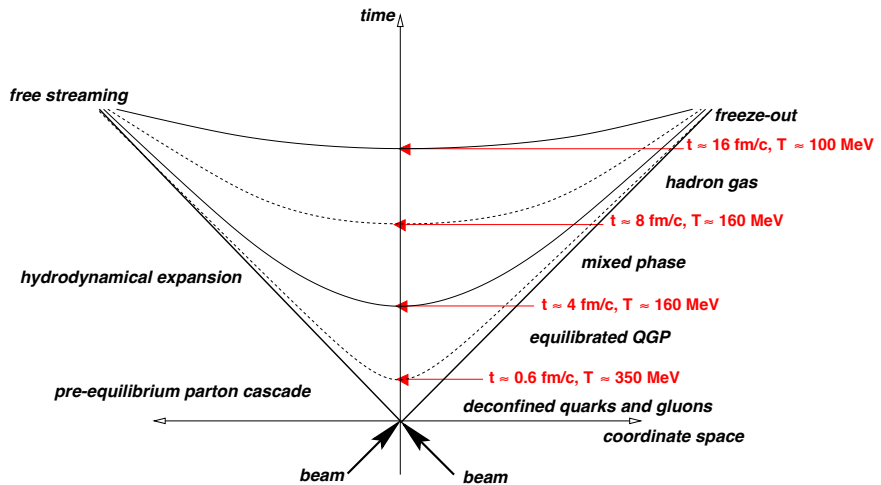


FIGURE 1.2: Space-time evolution of a nucleus-nucleus collision. The times and temperatures for the different phases are taken from [17].

1.2 Di-electron measurements

1.2.1 Overview

Di-electron measurement is a powerful tool to diagnose the strongly interacting matter formed in high-energy heavy ion collisions [4]. Di-electrons are not subject to the strong interaction. Therefore, they are not distorted by final state interactions and carry information about the properties of the matter at the time of their production.

Di-electrons are produced via various processes during all stages of the heavy-ion collision, from the initial parton-parton collisions till the hadron decays after freeze-out. To extract the information of the matter at a certain stage, e.g. the QGP, we need to disentangle the various sources.

Figure 1.3 illustrates the contributions of various sources to the invariant mass spectrum. The mass spectrum can be divided into three regions: the low mass region (LMR, $0\text{-}1.2 \text{ GeV}/c^2$), the intermediate mass region (IMR, $1.2\text{-}2.8 \text{ GeV}/c^2$) and the high mass region (HMR, $>2.8 \text{ GeV}/c^2$). Di-electrons coming from the decay of light mesons ($\pi^0, \eta, \eta', \rho, \omega, \phi$) are the dominant sources in the low mass region. In the intermediate and high mass regions, there are contributions from the semi-leptonic decays of charm and bottom mesons. Heavy quark pairs ($c\bar{c}$ or $b\bar{b}$) produced in the initial hard scattering of partons undergo fragmentation and form heavy meson pairs, e.g. D^+D^- . The subsequent semi-leptonic decays of these mesons produce correlated e^+e^- pairs. In the high mass region, there is also a contribution from charmonia ($J/\psi, \psi'$).

The hot/dense matter formed in heavy-ion collisions affects the spectrum in various ways. Sources of possible modifications are illustrated in Fig. 1.4. The main focuses of this manuscript are:

- Low mass, low p_T region:

The shape of the low mass region is expected to be modified due to the in-medium modification of low mass vector mesons, in particular ρ meson. (See Sec 1.2.2). In this thesis, we often present the inclusive mass spectrum, which is mainly affected by the modifications at low p_T .

- Intermediate mass region:

Theory predicts that the intermediate mass region is the most appropriate window to observe the thermal radiation from the QGP (See Sec 1.2.3).

- High mass region:

The charmonia are expected to be suppressed due to color screening (See Sec [1.2.4](#)).

The low mass, high p_T region is also an interesting region to study the thermal radiation from QGP. The consistency with previous measurements in this region is discussed in Section [5.5](#).

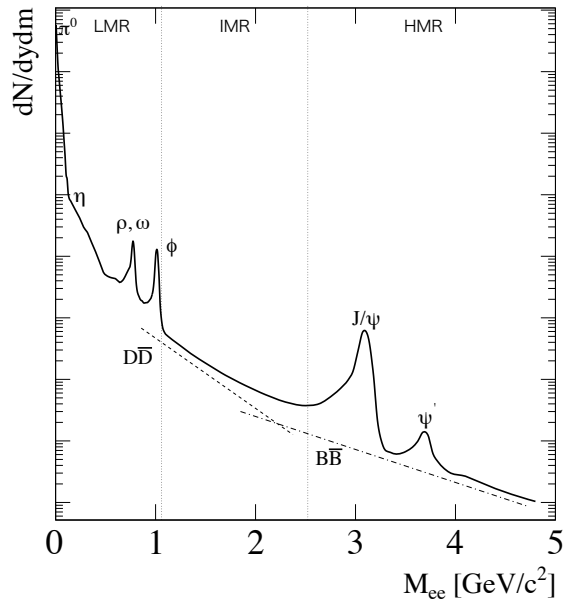


FIGURE 1.3: Expected sources of dielectron production as a function of invariant mass.

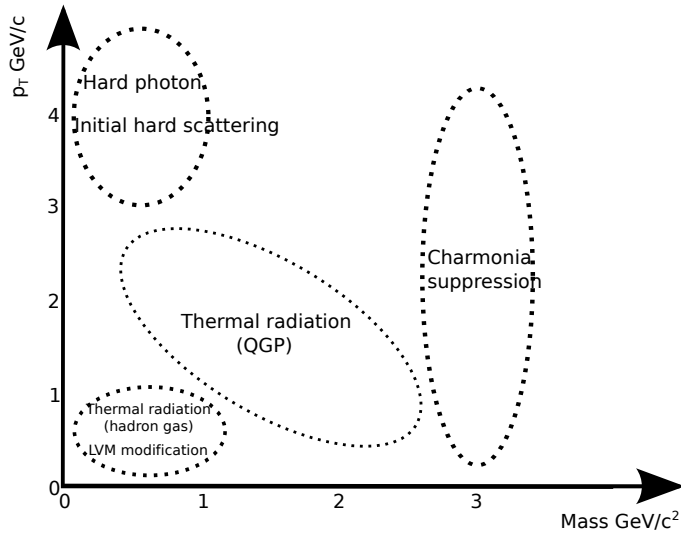


FIGURE 1.4: Schematic view of possible spectral modifications.

Di-electron measurements using heavy-ion collisions have been performed for decades. The major experiments are summarized in Table 1.1 [19].

The main experimental difficulty in the dilepton measurements is the huge combinatorial background of uncorrelated lepton pairs. Since single leptons do not carry any information about their source, all leptons in the same event are paired to calculate the invariant mass spectrum. Therefore, it is inevitable to form pairs where the electron and positron are coming from two different sources. The number of uncorrelated pairs increases quadratically with the event multiplicity. Typical signal-to-background ratios at SPS energies are 1/10-1/20 [31, 32] whereas at RHIC energies values of $\sim 1/200$ for minimum bias events are reported [35, 37].

Medium effects on dilepton mass spectra are observed as deviations from the expected di-lepton mass spectra in elementary collisions; therefore, a thorough understanding of all sources is essential. To confirm the understanding, most experiments measure the dilepton spectra in $p + p$ collisions as the reference and $p(d) + A$ collisions to establish possible cold nuclear matter effects. As an example of the reference measurement, Fig. 1.5 shows the di-electron spectra in $p + p$ collisions measured by PHENIX at $\sqrt{s_{NN}} = 200$ GeV [20, 21], using the same setup as in this analysis. The measured spectrum is well reproduced by the known hadronic sources. The spectrum of the known hadronic sources is referred to as “hadronic cocktail”.

TABLE 1.1: Summary of dilepton (e^+e^- or $\mu^+\mu^-$) measurements in heavy ion collisions [19]. The energy is quoted in GeV per nucleon in the lab. system with the exception of PHENIX and STAR where the energy per nucleon pair is in the c.m.s.

Accelerator	Experiment	Probe	System	Energy
BEVALAC	DLS	e^+e^-	$C + C, Ca + Ca$	1
GSI	HADES	e^+e^-	$C + C$	1, 2
SPS	HELIOS-3	$\mu^+\mu^-$	$p + W, S + W$	200
	CERES	e^+e^-	$p + Be, Au$	450
			$S + Au$	200
			$Pb + Au$	158
NA38, NA50		$\mu^+\mu^-$	$p + W, S + U$	200
			$Pb + Pb$	158
NA60		$\mu^+\mu^-$	$In + In$	158
RHIC	PHENIX (2004)	e^+e^-	$Au + Au$	200
	PHENIX (2010)	e^+e^-	$Au + Au$	200
	STAR (2010)	e^+e^-	$Au + Au$	19.6, 62.4, 200

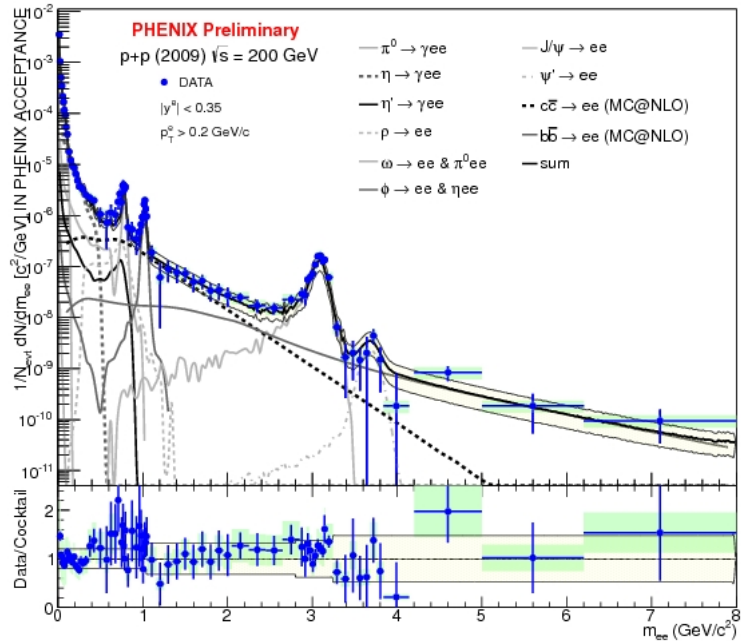


FIGURE 1.5: Di-electron invariant mass spectra in $p + p$ collisions at $\sqrt{s_{NN}} = 200$ GeV measured by PHENIX in the 2009 run [20, 21].

1.2.2 Low mass region

Low mass vector mesons (ρ , ω , ϕ) are interesting probes to understand chiral symmetry restoration [19, 22]. The low mass vector mesons are produced in the hot/dense hadron gas close to the phase boundary, where theoretical studies indicate the mass and width

of the mesons are modified. Among the low mass vector mesons, the modification of ρ is expected to be largest due to its short life time, $\tau \sim 1.3 \text{ fm}/c$.

At SPS energies, CERES observed an enhanced di-electron yield below $1 \text{ GeV}/c^2$ compared to the expected yield from hadronic sources in $S + Au$ and $Pb + Au$ collisions [29]. The enhancement is interpreted as the thermal radiation from the hadronic phase, dominated by the two pion annihilation:

$$\pi^+ \pi^- \rightarrow \rho \rightarrow e^+ e^- \quad (1.1)$$

Models using the vacuum ρ spectral shape could not explain the enhancement quantitatively and in-medium modifications of the intermediate ρ meson were introduced [23, 24, 25, 26, 27, 28]. Two main models with such in-medium modifications are:

- Dropping mass scenario following the Brown-Rho scaling [26, 33]:

The ρ meson mass scales with the quark condensate $\langle \bar{q}q \rangle$, which drops in the high baryon density medium.

- Broadening mass scenario [34]:

The ρ meson spectral function becomes broader due to the scattering of the ρ meson off baryons in the dense medium.

These two models reproduced equally well the CERES data obtained with the limited mass resolution of the original spectrometer [30]. After the observation, a significant breakthrough was achieved by the upgraded CERES experiment [31] and NA60 [32]. These experiments measured the enhancement with better precision, and now, there is almost a consensus that the approach to chiral symmetry restoration proceeds through broadening of ρ and no shift in its mass. Figure 1.6 shows the result of CERES and Figure 1.7 shows the result of NA60. Both spectra are compared to dropping mass scenario [26, 33] and broadening scenario [34] and favor the broadening scenario.

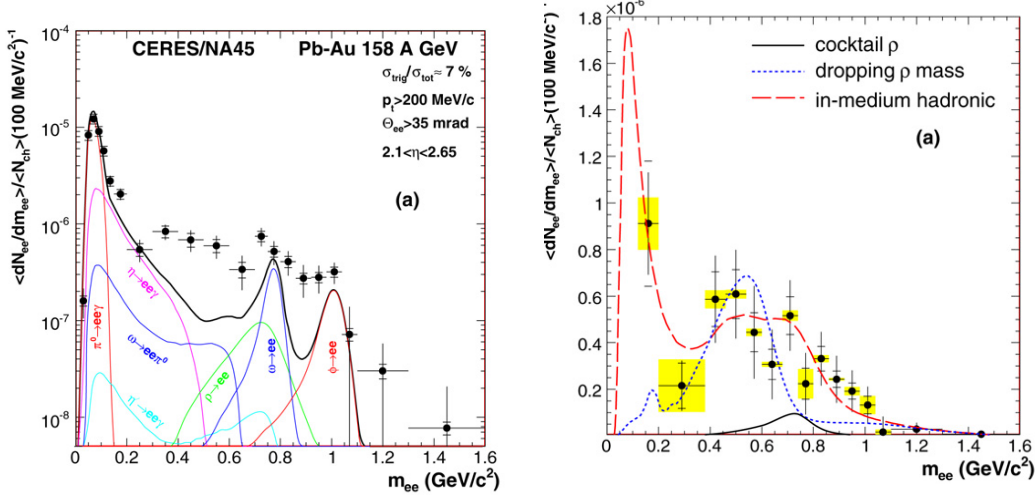


FIGURE 1.6: CERES results [31]. Left Panel: The mass spectrum on top of known hadron decays. Right panel: The mass spectrum after hadronic decay component subtraction. The spectrum is compared to the dropping mass scenario and broadening scenario.

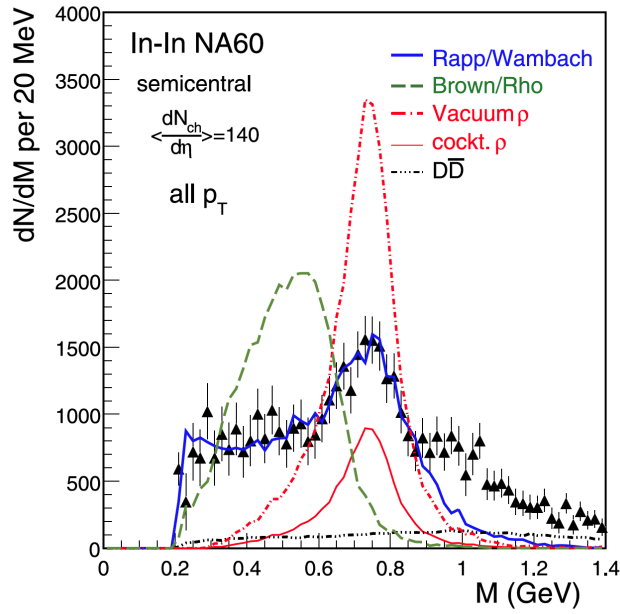


FIGURE 1.7: NA60 results [32]. The mass spectrum after hadronic decay component subtraction. The spectrum is compared to the dropping mass scenario and broadening scenario.

At RHIC in $Au + Au$ collisions at $\sqrt{s_{NN}} = 200$ GeV, PHENIX observed a large enhancement of di-electrons compared to the expected hadronic sources in the mass range $0.15 < M_{ee} < 0.75$ GeV/c^2 . They reported an enhancement by a factor of $4.7 \pm 0.4^{stat} \pm 1.5^{syst} \pm 0.9^{model}$ for minimum bias events [35]. Figure 1.8 shows the comparison of the invariant mass spectrum to the known hadron decays (left panel) and to several ρ meson spectral shape modification scenarios (right panel). None of the models is able to reproduce the enhancement and its origin is not understood. The di-electron yield per participating nucleon pair (N_{part}), integrated over two mass ranges, is compared to the expected yield from the hadronic cocktail in Fig. 1.9 as a function of N_{part} . The anomalous enhancement is visible only in the central collisions.

Recently, STAR also performed di-electron measurements and did not observe such a strong enhancement [36, 37]. The observed enhancement is $1.53 \pm 0.07^{stat} \pm 0.41^{syst}$ for minimum bias events and is compatible with the ρ broadening scenario. Figure 1.10 shows their preliminary mass spectra for different beam energies. The model calculations with ρ broadening scenario are also shown in the figure.

Therefore, it is crucial to perform an additional measurement and settle the inconsistency between the two experimental results.

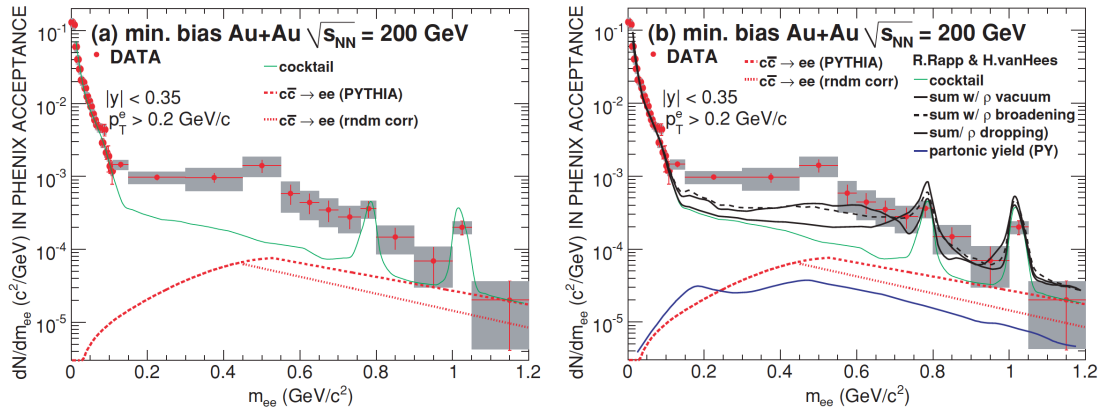


FIGURE 1.8: PHENIX results [35]. Left panel: The measured mass spectrum compared to the cocktail of known hadron decays including the open charm contribution. Right panel: The mass spectrum compared to several ρ meson spectral shape modification scenarios.

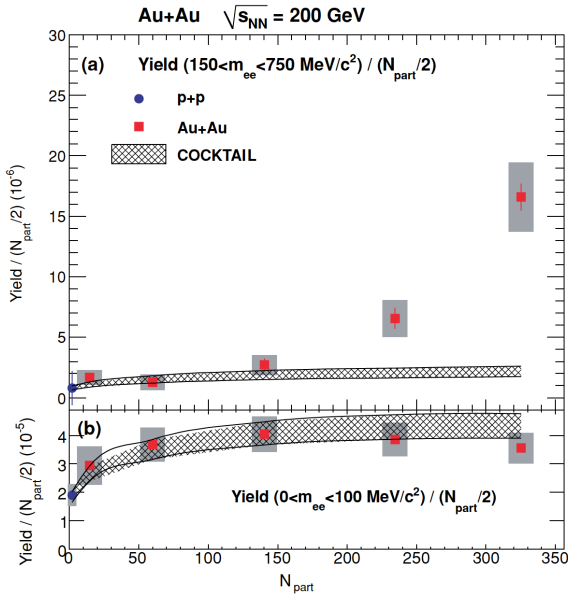


FIGURE 1.9: PHENIX results [35]. Di-electron yield per participating nucleon pair ($N_{part}/2$) as function of N_{part} for two different mass ranges ((a): $0.15 < m_{ee} < 0.75 \text{ GeV}/c^2$, (b): $0 < m_{ee} < 0.1 \text{ GeV}/c^2$) compared to the expected yield from the hadronic cocktail.

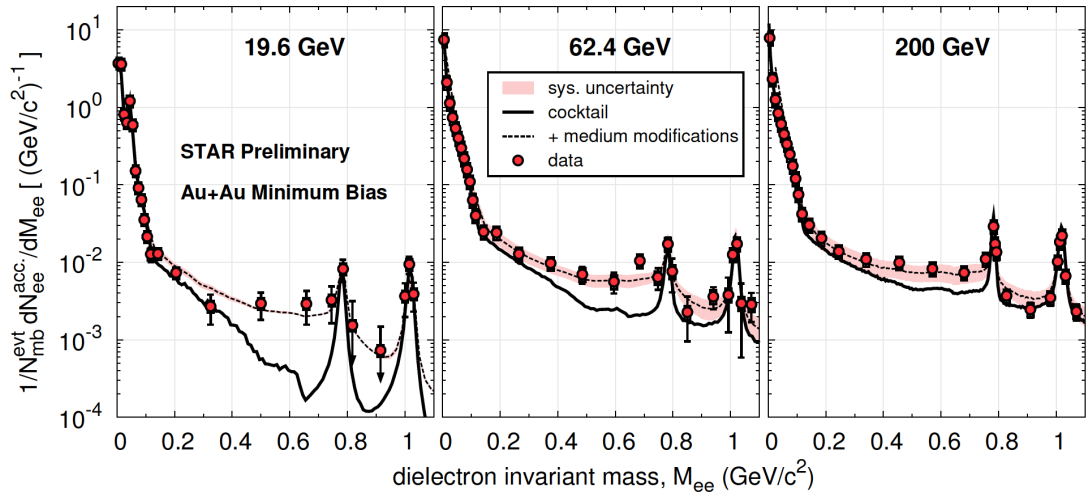


FIGURE 1.10: STAR preliminary results [37]. Di-electron mass spectra for different beam energies. The comparison with the broadening scenario is also shown in the plots.

1.2.3 Intermediate mass region

Theoretical models predict that the thermal radiation from QGP can be observed in the intermediate mass region [4, 38].

Di-leptons in the IMR have been measured at SPS energies initially by HELIOS-3 [39], and later by NA38 [40] and NA50 [41, 42]. All three experiments observed an excess with respect to the expected yield. Several models were able to describe the data equally well. Some models described the data using an enhancement of the $c\bar{c}$ production cross section [43, 44], and some models used thermal radiation to explain the excess [45, 46, 47, 48, 49].

The NA60 experiment measured the di-muon spectrum in 158 AGeV $In + In$ collisions and also found an excess in the IMR [50]. The big advantage of NA60 compared to the other experiments is the vertex information with a resolution of 10-15 μm , which enables the separation between a prompt source originating at the collision vertex and the semi-leptonic decays of heavy mesons originating at a displaced vertex. With this information, they proved that the excess is of prompt origin and interpreted it as thermal radiation from partonic processes.

The di-electron yield in the IMR behaves differently at RHIC. PHENIX observed N_{coll} scaling of its yield within the large experimental uncertainties as illustrated in Fig. 1.11 [35]. On the other hand, STAR observed the suppression of its yield in the most central collisions relative to N_{coll} scaling, although the discrepancy is still within the experimental uncertainties. Fig. 1.12 shows the data/cocktail ratio measured by STAR. The $c\bar{c}$ contribution in the cocktail is based on PYTHIA simulation scaled by N_{coll} . The suppression in the central events can indicate the modification of the charm contribution in the formed medium.

Although both results are consistent with N_{coll} scaling within the experimental uncertainties, there is a hint of spectral modifications. An additional measurement can provide further insight into those modifications.

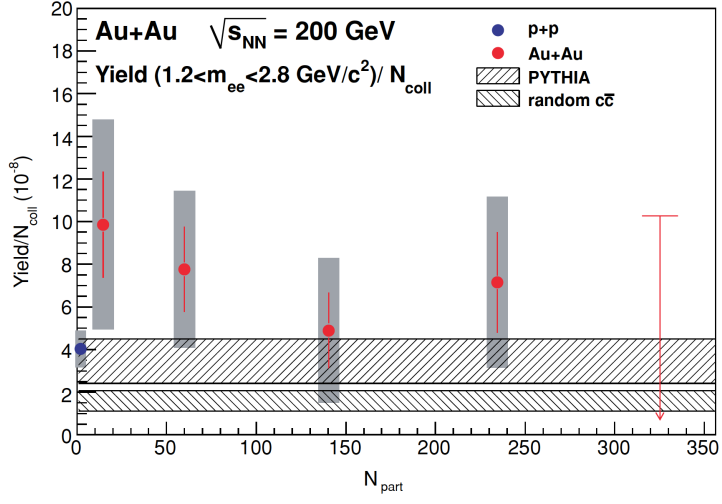


FIGURE 1.11: PHENIX results [35]: Di-electron yield in the IMR scaled with N_{coll} vs N_{part} .

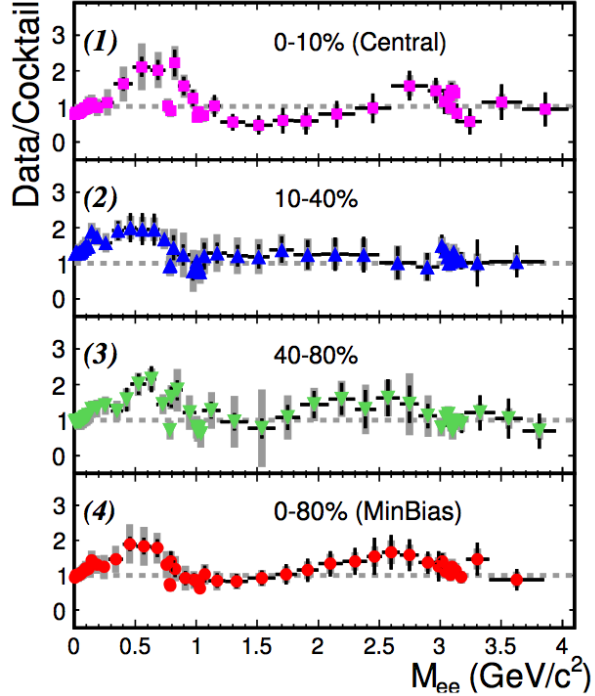


FIGURE 1.12: STAR preliminary results [37]: Data/cocktail ratio for each centrality bin. The $c\bar{c}$ contribution in the cocktail is based on PYTHIA simulation scaled by N_{coll} .

1.2.4 Charmonium J/ψ

The J/ψ yield in QGP was proposed to be suppressed because the color binding potential becomes short-ranged due to the Debye screening [51].

PHEIX and STAR performed J/ψ measurements at mid-rapidity ($|y| < 0.35$ for PHENIX and $|y| < 1$ for STAR). Figure 1.13 shows the nuclear modification factor R_{AA} as a function of N_{part} [52, 53]. The R_{AA} is defined as:

$$R_{AA} = \frac{\sigma_{AA}}{N_{coll} \sigma_{pp}} \quad (1.2)$$

where σ_{AA} and σ_{pp} are the cross sections in $Au + Au$ and $p + p$ collisions, respectively. The PHENIX and STAR results are consistent with each other. Therefore, the $J/\psi R_{AA}$ can be used to validate the di-electron analysis procedure.

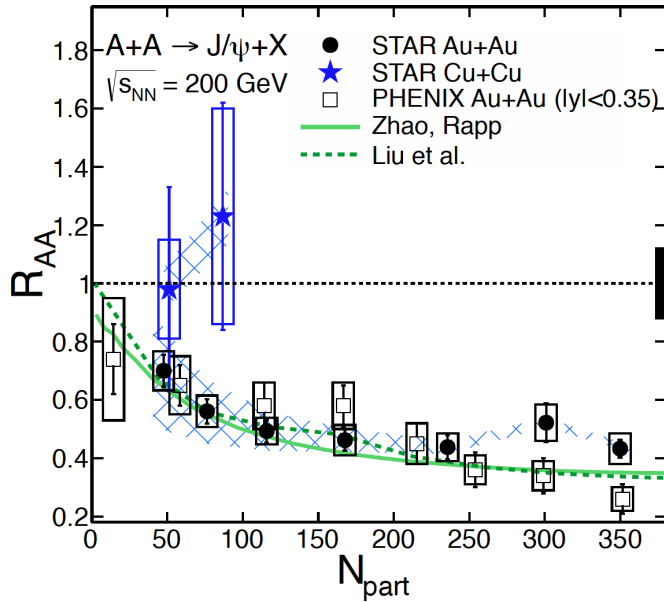


FIGURE 1.13: STAR and PHENIX results [52, 53]: The nuclear modification factor as a function of N_{part} measured by both experiments at mid-rapidity.

1.3 Purpose and organization of this thesis

Di-electron measurements in $Au + Au$ collisions at $\sqrt{s_{NN}} = 200$ GeV are already performed by PHENIX and STAR. (STAR results are still preliminary.) However, there is a large discrepancy between the two results in the low mass region.

Those previous experiments suffer from a large number of background electrons originating from π^0 Dalitz decays or γ conversions. A new detector, Hadron Blind Detector (HBD), is developed to reject those electrons by exploiting the fact that the opening angle of such pairs is very small compared to the opening angle of other sources like the light vector mesons.

The HBD was installed in PHENIX for 2010 $Au + Au$ runs (Run-10) and successfully operated. This manuscript presents the results of the first di-electron measurement at mid-rapidity using the HBD in $Au + Au$ collisions at $\sqrt{s_{NN}} = 200$ GeV. The major differences from the old PHENIX measurements are the following:

- The HBD is installed.
- Magnetic field is changed to make a field-free region for the HBD.

The organization of this thesis is as follows. Chapter 2 briefly describes the RHIC accelerator complex and the PHENIX detector. In Chapter 3, the calibration of HBD is explained. Detailed analysis procedure of di-electron measurement is summarized in Chapter 4. The results are presented in Chapter 5. Interpretations of the obtained results are also discussed in Chapter 5 by comparing the results with the old PHENIX measurement and theoretical models. Since the STAR results are still preliminary and acceptance corrected p_T spectra are not available yet, the comparison with the STAR results is not discussed in this thesis. In Chapter 6, the conclusion and an outlook for future di-electron measurements are summarized.

1.4 Major contributions

The major contributions of the author as a PHENIX collaborator are as follows:

1. Calibration of the HBD
2. Calibration of EMCal timing information
3. Di-electron analysis presented in this thesis

Chapter 2

Experimental setup

The data analyzed in this thesis are $Au + Au$ collisions at $\sqrt{s_{NN}} = 200\text{GeV}$ collected at the BNL Relativistic Heavy Ion Collider (RHIC) with the PHENIX detector. In this chapter the accelerator complex and the details of the PHENIX detector are presented.

2.1 Accelerator complex

The Relativistic Heavy Ion Collider (RHIC) is a collider type accelerator, whose circumference is 3.8 km, located at Brookhaven National Laboratory in the United States [54]. RHIC is a very flexible machine capable of accelerating a variety of nuclei at a variety of energies: Table 2.1 shows the nuclear species and energies that RHIC delivered from 2000 to 2013. This thesis uses the data from $Au + Au$ collisions at $\sqrt{s_{NN}} = 200\text{ GeV}$ collected in Run-10.

Figure 2.1 shows the path of a gold beam through the accelerator complex, Tandem Van de Graaff, Booster Synchrotron (BS), Alternating Gradient Synchrotron (AGS) and RHIC. The Au ions with negative charge (Au^-) originate from a pulsed sputter ion source and are delivered to the Tandem Van de Graaff. The Tandem accelerates the ions up to $\sim 1\text{ MeV/nucleon}$. Electron stripper foils are placed in the middle and at the end of the Tandem. Electrons are stripped and the ions become Au^{12+} and Au^{32+} , respectively. The Au^{32+} are then delivered to the BS and accelerated up to 100 MeV/nucleon. At the exit of the BS, another stripping foil brings the ions to be Au^{77+} . The ions are then injected into the AGS and accelerated up to $\sim 11\text{ GeV/nucleon}$. While transferring the ions to RHIC, the two remaining electrons are removed and the ions become Au^{79+} . The fully stripped gold ions are delivered to two RHIC super conducting rings: one is known as the Blue ring, where the beam circulates clockwise and the other one as the Yellow ring, where the beam circulates counterclockwise.

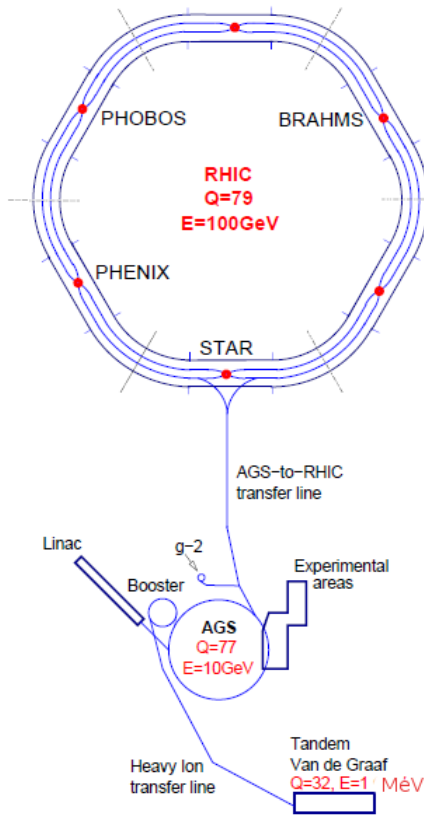


FIGURE 2.1: RHIC accelerator complex.

In Run-10, RHIC delivered $Au + Au$ collisions at a collision energy of $\sqrt{s_{NN}} = 200\text{ GeV/nucleon}$ and achieved an average luminosity of $20 \times 10^{26}\text{ cm}^{-2}\text{sec}^{-1}$, which is an order of magnitude above the design luminosity. The integrated luminosity during the 10.9 physics weeks was $\sim 10\text{ nb}^{-1}$ [55].

2.2 PHENIX overview

The PHENIX detector is a multi-purpose detector consisting of 4 spectrometers: two central arms [56] and two muon arms [57]. This thesis does not use the muon arms and therefore the muon arms are not described here. A schematic view of the two central arms, denoted as the East and West arms, is shown in Fig 2.2. Each arm covers ± 0.35 in pseudo-rapidity and 90° in azimuth with an offset of 67.5° from each other. The detectors used in the analysis are the following: Beam-beam counter (BBC), Zero Degree calorimeter (ZDC), Reaction Plane Detector (RXNP), Drift Chamber (DC), Pad

TABLE 2.1: Collision species and their energy delivered by RHIC from 2000 to 2013.

Run	Year	Species	$\sqrt{s_{NN}}$ (GeV)
1	2000	<i>Au + Au</i>	130
2	2001/2002	<i>Au + Au</i>	200
		<i>p + p</i>	200
3	2002/2003	<i>d + Au</i>	200
		<i>p + p</i>	200
4	2003/2004	<i>Au + Au</i>	200
		<i>Au + Au</i>	62.4
5	2004/2005	<i>Cu + Cu</i>	200
		<i>Cu + Cu</i>	62.4
		<i>Cu + Cu</i>	22.5
		<i>p + p</i>	200
6	2006	<i>p + p</i>	200
		<i>p + p</i>	62.4
7	2007	<i>Au + Au</i>	200
8	2008	<i>d + Au</i>	200
		<i>p + p</i>	62.4
9	2009	<i>p + p</i>	500
		<i>p + p</i>	200
10	2010	<i>Au + Au</i>	200
		<i>Au + Au</i>	62.4
		<i>Au + Au</i>	39
		<i>Au + Au</i>	7.7
11	2011	<i>p + p</i>	500
		<i>Au + Au</i>	19.6
		<i>Au + Au</i>	200
		<i>Au + Au</i>	27
12	2012	<i>p + p</i>	200
		<i>p + p</i>	510
		<i>U + U</i>	193
		<i>Cu + Au</i>	200
13	2013	<i>p + p</i>	510

Chamber 1 (PC1), Ring Imaging Čerenkov Counter (RICH), Electromagnetic calorimeter(EMCal), Time of Flight Detector in the east arm (TOFE) and Hadron Blind Detector (HBD). In addition, there is a central arm magnet with an integrated field integral $\int B dl \sim 0.43 T \cdot m$, for the charge and momentum determination of charged particles.

These subsystems can be categorized in five groups:

- Magnet
- Event characterization: BBC, ZDC, RXNP
- Tracking: DC, PC1

- Electron Identification: RICH, EMCal, TOFE, HBD
- π^0 Dalitz and γ rejection: HBD

A detailed description of each subsystem is given in the following sections. A data acquisition system, which enables the data collection from the high granularity detector, is also described in Section 2.8.

Figure 2.3 shows the global coordinate system used in PHENIX and Table 2.2 summarizes the coverage of each detector in terms of η and ϕ .

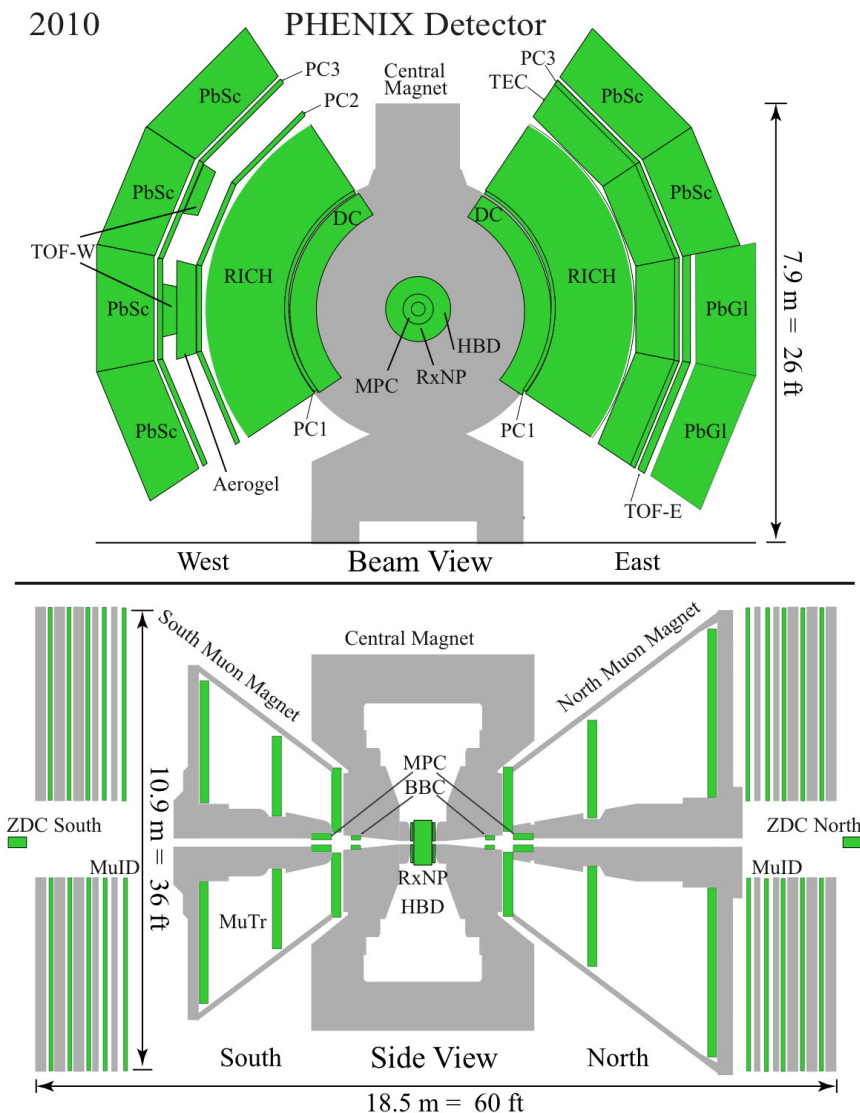


FIGURE 2.2: PHENIX configuration in 2010. The top panel shows the central arm from the beam view. The bottom panel shows the muon arms from the east side view.

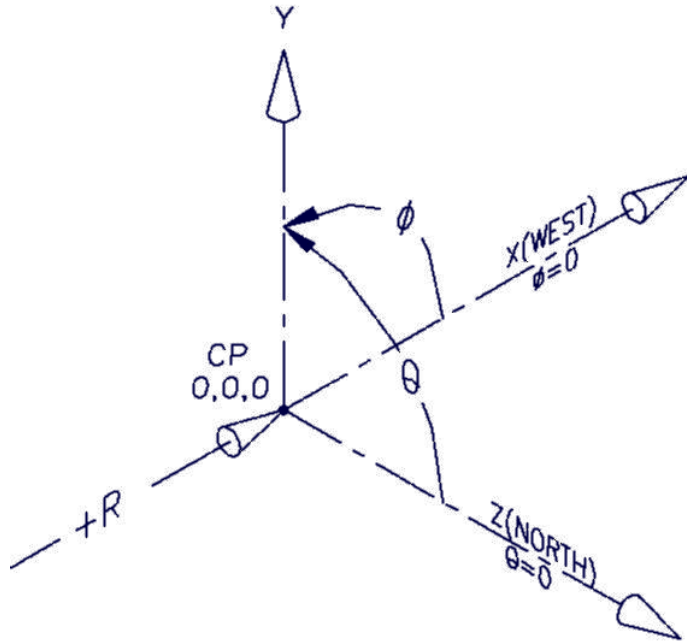


FIGURE 2.3: PHENIX coordinate system.

TABLE 2.2: Pseudo-rapidity $\Delta\eta$ and azimuthal $\Delta\phi$ coverage of each detector (Run-10 setup).

Subsystem	$\Delta\eta$	$\Delta\phi$
Magnet	± 0.35	360°
Beam-beam counters	± 3.1 to 3.9	360°
Zero-degree Calorimetr	± 2 mrad	360°
Drift Chamber	± 0.35	$2 \times 90^\circ$
Pad Chamber 1	± 0.35	$2 \times 90^\circ$
Ring Imaging Čerenkov Counter	± 0.35	$2 \times 90^\circ$
Time-of-Flight East	± 0.35	45°
PbSc EMCal	± 0.35	$90^\circ + 45^\circ$
PbGl EMCal	± 0.35	45°
HBD	± 0.45	$2 \times 112.5^\circ$

2.3 PHENIX Central Arm Magnet

The PHENIX magnet system consists of the Central Arm Magnet and the North and South Muon Magnets [58]. This section describes the Central Arm Magnet.

The PHENIX Central Arm Magnet provides a magnetic field parallel to the beam axis in the polar angle range from 70° to 110° , which corresponds to pseudo-rapidity range $|\eta| < 0.35$. The magnet is energized by two pairs of coils: outer coils and inner coils. These coils can be run with the fields for the two coils sets adding (the “++” or “––” configuration) or bucking (the “+–” or “–+” configuration). In Run-10, the “+–” configuration was used for the first half of the run duration and the “–+” configuration was used for the latter half. Figure 2.4 shows the magnetic field lines of the Central Arm Magnet for the “+–” configuration. The field strength as a function of the distance from the beam axis at $z \sim 0$ is shown in Fig 2.5 together with that of the “++” and only outer coil configurations. The field integral at $z \sim 0$ is 0.43 T·m in the “+–(–+)” configurations.

In the “+–(–+)” configuration, the current in the inner and outer coils go in opposite directions, resulting in an almost field free region below $\sim 60\text{cm}$. This field free region is essential for the Hadron Blind Detector as described in Section 2.7.

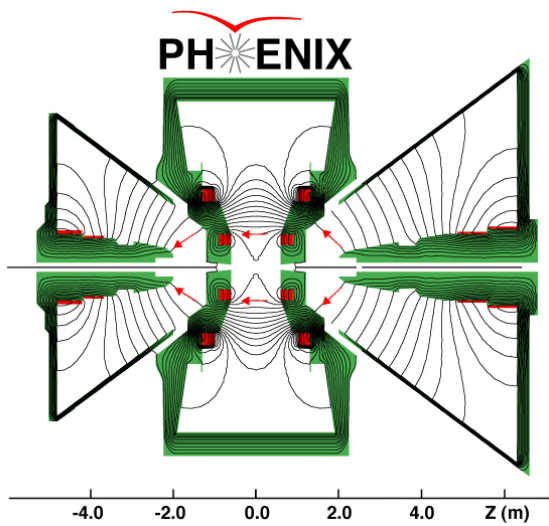


FIGURE 2.4: Magnetic field lines in the “+–” field configuration [58].

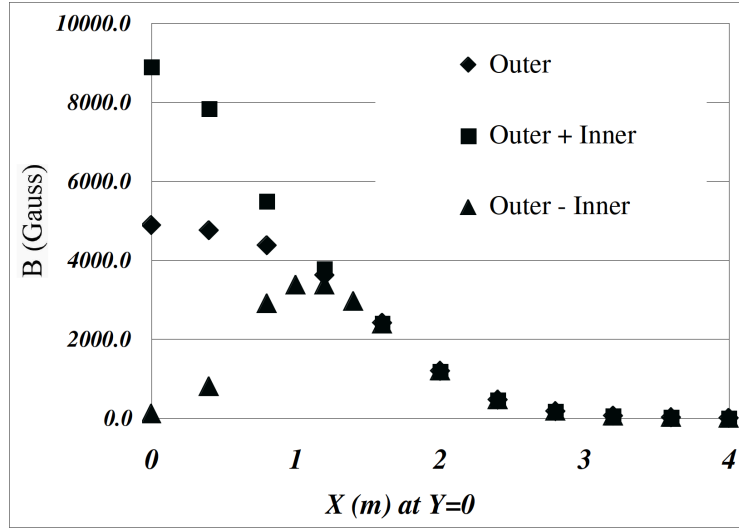


FIGURE 2.5: Magnetic field strength as a function of the distance from the beam axis [58].

2.4 Event Characterization

2.4.1 Beam-beam counter (BBC)

The main role of BBC is to provide the trigger for collisions, to measure the time of collisions with respect to the RHIC clock, to measure the vertex position along the beam axis and to determine the collision geometry [59, 60]. The determination of collision geometry is described in Sec 4.2.

The BBC consists of two identical sets of counters installed on both sides of the collision point along the beam axis, one on the North side and the other on the South side. (Fig. 2.6.) Each BBC is made up of 64 photomultiplier tubes, which have an intrinsic time resolution of ~ 50 ps, and are equipped with quartz Čerenkov radiators in front. The BBC counters are placed at 144 cm from the nominal $z=0$ interaction point and cover the pseudo-rapidity range of $3.0 < |\eta| < 3.9$ over the full azimuth.

The vertex (z^{BBC}) and the time (t_0^{BBC}) of collisions are determined from the hit time of the North and South BBC counters as follows:

$$t_0^{BBC} = \frac{t_N^{BBC} + t_S^{BBC}}{2} - \frac{L}{c} \quad (2.1)$$

$$z^{BBC} = c \frac{t_N^{BBC} - t_S^{BBC}}{2} \quad (2.2)$$

where L is 144 cm, c is the speed of light, t_N^{BBC} and t_S^{BBC} are the hit time of each BBC counter.

A coincidence of the two BBC counters and a vertex position along the beam axis constitutes the Minimum-Bias Level-1 trigger requirement. (See Sec 2.8)

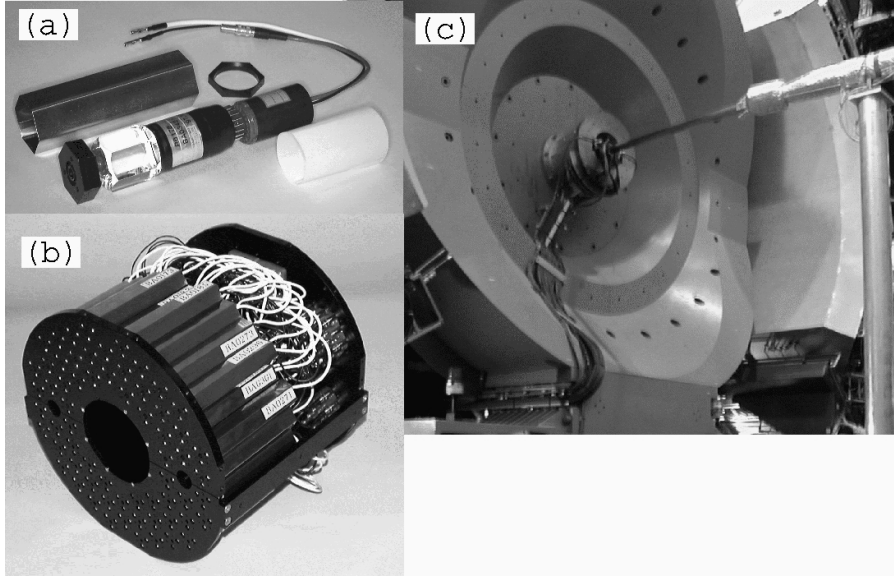


FIGURE 2.6: (a) Single Beam Beam counter consisting of one-inch mesh dynode photomultiplier tube mounted on a 3 cm quartz radiator. (b) A BBC array comprising 64 BBC elements. (c) The BBC is shown mounted on the PHENIX detector. The beam pipe is seen in the middle of the picture. The BBC is installed on a mounting structure just behind the central spectrometer magnet [59].

2.4.2 Zero degree calorimeter (ZDC)

The main purpose of the ZDC is to provide the trigger for collisions, to measure the vertex position and to monitor the beam luminosity. The ZDC measures the total energy and the hit time of the spectator neutrons [61].

The ZDCs are sampling type hadron calorimeters, which are located at ± 18 m from the interaction point, just behind beam bending magnets, such that charged particles will be deflected out of the acceptance before they can hit the ZDC. Figure 2.7 illustrates the plan view of the collision region showing the location of the ZDCs.

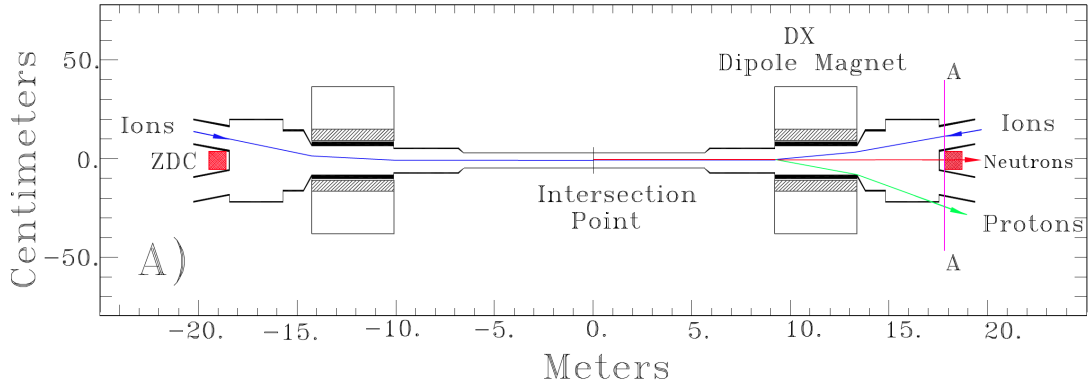


FIGURE 2.7: A plan view of the collision region showing the location of the ZDCs [61].

2.4.3 Reaction Plane Detector (RXNP)

The Reaction Plane Detector (RXNP) consists of two plastic scintillator paddle detectors [62]. The RXNP measures the reaction plane (RP) angle event-by-event. The reaction plane is defined as the plane spanned by the beam axis and the vector connecting the centers of the colliding nuclei illustrated as the x-z plane in Fig. 4.2.

The RXNPs are located along the beam pipe at a distance of ± 39 cm from the center of PHENIX and comprises a set of 24 scintillators on each arm. A schematic view of the scintillators arrangement is illustrated in Fig 2.8, where the inner and outer layers of one RXNP arm are highlighted. The hole in the center of the arm represents the position of the beam pipe. Each arm covers a pseudo-rapidity range of $1.0 < |\eta| < 2.8$ and 2π in azimuthal angle. Each scintillator is embedded with fiber light guides on the surface every 0.5 cm and uses PMTs as readout.

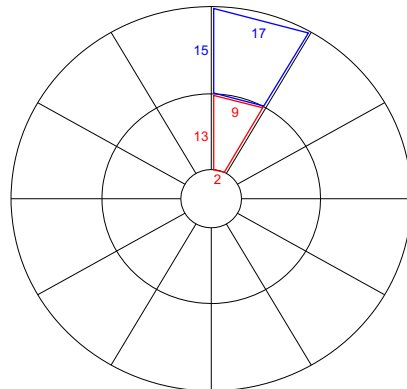


FIGURE 2.8: Schematic view of the arrangement of the scintillators in one RXNP arm. The length of each scintillator side is shown in centimeters [62].

2.5 Charged Particle Tracking

The charged particle tracking in PHENIX is performed in each central arm by DC and a set of PCs. The main detector features of DC and PCs are described below.

2.5.1 Drift Chamber (DC)

The PHENIX drift chamber is a multiwire gaseous detector located at a radial distance of $2.02 < R < 2.48$ m [65, 66]. The DC is made of two identical chambers, one in each arm, each one covering 90° in azimuth and 2 m along the z direction. The DC measures the trajectories of charged particles in the $r - \phi$ plane in order to determine their charge and transverse momentum p_T .

The active volume of the DC is filled with a mixture of 50% Argon and 50% Ethane. The mixture is chosen due to its good uniform drift velocity at an electric field of $E \sim 1$ kV/cm, high gain, and low diffusion coefficient. Each chamber volume is defined by a cylindrical titanium frame, divided into 20 identical sectors, each one covering 4.5° in ϕ . There are six types of wire modules in each keystone, called X1, U1, V1, X2, U2, and V2. The X1 and X2 wires are aligned parallel to the beam axis. The U and V stereo wires are oriented at an angle of $\sim 6^\circ$ relative to the X wires (See Fig. 2.9), and measure the z coordinate of the tracks. Each wire module contains alternating in azimuthal direction, four anode (sense) and four cathode planes,. In addition to anode and cathode wires, each plane contains “gate” wires and “back” wires as shown in the left panel of Fig. 2.9. The latter shape the electric field lines such that every sense wire is alternatively sensitive to drift charges from only one side, limiting the left-right ambiguity to a region of ± 2 mm. In order to allow for pattern recognition with up to 500 tracks, each sense wire is electrically insulated in the middle by a $100\ \mu\text{m}$ thick kapton strip. Each half of a sense wire is read out separately.

The single wire position resolution is found to be $165\ \mu\text{m}$ with a single wire efficiency of 95-96%.

2.5.2 Pad Chamber (PC)

The PCs consist of three layers of multiwire proportional chambers, with cathode pad readout [66, 67]. They provide space points along the trajectory of charged particles to determine the polar angle θ , used to calculate the p_z component of the momentum vector.

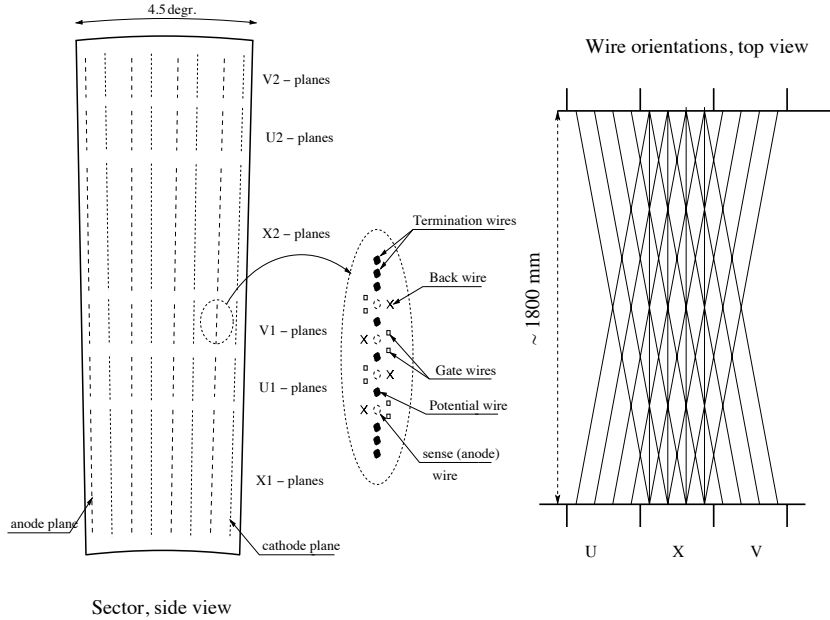


FIGURE 2.9: The layout of wire position within one sector and inside the anode plane (left). A schematic view of the stereo wire orientation (right) [66].

PC1 is essential for the 3D momentum determination by providing the z-coordinate at the exit of the DC. The DC and PC1 information are combined to determine the straight-line trajectories outside the magnetic field. PC2 and PC3 are needed to resolve ambiguities in the outer detectors where about 30% of the particles striking the EMCal are produced by either secondary interaction or decays outside the aperture of DC and PC1.

The PC1 is installed just behind the drift chambers, while PC3 sits in front of the EMCal. The PC2 is only present in the west arm following the RICH detector. Each PC contains a single layer of wires within a gas volume that is confined by two cathode planes located at ± 6 mm from the wire plane. One cathode plane is solid copper, while the other one is segmented into a fine array of pixels as shown in Fig. 2.10. The basic unit is a pad formed by nine non-neighboring pixels connected together, which are read out by one common channel. One cell contains three adjacent pixels in the ϕ direction and an avalanche must be sensed by all three pixels to form a valid hit. The three pixels in a cell always belong to different, but neighboring pads and each cell corresponds to a unique pad triplet. This interleaved design scheme saves a factor of nine in readout channels while allowing a fine position resolution. The achieved performance of the PCs are listed in Table 2.3.

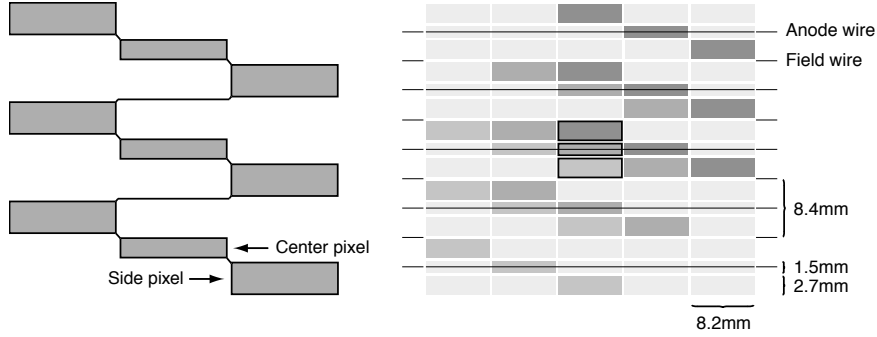


FIGURE 2.10: The pad and pixel geometry (left). A cell defined by three adjacent pixels is at the center of the right picture. The numbers shown in the figure are for PC1 [66].

TABLE 2.3: The performance of PC1, PC2 and PC3.

Performance	PC1	PC2	PC3
Position resolution in z (mm)	1.7	3.1	3.6
Efficiency	$\geq 99\%$	$\geq 99\%$	$\geq 99\%$

2.6 Electron identification

Electron identification is provided by the combined information of the following detectors: RICH, EMCal, TOFE and HBD. The details of the detectors are discussed in this section.

2.6.1 Ring Imaging Čerenkov Counter

Each central arm contains a RICH detector, that serves as the primary device for electron identification in PHENIX [68, 69, 70]. It is a threshold gas Čerenkov detector that provides an e/π separation below 4.87 GeV/ c .

Each RICH detector has a gas volume of 40 m^3 filled with CO₂, which has a refractive index $n = 1.000410$ at 20°C and 1 atm. This corresponds to a threshold velocity $\beta_t = 1/n = 0.99590168$, resulting in a Čerenkov threshold of $p_T = m\gamma\beta = 18 \text{ MeV}/c$ for electrons ($m_e = 0.511 \text{ MeV}/c^2$) and $4.87 \text{ GeV}/c$ for charged pions ($m_\pi = 139.57 \text{ MeV}/c^2$).

Figure 2.11 shows a schematic view of the RICH detector. The Čerenkov light is focussed by two intersecting spherical mirrors onto two arrays of 1280 photomultiplier tubes (PMT), located on either side of the entrance window. The PMTs are equipped with 2 inch diameter Winston cones and have magnetic shields that allow them to operate in

$120/\text{cm}^2$

trance and exit windows are $125\ \mu\text{m}$ thick, and are

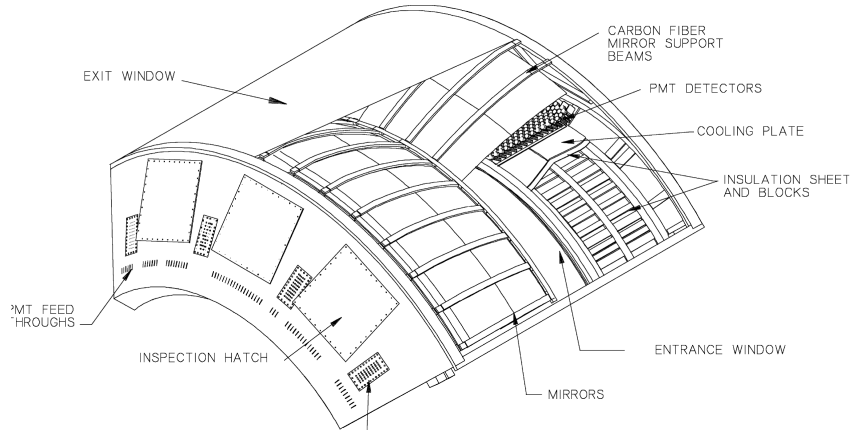


FIGURE 2.11: A cutaway view of the PHENIX RICH detector [68].

a magnetic field of up to 0.01T . In total, the RICH detector has $5120\ \text{PMTs}$ ($2\ \text{arms} \times 2\ \text{sides} \times 16\ \text{in } \theta \times 80\ \text{in } \phi$). An average of $10\ \text{photons per } \beta \approx 1$ particle are emitted under the angle θ_C ($1/(n\beta)$) $\approx 9\ \text{mrad}$ and get focussed to a ring on the PMT array with a diameter of about $11.8\ \text{cm}$.

The PMTs are connected to preamps mounted on small boards attached to the RICH vessel. The preamp output is fed into a charge integrating amplifier followed by a variable gain amplifier. Then the outputs are stored in Analog Memory Units (AMU) clocked at the RHIC beam clock frequency. If a Level 1 accept signal is received, the voltages of the AMU cell coinciding with the “previous(pre)” and “post” clock of the event are digitized. Once the digitization is completed, event data are collected from each module into Readout Modules and sent to Data Collection Modules (DCM). In the offline analysis, the signal is defined as the difference of the “pre” and “post” samples.

2.6.2 Electromagnetic Calorimeter

The EMCal measures the spacial position, energy and time-of-flight of electrons [71]. The EMCal consists of two subsystems with different technologies. The first one is a shashlik type sampling calorimeter [72] consisting of 15552 lead-scintillator (PbSc) towers that covers $3/4$ of the central arm acceptance. The other quarter is covered by a homogeneous detector of 9216 lead-glass (PbGl) Čerenkov calorimeters, which were previously used in the CERN experiment WA98 at the SPS.

Lead Scintillator Calorimeters (PbSc)

Each PbSc tower contains 66 sampling cells consisting of alternating tiles of Pb and scintillator. These cells are connected by penetrating optical fibers. The light is read out by phototubes at the back of the towers. Four optically isolated towers are grouped into a single structural entity called a module as shown in Fig. 2.12. Thirty six modules are held together forming a rigid structure called supermodule. Eighteen supermodules make a sector. There are 6 sectors, 4 in west and 2 in east. The energy resolution of PbSc obtained from electron beam test is:

$$\frac{\sigma_E}{E} = \frac{8.1\%}{\sqrt{E(\text{GeV})}} \oplus 2.1\% \quad (2.3)$$

The PbSc has a timing resolution of ~ 450 ps.

Lead Glass Calorimeters (PbGl)

Each PbGl tower or module has a cross-section of $4.0 \text{ cm} \times 4.0 \text{ cm}$ and is 40 cm long. The modules are grouped in arrays of 6×4 modules that form supermodules. The supermodules are in turn grouped into a PbGl sector made of 192 supermodules as an array of 16×12 supermodule(Fig. 2.13). At the back of the towers, PMTs are used for readout. The energy resolution of the PbGl obtained from electron beam tests is:

$$\frac{\sigma_E}{E} = \frac{5.9\%}{\sqrt{E(\text{GeV})}} \oplus 0.8\% \quad (2.4)$$

The PbGl has a timing resolution of ~ 700 ps.

2.6.3 East arm Time of Flight Detector

The TOFE is placed in front of part of the PbGl in the East Arm [70]. The TOFE consists of 10 panels of TOF walls and one TOF wall consists of 96 segments, each equipped with a plastic scintillator slat read out at both ends by PMTs. Figure 2.14 shows a picture of the TOFE mounted on the East Arm. All the 10 panels are shown in the picture. Figure 2.15 shows a schematic view of one panel.

The TOFE has a timing resolution of ~ 150 ps.

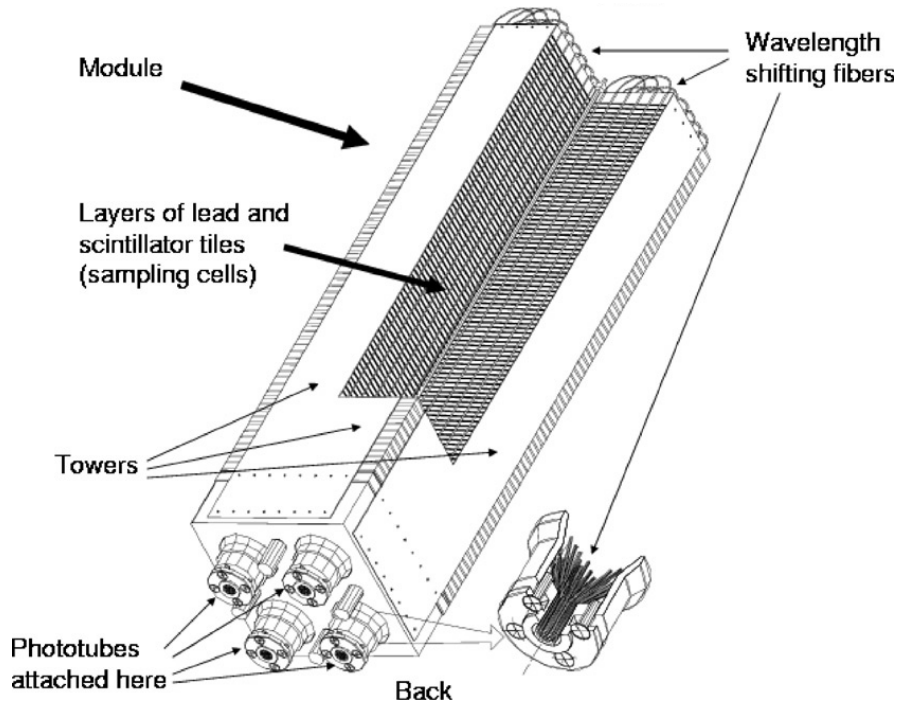


FIGURE 2.12: A schematic view of a PbSc module [71].

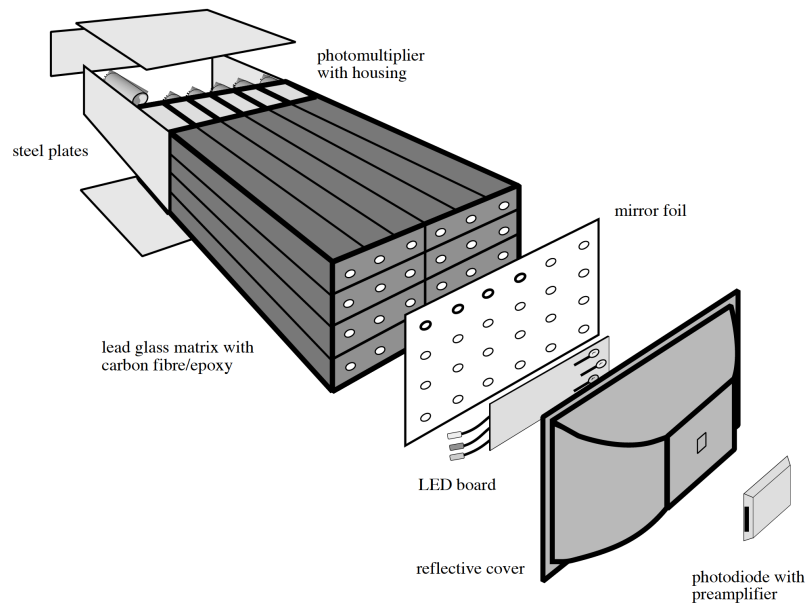


FIGURE 2.13: A schematic view of a PbGl supermodule [71].

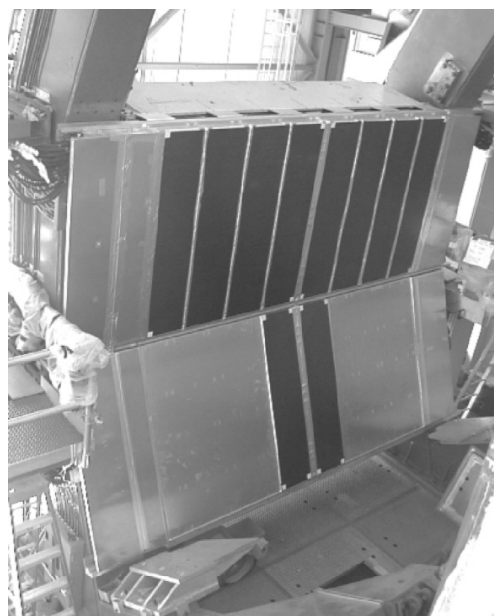


FIGURE 2.14: Picture of the TOFE mounted on the East arm [70].

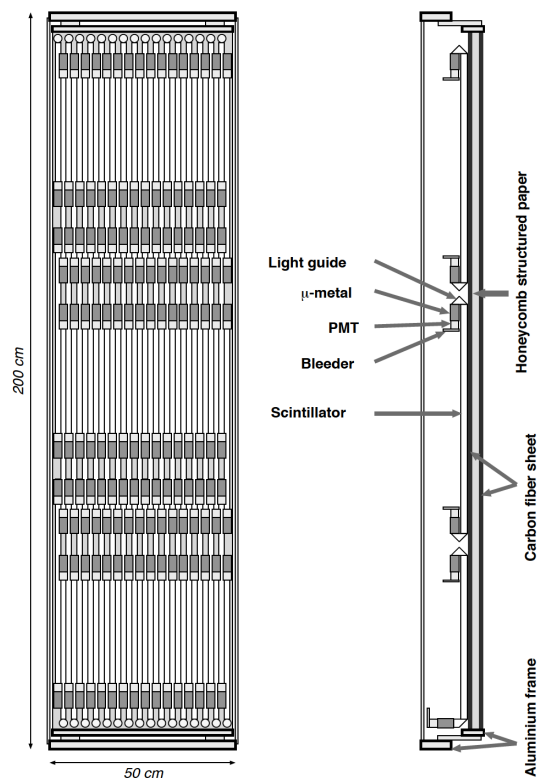


FIGURE 2.15: Schematic view of one TOFE panel [70].

2.7 Hadron Blind Detector (HBD)

The Hadron Blind Detector (HBD) aims at rejecting electrons coming from π^0 Dalitz decays and γ conversions, which are major background sources in electron measurements [73, 74]. This is achieved by exploiting the fact that the opening angle of electron pairs from these sources is very small compared to the opening angle of other sources like the light vector mesons. To preserve the opening angle, the HBD is placed in a field free region.

The HBD is a Čerenkov detector consisting of a 50 cm long radiator operated with pure CF_4 and directly coupled to a triple Gas Electron Multiplier (GEM) photon detection element. The principle of electron detection is illustrated in the right panel of Fig. 2.16. The Čerenkov photons emitted by an electron track form a circular image, which we call “blob”, on the top GEM. On the top surface of the top GEM, a CsI photocathode is evaporated to convert the Čerenkov photons into photoelectrons. The quantum efficiency of CsI in vacuum and CF_4 is shown in Fig. 2.17 [75]. The photoelectrons are collected and amplified by the triple GEM foils and finally detected by an hexagonal pad readout at the bottom. Each pad has an area of $\sim 6.2 \text{ cm}^2$, which is slightly smaller than the Čerenkov blob size.

The readout pads are connected to individual hybrid preamplifiers mounted at the back of the detector. Then, the differential output from the preamplifier is delivered to the Front End Module (FEM). In the FEM, after a further shaping, the signals are digitized using a 65 MHz 12 bit flash ADC. Upon receiving a Level 1 trigger, 12 samples per ADC channel are sent to Data Collection Modules (DCM) via optical fiber. In the offline analysis, the signal is defined as the difference of the samples $(8+9+10) - (0+1+2)$.

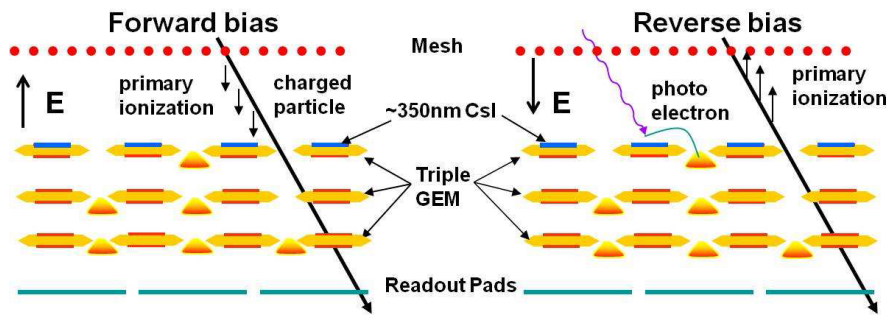


FIGURE 2.16: Triple GEM stack operated in the standard forward bias mode (left) and reverse bias mode (right) [74].

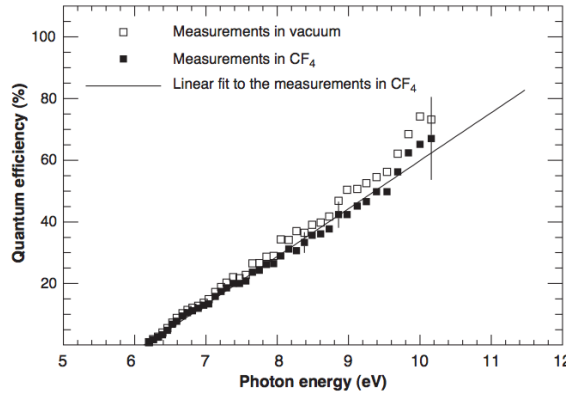


FIGURE 2.17: Absolute quantum efficiency of CsI in vacuum and CF_4 over the band-width 6.2-10.3 eV [75].

A 3D view of the HBD is shown in the left panel of Fig. 2.18. The HBD is made of two identical arms placed around the beam pipe. Each arm covers 135° in azimuth and ± 0.45 in pseudorapidity. The right panel of Fig 2.18 shows each component of one HBD arm. The total material budget of the HBD in the PHENIX central arm acceptance is 2.4% including 0.56% from CF_4 and 1.8% from the backplane of the HBD.

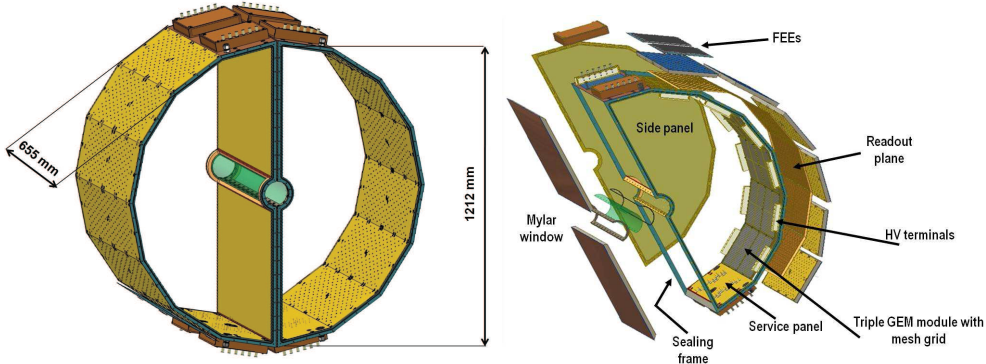


FIGURE 2.18: The 3D view of the two arm HBD. (left) Exploded view of one HBD arm. (right) [74].

One HBD arm consists of 12 detector modules, 6 modules in ϕ and 2 modules in z . The size of each detector module is $\sim 23 \times 27\text{cm}^2$. In Run-10, 9 modules in east arm and 10 modules in west arm were operated.

The HBD becomes insensitive to hadrons when the triple GEM stack is operated in the so-called reverse-bias mode as shown in the right panel of Fig. 2.16. The regular

forward-bias mode is also shown in the left panel of the figure. In the reverse bias mode, the voltage of the mesh is set higher than the voltage of the top GEM. As a result, the ionization electrons produced by hadrons drift towards the mesh and are not detected by the readout pads.

In Run-9 $p + p$ collisions, the HBD was successfully operated and its ability to identify electrons from π^0 Dalitz decays and γ conversions was confirmed [74]. As mentioned above, the opening angle of the electron pairs from those sources is small, therefore, they produce a double signal amplitude compared to that of a single electron. The HBD responses of the single and double electrons are extracted using pairs with their mass below $150 \text{ MeV}/c^2$. In the mass region, the contribution from the combinatorial background is negligible. The extracted responses are shown in the left and the right panel of Fig. 2.19. The single electron response peaks around 20 photoelectrons and the double electron response peaks at around 40 photoelectrons. With the achieved number of photoelectrons, $\sim 80\%$ of the double electrons can be rejected with an efficiency of $\sim 90\%$.

Using this performance, the benefit of the HBD on a di-electron analysis can be estimated. Assuming half of the background electrons produces the overlapping double response, the average efficiency of background electrons becomes $0.5 \cdot 0.9 + 0.5 \cdot 0.2 = 0.55$. Two figures of merit, the effective signal (S/\sqrt{B}) and the signal-to-background ratio(S/B), are calculated as:

$$\frac{S}{\sqrt{B}} \propto \frac{\epsilon_{single}^2}{\epsilon_{background}} \sim 1.5 \quad (2.5)$$

$$\frac{S}{B} \propto \frac{\epsilon_{single}^2}{\epsilon_{background}^2} \sim 3 \quad (2.6)$$

where ϵ_{single} is the single electron efficiency (0.9) and $\epsilon_{background}$ is the background electron efficiency (0.55). Therefore, the HBD is expected to improve the effective signal by 50% and the signal-to-background ratio by a factor of 3.

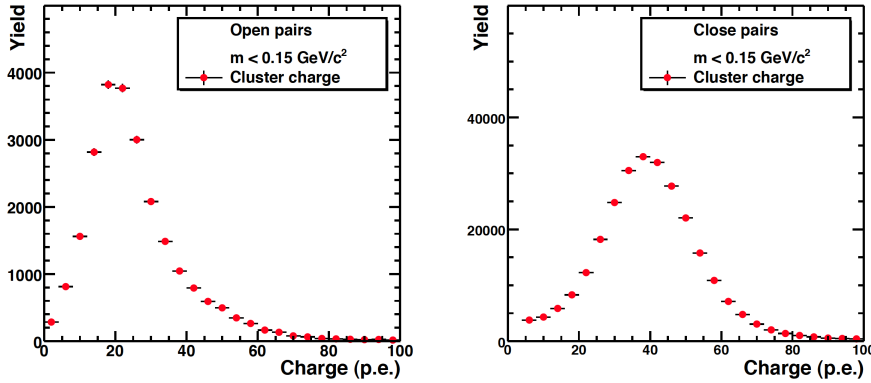


FIGURE 2.19: HBD response to single electrons (left) and to unresolved double hits (right) [74].

2.8 Trigger

In Run-10, PHENIX collected data using a minimum bias trigger based on the response of BBC. The Minimum Bias trigger requires at least two hits in each of the BBCs. In addition, two types of vertex ranges are required: one is $|z| < 25 \text{ cm}$ and the other is $|z| < 38 \text{ cm}$. They are referred to as “narrow vertex trigger” and “wide vertex trigger”. The “narrow vertex trigger” is used when beam luminosity is high, e.g. at the beginning of a fill.

The offline Minimum Bias trigger also requires one hit in one of the ZDCs. The trigger efficiency is estimated to be $92^{+2.5}_{-3.0} \%$ of the $Au + Au$ inelastic cross section.

2.9 Data Acquisition

The PHENIX data acquisition (DAQ) system [76] processes the signals from each detector subsystem, produces the trigger decision and stores the triggered data.

The DAQ can handle the large event sizes ($\sim 200 \text{ kbytes}$) of the high multiplicity $Au + Au$ events at an interaction rate of 10 kHz. A schematic view of the data acquisition flow is shown in Fig. 2.20.

The overall control of the DAQ is provided by the Master Timing Module (MTM), the Granule Timing Module (GTM), and the GL1. The MTM receives the RHIC clock and delivers it to the GTM and GL1. The GTM delivers the clock, the control commands

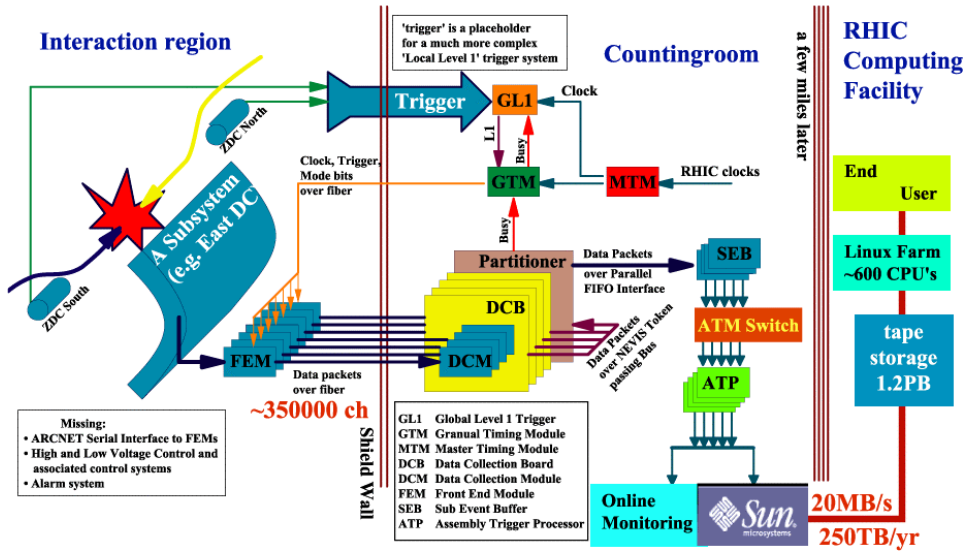


FIGURE 2.20: Schematic diagram of the data acquisition system [76].

(Mode Bits), and the event accept signal to the Front End Modules (FEMs) of each detector.

The FEM of each detector is designed to convert the analog response of the detectors into a digitized signal. The LVL 1 trigger signals are simultaneously generated. The generation of the global decision, whether an event should be taken or not, takes ~ 30 bunch crossings. During that time, the event data is stored in the FEM. After receiving the accept signal, each FEM starts digitizing the data.

The data collection from each FEM is performed by a Data Collection Module (DCM) connected to the FEM via an optical fiber cable. The DCMs provide data buffering, zero suppression, error checking and data formatting. The DCMs send the compressed data to the Event Builder (EvB).

The EvB consists of 39 Sub Event Buffers (SEBs), an Asynchronous Transfer Mode (ATM) switch and 52 Assembly Trigger Processors (ATPs). The SEBs are the front end of the EvB and communicate with each granule. The SEBs transfer the data from granule to the ATP via the ATM, where the event assembly is performed. The combined data are stored on disk with a maximum logging rate of 400 Mbytes/s.

Chapter 3

HBD calibration and performance

HBD is a new detector installed in the PHENIX setup for first physics running in 2010. This chapter describes the software that had to be developed to make use of the HBD in the data analysis. Gain calibration and quantum efficiency correction are described in Section 3.1 and 3.2, respectively. The alignment of the HBD relative to the central arms is described in Section 3.3. Then, the scintillation background subtraction is described in Section 3.4. Finally, pattern recognition algorithms are discussed in Section 3.5.

3.1 Gain calibration

3.1.1 Gain determination

The gain of each detector is determined using the scintillation light emitted by charged particles traversing the CF_4 radiator. The scintillation light response has a characteristic feature being a single pad hit which is not associated to any of the central arm charged tracks. Figure 3.1 shows a pulse height distribution of such pads. The exponential component in the very low amplitude part is due to the scintillation light. Using the slope S of the exponential distribution, the gain G of a module is calculated as:

$$G = S^{-1} \tag{3.1}$$

The expression is true only when the average number of scintillation photons in a fired pad is one. This assumption breaks in central $Au + Au$ collisions, where the probability of scintillation pile up is significant as shown in Section 3.4. Therefore, the gain in $Au + Au$ collisions has been determined selecting only very peripheral events with a centrality $> 60\%$. (See Section 4.2 for the determination of centrality.)

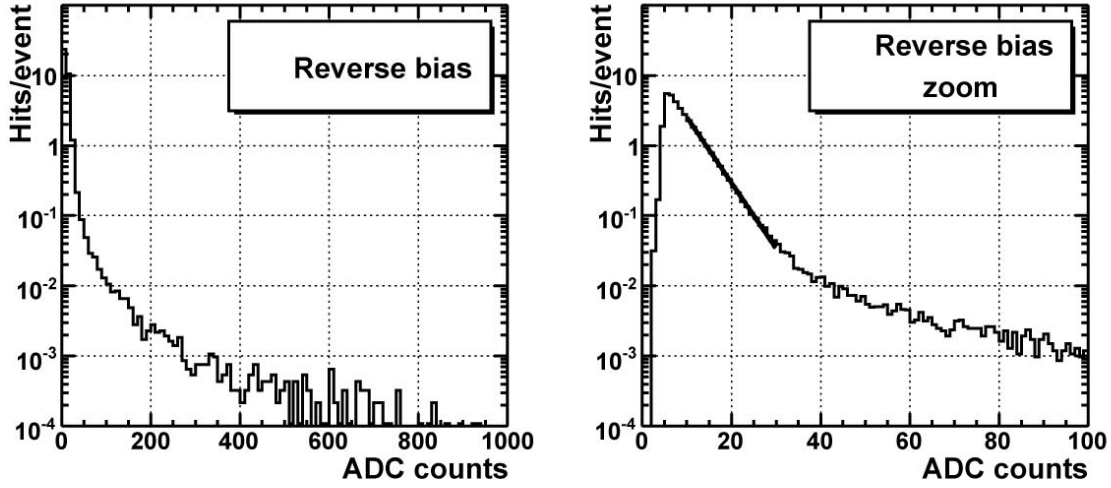


FIGURE 3.1: Pulse height distribution in one detector. The ordinate is normalized to represent the number of hits per event.

The gain in the detector varies as function of time due to two factors:

- Variations of pressure P and temperature T produce variations in the gain. For example a change of P/T by $\sim 6\%$ induces a gain variation by a factor of 2 [74]. To avoid large excursions of the gain during the run, the detector HV was varied automatically whenever the P/T value crossed the boundaries of 5 pre-determined P/T windows. These windows were chosen such that within each window the gain variations are limited to $\sim 20\%$. The voltage changes were applied only before the start of a new run. As an example, Fig. 3.2 shows the gain in ADC channels units versus run sequential number for the 9 modules of the East arm.
- Charge up effects. It is known that some GEMs show an initial rise of gain after switching on the high voltage or even after switching from standby (i.e. voltage below any gas amplification) to operational voltage. Since during the run the HBD HV was usually at standby or even off before a new fill, the charge up effect is clearly visible at the beginning of new runs corresponding to a new fill. An example is shown in Fig. 3.3. Over a time scale of a few hours the gain is observed to increase between a few percent up to a few tens of percent.

To cope with these gain variations, we determine the gain of each module every 3 minutes of data taking. For that we use the beam clock information stored in each event during data acquisition.

To summarize, the gain calibration during the entire run was done as follows. For each 3 minutes of data taking and for each module:

- Select peripheral events (centrality > 60%)
- Correct the pad amplitude by the pad to pad equilibration factor described in the next section
- Determine the module gain using the scintillation hits

During the analysis of HBD data, each fired pad is first corrected by the pad to pad equilibration factor described in the next section and then the corrected amplitude is divided by the gain corresponding to the same time stamp in order to convert the pad signal into photoelectrons.

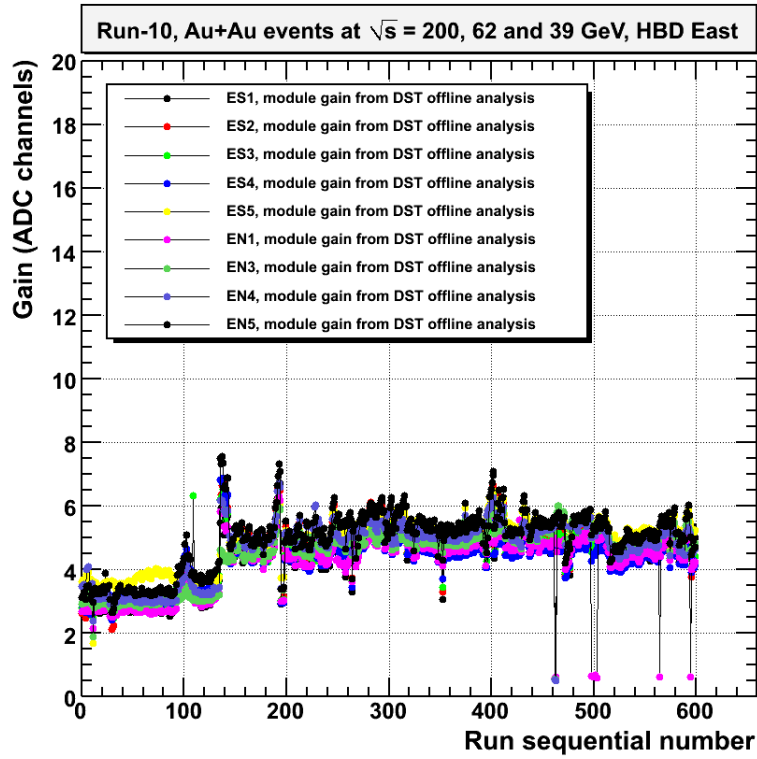


FIGURE 3.2: Gain versus run number.

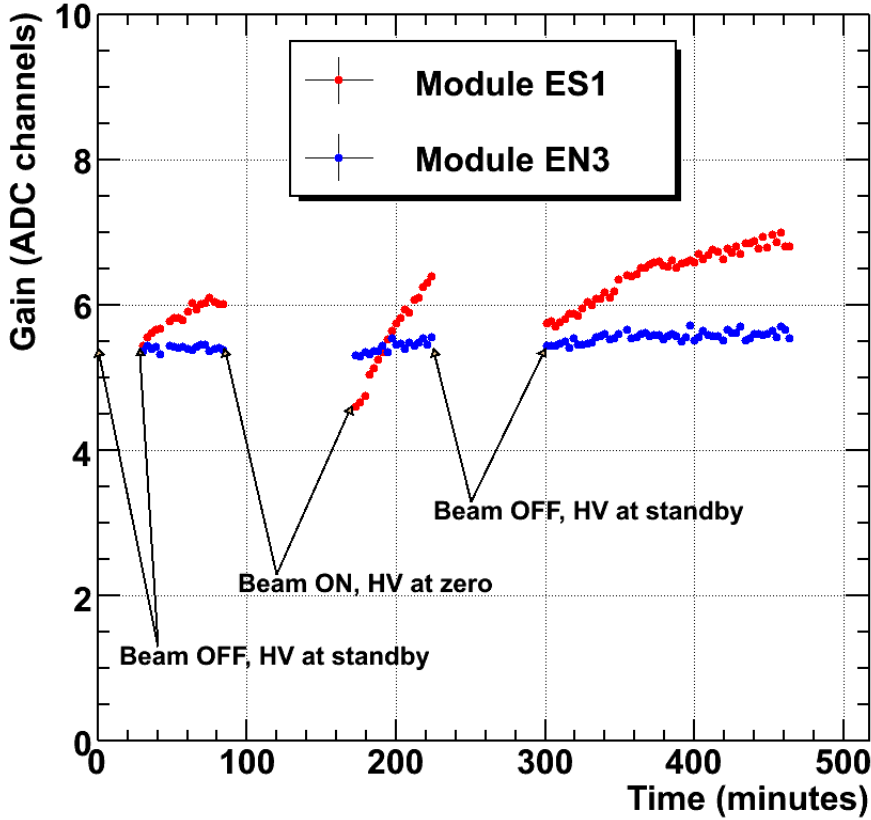


FIGURE 3.3: Gain versus time for two detector modules. The data are from a few runs taken at the end of the 200 GeV part of Run 10.

3.1.2 Pad-to-pad gain equilibration

Although the detector gain is determined for each module and for each run separately, the gain is not necessarily uniform over the entire module area. There are gain variations across each GEM's area, which arise from small differences in the size of the holes and from the mechanical tolerances of the gaps. In order to correct for these variations, we use a gain equilibration procedure that normalizes the gain of each pad, G_{pad} , in a given module to the average gain of the module $\langle G \rangle$.

The procedure applied to determine the gain of each pad, is the same as the one to obtain the gain in the whole module. We select only the scintillation hits, i.e. single pad hits not associated with any particle track. For this we use peripheral events selected with less than 5 central arm tracks. The lower part of the spectrum is fitted with an exponent, as shown in Figure 3.4, and the gain is extracted as the inverse of the fitted slope. The fit is made in the histogram of ADC counts, in the range determined by $(\text{maximum} + 2) - (\text{mean} + 12)$. A single run with large statistics ($\sim 45M$ events) is

sufficient to derive the equilibration constants, $c_{\text{pad}} = \langle G \rangle / G_{\text{pad}}$. The same equilibration constants are applied for all the runs. This means that the signal in each pad, A_{pad} , is corrected according to:

$$A_{\text{pad}}^* = c_{\text{pad}} \times A_{\text{pad}} \quad (3.2)$$

where A_{pad}^* is the corrected amplitude.

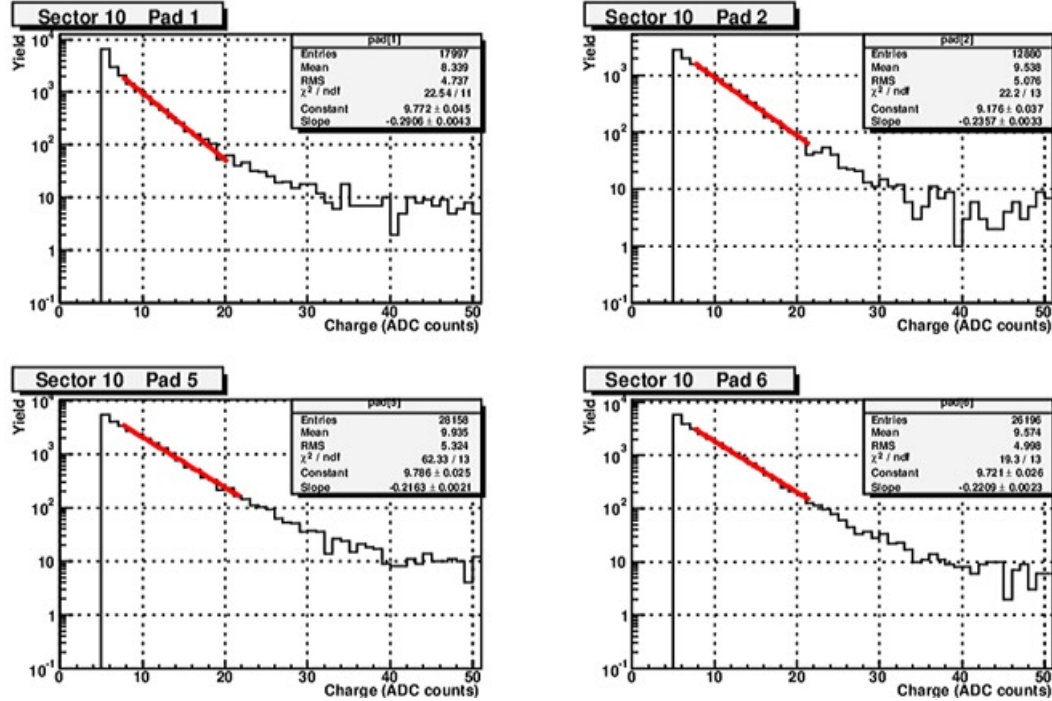


FIGURE 3.4: An example for pad gain determination, by fitting the exponential. Shown are four pads from WN2 module.

The equilibration procedure is evaluated using a run different than the one used to derive the constants. The results show that gain variation across the modules are successfully minimized as demonstrated in Fig. 3.5.

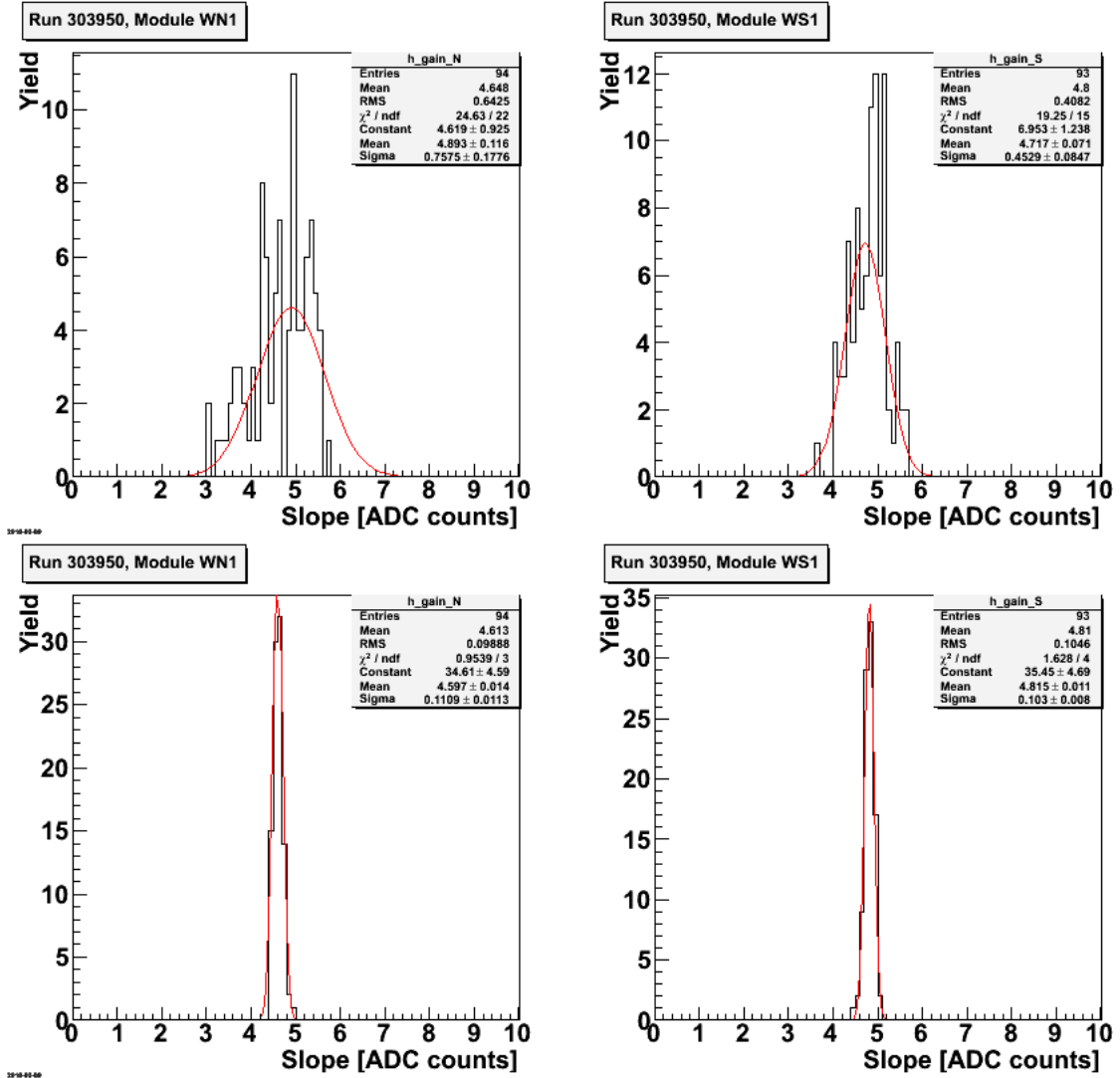


FIGURE 3.5: The distribution of pad gains in two modules WS1 and WN1. Top: before the equilibration, bottom: after the equilibration.

Since the pad-to-pad gain variations arise from mechanical properties of the GEMs and the modules, we expect them to be stable throughout the duration of the Run-10. This is checked by probing the pad-to-pad gain variation for various runs taken at different times during the 200 GeV part of Run-10. The tests show that the equilibration is stable for all modules. As an example, the stability of ES modules is demonstrated in Fig. 3.6, where the blue and the red symbols represent the RMS of the gain distribution of all pads belonging to a given module before and after the equilibration, respectively. The yellow and the green square symbols mark the run used for deriving the equilibration constants.

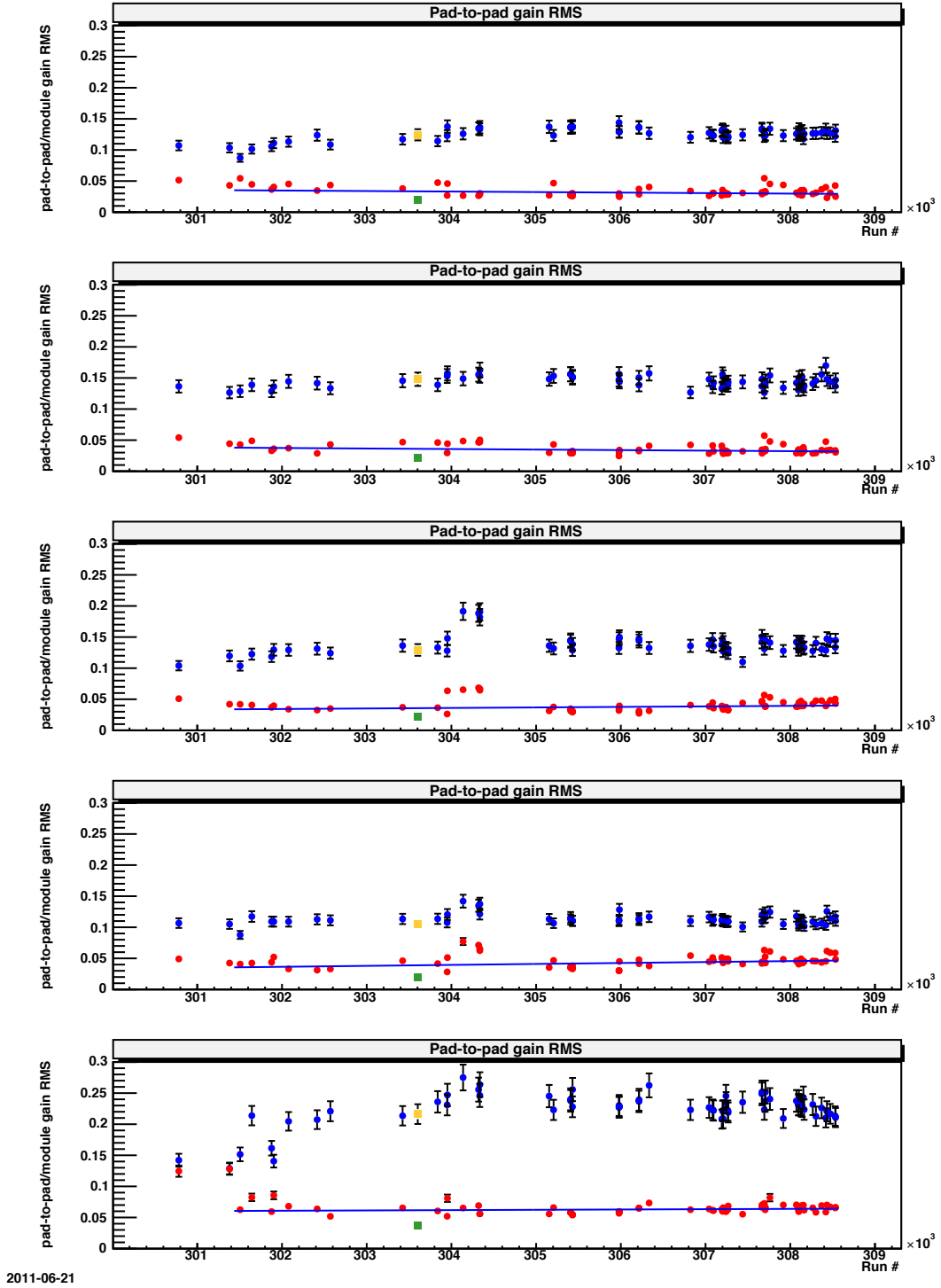


FIGURE 3.6: Stability of the pad-to-pad gain equilibration throughout the 200 GeV portion of Run-10 for the ES modules (1-5 from top to bottom). Blue (red) points are before (after) the gain equilibration.

3.2 Quantum Efficiency (QE) correction

Even after the gain correction, time and module dependencies of the HBD response were observed. These dependencies are attributed to variations of the quantum efficiency. The quantum efficiency correction is performed using central arm electrons and their Čerenkov response in the 60-92% centrality bin. The black histogram in Fig. 3.7 shows the charge distribution of the clusters associated with central arm electrons. The charge distribution consists of two components: one is the Čerenkov response of the HBD hit associated to the track and the other is the scintillation light response randomly matched to the track. The contribution of the scintillation light is estimated by track swapping (Red histogram in Fig. 3.7) and subtracted to obtain the charge distribution of the Čerenkov response (Blue histogram in Fig. 3.7).

Using the extracted Čerenkov response, the quantum efficiency correction is applied in the following way:

1. Time dependence correction

All runs are chronologically divided into 29 groups and one of them is arbitrarily defined as reference group. The cluster charge of the reference group is scaled to reproduce the other group's charge distribution. This is performed module-by-module. The obtained charge scaling factor λ_t for the ES4 module is shown in Fig. 3.8. The scaling factor is cross-checked using fully reconstructed conversion pairs that produce a double charge singnal in the HBD. The peak position of the double charge distributions before and after the correction for ES4 is shown in Fig. 3.9.

2. Module dependence correction

The module dependence is corrected in the same way as the time dependence. The scaling factor is also cross-checked with double charge hits. The double charge distribution before and after the correction is shown in Fig 3.10.

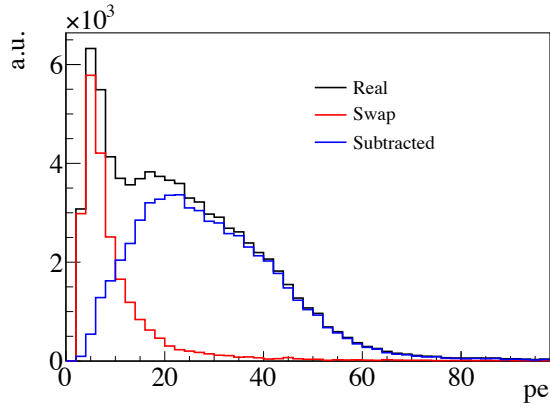


FIGURE 3.7: HBD cluster charge distribution associated with central arm electrons (Black). Contribution from scintillation light is estimated with track swapping (Red) and subtracted to obtain the Čerenkov response (Blue).

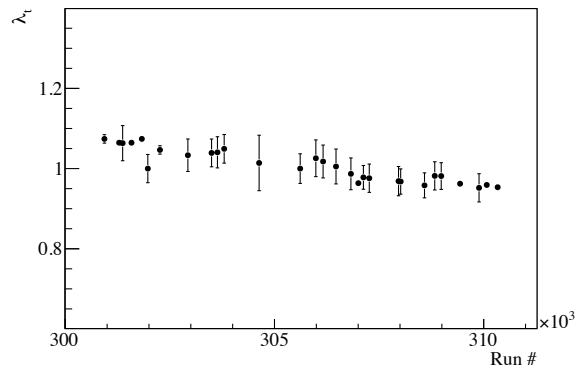


FIGURE 3.8: Charge scaling factor λ_t of different run groups for ES4 module of the east arm.

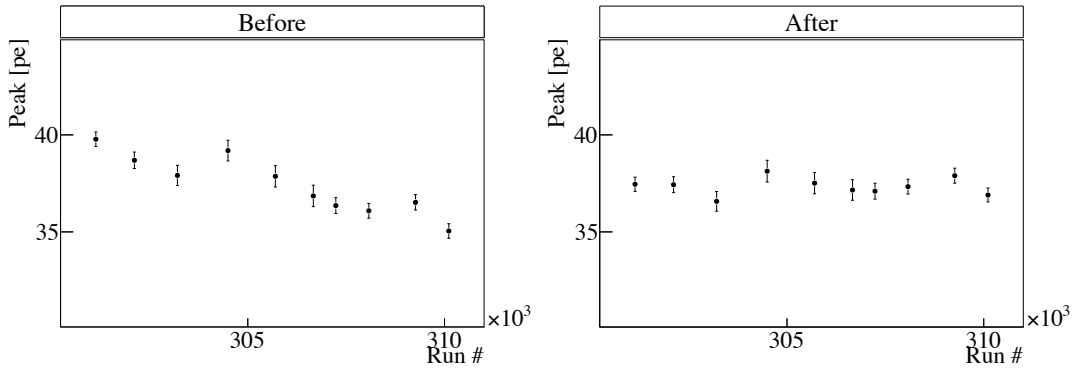


FIGURE 3.9: Peak of “double” charge distribution before and after the quantum efficiency correction for ES4 module.

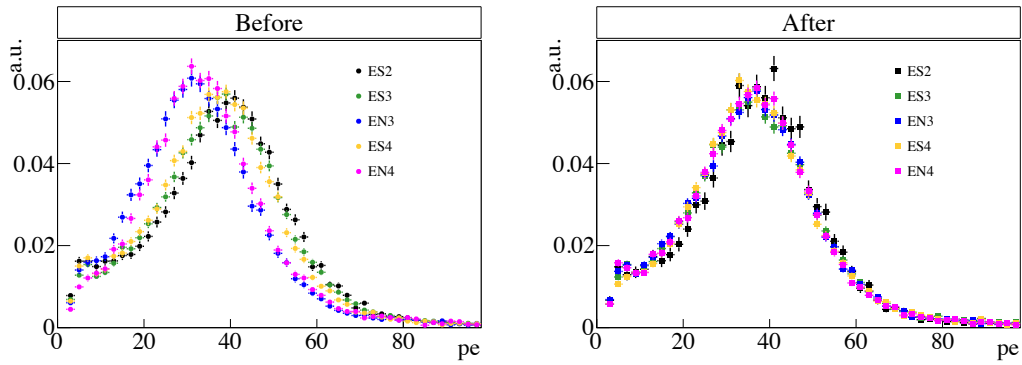


FIGURE 3.10: “Double” charge distribution before and after the quantum efficiency correction for five modules of the east arm.

3.3 Alignment

High precision alignment of the HBD with respect to the central arms is crucial for the pattern recognition algorithm based on the central arm track projections. (See Section 3.5) The alignment is performed using a hadron track and its associated cluster.

The offsets `hbddx`, `hbddy`, `hbddz` are defined as the difference of the reconstructed HBD hit and the central arm track projection point in the x, y and z coordinates. Two kinds of corrections are applied such that the `hbddx`, `hbddy`, and `hbddz` distributions peak at zero independently of position and time. These are referred to as the tilt correction and the time variation correction.

A schematic drawing of the tilt correction around the x-axis is shown in Fig 3.11. The tilt angle α in the figure is estimated to be ~ 5 mrad. This tilt correction is the same for all the runs.

After applying the tilt correction, the residual offset correction is extracted for each module. The correction is applied to different run groups in which the offsets are approximately constant.

Fig 3.12 shows the offsets in phi and z direction after applying the corrections. The residual offsets are minimal and stable in time.

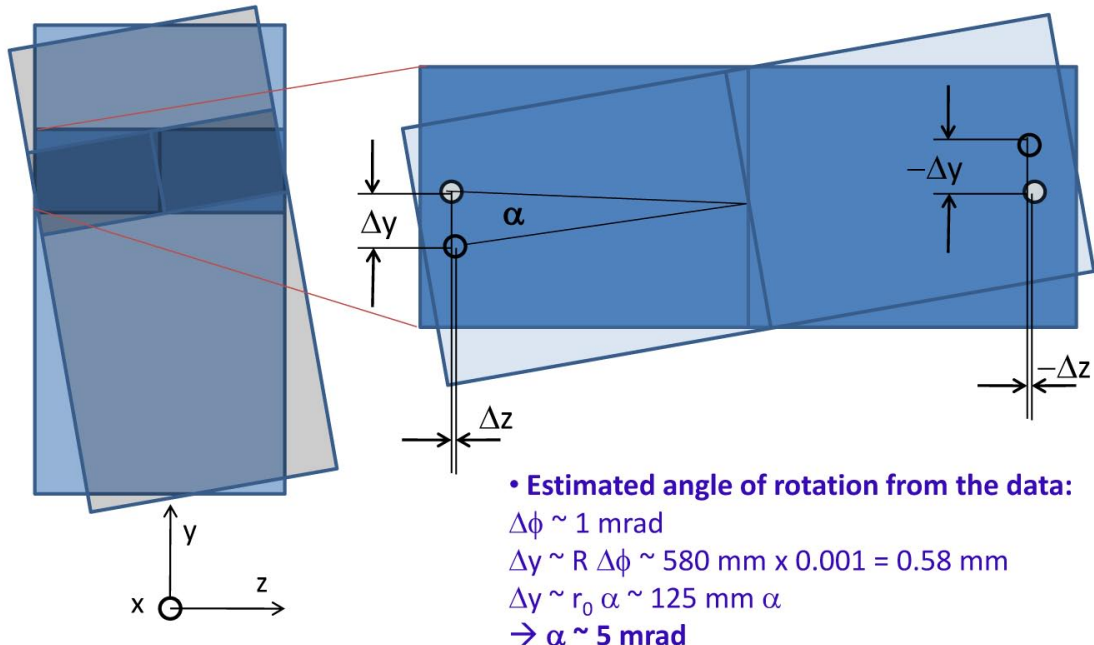


FIGURE 3.11: The schematic drawing depicting the HBD arm rotation around the x-axis (PHENIX coordinates). On the left is the view of one HBD arm from x-direction and on the right is a zoomed drawing of one HBD sector, containing two modules.

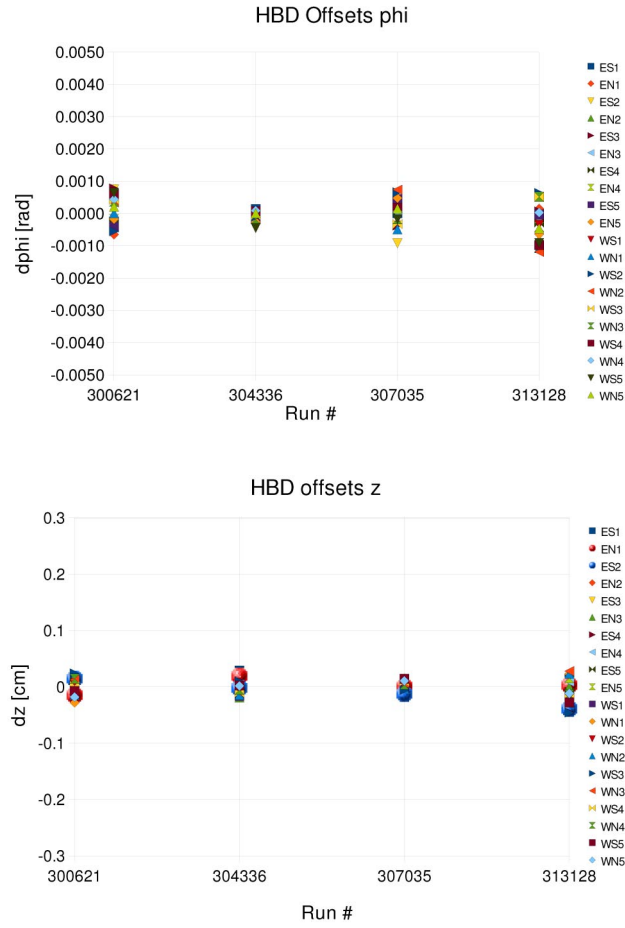


FIGURE 3.12: The HBD module offsets after applied correction.

3.4 Scintillation background subtraction

High track multiplicity in central $Au + Au$ collisions, results in a high occupancy of the HBD. This is due to the large amount of UV scintillation photons produced by charged particles traversing the CF_4 radiator gas. The scintillation spectrum of CF_4 is shown in Fig. 3.13 [79]. The CsI is sensitive to the line at ~ 160 nm and produce photoelectrons. This scintillation background increases with centrality and consequently the cell charge grows with the centrality class as well. This is illustrated in Fig. 3.14 that shows the distribution of the cell charge per unit area (Q_{cell}/a_{cell}) in module WN2 for different centrality classes.

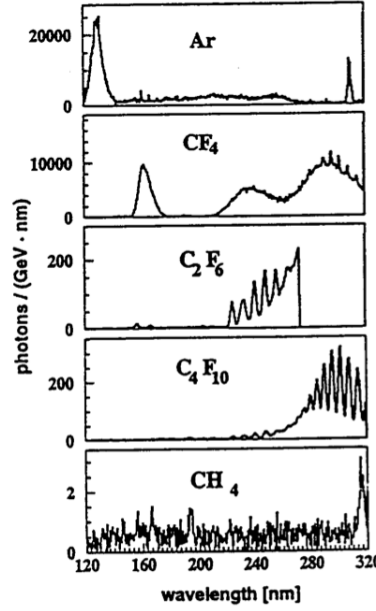


FIGURE 3.13: Photon yield for various scintillating gases excited by ^{16}O ions of $E_{kin} = 80 \text{ MeV}$ [79]. Intensities are normalized with respect to constant energy loss.

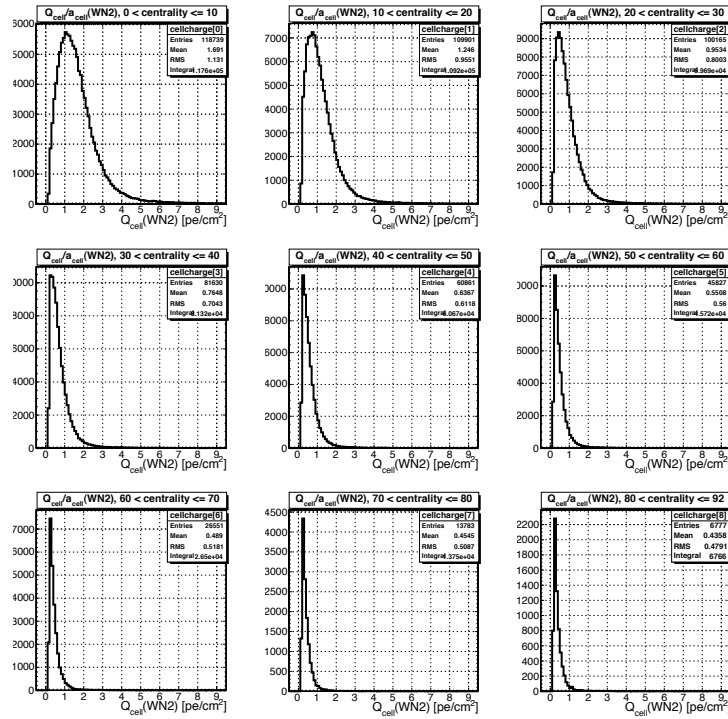


FIGURE 3.14: Cell charge per unit area (Q_{cell}/a_{cell}) for different centrality ranges. The displayed data are for module WN2.

Consequently, the electron signals produced by Čerenkov photons, sit on top of the piled-up scintillation charge, which we denote as the underlying event charge. In order to recognize the electron response in the HBD, the charge of the underlying event needs to be subtracted. The subtraction is performed on an event-by-event basis, separately for each HBD module. It is done after the gain equilibration and the quantum efficiency correction. For each event and for each module we calculate the average charge per unit area and we subtract it from the charge in each cell, taking into account the cell area. This can be described as:

$$\langle Q \rangle = \sum Q_{cell} / \sum a_{cell} \quad (3.3)$$

$$Q_{cell}^* = Q_{cell} - \langle Q \rangle \times a_{cell} \quad (3.4)$$

where $\langle Q \rangle$ is the average charge per unit area in a given module, Q_{cell} is the cell charge, a_{cell} is the cell area and the Q_{cell}^* is the new cell charge used for further analysis. The summation in Eq 3.3 is carried out over the cells satisfying the following conditions:

- The cell charge is less than ~ 80 photoelectrons.
- The cell and its first neighbors do not have an electron track projection. Electron tracks are selected by the central arm. This condition is introduced to avoid oversubtraction of the underlying event and the correlation between tracks in the same HBD module.

3.5 Pattern recognition

Two kinds of pattern recognition algorithm are applied on the charges obtained in the previous section: a standalone algorithm and a non-standalone algorithm. The simple standalone algorithm works well for $p + p$ collisions and peripheral $Au + Au$ collisions. However, in central $Au + Au$ collisions, there is a large background charge mainly due to the scintillation light emitted by charged particles in the CF_4 radiator. Such charge can accidentally mimic a real electron signal that can be associated to a backplane-conversion electron, which in principle does not have a corresponding signal in HBD. As a result, backplane-conversion electrons contaminate the electron sample. The non-standalone algorithm minimizes the effect of scintillation background by using only a limited number of pads around the track projection. The standalone and non-standalone algorithms are described below.

3.5.1 Standalone algorithm

In the standalone algorithm, clusters are built around a seed pad having a charge larger than 3 photoelectrons. Then, the charge of the fired pads among the first six neighbors of the seed are added to the seed charge to determine the cluster charge. The center of gravity of the cluster is taken as the hit position of the incident particle.

3.5.2 Non-standalone algorithm

The non-standalone algorithm pre-determines the pads that can potentially contribute to an electron cluster, which we call cluster size, based on the central arm track projection point into the HBD. The algorithm is as follows:

1. Find the track projection point at the HBD, which is calculated using central arm data.
2. Form a cluster using pre-assigned pads around the projection point. The pre-assigned pads depend on the projection point in a pad and are determined using simulations. The hexagonal pad is divided into 6 equilateral triangles and each of these is in turn divided into 16 small equilateral triangles of ~ 4 mm side as shown in Fig 3.15. When the central arm track points to triangles 0-8, the cluster includes pad0 only, when it points to triangles 10-14, the cluster includes (pad0 \oplus pad1) and when it points to triangles 10 and 15, the cluster consists of (pad0 \oplus pad1 \oplus pad2) or (pad0 \oplus pad1 \oplus pad3), respectively. See Appendix A.1 for the details of the cluster size optimization.
3. Apply a threshold to the total charge of the cluster to identify electrons. The threshold is determined so as to reject a given amount of backplane-conversion electrons and it depends on centrality, cluster size and HBD modules. A variable which takes into account all of these effects is referred to as `hbdid`. The `hbdid` variable is an integer number between 1 and 25 and a larger number corresponds to a stronger rejection of backplane conversion electrons. For example, $\text{hbdid} \geq 5$ rejects 80% and $\text{hbdid} \geq 10$ rejects 90% of backplane conversion electrons, respectively. See Appendix A.2 for the detailed definition of the variable.

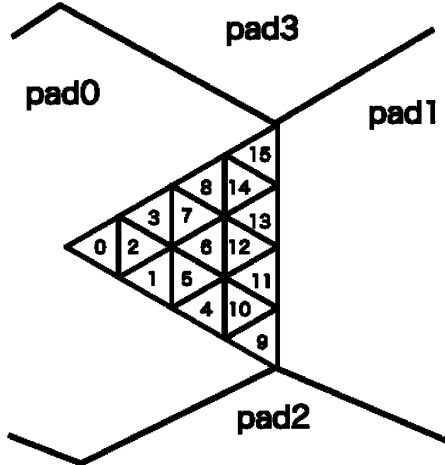


FIGURE 3.15: Schematic drawing of HBD readout hexagonal pads. One pad is divided into 4 mm triangles in the clustering algorithm described in the text.

3.6 Performance

To evaluate the performance of the HBD in di-electron analysis, two types of figure of merit, the effective pair signal S/\sqrt{B} and the signal-to-background ratio S/B , are considered. Since the pair signal efficiency is proportional to the signal track efficiency squared ϵ^2 and the background pair rejection is proportional to the background track rejection squared R^2 , those figures of merit scale as:

$$\frac{S}{\sqrt{B}} \propto \epsilon^2 \cdot R \quad (3.5)$$

$$\frac{S}{B} \propto \epsilon^2 \cdot R^2 \quad (3.6)$$

The single track efficiency ϵ is estimated using a $\phi \rightarrow ee$ GEANT simulation. (See Section 4.5 for details about the detector simulation.) The Čerenkov response of the HBD is embedded in real events to have a realistic scintillation background.

The background track rejection R is estimated using a π^0 GEANT simulation. A generated π^0 decays into $\gamma\gamma$ or $ee\gamma$, and the produced γ s convert into e^+e^- pairs inside materials. The Čerenkov response of the HBD is again embedded in real events.

The ϵ and R are estimated for three types of cuts:

- Only the central arm cuts (CA)

- The central arm cuts and the HBD single cut ($\text{hbdid} \geq 10$)

The HBD single cut is applied to reject the electrons originating from the γ conversion inside the HBD backplane.

- The central arm cuts, the HBD single cut ($\text{hbdid} \geq 10$) and the HBD double cut ($\text{hbdcharge} < 30$), where hbdcharge is the total charge in the standalone algorithm's cluster.

The HBD double cut is applied to reject the double tracks, such as π^0 Dalitz decays or the γ conversions inside the beam pipe ($X_0 \sim 0.3\%$).

The derived effective signal and the signal-to-background ratio are shown in Fig. 3.16 for each cut and for each centrality bin. The effective signal and the signal-to-background ratio for the central arm cuts are normalized to be one. In the 40-60% and 60-92% bin, the HBD single cut and the HBD double cut both improve the effective signal and the signal-to-background ratio. This demonstrates the effectiveness of the HBD. However, in the 0-10% and 10-20% bin, since the scintillation background smears the response of the HBD, the single cut and the double cut are no longer as effective as in peripheral events. The double cut even lowers the effective signal. The double cut is effective only for the centrality above $\sim 30\%$, which is equivalent to the number of charged particles below $\sim 0.01 \text{ /cm}^2/\text{evt}$.

As shown above, the performance of the HBD degrades in central $Au + Au$ collisions. Therefore, in this analysis, all the cut parameters including the central arm variables are revised from the previous measurement to achieve a sufficient performance for a di-electron analysis as discussed in the next chapter.

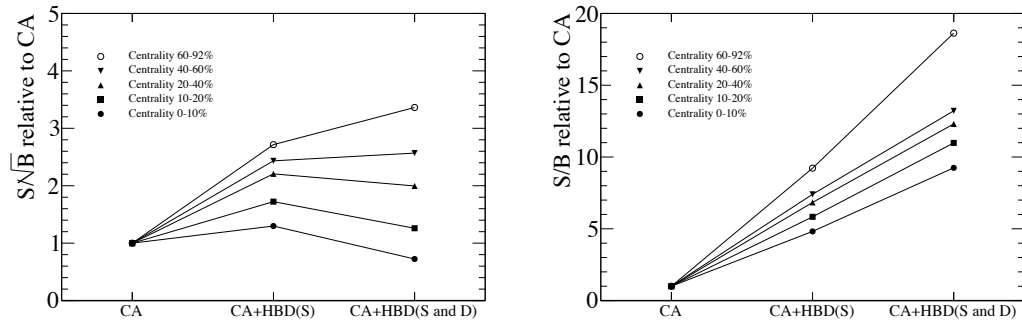


FIGURE 3.16: The effective signal (left) and the signal-to-background ratio (right) for three types of cuts and for each centrality bin. Those values for the central arm cuts are normalized to be one. HBD(S) refers to the HBD single cut, $\text{hbdid} \geq 10$, and HBD(D) refers to the HBD double cut, $\text{hbdcharge} < 30$.

Chapter 4

Data analysis

In this chapter, the di-electron analysis of $Au + Au$ collisions at $\sqrt{s_{NN}} = 200$ GeV is presented. An analysis overview is described first, and the details of each step are discussed in the subsequent sections.

4.1 Analysis overview

The analysis is performed on the data set recorded during the RHIC run in 2010. The data were collected with the Minimum Bias triggers. There are two vertex ranges, the narrow vertex trigger and the wide vertex trigger, as described in Sec 2.8. In addition to the online trigger, one hit in one of the ZDCs is also required.

The analysis flow is illustrated in Fig. 4.1.

First single track cuts are applied to obtain clean electron tracks. Here we reject not only hadrons but also electrons coming from γ conversion or π^0 Dalitz decays. Then, pair ghost cuts are applied to reject unphysical correlations in the electron sample through hit sharing in the various detectors. The electron tracks which pass these cuts are used for further pair analysis.

Ideally, we would like to analyze only the “physical” pairs. The “physical” pairs are defined as e^+e^- pairs from the same parent particle, e.g. an electron and a positron from a ϕ decay, or e^+e^- pairs from semi-leptonic $D\bar{D}$ or $B\bar{B}$ decays, which are correlated through flavor conservation. However, the sources of electrons and positrons are not known in a real event. Therefore, all electrons and positrons in the same event are combined to form “foreground” pairs. An electron with a four momentum $(E_-, p_{x,-}, p_{y,-}, p_{z,-})$ and a positron with a four momentum $(E_+, p_{x,+}, p_{y,+}, p_{z,+})$ form

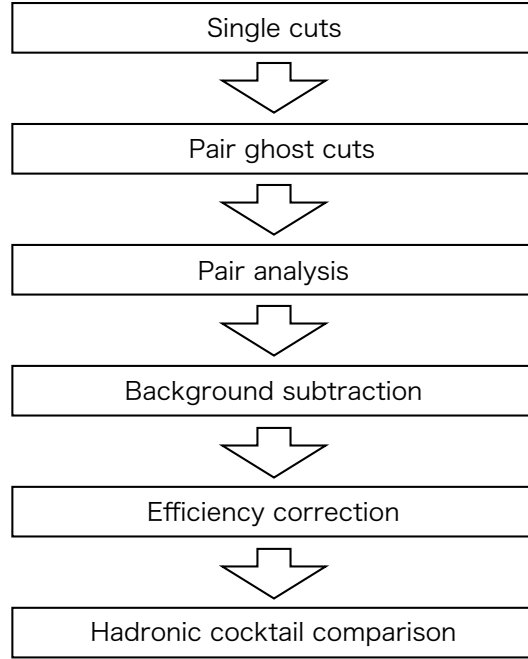


FIGURE 4.1: Analysis flow.

a foreground pair with invariant mass m_{ee} and transverse momentum p_T calculated as follows:

$$m_{ee}^2 = (E_+ + E_-)^2 - (p_{x,+} + p_{x,-})^2 - (p_{y,+} + p_{y,-})^2 - (p_{z,+} + p_{z,-})^2 \quad (4.1)$$

$$p_T^2 = (p_{x,+} + p_{x,-})^2 + (p_{y,+} + p_{y,-})^2 \quad (4.2)$$

The $(p_{x,\pm}, p_{y,\pm}, p_{z,\pm})$ are measured with DC/PC1 and the E_\pm is calculated as:

$$E_\pm = \sqrt{p_{x,\pm}^2 + p_{y,\pm}^2 + p_{z,\pm}^2 + m_e^2} \quad (4.3)$$

where $m_e = 511 \text{ keV}/c^2$.

The inclusive foreground pairs so formed contain the physical signal and a large background of unphysical pairs. The (m_{ee}, p_T) distribution of the physical pairs is obtained by subtracting the (m_{ee}, p_T) distribution of “unphysical” pairs from the (m_{ee}, p_T) distribution of the inclusive foreground pairs. The background of unphysical pairs consists of the following types:

- Combinatorial pairs

The combinatorial pairs are random combinations of electrons and positrons from different parent particles and are just the result of combining all electrons and positrons in an event. The combinatorial pairs account for more than 99% of the total background in the most central collisions.

- Cross pairs

The cross pairs occur when there are two e^+e^- pairs in the final state of a meson, e.g. $\pi^0 \rightarrow ee\gamma \rightarrow eeee$. The combination of an electron directly from π^0 and a positron from γ do not have the same parent particle but they are correlated through the same “grand parent” particle.

- Jet pairs

The jet pairs are produced by two electrons generated in the same jet or in back-to-back jets.

- Electron-hadron pairs

The electron-hadron pairs result from the residual detector correlations which cannot be handled by the pair cuts.

The background model is verified using the like-sign, e^+e^+ and e^-e^- , mass spectra, which have contributions from only “unphysical” pairs.

The spectrum after the background subtraction is corrected for reconstruction efficiency within the nominal PHENIX detector acceptance. The obtained spectra are compared to the hadronic cocktail described in the next chapter.

In this chapter, we first discuss the centrality determination (Section 4.2), charged particle track reconstruction and momentum determination (Section 4.3). We also introduce various variables used for the electron identification in Section 4.4. These variables need to be well reproduced in Monte Carlo simulations because the simulations are intensively used in various steps of this analysis: cut optimization, correlated background simulation and efficiency correction. The details of the Monte Carlo simulations are discussed in Section 4.5. Then, after describing event and run selections in Section 4.6 and 4.7, the analysis flow between single cuts and background subtraction is described in Sections 4.8-4.12. The acceptance and efficiency correction is generated using the hadronic cocktail, therefore, the correction is described in Section 4.13.7 as a part of hadronic cocktail section (4.13). The comparison between the corrected spectrum and cocktail is shown in the next chapter.

4.2 Collision geometry and centrality determination

At high energies, a simple geometric “participant-spectator” picture is often used to describe the heavy ion collisions. The nucleons inside the colliding nuclei are assumed to move along parallel, straight-line trajectories and only the nucleons in the overlapping region interact with each other. The interacting nucleons are called “participants” and the remaining nucleons are called “spectators”.

Figure 4.2 shows a 2D view of a heavy ion collision. The perpendicular distance between the paths of the two nuclei is the impact parameter b . Since the impact parameter cannot be directly measured, we usually use any observable that is a monotonic function of the overlapping volume to define centrality.

In PHENIX, centrality is determined using the measured BBC total charge. The distribution is shown in Fig. 4.3. The events having the maximum and minimum BBC charge are assigned to centrality of 0% and 92%, respectively. The value of 92% is determined by the Minimum Bias trigger efficiency. The total charge distribution is sliced into 92 bins with the same number of events in each bin. The centrality classification is performed with a 5 cm binning of the collision vertex.

The centrality class is related to impact parameter via a Glauber model calculation [80]. In the Glauber model, a nucleus-nucleus collision is treated as a multiple nucleon-nucleon collision. The nucleons in a nucleus are randomly distributed following the nuclear density profile and a nucleon-nucleon occurs whenever their distance is less than $\sqrt{\sigma_{NN}/\pi}$, where σ_{NN} is the total inelastic cross section.

The Glauber model also provides the number of participant nucleons N_{part} and the number of binary nucleon-nucleon collisions N_{coll} values for a given impact parameter. The N_{part} and N_{coll} are useful quantities to compare the results from different collision species, such as $d + Au$ and $Au + Au$.

The estimated impact parameter, N_{part} and N_{coll} values of each centrality bin in $Au + Au$ collisions at $\sqrt{s_{NN}} = 200$ GeV are summarized in Table 4.1. The systematic uncertainties estimated by varying the input parameters of the Glauber model calculation, such as the size of the nucleus and inelastic cross section, are also shown in the table.

TABLE 4.1: Average N_{part} and N_{coll} of each centrality bin in $Au + Au$ collisions at $\sqrt{s_{NN}} = 200$ GeV.

Centrality class	$\langle b \rangle$ (syst) fm	$\langle N_{part} \rangle$ (syst)	$\langle N_{coll} \rangle$ (syst)
Minimum Bias	9.5 (0.4)	109.1 (4.1)	257.8 (25.4)
0-10%	3.2 (0.2)	325.2 (3.3)	955.4 (93.6)
10-20%	5.7 (0.3)	234.6 (4.7)	602.6 (59.3)
20-40%	8.1 (0.4)	140.4 (4.9)	296.8 (31.1)
40-60%	10.5 (0.4)	60.0 (3.6)	90.7 (11.8)
60-92%	13.0 (0.5)	14.5 (2.5)	14.5 (4.0)

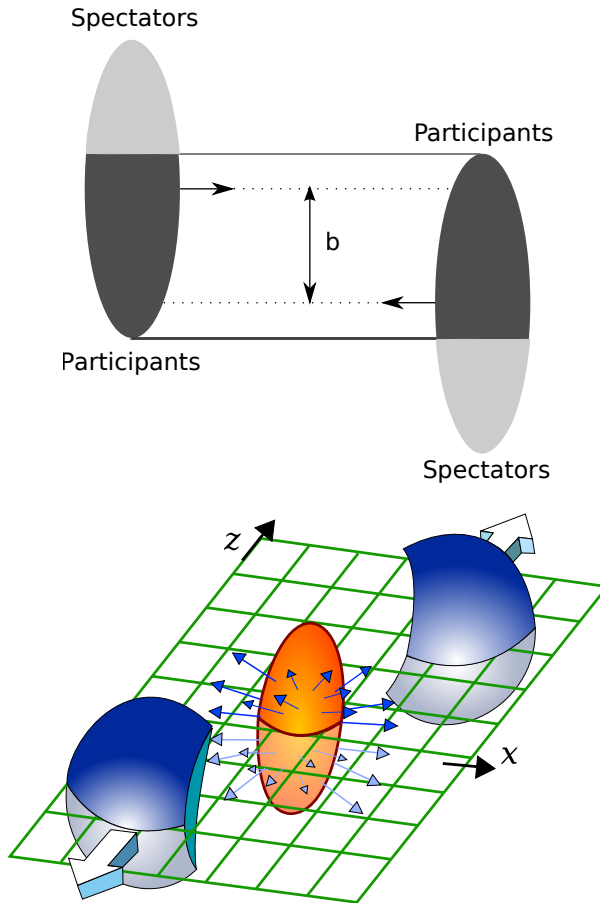


FIGURE 4.2: Collision geometry in 2D (Top) and 3D (Bottom) view.

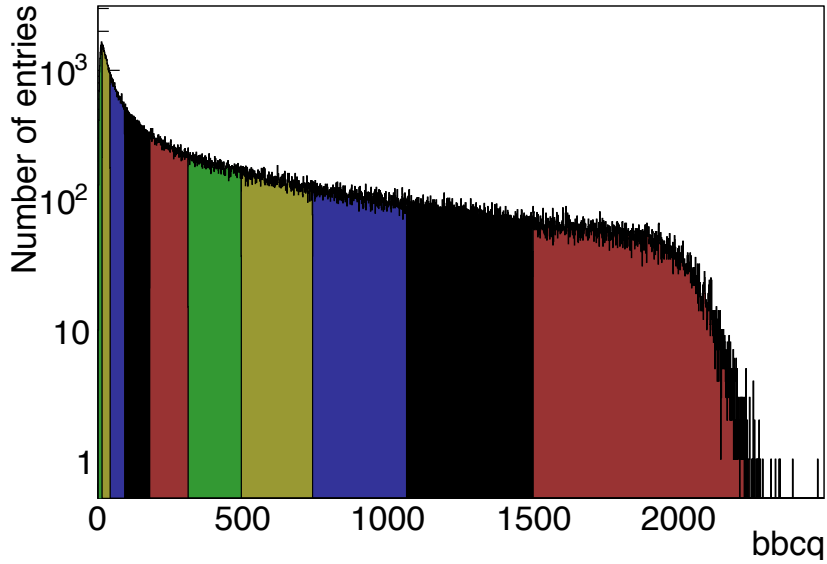


FIGURE 4.3: Distribution of the BBC total charge for the events with $0 < |z_{vtx}| < 5$ cm. Each slice corresponds to a 10% centrality bin.

4.3 Charged track reconstruction and momentum determination

Figure 4.4 shows the path of a charged particle in the bending $r - \phi$ plane (left) and in the $r - z$ plane (right). The coordinates measured with DC and PC1 to reconstruct the particle trajectory are defined as follows:

- ϕ : Azimuthal angle of the intersection point of the track candidate with a reference circle located at a radius of 2.2 m, at the middle of the DC.
- ϕ_0 : Track's azimuthal angle at the vertex.
- α : Angle of the track candidate with respect to an infinite momentum track having the same intersection point with the reference circle in the $r - \phi$ plane.
- zed : z coordinate of the track at the intersection point with the reference circle of the DC.
- β : Inclination angle of the track with respect to the z-axis at the intersection point in the $r - z$ plane.

- δ : Inclination angle of the track with respect to an infinite momentum track at the DC reference radius of 2.2 m in the r - z plane.
- θ : The polar angle of the infinite momentum track.
- θ_0 : The polar angle of the track at the vertex.

The first stage of track finding [77] utilizes a combinatorial Hough transform technique in the r - ϕ plane. In this technique, the DC hits in X1 and X2 are mapped pair-wise into a 2-dimensional space defined by the azimuthal angle ϕ and the track bending angle α . The basic assumption is that tracks are straight lines within the DC. In this case, all hit pairs of a given track will have the same (ϕ, α) , thus resulting in a local maximum in the mapped space. The algorithm first looks for tracks having both X1 and X2 hits, and then looks for tracks with only X1 or X2 hits.

Tracks are then reconstructed in the r - z plane by combining the information of PC1 hits, UV wire hits and the collision vertex measured by the BBC. First, the straight line track in the r - ϕ plane is extended to PC1. If there is an unambiguous PC1 hit association within 2 cm distance between the track projection point and the PC1 hit position in the r - ϕ plane, the track vector in the r - z plane is fixed by the PC1 hit z coordinate and the z vertex measured by the BBC. If there is no PC1 cluster association, or if there are multiple PC1 association solutions, the track vector in the r - z plane is fixed by the DC UV hits.

Reconstructed tracks by DC and PC1 are confirmed by associated hits in the outer detectors, PC2 in the west arm and PC3 in the east arm. If no associated hits are found in PC2 or PC3, the track can still be confirmed by associated hits in PC3/EMCal for the west arm and EMCal for the east arm. The hits are considered to be valid if they are within 3σ of their resolution in z and ϕ . It is convenient to define matching variables normalized to their resolution as a function of p_T , charge and sectors. These variables are referred to as reduced variables. For example, in the case of EMCal matching, the reduced variables ($\text{emcsd}\phi$, emcsdz) are defined as:

$$\text{emcsd}\phi = \frac{\text{emcd}\phi}{\sigma_\phi(p_T, \text{charge}, \text{sector})} \quad (4.4)$$

$$\text{emcsdz} = \frac{\text{emcd}z}{\sigma_z(p_T, \text{charge}, \text{sector})} \quad (4.5)$$

where ($\text{emcd}\phi$, $\text{emcd}z$) are the distance between the projection point of a reconstructed track on the EMCal surface and the centroid of its associated electromagnetic shower, and (σ_ϕ, σ_z) are the EMCal resolutions in azimuthal and longitudinal directions, respectively.

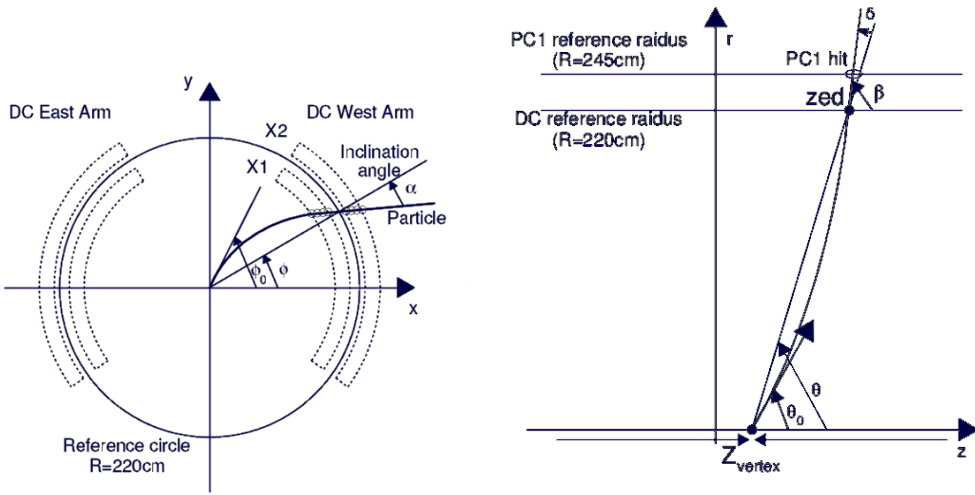


FIGURE 4.4: Left: Shematic view of a track in the DC $r - \phi$ plane. Right: Shematic view of a track in the DC $r - z$ plane [77].

Due to the complicated, non-uniform shape of the magnetic field, an analytic solution for the momentum determination of a particle is not available. Therefore, we use a non-linear grid interpolation technique [78]. The technique determines the momenta of particles using a “look-up” table of field integrals in a four dimensional grid. The four variables are the total track momentum, the polar angle, the radius from the beam axis and the z coordinate of the collision vertex. The grid is generated by propagating particles through the measured magnetic field.

The momentum resolution depends on the intrinsic position resolution of the DC and the multiple scattering inside the materials before DC. As a result, the momentum resolution is about 1.7% for tracks with $p_T = 1$ GeV/ c and the reconstruction efficiency is above 99%.

Since the acceptance for electrons and positrons changes with the magnet polarization, it is more convenient to use the bending direction of a particle to classify its charge. In the following analysis, the tracks with $\alpha < 0$ and $\alpha > 0$ are referred to as “Type1” and “Type2”, respectively.

4.4 Electron identification variables

4.4.1 RICH

The measured ADC value is converted in the number of photoelectrons as follows:

$$N_{p.e.}(i) = \frac{ADC(i)}{ADC_{1p.e.}(i)} \quad (4.6)$$

where i is the PMT id, $ADC(i)$ is the measured ADC value and $ADC_{1p.e.}(i)$ is the ADC value of one photoelectron peak. Here, the ADC value refers to the difference of ADC values between “pre” and “post” samples as described in Section 2.6.1.

Track association with RICH is performed with the hit information of PC1 and PC2 in the west arm and PC1 and PC3 in the east arm. If no associate hits are found in PC2 and PC3, the hit position of the outer detector (the PC3/EMCal for the west arm and EMCal for the east arm) or DC-PC1 tracks are used. The lines connecting the two detectors hits are reflected by the RICH mirrors onto the RICH PMT plane. Figure 4.5 shows a part of the PMT array surface with the definition of the variables which characterize the association between a track and hit PMTs. The distance between the center of hit PMT \vec{R}_i and the track projection vector is calculated as r_{cor}^i . Figure 4.6 shows the r_{cor} distribution of electron tracks from simulation. The $\langle r_{cor} \rangle$ of 5.9 cm is the ideal ring radius and most of the associated phototubes are within a radius of 11 cm. The shaded area shows the r_{cor} range of 5.9 ± 2.5 cm corresponding to $\pm 1\sigma$ region. The number of associated fired PMTs within the 1σ range, $n0$, is the primary variable for identifying electrons:

$$n0 = \text{Number of fired PMTs in the range } 3.4 < r_{cor}^i < 8.4 \text{ cm}$$

The number of photoelectrons in the associated PMTs, $npe0$, is defined as:

$$npe0 = \sum_{3.4 < r_{cor}^i < 8.4 \text{ cm}} N_{p.e.}(i)$$

The ring center is reconstructed as the center of gravity of the hit PMTs within 11 cm from the projection point.

$$\vec{R}_{center}(z_{center}, \phi_{center}) = \frac{\sum_i N_{p.e.}(i) \vec{R}_i}{\sum_i N_{p.e.}(i)} \quad (4.7)$$

where \vec{R}_i is the location of the i -th PMT. The distance between the track projection point and the ring center is designated as $disp$.

In addition, the quality of the measured ring shape is expressed in terms of the difference to the expected ring shape:

$$\chi^2/\text{npe0} = \frac{\sum_i N_{p.e.}(i)(r_{cor}^i - r_0)^2}{\sum_i N_{p.e.}(i)} \quad (4.8)$$

where r_0 is the ideal ring radius of 5.9 cm.

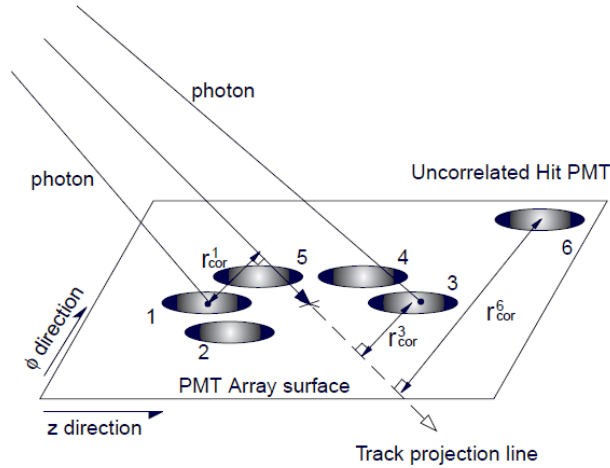


FIGURE 4.5: Schematic description of the variables which characterize a RICH ring. A track projection vector and five PMTs with correlated hits are also shown.

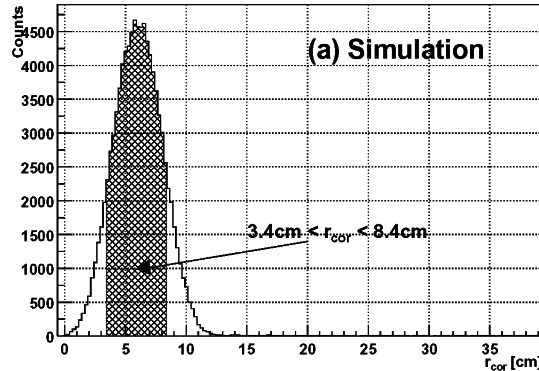


FIGURE 4.6: The r_{cor} distribution from single electron simulation. The shaded area shows the r_{cor} region between 3.4 cm and 8.4 cm.

4.4.2 EMCAL and TOFE

In addition to the EMCAL reduced matching variables ($\text{emcsd}\phi$, emcsdz), the deposited energy information of the associated cluster is used for electron identification. Since the electron mass is negligible compared to its momentum $p > 0.3$ GeV/c and all its energy is deposited in the EMCAL, the ratio of the deposited energy (ecore) measured by the

EMCal and the total momentum (p) measured by DC is expected to be 1. In practice, the ratio is not exactly at one for several experimental reasons: detector resolution, EMCal shower overlapping and mis-reconstructed momenta of electrons from off-vertex γ conversions. The last reason, mis-reconstructed momenta, is due to the fact that the tracking algorithm assumes all tracks originate at the collision vertex. Electrons from γ conversions in materials outside the radius of ~ 55 cm traverse less magnetic field, and are therefore bent less, resulting in a larger reconstructed momenta and $e_{\text{core}}/p < 1$. In analogy to the EMCal matching variables, e_{core}/p is expressed in terms of a reduced variable, which is centered at zero and has a sigma value of one. The reduced variable is referred to as `dep` and it is determined separately for each EMCal sector, each charge and each p_T bin.

Shower shape information is also used for the electron identification. The probability that the associated EMCal cluster is an electromagnetic shower is referred to as `prob`. This variable is calculated from the χ^2 value between the actual tower energy distribution and the expected distribution of an electromagnetic shower.

The PbSc has a timing resolution of ~ 450 ps. For example, the difference in time-of-flight from the collision vertex to EMCal ($R \sim 500$ cm) between a electron and a pion is 640 ps for $p = 500$ MeV/ c . The reduced time-of-flight variable is referred to as `stof(PbSc)`. The timing information of PbGl is not used in this analysis due to its bad resolution (~ 700 ps). Instead, the timing information of TOFE, which covers ~ 60 % of the PbGl acceptance, is used. The timing resolution of TOFE is ~ 150 ps. In the same way as PbSc, reduced time-of-flight variable is referred to as `stof(TOFE)`. Figure 4.7 shows the contour plot of time-of-flight (ToF) of PbSc and TOFE as a function of the reciprocal momentum in the 0-10% centrality bin. The vertical lines around $\text{ToF} \sim 0$ corresponds to electrons and the tilted lines correspond pions. A clear separation between electrons and hadrons is visible.

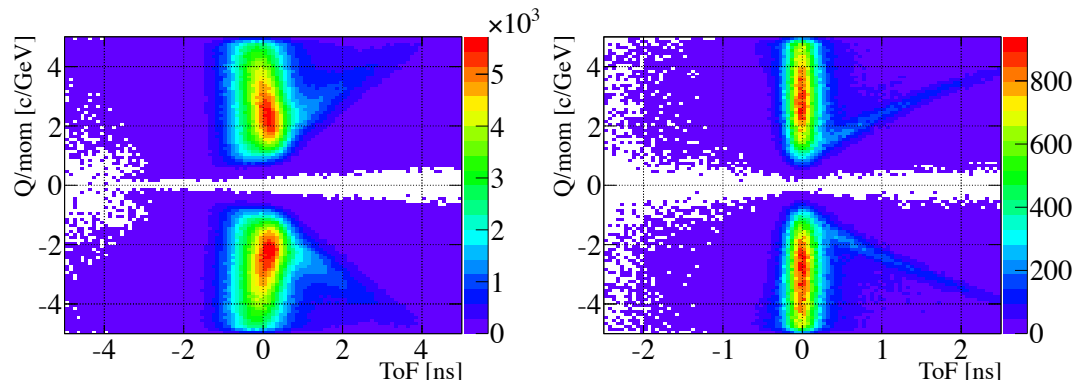


FIGURE 4.7: Charge over momentum (Q/mom) vs ToF for PbSc(left) and TOFE(right) in the 0-10% centrality bin.

4.4.3 HBD

The charge information of clusters formed by the two algorithms described in Section 3.5 is used for electron identification.

The total cluster charge in the standalone algorithm’s cluster is referred to as `hbcharge` and the number of pads in the cluster is referred to as `hbdsiz`. The pad with the largest charge in the cluster is referred to as `maxpadcharge`.

The reduced cluster charge variable `hbdid` described in Section 3.5.2 is used as the major eID variable from the non-standalone algorithm. The total charge of the pads inside the non-standalone algorithm’s cluster is referred to as `HBDCHARGE` and the number of pads in the cluster is referred to as `HBDSIZE`.

4.4.4 Summary of eID variables

The eID variables mentioned in the previous subsections are summarized in Table 4.2. Subsets of this large list of eID variables are used to reject HBD backplane conversions, hadrons misidentified as electrons in the central arms and for the final electron identification. Instead of applying a sequence of one-dimensional cuts which would result in a large efficiency loss, a multivariate approach is implemented in the analysis. In particular, we use the neural network from the root package TMultilayerPerception. Details for the various neural networks used are given in Sections 4.9 and 4.10.

4.5 Detector simulations

The detector simulations are performed in the following way:

1. We first generate tracks with event generators, such as EXODUS (the PHENIX internal single particle event generator) or PYTHIA [87].
2. The generated particles are passed through the detector simulation software, PISA (“PHENIX integrated Simulation Application”), developed within the framework of GEANT3. PISA tracks the primary particles, as well as secondaries produced from the interaction of the primary particles with the detector materials, such as γ conversions, and simulates the response of each detector to produce hit information.

TABLE 4.2: Variables used for the electron identification in the analysis.

Variable	Detector	Short description
n0	RICH	Number of hit PMTs
disp	RICH	Distance between a track projection and its associated ring center
$\chi^2/npe0$	RICH	A χ^2 -like shape variable of the RICH ring
emcsd ϕ	EMCal	Distance in ϕ between a track projection and its associated cluster
emcsdz	EMCal	Distance in z between a track projection and its associated cluster
prob	EMCal	The χ^2 -like shape variable
ecore	EMCal	Measured energy
dep	EMCal	Reduced ecore/ p
stof(PbSc)	EMCal	Reduced time-of-flight
stof(TOFE)	TOFE	Reduced time-of-flight
hbdcharge	HBD	Cluster charge from the standalone algorithm
hbdsiz	HBD	Cluster size from the standalone algorithm
maxpadcharge	HBD	Max pad charge in the cluster from the standalone algorithm
hbdid	HBD	Reduced cluster charge from the non-standalone algorithm
HBDCHARGE	HBD	Cluster charge from the non-standalone algorithm
HBDSIZE	HBD	Cluster size from the non-standalone algorithm

3. The PISA hit information is run through the PHENIX reconstruction software. The reconstruction is performed without any dead areas, i.e. within the ideal PHENIX acceptance.
4. The reconstructed Čerenkov response of HBD is embedded in real events. This step is required because PISA does not simulate the scintillation background from charged particles in a real event and the performance of HBD strongly depends on the amount of scintillation background. The HBD clustering is done using the new embedded charges.
5. The output is analyzed in the same way as the data. The fiducial cuts described in Section 4.8 are applied at this stage to have realistic acceptance. Since the event generators use a flat z vertex distribution, weighting factors are applied to have a realistic vertex distribution.

It is important to ensure that the detector response in the simulations is the same as in the real data for all the subsystems involved in the analysis. To compare the simulations and data, we need to extract clean electron tracks from data. This is achieved by using the low mass unlike-sign pairs. The pairs are selected with the following cuts:

- Event cut

Centrality 60-92 % bin, where the effect of occupancy in the central arm is small and can be ignored.

- Single cut $p_T > 0.3$ GeV/c, `nnout0` cuts described in Section 4.10.2, `hbdid` cuts described in Section 4.10.3, fiducial cuts described in Section 4.8.
- Pair cut

$0.025 < m_{ee} < 0.05$ GeV/ c^2 , $0.8 < \phi_V < 2.6$, opening angle larger than 100 mrad. The ϕ_V is the angle between the plane formed by the pair and the plane perpendicular to the magnetic field, which is parallel to the z-axis. The ϕ_V cut is applied to reject conversions. The pairs selected with these conditions are referred to as “open Dalitz pairs”.

The combinatorial background is subtracted using the event-mixing technique. The eID variables of the two legs of the pairs are compared with those of $\pi^0 \rightarrow ee\gamma$ simulations passed through PISA. The comparisons of major eID variables are shown in Fig. 4.8 . The comparisons of neural network outputs described in Sections 4.9 and 4.10 are also shown in the figure.

The quantitative agreement between the detector simulation and data is discussed in Section 4.13.7.

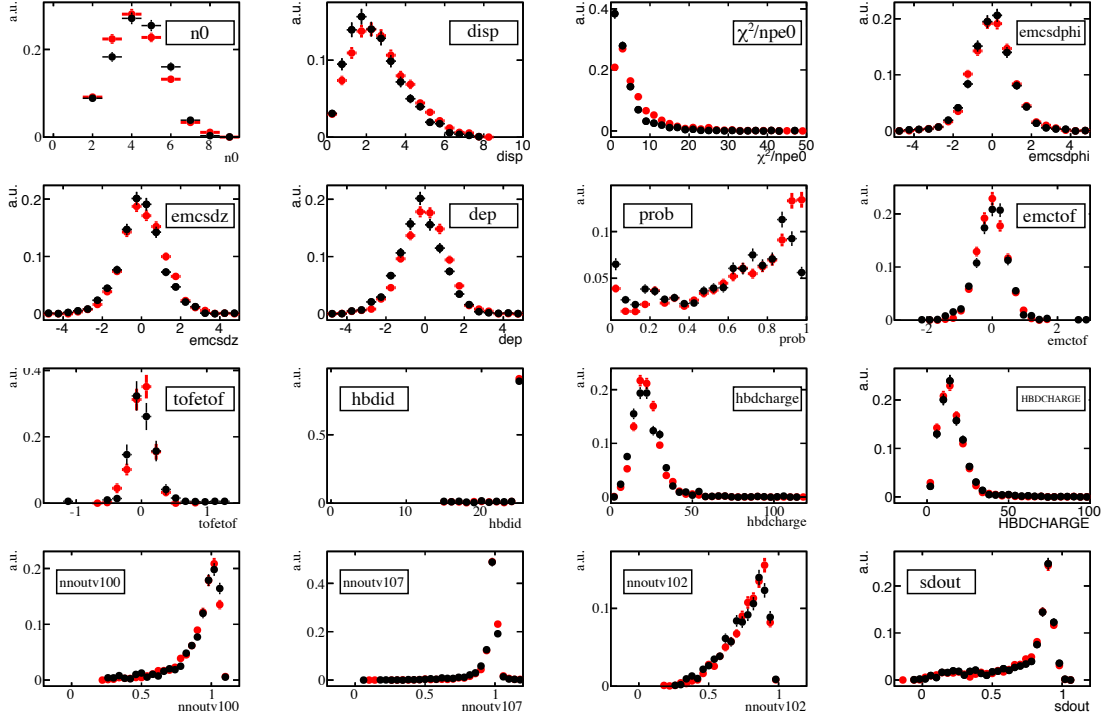


FIGURE 4.8: The comparison of major eID variables in data (Black) and in the detector simulation (Red) using the open Dalitz pairs in the 60-92% centrality bin. The comparisons of neural network outputs described in Section 4.9 and 4.10 are also shown in the lowest panels.

4.6 Event cuts

Figure 4.9 shows the vertex (bbc_{z}) distributions of runs taken with the narrow vertex trigger and the wide vertex trigger. The distribution of electron tracks per event as function of the vertex position is shown in Fig. 4.10. The peaks at $\text{bbc}_{\text{z}} \sim -35$ and 30 cm are due to the electrons originating from the γ conversion inside the magnet nose cones. To avoid these electrons, we apply offline vertex cuts of $-20 < \text{bbc}_{\text{z}} < 20$ cm for the narrow vertex runs and $-30 < \text{bbc}_{\text{z}} < 25$ cm for the wide vertex runs.

4.7 Run selection

It is important to have stable performance and acceptance of the detectors involved in the analysis over the entire run, so as to avoid any extra corrections and systematic

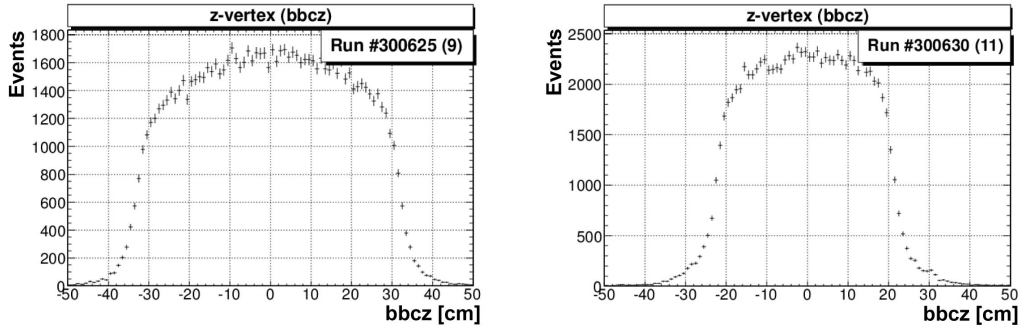


FIGURE 4.9: Vertex distribution for a run taken with a ± 30 cm vertex trigger (left) and a run taken with a ± 20 cm vertex trigger (right).

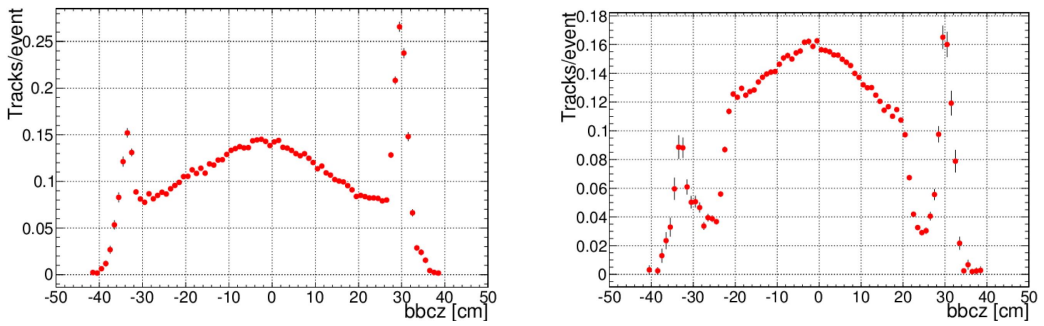


FIGURE 4.10: Electron-tracks per event distributions as function of the vertex position for a run with wide vertex trigger (left) and narrow vertex trigger (right).

errors. Changes can occur by a variety of reasons, such as loss of active areas in the detector, unstable DAQ conditions, or high voltage problems.

We performed Quality Assurance of the central arm detectors and HBD by inspecting the following variables on a run by run basis:

- HBD: average charge per pad in central events
- Central arm eID parameters: p , $n0$, disp, $\chi^2/npe0$, emcd ϕ and emcd z .
- Acceptance

The QA of HBD and the central arm eID parameters are performed in a similar way. Here, the QA of disp is shown as an example.

1. Calculate the mean (μ_{all}) and rms (σ_{all}) values of disp using all runs.
2. Calculate the mean (μ_{run}) of disp for each run. If the run does not satisfy the following condition, the run is regarded as “bad run” and discarded.

$$|\mu_{run} - \mu_{all}| < 5\sigma_{all} \quad (4.9)$$

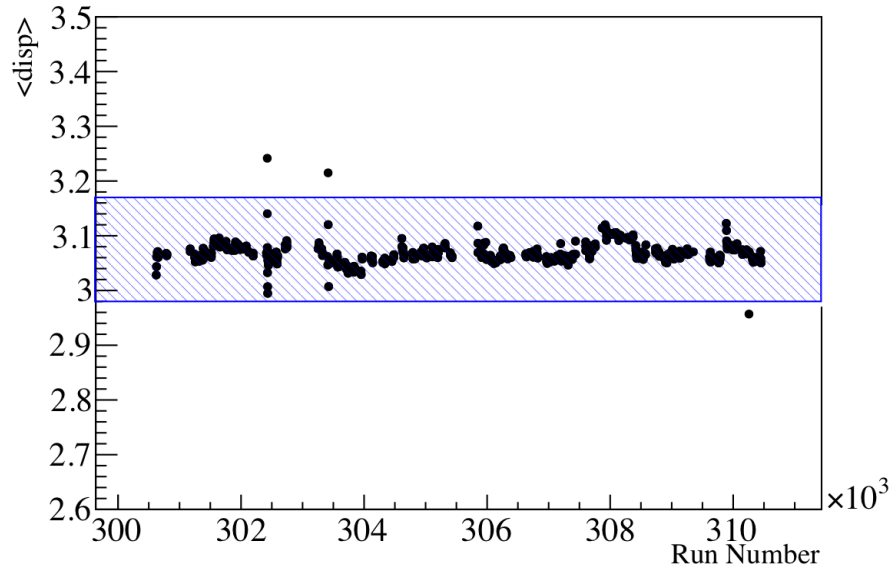


FIGURE 4.11: $\langle \text{disp} \rangle$ as a function of run number. The runs inside the shadowed band are accepted as good runs.

3. Repeat 1. and 2. until all runs satisfy the condition above.

Figures 4.11 shows the $\langle \text{disp} \rangle$ as a function of run number. The runs inside the shadowed bands are accepted as good runs. The same procedure is performed for the other parameters.

In addition to the procedure described above, the hit maps of DC, PC1 and EMCAL are examined by eye and the runs with large dead areas are discarded.

Approximately 1 Billion events are discarded by the QA procedure. This analysis is based on 5.6 Billion events that passed all the event and QA cuts.

4.8 Fiducial cuts

4.8.1 HBD projection cut

The HBD projection cut selects the central arm tracks pointing to the active areas of the HBD and excludes the tracks pointing to the EN2 module, which was not operational during Run-10. This is shown in Figure 4.12.

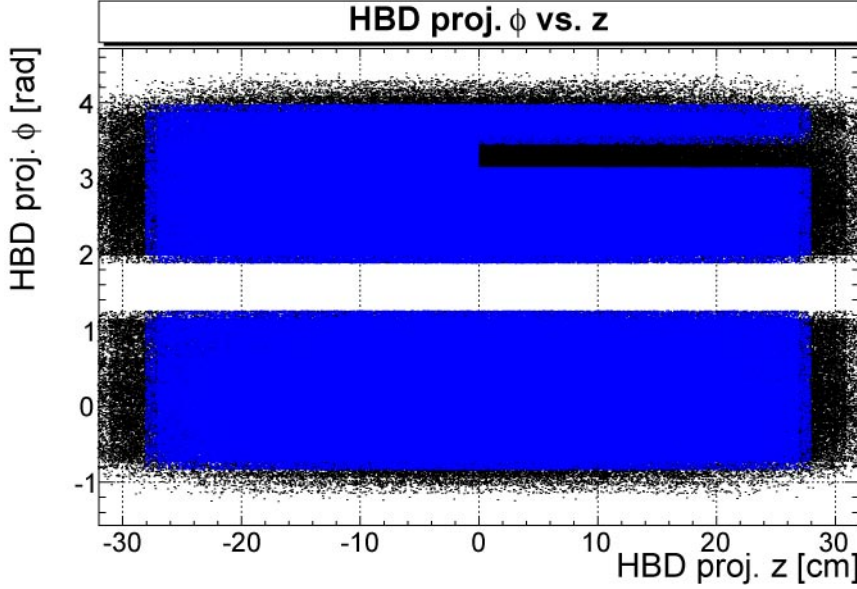


FIGURE 4.12: Track projections onto the HBD in the $\phi - z$ plane. The black points represent the tracks before applying the HBD projection cut and the blue points are the tracks accepted by the projection cut. Minimum bias data.

4.8.2 HBD support structure conversion cuts

This cut is used to remove the conversion electrons originating from the HBD support structure. These conversions are mostly localized in ϕ , therefore, tracks satisfying the following conditions are rejected.

$$\begin{aligned} \text{phbd}\phi > 1.05 \quad \&\& \quad \text{phbdphi} < 1.2 \quad \&\& \quad \phi_0 > 1.05 \quad \&\& \quad \phi_0 < 1.2 \\ \quad \&\& \quad \text{phbd}\phi < 0.04/p_T + 0.96 + 0.08 \\ \quad \&\& \quad \text{phbdphi} > 0.05/p_T + 0.96 - 0.10 \end{aligned} \quad (4.10)$$

OR

$$\begin{aligned} \text{phbd}\phi > 1.95 \quad \&\& \quad \text{phbdphi} < 2.1 \quad \&\& \quad \phi_0 > 1.95 \quad \&\& \quad \phi_0 < 2.1 \\ \quad \&\& \quad \text{phbd}\phi < -0.04/p_T + 2.14 + 0.10 \\ \quad \&\& \quad \text{phbdphi} > -0.032/p_T + 2.14 - 0.05 \end{aligned} \quad (4.11)$$

where $\text{phbd}\phi$ is the projection on HBD in ϕ .

The effect of the cut is visualized in Fig. 4.13.

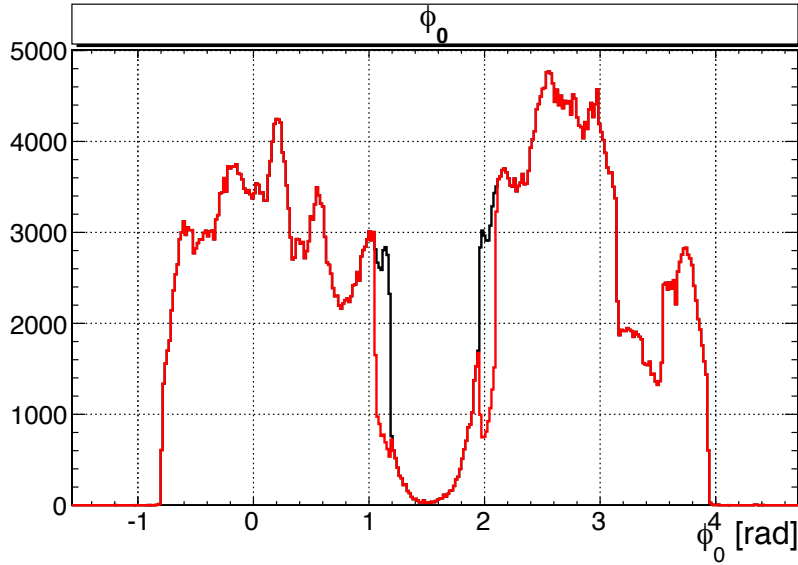


FIGURE 4.13: The ϕ_0 distribution of all tracks (black) and the tracks accepted by the cut (red) that removes conversions from the HBD support structure. Minimum bias data.

4.8.3 Drift chamber fiducial cuts

Drift chamber fiducial cuts are applied in order to homogenize the detector response over a sizable fraction of the run time.

The entire 200 GeV data set was divided into 5 groups, with fiducial cuts applied to each group separately. Two-dimensional plots of α vs DC board number for the four sectors (NE, SE, NW and SW) in Group 1 is shown in Fig. 4.14. The plots for other groups are shown in Appendix B.

4.8.4 Other fiducial cuts

The tracks pointing to dead/low efficiency areas in PC1 and EMCAL are also explicitly removed. The dead region of PC1 and EMCAL is less than 5% of the total acceptance. In addition, a dead region around $z \sim 0$ found by looking at the correlation between $\cos \theta_0$ and b_{bcz} is also removed as shown in Fig. 4.15.

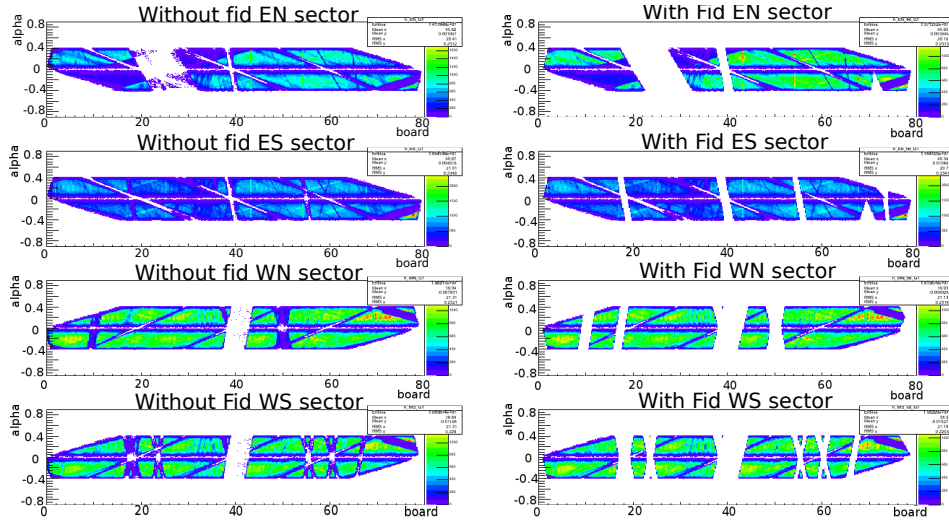


FIGURE 4.14: α vs board number for e^\pm yield without fiducial cut (left column) and with fiducial cut (right column) for all the four sectors in Run Group 01.

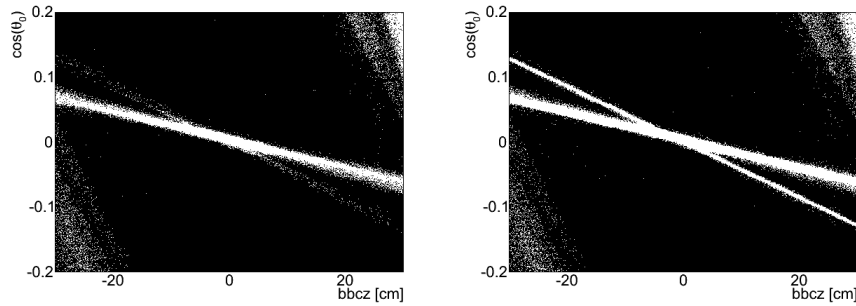


FIGURE 4.15: Correlation between $\cos(\theta_0)$ and $bbcza$. The left panel shows the raw correlation map and the right panel shows the correlation map after applying the fiducial cut that removes the tracks around $z \sim 0$.

4.9 HBD double hit rejection

The reduction of the combinatorial background is the main task of the HBD. Most of the combinatorial background in PHENIX originates from π^0 Dalitz decays and conversions where only one electron from the pair is reconstructed and the other is lost due to limited acceptance. However, the e^+ and e^- from π^0 Dalitz decays and conversions have a small opening angle and therefore leave overlapping responses in the HBD.

A neural network is used for the separation between the single and double hits in the HBD. The training sample is provided by single particle simulations, with the HBD response embedded into data to get realistic cluster charge distributions. The $\phi \rightarrow e^+e^-$ decay, where the two legs are relatively far apart, and therefore result in separated HBD responses (single hits), is used to define the signal in the training sample. The background for the training sample is provided by $\pi^0 \rightarrow e^+e^-\gamma$ decay, where the two legs are close, and result in overlapping HBD responses (double hits).

The input information for the neural network is:

- **HBDCHARGE** - the charge of the cluster provided by the non-standalone algorithm.
The cluster size is up to 3 pads.
- **hbdcharge** - the charge of the cluster provided by the standalone algorithm. The cluster size is up to 7 pads.
- **maxpadcharge** - the maximum pad charge in the cluster of the standalone algorithm.

The reasoning for the choice of these variables is the following: the non-standalone algorithm uses the track projection and forms a cluster around the track projection point on the HBD. This results in a more precise selection of the hit and a less probable pick up of a fake hit. However the limited cluster size (up to 3 pads) truncates the charge information, which is important for the distinction between single and double hits. Therefore the standalone cluster information is also used. These clusters are formed by summing all the fired pads around a seed and can result in a cluster containing up to 7 pads. In this way more charge information is preserved, which is especially important since the double hits can have a small but finite opening angle. In addition, the maximum pad charge information is used to distinguish those cases where all or most of the charge is deposited in a single pad.

Separate neural networks are trained for each centrality bin (0-10%, ..., 80-90%) and for each cluster size of the non-standard algorithm (**HBDSIZE** = 1,2,3). This last step is necessary since the **HBDSIZE** and therefore the **HBDCHARGE** depend on the projection

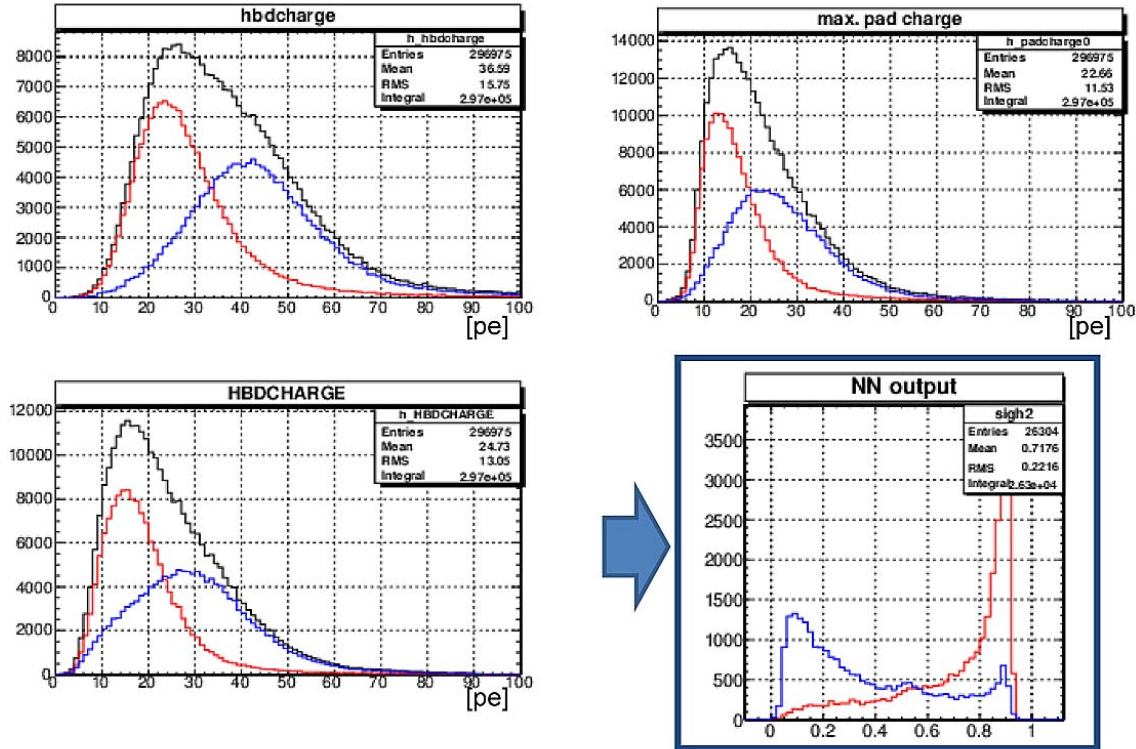


FIGURE 4.16: The input variables for the neural network (top panels and bottom left). The red lines correspond to single hits (signal) and the blue lines to double hits (background). The black is the sum of the two. The resulting neural network output is shown in the bottom right panel. This is an example for centrality 30-40% and HBDSIZE=2 from the Monte-Carlo simulation.

point. Hence in total there are $9 \times 3 = 27$ cases. An example of the input variables, along with the resulting neural network output is shown in Figure 4.16. The neural network output is referred to as `nnoutsd`.

4.10 Electron Identification

Our electron identification procedure consists of several steps to deal with the high occupancy of RICH, which is the primary electron identification tool in PHENIX, in the most central events:

EWG The following 1D cuts are applied at the very beginning of this analysis and only these tracks are analyzed.

- $p_T > 0.12 \text{ GeV}/c$
- $0.4 < \text{ecore}/p < 10.0$
- $n0 \geq 1$

- $\text{disp} < 8.0 \text{ cm}$

These initial weak cuts are referred to as EWG (Electron Working Group) cuts.

Step 0 A neural network optimized to reject hadrons. At this stage, we use only the central arm variables and apply loose cuts.

Step 1 In the central arm, a charged hadron track parallel to an electron track is matched to the PMTs fired by the electron due to the spherical mirror properties of the RICH detector, and is therefore misidentified as an electron. This RICH ring sharing effect occurs because the RICH ring reconstruction allows multiple use of fired PMT by different tracks. The effect occurs for all genuine electrons traversing the RICH including background electrons generated by γ conversion. We can reduce this effect not only by rejecting background electrons but also by erasing their associated PMTs. In step 1, RICH PMTs fired by background electrons are erased and new RICH rings are reconstructed. The RICH variables, n_0 , disp and χ^2/n_{pe0} are recalculated. Those re-calculated variables are referred to as $n_0(\text{new})$, $\text{disp}(\text{new})$ and $\chi^2/n_{\text{pe0}}(\text{new})$.

Step 2a Neural network optimized to reject hadrons using the re-calculated RICH variables.

Step 2b Neural network optimized to reject HBD backplane conversion electrons.

In this section, the neural network trainings performed for Step 0, Step 2a and Step 2b are discussed first, and then the applied cuts on the neural network outputs are described in the subsequent sections.

4.10.1 Neural Network training

The neural networks are trained on HIJING samples [88, 89, 90, 91]. HIJING events covering all centralities are produced and filtered with the same cuts as applied to the data.

The neural networks are trained to distinguish between “signal” and “background” tracks. The signal and background tracks used for each neural network are summarized in Table 4.3. In step 2a, electrons coming from γ conversion are excluded from the signal because both conversion electrons generated at the HBD backplane and hadrons do not leave a signal in the HBD and the neural network training can be confused.

TABLE 4.3: Signal and background definition for the neural network trainings

Step	Signal	Background
0	e^\pm	Hadrons
2a	e^\pm not originating from γ conversion	Hadrons
2b	e^\pm not originating from γ conversion or π^0	e^\pm from γ conversion inside HBD backplane

The input parameters are summarized in Table 4.4. Three sets of input parameters are used for step 0 and step 2a because the available timing information is different for the three subsystems: PbSc, TOFE and PbGl outside TOFE acceptance.

TABLE 4.4: Input parameters of each neural network

Step	Type	Input parameters
0	PbSc	n0, disp, $\chi^2/npe0$, dep, emcsdr, stof(PbSc)
	TOFE	n0, disp, $\chi^2/npe0$, dep, emcsdr, stof(TOFE)
	No TOF	n0, disp, $\chi^2/npe0$, dep, emcsdr
2a	PbSc	n0(new), disp(new), $\chi^2/npe0$ (new), dep, emcsdr, stof(PbSc), hbddid, hbdcharge, hbdsiz
	TOFE	n0(new), disp(new), $\chi^2/npe0$ (new), dep, emcsdr, stof(TOFE), hbddid, hbdcharge, hbdsiz
	No TOF	n0(new), disp(new), $\chi^2/npe0$ (new), dep, emcsdr, hbddid, hbdcharge, hbdsiz
2b		dep, hbddid, hbdcharge, hbdsiz

The step 0 and step 2b neural networks are trained separately for centrality 0-10%, 10-20% and 20-40% centrality bins. The neural network trained with centrality 20-40% is also used for the 40-60% and 60-92% centrality bins because the signal to background ratio in those bins are large and fine tuning of eID cuts is not necessary. The step 2a neural network is trained separately for the 0-10%, 10-20%, 20-40%, 40-60% and 60-92% centrality bins.

The output of the neural network is a single probability-like variable with a value between 0 and 1, where 0 corresponds to background and 1 corresponds to signal. We refer to the output of step 0 as nnout0, output of step 2a as nnout2a and output of step 2b as

`nnout2b`. The distribution of each neural network output is shown for signal tracks and background tracks in Figs. 4.17-4.19 for the 20-40% centrality bin.

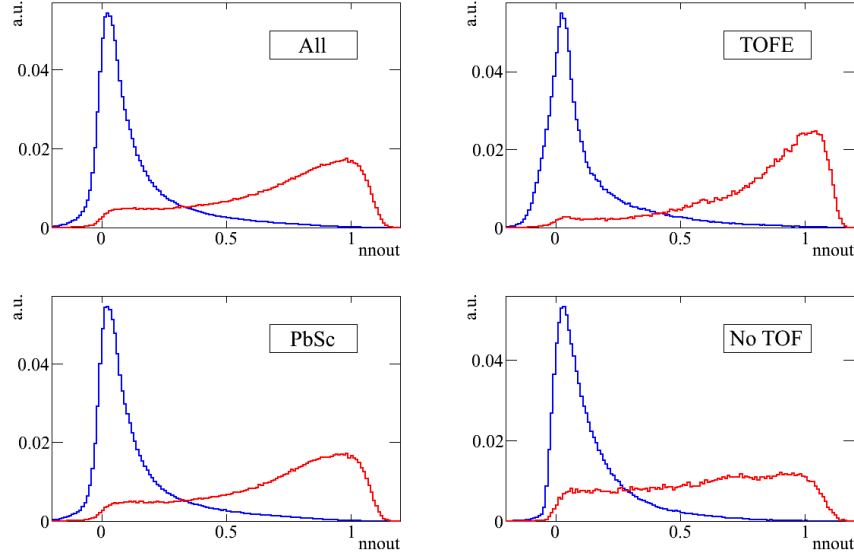


FIGURE 4.17: `nnout0` distribution in the 20-40% centrality bin. The red line corresponds to signal hits and the blue line corresponds to background hits.

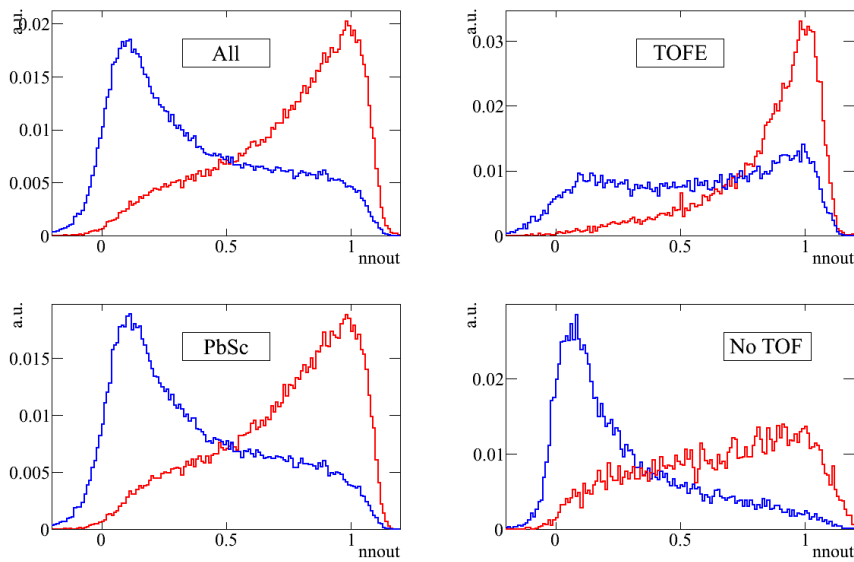


FIGURE 4.18: `nnout2a` distribution in the 20-40% centrality bin. The red line corresponds to signal hits and the blue line corresponds to background hits.

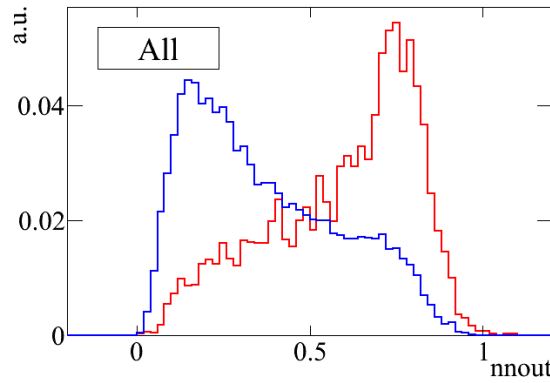


FIGURE 4.19: `nnout2b` distribution in the 20-40% centrality bin. The red line corresponds to signal hits and the blue line corresponds to background hits.

4.10.2 Step 0: Loose eID cuts

At the beginning of the eID flow, obvious hadrons are removed from the electron sample using the step 0 neural network. The thresholds applied to `nnout0` are chosen such that the efficiency is more than 80% resulting in threshold values that vary from 0.15 to 0.25 for the different centrality classes.

4.10.3 Step 1: PMT erasing

The RICH PMTs fired by the following types of electrons are erased from the fired PMT list.

- Clear HBD Backplane conversions selected by loose `hbdid` cuts
 $\text{hbdid} < 5$ (0-10%), $\text{hbdid} < 10$ (10-20%), $\text{hbdid} < 8$ (20-30%), $\text{hbdid} < 9$ (30-40%),
 $\text{hbdid} < 10$ (40-60%) and $\text{hbdid} < 15$ (60-92%)
- HBD double signal

The applied thresholds are optimized in Section 4.10.4 together with the Step 2a and Step 2b thresholds.

- Low pT tracks
 $p_T < 0.3 \text{ GeV}/c$
- Electron tracks outside HBD acceptance

See Sec 4.8.1.

- Electron tracks from HBD support conversion

See Sec 4.8.2.

For all cases, `nnout0` is used to confirm that the selected tracks are electrons. The thresholds are optimized such that the probability for a track to be an electron is higher than the probability to be a hadron. Since the hadron contamination is small even without optimization for 40-60% and 60-92% centrality bins, the same thresholds as the 20-40% centrality bin is applied for them. The threshold values are varied between 0.3 and 0.5 for the different cases.

4.10.4 Step2a, Step2b and HBD S/D: Cut optimization

The cut thresholds applied to `nnout2a`, `nnout2b` and `nnoutsd` are optimized using HIJING. Depending on the cuts one obtains a certain rejection of the background tracks with some efficiency for the signal tracks. The cuts are selected in a such a way as to maximize the effective signal, S/\sqrt{B} , where S is defined as the number of electrons from charm decay per event and B is defined as the total number of electron tracks per event. The thresholds are varied between 0.45 and 0.75 in steps of 0.05 for `nnout2a` and between 0 and 0.6 in steps of 0.05 for `nnout2b`. The `nnoutsd` threshods are shifted relative to the reference values shown in Table 4.5 by -0.3, -0.2, -0.1, 0.0, +0.1 and +0.2 and the shifts are independent of `HBDSIZE`.

The effective signal is maximized within the setups satisfying the following conditions.

- Hadron contamination $<\sim 5\%$
- The three types of neural networks, one with PbSc timing information, one with TOFE timing information and one without any timing information, have similar efficiencies with differences of less than 10%.

Figure 4.20 show the scatter plots of S/\sqrt{B} vs. S/B of for each centrality bin. The finally selected setup is shown with yellow square boxes in the figures. The corresponding thresholds are summarized in Table 4.6.

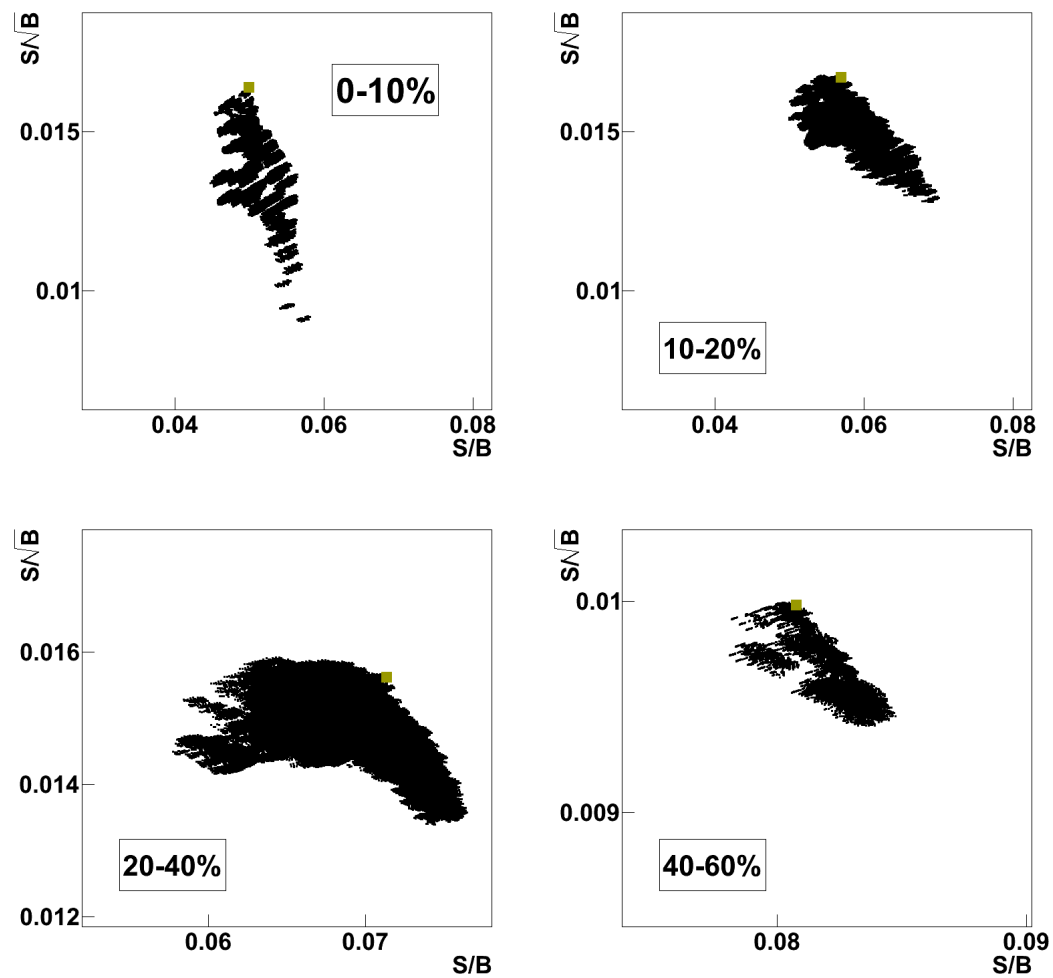


FIGURE 4.20: Scatter plots of the effective signal versus the signal-to-background. The point shown with the yellow square is the setup selected for the analysis.

TABLE 4.5: S/D cuts threshold used as a reference.

Centrality	HBDSIZE		
	1	2	3
0-10%	0.4	0.36	0.35
10-20%	0.42	0.40	0.44
20-30%	0.39	0.39	0.41
30-40%	0.43	0.46	0.47
40-50%	0.44	0.49	0.54
50-60%	0.45	0.46	0.52
60-70%	0.57	0.61	0.69
70-80%	0.58	0.62	0.70
80-92%	0.60	0.65	0.74

TABLE 4.6: Optimized nnout threshold. The nnoutsd thresholds are shown as the shifts relative to the values listed in Table 4.5.

Centrality	TOFE			PbSc			No TOF		
	S/D	2a	2b	S/D	2a	2b	S/D	2a	2b
0-10%	-0.3	0.7	0.35	-0.3	0.7	0.3	-0.2	0.55	0.1
10-20%	+0.1	0.55	0.2	-0.1	0.65	0.25	-0.3	0.55	0.15
20-40%	-0.1	0.7	0.45	0.0	0.7	0.3	-0.1	0.55	0.2
40-60%	-0.1	0.6	0.45	+0.1	0.7	0.4	-0.1	0.45	0.25
60-92%	-0.1	0.75	0.45	+0.1	0.75	0.4	-0.1	0.75	0.25

4.11 Pair ghost cut

Pair cuts are needed in order to remove pairs generated by artificial correlations induced in various detectors. The most prominent one is the ring sharing cut in the RICH detector. When two tracks are parallel after the DC, they share the same RICH response, i.e. they share the same RICH ring. If one of them is an electron, any other parallel track, including hadron tracks, will appear to have a Čerenkov response and will be misidentified as electron. Similar ghost pairs are generated in other detectors (EMCal, DC/PC1 and HBD) if a track happens to be in close proximity to a real electron track,

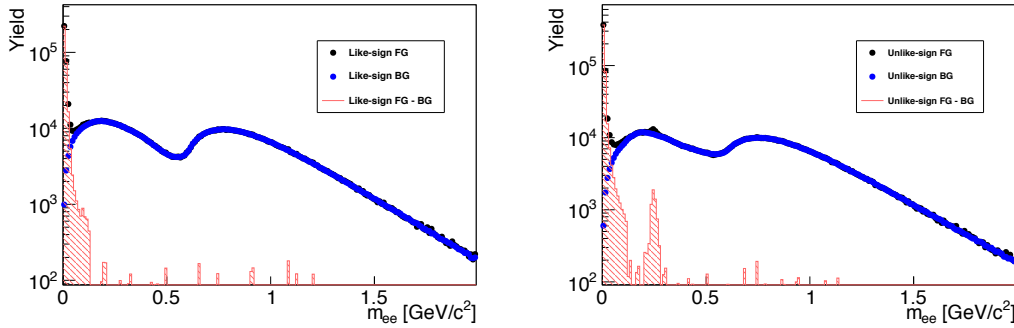


FIGURE 4.21: Left panel: like-sign foreground, mixed background, and the subtracted spectra. One can see a large correlation at low masses. Right panel: unlike-sign foreground and mixed background and the subtracted yield , where a clear correlation peak is visible at 0.25 GeV/\$c^2\$. The plots are for 0-10% centrality.

or more precisely whenever the two tracks hit the detector within a distance smaller or equal to the double hit resolution in that detector. The ring sharing artifact as well as the track proximity in DC/PC1, EMCal and HBD create correlated pairs which cannot be removed by the mixed event background subtraction. Since we do not know which track of the pair is a real electron, and since the probability for these pairs is relatively small we adopt the approach of rejecting the entire event whenever such a pair is found in that event.

The correlated pairs mentioned above are clearly seen in the mass spectra. For example, the correlation due to the RICH ring sharing introduces a peak at around 0.25 GeV/\$c^2\$ in the unlike-sign pair yield and a peak close to zero masses in the like-sign yield. This is demonstrated in Figure 4.21.

4.11.1 RICH cut

The ghost pairs in the RICH detector are clearly identified by looking at the $\Delta\phi - \Delta z$ distributions of track pairs in RICH. They are defined as $\Delta\phi = \phi_1 - \phi_2$ and $\Delta z = z_1 - z_2$, where 1 and 2 refer to the first and the second track, respectively. These distributions are shown in Figure 4.22.

The projections on the vertical and horizontal axes show Gaussian distributions with standard deviations of $\sigma_\phi = 0.01$ rad and $\sigma_z = 3.6$ cm, for the $\Delta\phi$ and Δz distributions, respectively. We define the total standard deviation in units of sigma as:

$$\sigma_{tot} = \sqrt{\left(\frac{\Delta\phi}{\sigma_\phi}\right)^2 + \left(\frac{\Delta z}{\sigma_z}\right)^2} \quad (4.12)$$

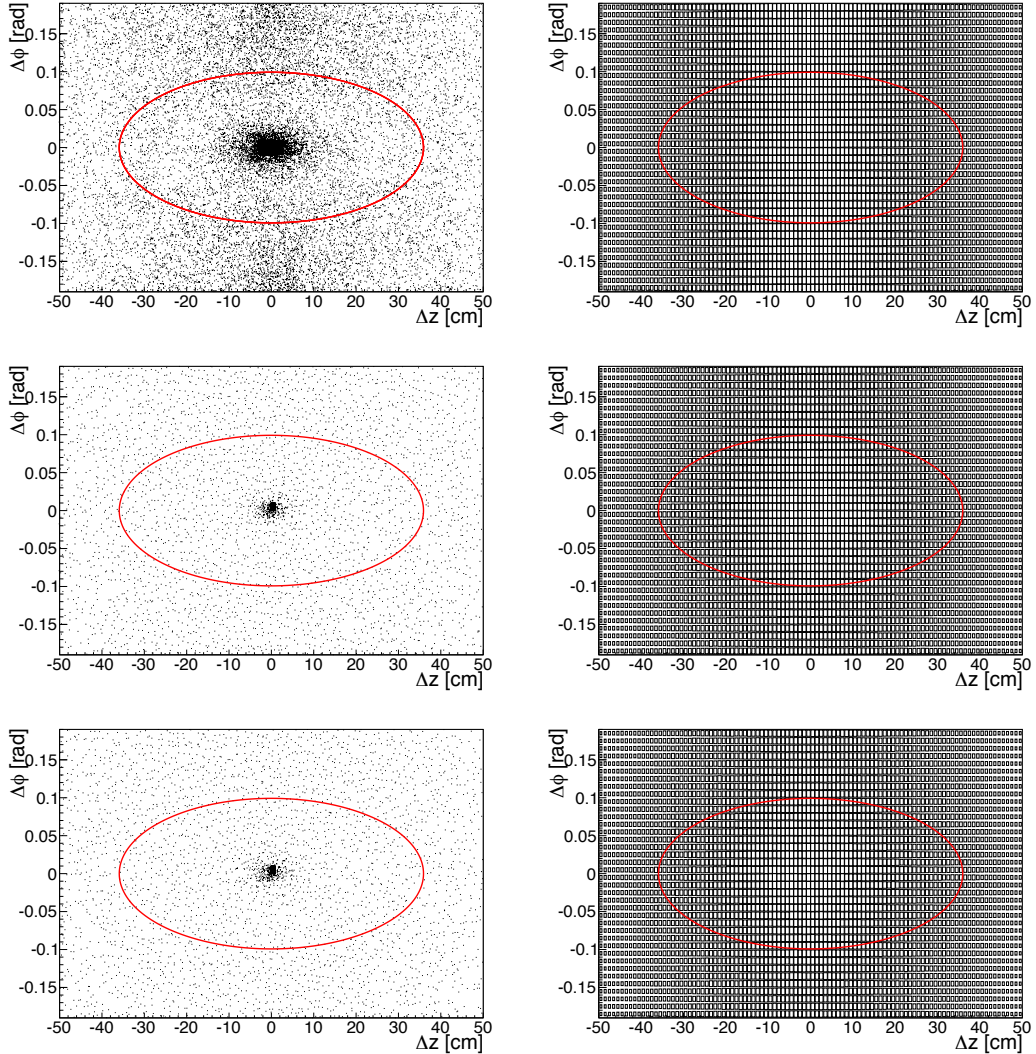


FIGURE 4.22: The $\Delta\phi - \Delta z$ distributions in RICH. The left panels show unlike-sign foreground (top), like-sign foreground ++ (middle) and like-sign foreground -- (bottom). The right panels show unlike-sign mixed background (top), like-sign mixed background ++ (middle) and like-sign mixed background -- (bottom).

and apply a cut at $n\sigma_{tot}$. The question arises: what is the optimal value of n ? To answer this question we examine the yield in the affected region of the unlike-sign mass spectrum, after subtracting the mixed background¹ and after correcting for the efficiency losses of the cut. This is repeated for the following values of $n = 0, 3, 5, 7, 10, 12, 15$. In each case, if a pair is found within the given $n\sigma_{tot}$, the entire event is rejected. The results are shown in Figure 4.23. The yield decreases with increasing n , since the correlation is removed. The yield has a minimum at 5 sigma, By increasing the cut the corrected

¹The normalization factor for the mixed background is derived as $\sqrt{n f_{++} n f_{--}}$, where $n f_{++}$ and $n f_{--}$ are obtained by normalizing the like-sign foregrounds to the like-sign backgrounds in the mass region $0.64-1.5 \text{ GeV}/c^2$.

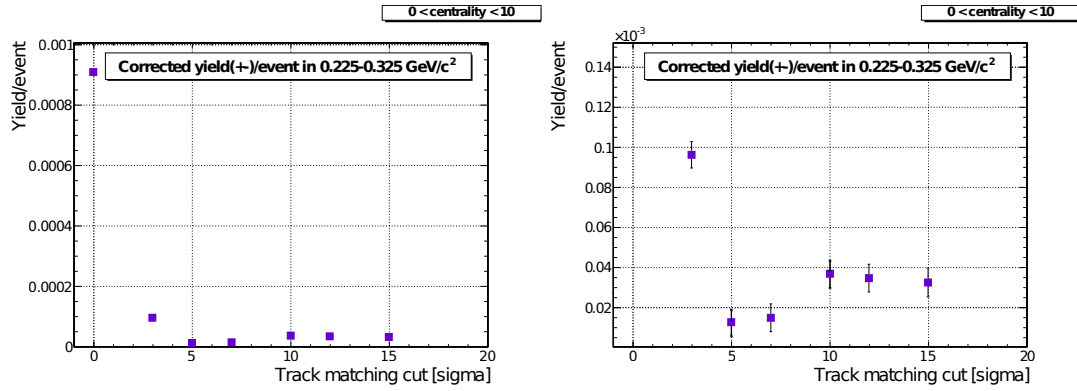


FIGURE 4.23: The corrected yield vs. the ring sharing cut value. The right plot is a zoom of the y-axis. The data are for 0-10% central events.

yield saturates after 10 sigma and this is where the final cut is placed. This distance is equivalent to 2 ring radii in RICH.

4.11.2 EMCAL cut

After rejecting the tracks parallel in RICH by the 10 sigma cut, we investigate track proximity effects in EMCAL. To find the correlated yield we look at the $\Delta y - \Delta z$ distributions. They are defined as $\Delta y = y_1 - y_2$ and $\Delta z = z_1 - z_2$, where 1 and 2 refer to the first and the second track, respectively. These distributions are shown in Figure 4.24.

The proximity cut in EMCAL is studied using the same procedure as for the RICH ring sharing cut: apply the cut with increasing width and determine the optimal value from the corrected yield. The EMCAL proximity variable is based on y and z indices associated to the cluster's center-of-gravity and is defined as:

$$\Delta_{EMC} = \sqrt{(\Delta z)^2 + (\Delta y)^2} \quad (4.13)$$

Since y and z assume only discrete values, $\Delta_{EMC} = 0, 1, 1.41, 2, 2.24, 2.83, 3$, etc.

The signal is extracted by subtracting the mixed event, normalized using the like-sign foregrounds and backgrounds in the mass region above 1 GeV/c². The subtracted signal is then corrected for the cut efficiency. The yield is integrated in the region affected by the cut: 0.19-0.22 GeV/c² and the results are shown in Figure 4.25. They show that the yield saturates for a cut value larger than ~ 2.5 , hence $\Delta_{EMC} > 2.5$ is considered to be the optimal cut condition.

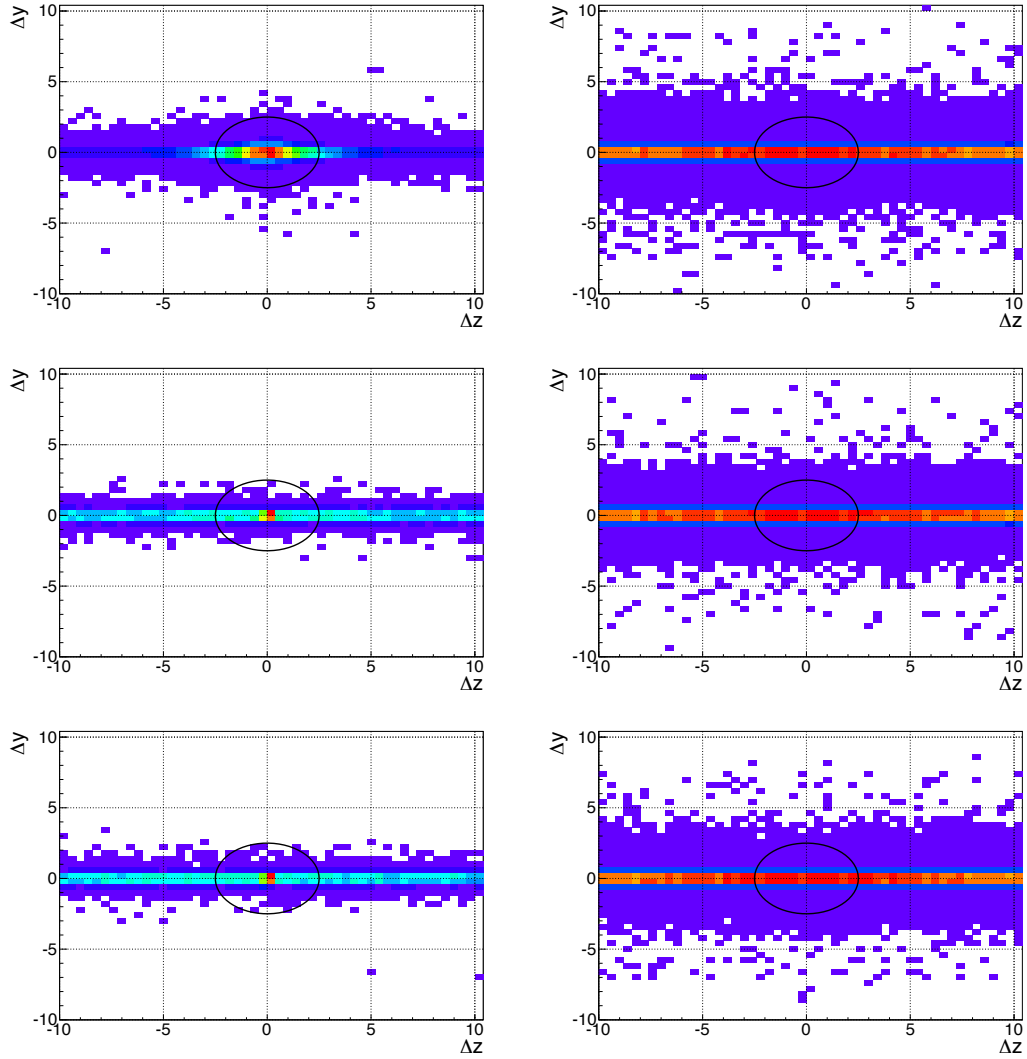


FIGURE 4.24: The $\Delta y - \Delta z$ distributions in EMCAL. The left panels show unlike-sign foreground (top), like-sign foreground ++ (middle) and like-sign foreground -- (bottom). The right panels show unlike-sign mixed background (top), like-sign mixed background ++ (middle) and like-sign mixed background -- (bottom).

4.11.3 PC1 cut

The proximity cut in PC1 is needed for two reasons: the PC1 double hit resolution and the PHENIX tracking algorithm.

The effect of double hit resolution is clearly visible in the PC1's $\Delta_\phi - \Delta_z$ distributions in the foreground and in the mixed background as shown in Fig. 4.26. In the unlike-sign foreground one notices a region with correlated yield (red circle) and a region of anti-correlated yield (cyan ellipse, half axis 0.02 rad in ϕ and 5 cm in z). The same is seen in the like-sign foreground. Since none of these effects is reproduced in the mixed

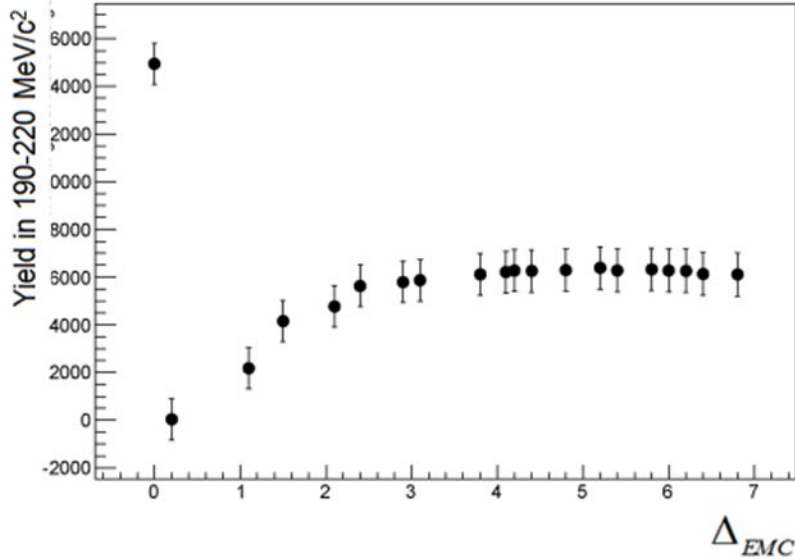


FIGURE 4.25: The corrected yield vs. the EMCAL cut value. The data are for 0-10% central events.

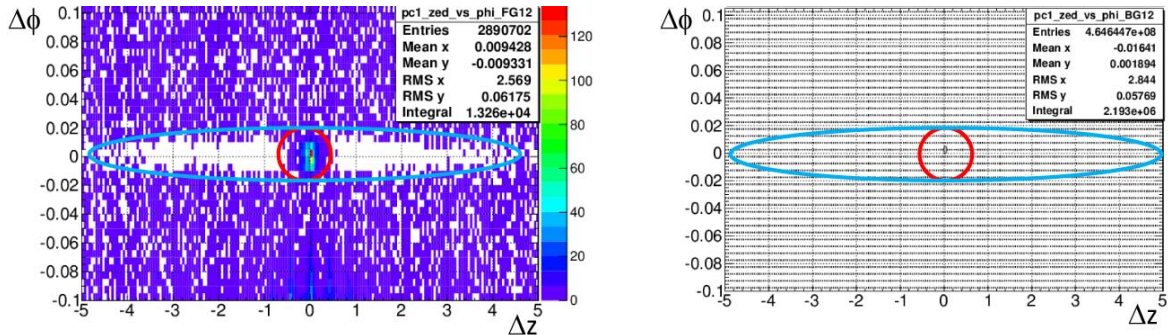


FIGURE 4.26: The $\Delta_\phi - \Delta_z$ in PC1, unlike-sign foreground (left), unlike-sign mixed background (right). The red ellipse marks the region with extra yield in the foreground and the magenta ellipse marks the region with missing yield in the foreground.

background, we select to cut on the cyan ellipse keeping only the yield outside, where there is no correlation or anti-correlation neither in foreground nor in the background.

The PHENIX tracking algorithm first reconstruct tracks using X1 and X2 DC planes and then extrapolate the tracks to PC1 as described in Section 4.3. If there is an unambiguous PC1 hit, PC1 is used, if not, DC UV planes are used to determine the z coordinate of the tracks. Therefore if two tracks are hitting PC1 with similar ϕ , UV planes are used in the foreground and PC1 is used only in mixed-background. This produces a dip in the PC1 Δ_ϕ distribution as shown in Fig 4.27. To avoid the effect, if two tracks have a Δ_ϕ difference of less than 0.014 rad on the same side of DC, the two tracks are rejected.

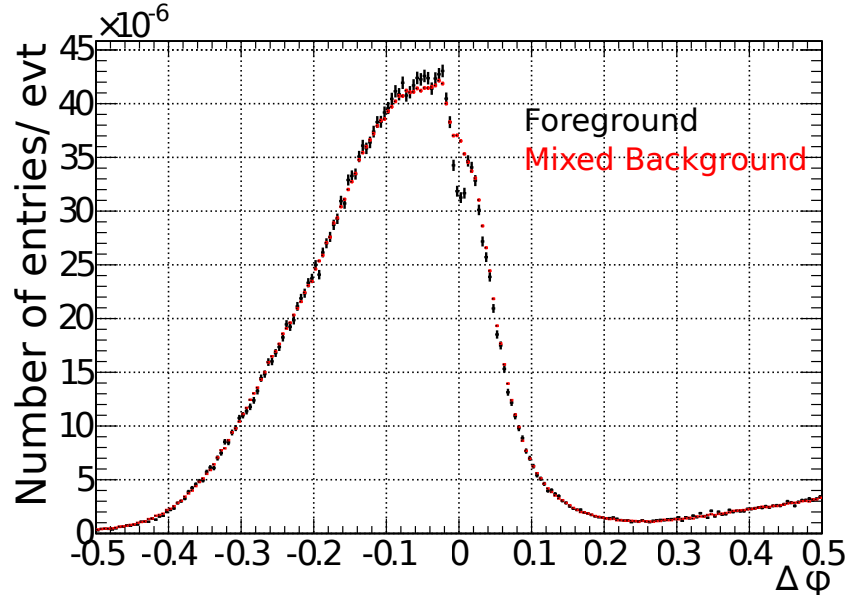


FIGURE 4.27: PC1 $\Delta\phi$ distribution to see the effect of the PHENIX track reconstruction algorithm on the proximity hits in PC1. This $\Delta\phi$ distribution is obtained with the ellipse cut shown in Fig 4.26.

4.11.4 HBD cut

When hadrons or HBD backplane conversion electrons share HBD hits with other electrons originating before the HBD backplane, they cannot be rejected by HBD. This correlation results in extra foreground yield at small opening angle as shown in Fig 4.28. To eliminate such correlated yield, an opening angle cut 0.1 rad is applied.

4.11.5 The affected mass regions

The proximity cut of HBD removes yield at $m_{ee} \sim 0$ for both like-sign and unlike-sign spectra. However, the other pair cuts affect the like-sign and unlike-sign spectra differently as shown in Fig. 4.29. The figure shows the foreground spectra without any pair cuts and with RICH, PC1 and EMCAL pair cuts. The like-sign yield around $m_{ee} \sim 0$ GeV/c^2 is affected by all the cuts, on the other hand, two dips are visible in the unlike-sign spectra. The dip at $m_{ee} \sim 0.25$ GeV/c^2 is created by the RICH pair cut and the dip at $m_{ee} \sim 0.15$ GeV/c^2 is created by the PC1 pair cut. The EMCAL pair cut removes the yield around 0.20 GeV/c^2 , but the effect is small compared to the other cuts.

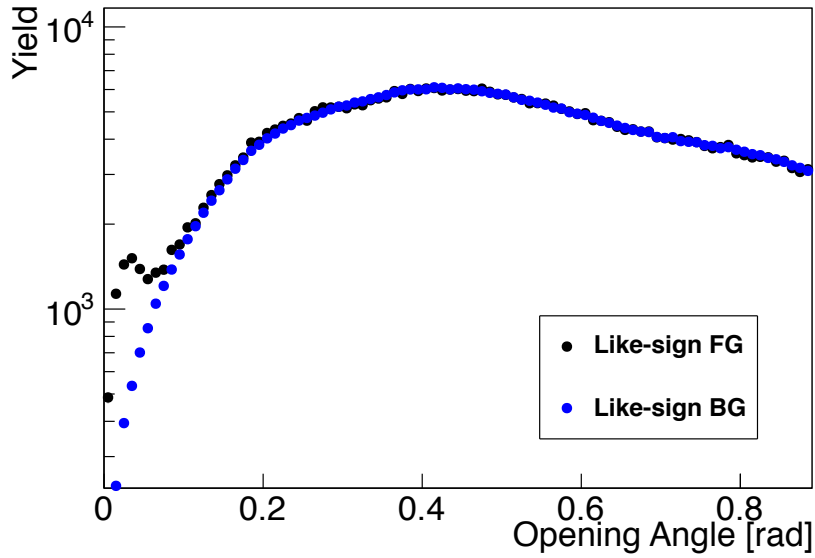


FIGURE 4.28: Like-sign pair's opening angle distribution. The plot is for 0-10% centrality bin.

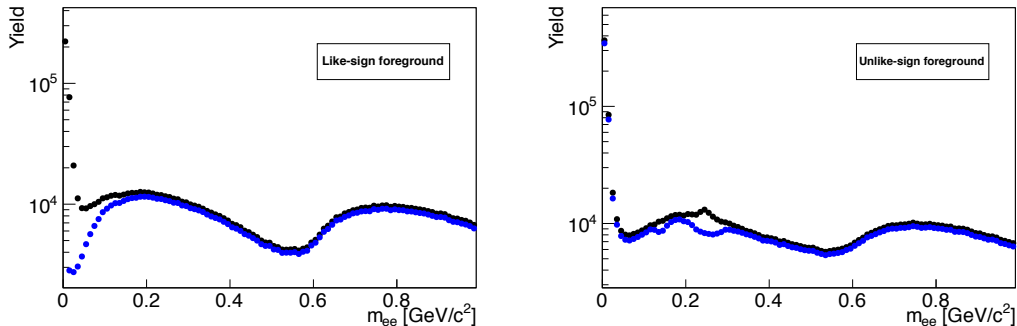


FIGURE 4.29: Like-sign (left) and unlike-sign (right) foreground spectra without any pair cuts (Black) and with RICH, EMCal and PC1 pair cuts (Blue). The plots are for the 0-10% centrality bin.

4.12 Background subtraction

4.12.1 Combinatorial pairs

We use the “event mixing” technique to simulate the combinatorial pairs. The “event mixing” technique combines tracks from different events with similar characteristics. In this analysis, all the events are classified into 12 bins in z between ± 30 cm and 10 bins in centrality between 0 – 100 % and the “event-mixing” is performed for events in the same bin. In the following these bins are referred to as pools.

We generate mixed-event pairs in a pool as follows.

1. Tracks from a given event, passing the single cuts and the pair cuts described in the previous sections are stored in the pool corresponding to that event. Once a pool accumulates a certain number of events, which we call “depth”, mixed events are generated using the tracks in the pool. The depth used in the analysis is 1000.
2. First, we choose the number of electrons and positrons in the mixed event. The numbers are randomly taken from the distribution of real events. Then, we select the specified number of electrons and positrons from the pool and form the like-sign and unlike-sign pairs of the generated mixed event. The tracks are chosen so that tracks from the same event are not used.
3. The pair cuts are applied to the pairs of the generated mixed events. Mixed events do not have ghost pairs, however, this step is needed to make the phase space covered by mixed-event pairs to be same as that of foreground pairs.
4. The (m_{ee}, p_T) spectra are generated for both unlike-sign and like-sign pairs. The generated spectra are referred to as “mixed event background” or “mixed background”.

Figure 4.30 shows the ratio between the foreground mass spectrum and the mixed background spectrum generated as described above in the 20-40% centrality bin. The ratio is not flat at all because the mixed-event pairs do not have the effect of “elliptic flow”, which is intrinsic to heavy ion collisions [81, 82, 83, 84, 85]. Figure 4.31 shows the interacting region of two heavy ions crossing each other. The non-isotropic initial collision geometry results in a partonic pressure gradient and then in a non-uniform distributions of emitted particles. Figure 4.32 shows the inclusive single electron yield as a function of the azimuthal angle with respect to the reaction plane in the p_T range 0.7-0.8 GeV/c for the 20-30% centrality bin. The result of fitting the distribution to the second Fourier component, $1 + 2v_2 \cos(2(\phi - \Psi))$, is also shown in the figure. The mixed-event background pairs are formed by randomly picking up two tracks from different events and thus on the average do not have any flow effect.

The elliptic flow is introduced into the mixed-events by “weighting method”. If particles are generated according to the following distribution function:

$$1 + 2v_2 \cos(2(\phi - \psi)) \quad (4.14)$$

where ϕ is the particle’s emission angle in azimuth and ψ is the reaction plane angle, random pairs formed from these particles are distributed as:

$$P(\Delta\phi) = 1 + 2v_2 v_2 \cos 2(\phi_1 - \phi_2) \quad (4.15)$$

where ϕ_1 and ϕ_2 are emission angle of the particles forming the pair. Eq. (4.15) is used as a weighting factor when filling pair histograms in the step 4 mentioned above. See Appendix C for a detailed derivation of the weighting factor.

The method is evaluated in a Toy Monte Carlo (ToyMC) simulation. The ToyMC generates electrons and positrons following a Poisson distribution with a mean value of three. The particles are uniformly distributed in pseudorapidity between ± 0.35 and their momentum distribution is taken from data. The azimuthal emission angle ϕ is determined according to the distribution $1 + 2v_2 \cos 2(\phi - \psi)$, where ψ is the reaction plane angle, which is uniformly distributed between $\pm \frac{\pi}{2}$. The v_2 values are taken from the inclusive single electron analysis in the 20-40 % centrality bin (see below). The tracks that pass the PHENIX acceptance filter are used in the pair analysis.

Figure 4.33 shows the ratio of the mass spectra between foreground pairs and mixed background pairs. Black points correspond to the simple mixed-event technique without introducing flow. We can see that in this approach the foreground shape is not reproduced by the background shape. A slope is observed which is very similar to the one seen in data. Red points correspond to the weighting method. The ratio is completely flat and this method is used for the data analysis.

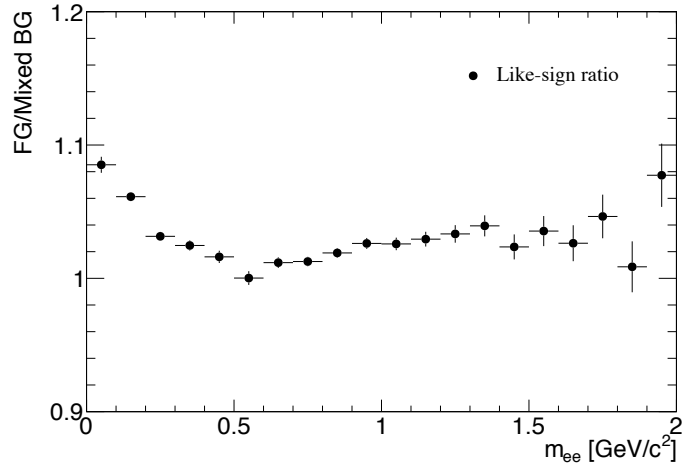


FIGURE 4.30: The ratio between the foreground mass spectrum and the simple mixed background without flow effect for the 20-40% centrality bin.

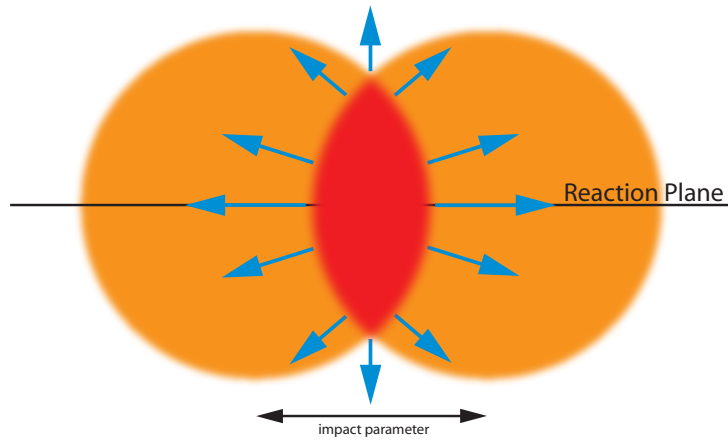
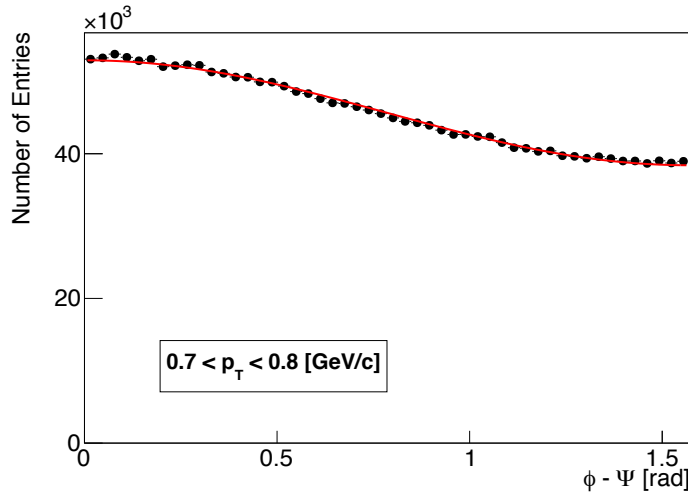


FIGURE 4.31: 2D flow cartoon.

FIGURE 4.32: The inclusive single electron yield as a function of the angle relative to the reaction plane for $0.7 < p_T < 0.8$ GeV/c in the 20-30 % centrality bin.

To use the weighting method, the inclusive single electron v_2 needs to be determined prior to the pair analysis. The v_2 is determined as a function of centrality and electron p_T using exactly the same single and pair cuts as in the pair analysis. First, the $\phi - \psi$ distributions are fitted to $1 + 2v_2^{obs} \cos 2(\phi - \psi)$ as shown in Fig 4.32. The v_2^{obs} is different from the true v_2 due to the finite reaction plane resolution σ_{RP} . The true v_2 is calculated as:

$$v_2 = \frac{v_2^{obs}}{\sigma_{RP}} \quad (4.16)$$

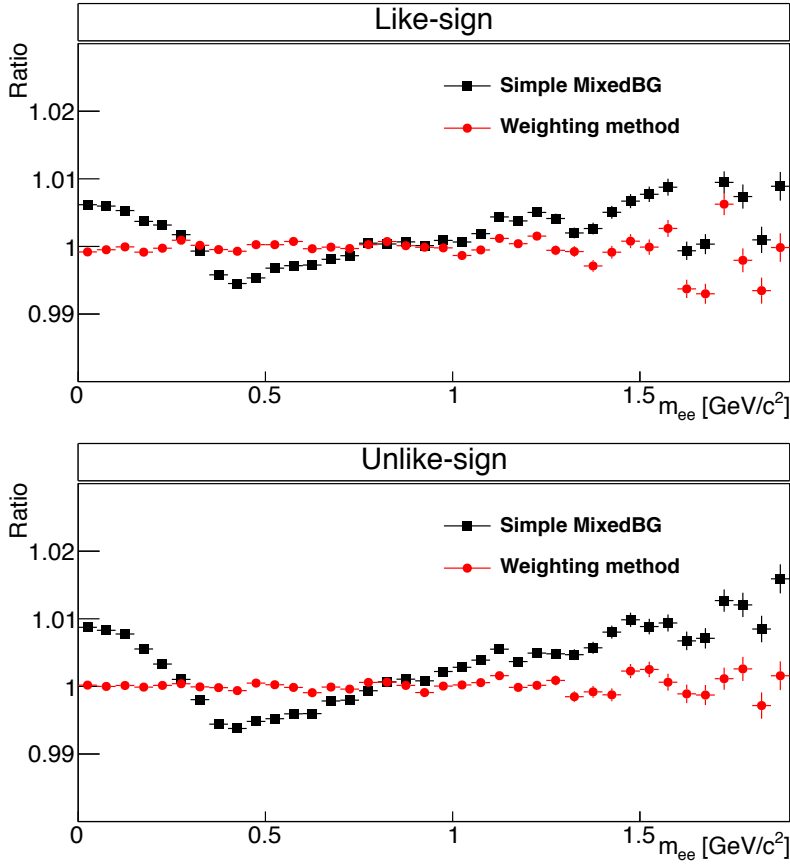


FIGURE 4.33: The ratio between foreground and mixed background mass spectra in ToyMC with and without flow effect in the mixed background. Black: simple mixed-event technique. Red: weighting method.

The σ_{RP} estimated in 2007 runs are used in the analysis and shown in Fig. 4.34 [86]. The derived v_2 values are shown as a function of centrality for each centrality bin in Fig 4.35.

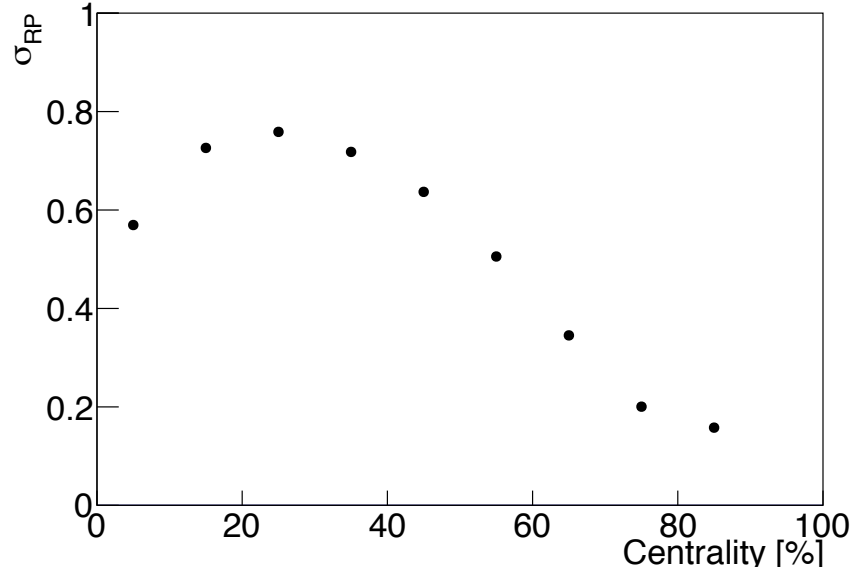
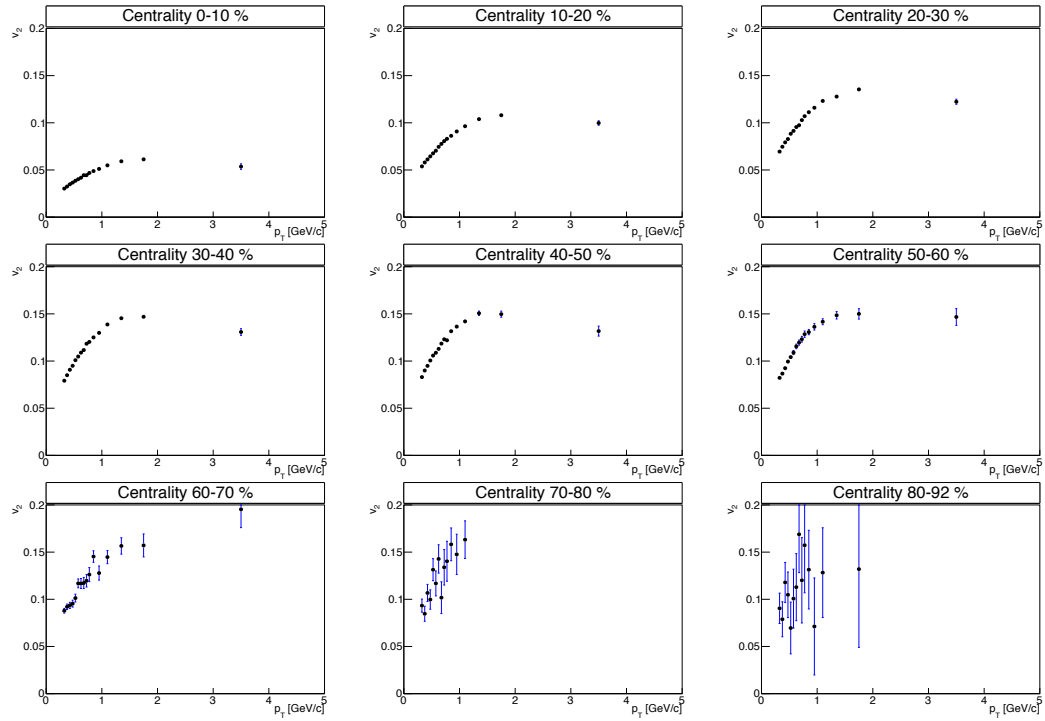


FIGURE 4.34: Reaction plane resolution as a function of centrality [86].

FIGURE 4.35: Inclusive single electron v_2 .

So far, we discussed only the shape of the mixed background. The next question is how to normalize it. We determine the normalization factors of the mixed event like-sign spectra and uses them to “absolutely” normalize the unlike-sign mixed background.

It is known that, as long as electrons and positrons are produced in pairs, the unlike-sign combinatorial background is the geometric mean of the like-sign background, independent of single electron efficiency and acceptance [35]:

$$\int BG12 \, dm_{ee} = 2\sqrt{\int BG11 \, dm_{ee} \int BG22 \, dm_{ee}} \quad (4.17)$$

This equation does not hold true when pair cuts are applied to the spectra because any pair cuts affect the unlike-sign and like-sign spectra differently. Therefore, the number of generated pairs before applying the pair cuts are monitored in the step 3 of the mixed-event procedure: $N11^{org}$, $N22^{org}$ and $N12^{org}$. The generated unlike-sign spectrum in step 4 is scaled by $2\sqrt{N11^{org}N22^{org}}/N12^{org}$ to force Eq. (4.17) before applying pair cuts. From here, the “Mixed BG12” represents the scaled spectrum.

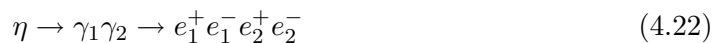
Assuming the effects of the pair cuts on the foreground and mixed-event background are the same, the normalization factor of the unlike-sign mixed background $nf12$ can be calculated from the normalization factors of the like-sign mixed background, $nf11$ and $nf22$ as:

$$nf12 = \sqrt{nf11 \cdot nf22} \quad (4.18)$$

The normalization of the like-sign mixed background is discussed in Section 4.12.5 together with the normalization of the other background sources.

4.12.2 Cross pairs

The cross pairs can be produced when a hadron decays with two e^+e^- pairs in the final state. The following hadron decays lead to cross pairs.



The “cross” combinations give rise to two unlike-sign pairs ($e_1^+e_2^-$ and $e_2^+e_1^-$) as well as two like-sign pairs ($e_1^+e_2^+$ and $e_1^-e_2^-$) that are not purely combinatorial, but correlated via the π^0 or η mass. Therefore, this contribution is not reproduced by the “event-mixing” technique.

To calculate the cross pairs, we use EXODUS to generate π^0 and η with the following input parameters:

- Flat vertex distribution with $|z| < 30$ cm
- Flat rapidity distribution with $|\eta| < 0.6$ and uniform in ϕ with $0 < \phi < 2\pi$.
- Momentum distribution following Hagedorn function:

$$E \frac{d^3N}{d^3p} = \frac{c}{(exp(-ap_T - bp_T^2) + p_T/p_0)^n} \quad (4.23)$$

where the parameters a , b , c , p_0 and n for each centrality bin are shown in Section 4.13.

The generated π^0 and η are passed through the detector simulation machinery described in the previous section. The decays of π^0 and η are handled in PISA, in which only the relevant decays (4.19) - (4.22) are activated. In addition, to enhance the production yield of cross pairs, the cross section of γ conversion is multiplied by 20. The enhanced cross section is compensated by applying a weighting factor to the electrons coming from γ conversion. By selecting reconstructed cross pairs, one can determine the shape of the cross pairs invariant mass spectrum. The obtained spectra are then absolutely normalized using the rapidity density dN^{π^0}/dy and dN^{η}/dy measured by PHENIX as a function of centrality. The measured dN/dy are summarized in Section 4.13.

4.12.3 Jet pairs

The jet pairs are reproduced with PYTHIA. The PYTHIA code is a widely used Monte Carlo simulation package of high-energy elementary particle collisions such as $p + p$. PYTHIA 6.319 with CTEQ5L parton distribution functions has been used. The following hard QCD processes are activated [35]:

- MSUB 11: $f_i f_j \rightarrow f_i f_j$
- MSUB 12: $f_i \bar{f}_i \rightarrow f_k \bar{f}_k$
- MSUB 13: $f_i \bar{f}_i \rightarrow gg$

- MSUB 28: $f_i g \rightarrow f_i g$
- MSUB 53: $g g \rightarrow f_k \bar{f}_k$
- MSUB 68: $g g \rightarrow g g$

where g denotes a gluon, $f_{i,j,k}$ is a fermion with flavor i, j, k and $\bar{f}_{i,j,k}$ is the corresponding antiparticle. A Gaussian width of 1.5 GeV for the primordial k_T distribution (MSTP(91)=1, PARP(91)=1.5) and 1.0 for the K-factor (MSTP(33)=1, PARP(31)=1.0) are used. The minimum parton p_T is set to 2 GeV/ c (CKIN(3)=2.0).

From the PYTHIA output, π^0 and η are extracted and passed through PISA. The z coordinate of the vertex position is uniformly distributed between ± 30 cm. In addition to changing the cross section of γ in the same way as for the cross pair simulation, the branching ratios of the π^0 and η decays are also modified to increase the sample of e^+e^- pairs. The branching ratios used in the simulation are summarized in Table 4.7. The effect of these modifications is corrected by applying weighting factors according to the source of electrons.

The foreground pairs from PYTHIA consist of jet pairs, “physical” pairs, cross pairs and combinatorial pairs. The “physical” pairs and cross pairs are excluded from the foreground pairs by requiring that electrons and positrons do not share the same particle in their history. The combinatorial background is statistically subtracted using the “event-mixing” technique. The mixed event like-sign pairs are normalized to the foreground like-sign pairs in the range $1.4 < \Delta\phi_0^{prim} < 1.7$, where $\Delta\phi_0^{prim}$ is the difference in the azimuthal angle of primary particles, π^0 or η . Figure 4.36 shows $\Delta\phi_0^{prim}$ distributions of the foreground pairs and the normalized mixed-event pairs. The excess yield around $\Delta\phi_0^{prim} \sim 0$ corresponds to “near-side” jet and $\Delta\phi_0^{prim} \sim \pi$ corresponds to “away-side” jet.

After subtracting the combinatorial background, the PYTHIA spectra are scaled to reproduce the jet contribution in $Au + Au$ collisions. First, the subtracted spectra are scaled to give the yield per $p + p$ minimum bias event. The scaling factor is determined such that the π^0 yield in the PYTHIA simulation matches the measured π^0 yield. The value is determined to be 1/3.9. Second, the spectra are scaled by the average number of binary collisions ($\langle N_{coll} \rangle$) for each centrality bin. In addition, the jets in heavy ion collisions are known to be suppressed. The suppression factor is estimated as the square of the single particle suppression factor (R_{AA}).

$$R_{AA}(p_T) = \frac{d^2N^{AA}/dp_T dy}{\langle N_{coll} \rangle d^2N^{pp}/dp_T dy} \quad (4.24)$$

where p_T is the transverse momentum, y is the rapidity. The values of R_{AA} are taken from the published charged and neutral pion measurements by PHENIX [92, 93]. The charged pion data are used for the low momentum region where neutral pion data are not available. Figures 4.37 and 4.38 show R_{AA} as a function of p_T . The R_{AA} of η is assumed to be same as that of pions. In summary, a jet pair originating from tracks with primary momenta $p_{T,1}$ and $p_{T,2}$ is scaled by $\langle N_{coll} \rangle \cdot R_{AA}(p_{T,1}) \cdot R_{AA}(p_{T,2})$.

TABLE 4.7: Branching ratio (BR) used in the jet simulation.

Initial state	π^0		η					
Final state	$\gamma\gamma$	$ee\gamma$	$\gamma\gamma$	$3\pi^0$	$\pi^+\pi^-\pi^0$	$\pi^+\pi^-\gamma$	$ee\gamma$	$\mu\mu\gamma$
Original BR	98.802	1.198	39.31	32.57	22.74	4.60	0.69	0.09
Modified BR	70.05	29.95	23.12	19.17	13.41	2.78	41.40	0.12

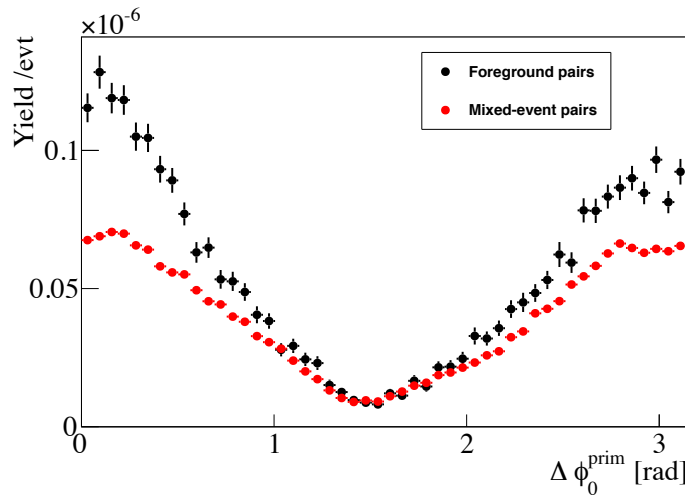


FIGURE 4.36: PYTHIA like-sign foreground spectrum scaled by $1/3.9 \cdot \langle N_{coll} \rangle \cdot R_{AA}(p_{T1}) \cdot R_{AA}(p_{T2})$ of 20-40% centrality bin. The normalized and scaled mixed background is also shown in the figure.

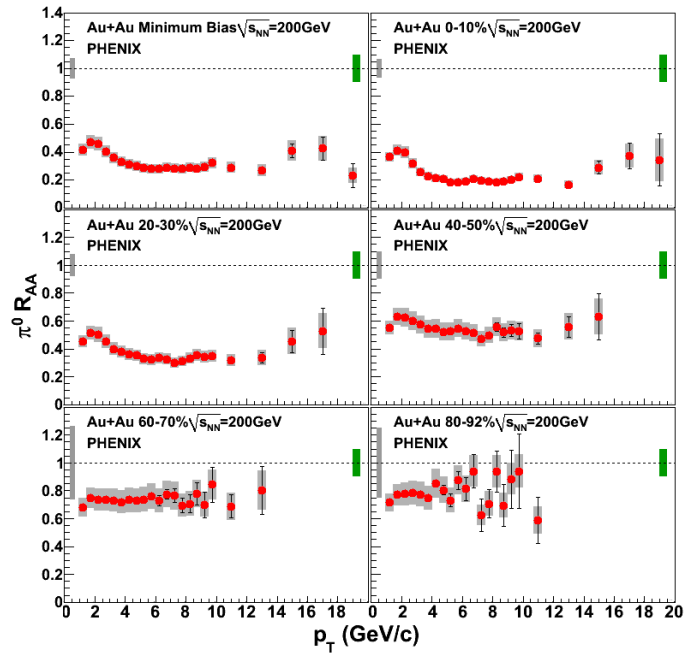


FIGURE 4.37: R_{AA} of neutral pion as a function of p_T from [92].

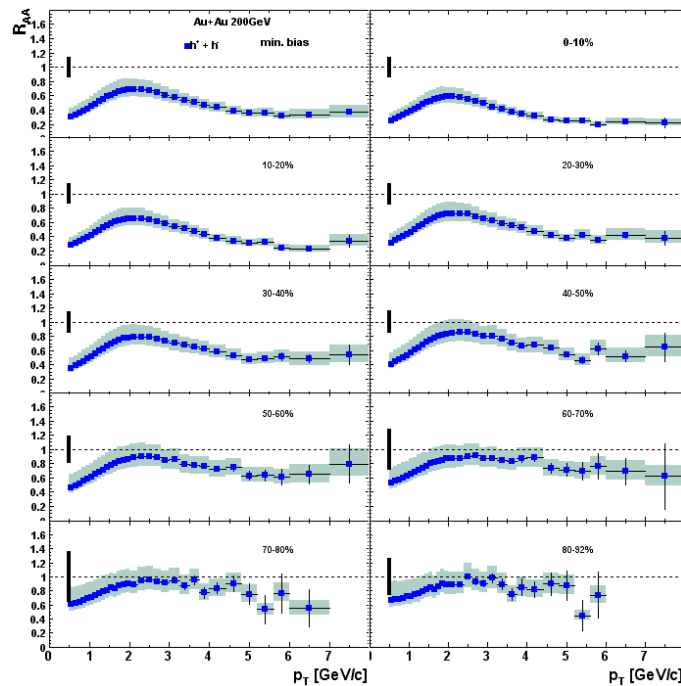


FIGURE 4.38: R_{AA} of charged pion as a function of p_T from [93].

4.12.4 Electron-hadron pairs

Even after applying pair cuts, electron hadron pairs correlated through detectors remain in the foreground pairs. Figure 4.39 illustrates an example of such an electron hadron pair. First, an electron-positron pair is generated by any source, e.g. a photon conversion. Then, the positron shares photomultipliers in the RICH detector with a parallel hadron track and the hadron is mis-identified as an electron. If both the positron and the mis-identified hadron are detected, the event is rejected as described before. However, if the positron is not detected due to detector efficiency or acceptance, the electron and the mis-identified hadrons are allowed to form a pair in the end. This pair is not a combinatorial pair but correlated through the positron. Although the mis-identification of hadrons via hit sharing occurs also in other detectors, the amount is small compared to that of RICH. Therefore, only RICH is considered as the source of such correlated pairs.

We simulate the electron hadron pair using electrons from π^0 and η simulation and hadrons from data. The π^0 and η simulations are the same ones used for cross pair simulation. The hadrons in data are all the tracks that fail the eID cuts.

The simulation is performed in the following way: First, an event is formed using “electrons” from one π^0 or η and “hadrons” from a real event. Then, their associated PMT information is merged and new rings are reconstructed. The original RICH eID variables, `n0`, `disp`, $\chi^2/\text{npe0}$ are overwritten with those from the new rings. Using the new RICH variables, the regular analysis procedure, eID cuts and pair cuts, is performed on the event. Finally, the combination of tracks from simulation and data are extracted. The spectra are absolutely normalized using the measured dN/dy shown in Section 4.13.

4.12.5 Normalization

Since the crosspairs, jet and electron-hadron pairs are absolutely normalized, the only free parameters are the normalization factors of the mixed background spectra, $nf11$, $nf22$ and $nf12$. Once the $nf11$ and $nf22$ are determined, $nf12$ can be determined by Eq 4.18. The like-sign spectra consist of only the background sources, and therefore, the $nf11$ and $nf22$ are calculated in a normalization window as follows:

$$nf11 = \frac{N_{\text{FG}11} - N_{\text{crosspair}11} - N_{\text{jet}11} - N_{\text{eh}11}}{N_{\text{mixedBG}11}} \quad (4.25)$$

$$nf22 = \frac{N_{\text{FG}22} - N_{\text{crosspair}22} - N_{\text{jet}22} - N_{\text{eh}22}}{N_{\text{mixedBG}22}} \quad (4.26)$$

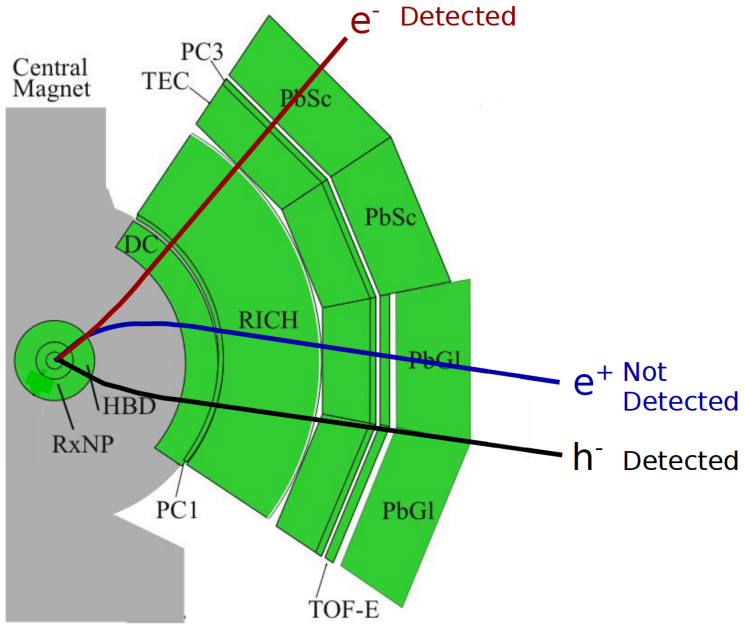


FIGURE 4.39: Illustration of the a possible electron hadron correlation.

where $N_{\text{FG}11(22)}$, $N_{\text{crosspair}11(22)}$, $N_{\text{jet}11(22)}$, $N_{\text{eh}11(22)}$ and $N_{\text{mixedBG}11(22)}$ are the number of pairs of each source in the normalization window.

The normalization window needs to satisfy two competing conditions. On the one hand, a small normalization window containing only combinatorial pairs is preferred to avoid being affected by other background sources. On the other hand, a wide normalization window is required to achieve good statistical accuracy. As a result, the normalization window is varied for each centrality bin. The chosen normalization windows are shown in Table 4.8 together with the number of like-sign pairs in the windows ($N_{\text{like-sign}}$).

Figure 4.40 shows the foreground pairs and the normalized background sources for each centrality bin. The unlike-sign spectra after all the background subtraction is shown in Fig. 4.41. The background subtraction procedure is verified using like-sign spectra. The like-sign residual yields after all the background subtraction divided by the mixed background yields are shown as a function of mass in Fig. 4.42. The grey shadowed bands represent the normalization error due to the limited statistics in the normalization window. Most of the points are inside the bands, showing that the background model reproduces the data. However, there are a few regions where the data points are systematically higher than the bands. The deviations in low mass region for all the centrality bins, $m_{ee} < 200 \text{ MeV}/c^2$, are attributed to the scale error of cross pairs. The points in this region are fitted to a flat line and the fit results are used as the systematic uncertainties in this mass region. In addition, data points are always higher than the bands above $1 \text{ GeV}/c^2$ in the 20-40% centrality bin. This might indicate the existence

of additional back-to-back correlation, and therefore, to be conservative, the data points are fitted to a flat line above $1 \text{ GeV}/c^2$. If the fit gives a value larger than the upper limit of shadowed bands, the fit result is used as systematic error in the region. The same procedure is performed for all the centralities and additional systematic errors are assigned for 10-20% and 20-40%. The resulting total systematic errors coming from background subtraction are shown by the solid black lines in Fig. 4.42.

TABLE 4.8: Normalization window for each centrality bin. The number of like-sign pairs in the window is also shown in the table.

Centrality	Normalization window	$N_{\text{like-sign}}$
0-10%	$0.7 < \Delta\phi_0 < 3.14$	1.9M
10-20%	$0.7 < \Delta\phi_0 < 2.3$	440K
20-40%	$0.9 < \Delta\phi_0 < 2.1$	160K
40-60%	$0.9 < \Delta\phi_0 < 2.1$	16K
60-92%	$0.9 < \Delta\phi_0 < 2.1$	1.1K

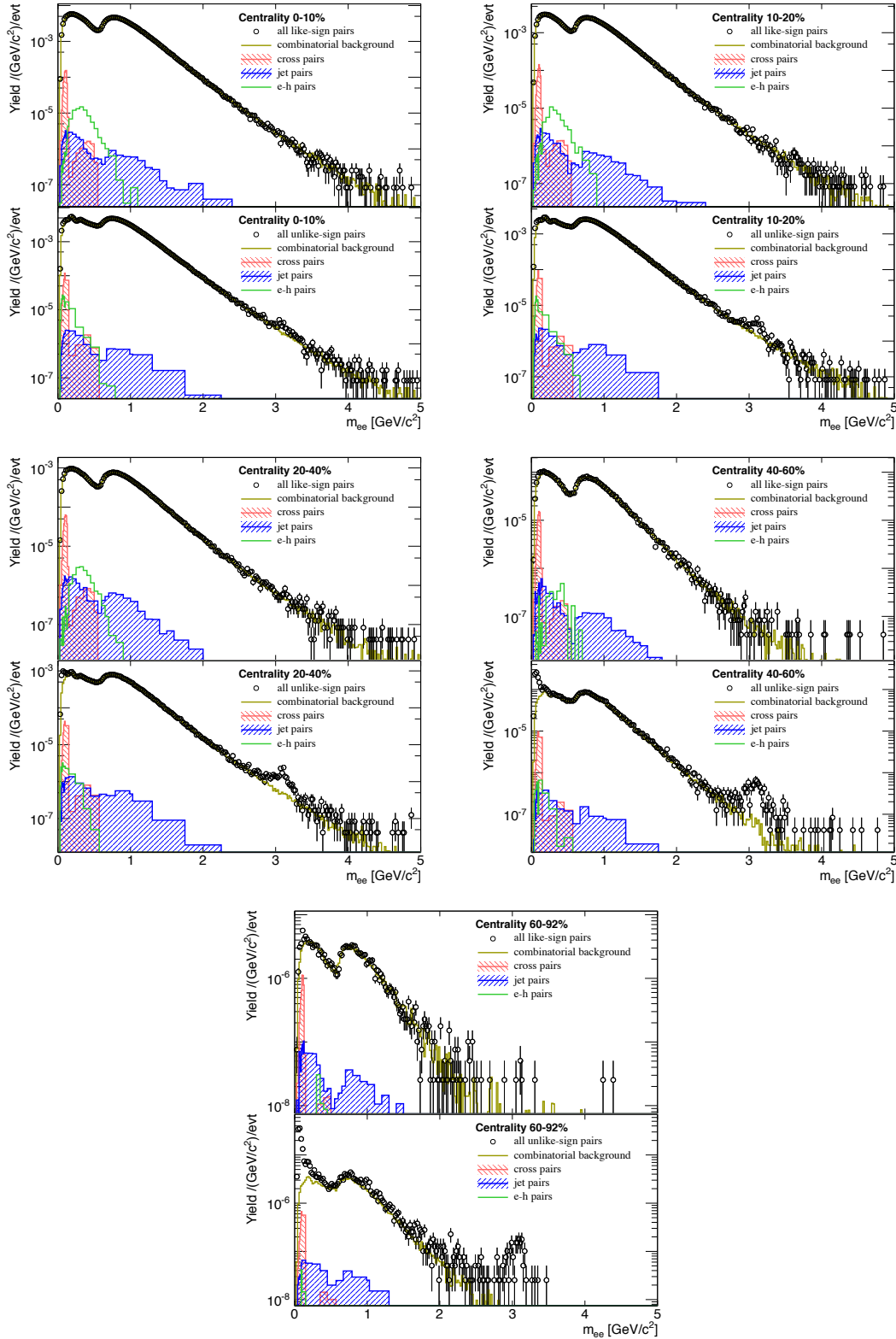


FIGURE 4.40: Foreground pairs and normalized background sources in each centrality bin.

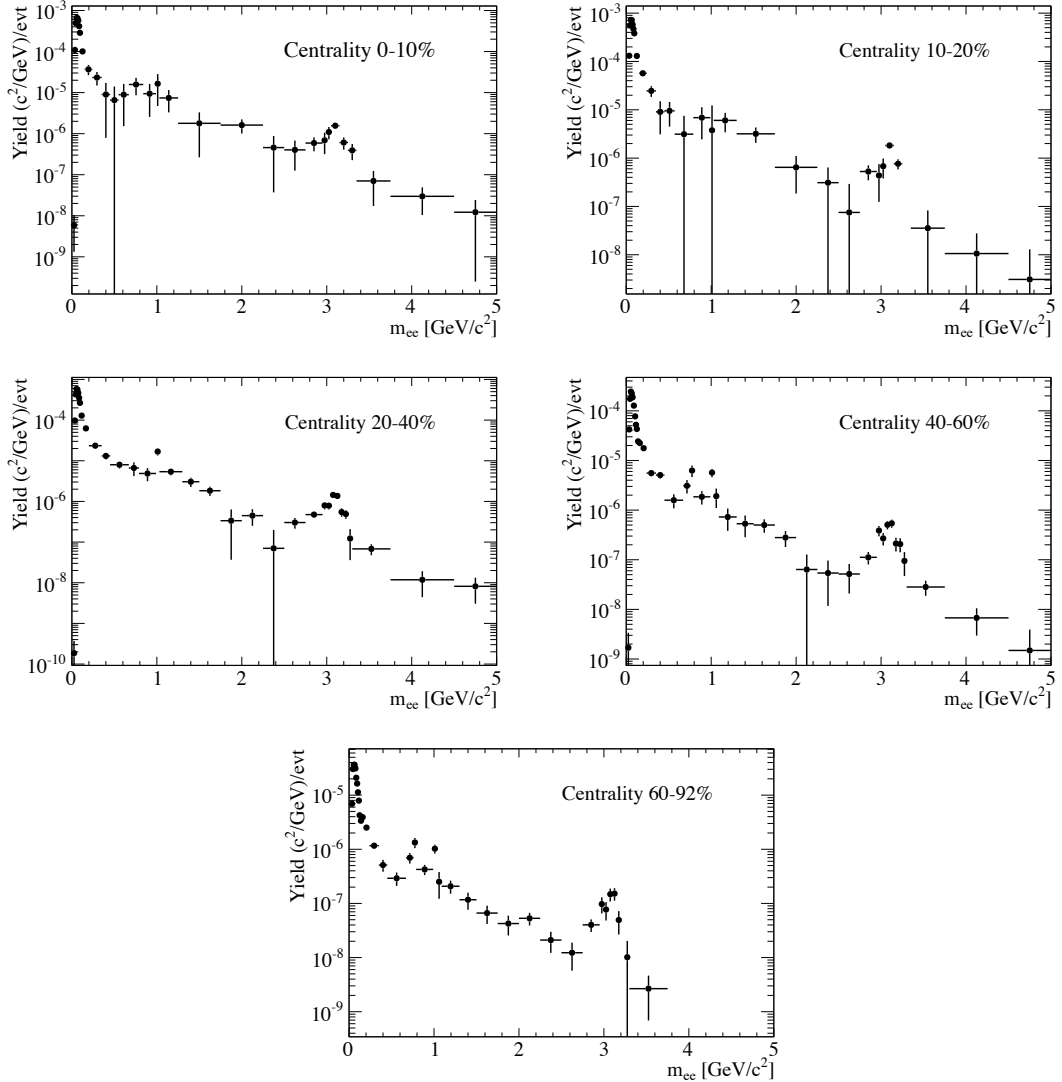


FIGURE 4.41: Unlike-sign pairs after background subtraction. Only statistical errors are shown in the figure.

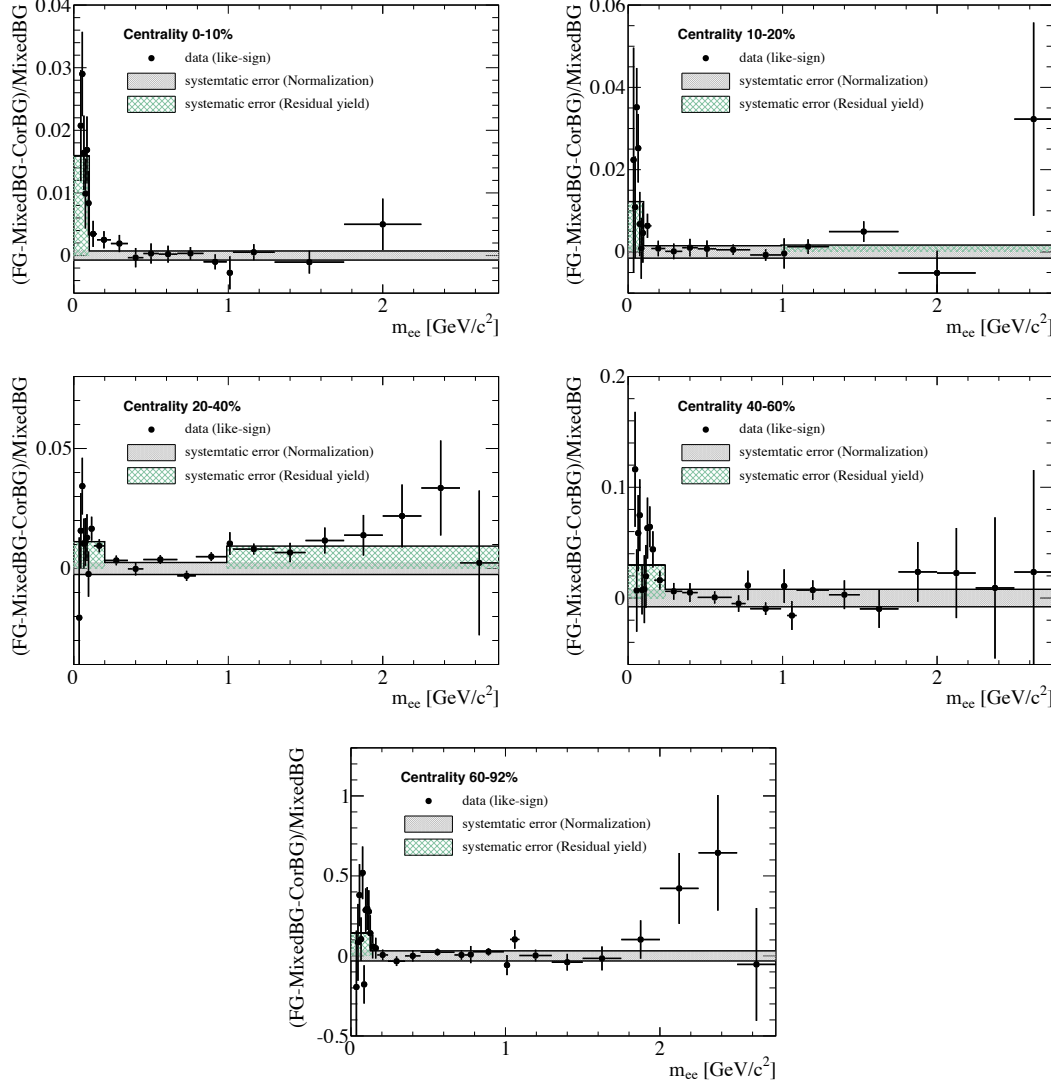


FIGURE 4.42: Like-sign residual yield divided by the mixed background yield as a function of mass for each centrality bin. The grey shadowed bands represent the normalization error of the mixed background. The green bands represent the systematic error due to the like-sign residual yields.

4.13 Hadronic cocktail

The extracted signal in the data analysis is dominated by the e^+e^- pairs from hadron decays, which we call ‘‘cocktail’’. The procedure to calculate the expected pair yield from those sources is described in Section 4.13.1 - 4.13.6. In addition, the reconstruction efficiency derived using the cocktail is also discussed in Section 4.13.7.

The cocktail consists of three ingredients:

- The photonic sources (Dalitz decays of light neutral mesons: $\pi^0, \eta, \eta' \rightarrow e^+e^-\gamma$ and $\omega \rightarrow e^+e^-\pi^0$) and the non photonic sources (di-electron decays of the light vector mesons: $\rho, \omega, \phi \rightarrow e^+e^-$) generated with the EXODUS package.
- The correlated pairs from semi-leptonic decays of heavy flavor (charm and bottom) mesons generated with the MC@NLO package or PYTHIA.
- The heavy meson J/ψ parameterized using 2009 pp data taken with the HBD and with the same magnetic field configuration as used in the 2010 run.

After generating the various sources with EXODUS, MC@NLO or PYTHIA, the cocktail is filtered through the ideal acceptance of the PHENIX detector and smeared with the detector resolution. This cocktail is then ready to be compared to the measured invariant mass spectrum.

4.13.1 Neutral pion

π^0 is the dominant electron source and also the fundamental input for EXODUS. The pion spectra are parametrized using the modified Hagedorn function:

$$E \frac{d^3N}{d^3p} = \frac{c}{(\exp(-ap_T - bp_T^2) + p_T/p_0)^n} \quad (4.27)$$

The parameters, a, b, c, p_0 and n , are obtained by a simultaneous fit of the PHENIX published results for π^0 [94, 95] and charged pions [96]. The resulting fit parameters are shown in Table 4.9. The dN_{π^0}/dy obtained by integrating the function over p_T is also shown in the right most column.

For 60-92%, our measured dN_{π^0}/dy turned out to be smaller than that of [94, 95, 96] by factor ~ 2 . Since the dN/dy measurements in peripheral events suffers from the large

systematic uncertainty in N_{part} and since the dN_{π^0}/dy measurements are consistent in other centrality bins (See Section 5.2), dN_{π^0}/dy derived in this analysis is used for the 60-92% centrality bin.

TABLE 4.9: Fit parameters derived from the π^0 and charged pion p_T distributions for different centralities using the modified Hagedorn function [94, 95, 96].

Centrality	c [(GeV/c) $^{-2}$]	a [(GeV/c) $^{-1}$]	b [(GeV/c) $^{-2}$]	p_0 [GeV/c]	n	dN_{π^0}/dy
0 - 10 %	1331	0.57	0.19	0.74	8.4	281
10 - 20 %	1001	0.53	0.16	0.75	8.3	201
20 - 40 %	634	0.43	0.11	0.79	8.5	117
40 - 60 %	313	0.36	0.13	0.76	8.4	48
60 - 92 %	81.9	0.33	0.088	0.74	8.4	11

4.13.2 Other mesons

The spectra of other mesons are based on the parametrization of the pion spectrum and assuming m_T scaling i.e. the modified Hagedorn parametrization is used with p_T replaced by $\sqrt{p_T^2 + m_{meson}^2 - m_{\pi^0}^2}$. The absolute normalization for each meson is provided by the ratio of the meson to π^0 invariant yields at high p_T . We use the values as given in ref [97] and we assume those values to be independent of centrality:

- $\eta/\pi^0 = 0.48$
- $\rho/\pi^0 = 1.00$
- $\omega/\pi^0 = 0.90$
- $\eta'/\pi^0 = 0.25$
- $\phi/\pi^0 = 0.40$

The resulting p_T integrated yields, dN/dy , for the various mesons and different centralities are listed in Table 4.10.

4.13.3 Open heavy flavor

The correlated e^+e^- yield from open heavy flavor decays is calculated using the MC@NLO package and the cross sections obtained from Run-8 $d + Au$ collisions [99, 100]. The MC@NLO package (vers. 4.03) [101, 102] is a next-to-leading order simulation to generate hard scattering events. These events are fed to Herwig (vers. 6.520) [103] for fragmentation in the vacuum.

TABLE 4.10: p_T integrated yield of π^0 s and the other light mesons in different centralities. For the 60-92% bin, the value from this analysis is used.

Centralities	$(dN/dy)_{\pi^0}$	$(dN/dy)_\eta$	$(dN/dy)_\rho$	$(dN/dy)_\omega$	$(dN/dy)_{\eta'}$	$(dN/dy)_\phi$
0 - 10 %	281	32	39	34	5.5	7.2
10 - 20 %	201	22	27	24	3.9	5.1
20 - 40 %	117	12	15	13	2.2	2.9
40 - 60 %	48	4.6	5.6	4.9	0.81	1.1
60 - 92 %	6.1	0.51	0.62	0.53	0.08	0.11

The $b\bar{b}$ and $c\bar{c}$ cross sections for $d + Au$ collisions are derived in [100] by fitting the MC@NLO spectra to the measured di-electron spectra. Then, the obtained cross sections are scaled by the average number of binary collisions (N_{coll}) to give the $p + p$ equivalent cross sections:

$$\sigma_{cc}^{pp} = 958 \pm 96(stat) \pm 335(syst) \mu\text{b} \quad (4.28)$$

$$\sigma_{bb}^{pp} = 3.4 \pm 0.8(stat) \pm 1.1(syst) \mu\text{b} \quad (4.29)$$

In this analysis, the MC@NLO spectra are first scaled to the cross section and then scaled by N_{coll} of the corresponding centrality bins.

The $c\bar{c}$ contribution is also calculated using PYTHIA version 6.421 with the following sets of parameters [100]:

- MSEL = 4
- MSTP(91) = 1
- PARP(91) = 1.5
- MSTP(33) = 1
- PARP(31) = 1.0
- MSTP(32) = 4
- PMAS(4) = 1.25

with $\sigma_{cc}^{pp} = 567 \mu\text{b}$ [104]. The cocktail with the open heavy flavor contribution using PYTHIA is used for the efficiency calculation described in Subsection 4.13.7.

All results shown on this thesis are with the heavy flavor contributions calculated with MC@NLO unless otherwise specified.

4.13.4 J/ψ

For the J/ψ decay into e^+e^- pairs, we use the line shape as measured in Run-9 $p + p$ collisions and scale the $p + p$ dN/dy yield with N_{coll} .

4.13.5 Systematic uncertainties on cocktail

The following systematic errors are assigned to each cocktail source:

- π^0 : 10% [35]
- η, ω, ϕ : 30% [35]
- ρ : 33% [35]
- η' : 100% [35]
- J/ψ : 25% [20, 21]

For the charm and bottom components, calculated with MC@NLO we use the values from ref. [100], namely $\pm 35\%$ for the charm and $\pm 33\%$ for the bottom contributions.

4.13.6 The Au+Au Run-10 cocktail

In order to compare it with data, the cocktail, calculated as described above, is filtered through the ideal acceptance of the PHENIX detector and smeared with the detector resolution. The acceptance in the $+-$ magnetic field configuration for a track with charge q , transverse momentum p_T and emission angle (ϕ_0, θ_0) can be described as:

$$\phi_{min} \leq \phi_0 - q \frac{k_{DC}}{p_T} \leq \phi_{max} \quad (4.30)$$

$$\phi_{min} \leq \phi_0 - q \frac{k_{RICH}}{p_T} \leq \phi_{max} \quad (4.31)$$

$$\theta_{min} \leq \theta_0 \leq \theta_{max} \quad (4.32)$$

The values of the parameters are summarized in Table 4.11. The ideal PHENIX acceptance is illustrated in Figure 4.43.

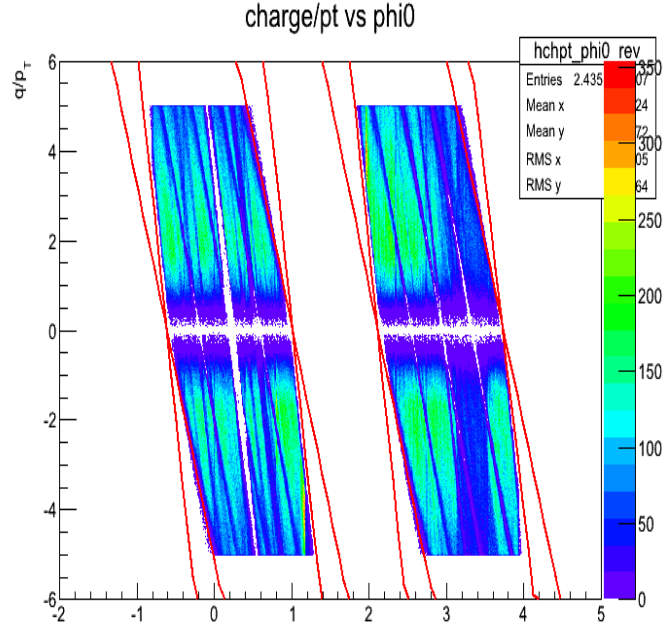


FIGURE 4.43: Ideal acceptance of the PHENIX detector in the $+-$ magnetic field configuration. The Y axis is charge/ p_T and the X axis is the DC ϕ_0 variable. The red lines are the parametrization used in EXODUS to define the ideal acceptance.

TABLE 4.11: Acceptance filter parameters in the $+-$ magnetic field configuration.

Parameter	Value
k_{DC}	0.060
k_{RICH}	0.118
θ_{min}	1.23
θ_{max}	1.92
$\phi_{min}(East)$	2.153
$\phi_{max}(East)$	3.718
$\phi_{min}(West)$	-0.570
$\phi_{max}(West)$	0.983

To determine the detector resolution, we use electrons generated by EXODUS from the decay of $\phi \rightarrow e^+e^-$ and pass them through PISA and the full reconstruction chain. The deviation of the reconstructed tracks from the generated tracks gives the information about the resolution. Fig. 4.44 shows the deviation in momentum (left panel), theta (middle panel) and phi (right panel) for one particular momentum bin. The momentum

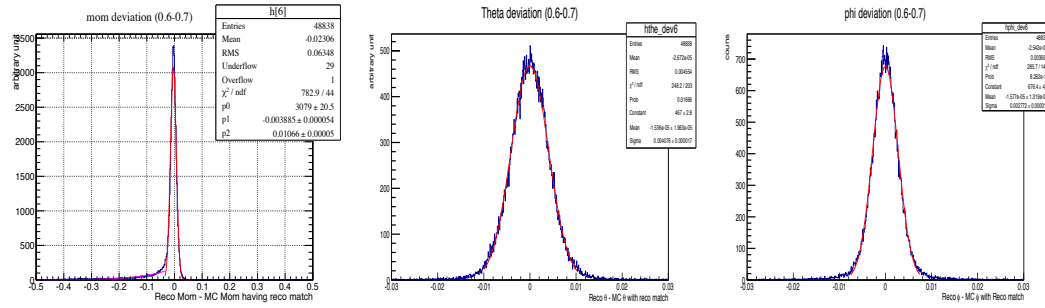


FIGURE 4.44: Deviation in reconstructed momentum (left), theta (middle) and phi (right) in the 600-700 MeV/c momentum bin. The momentum deviation is fitted with a Gaussian and an exponential function to account for the radiative tail. The θ and ϕ deviations are very well fitted by a Gaussian function only.

deviation is fitted with a Gaussian and an exponential function to account for the radiative tail. The θ_0 and ϕ_0 deviations are very well fitted by a Gaussian function only. The fit parameters are determined as function of momentum and used to smear the generated tracks.

The final cocktail for minimum bias collisions is shown in Figure 4.45.

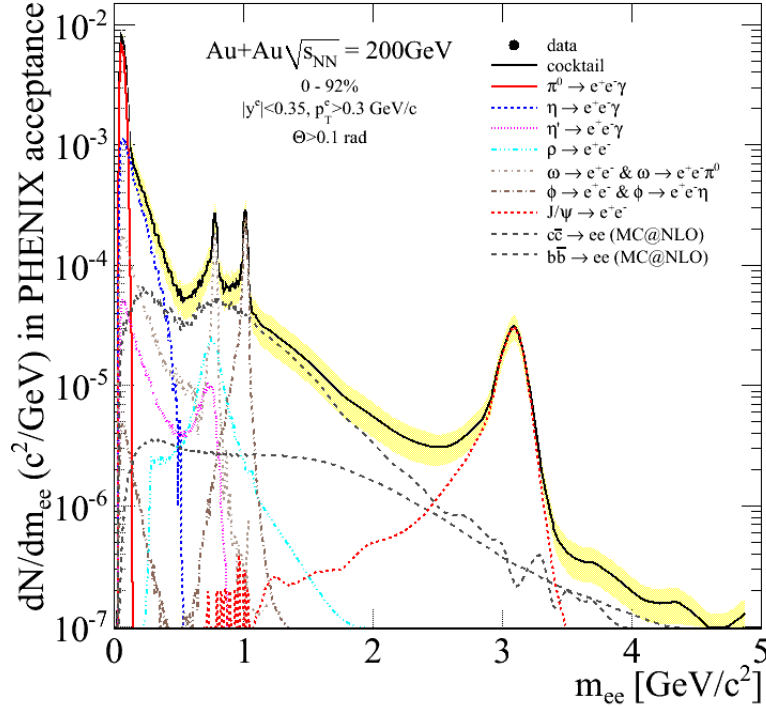


FIGURE 4.45: Run10 dielectron cocktail for minimum bias events. The mesonic contributions are obtained from EXODUS. The correlated $e^+ e^-$ pair yield form the semileptonic decays of heavy flavor mesons is from MC@NLO. The J/ψ decay into $e^+ e^-$ is taken from Run-9 $p + p$ collisions after scaling with N_{coll} . The systematic uncertainties in the cocktail are shown as the yellow band and discussed in Section 4.13.5.

4.13.7 Acceptance and efficiency correction

The e^+e^- mass spectra are corrected for the total pair reconstruction efficiency ϵ_{pair}^{total} to give the invariant e^+e^- pair yield inside the ideal PHENIX acceptance:

$$\frac{dN}{dm_{ee}} = \frac{1}{N_{evt}} \frac{N(m_{ee})}{\Delta m_{ee}} \frac{1}{\epsilon_{pair}^{total}} \quad (4.33)$$

where N_{evt} is the number of events, $N(m_{ee})$ is the number of e^+e^- pairs with its invariant mass m_{ee} and Δm_{ee} is the bin width. The p_T spectra are further corrected for the pair geometric acceptance (ϵ_{pair}^{geo}) to give the invariant pair p_T yield in full azimuth and in one unit of rapidity.

$$\frac{1}{2\pi p_T} \frac{d^2N}{dp_T dy} = \frac{1}{2\pi p_T} \frac{1}{N_{evt}} \frac{N(p_T)}{\Delta p_T \Delta y} \frac{1}{\epsilon_{pair}^{total}} \frac{1}{\epsilon_{pair}^{geo}} \quad (4.34)$$

where N_{evt} is the number of events, $N(p_T)$ is the number of e^+e^- pairs with the pair p_T , Δp_T is the bin width in p_T axis and Δy is the bin width in rapidity. The p_T spectra for minimum bias events are further corrected by the BBC efficiency 92% to give absolute yield.

The total pair reconstruction efficiency ϵ_{pair}^{tot} can be written as:

$$\epsilon_{pair}^{total} = \epsilon_{pair}^{eID} \cdot \epsilon_{pair}^{live} \cdot \epsilon_{pair}^{ghost} \cdot \epsilon_{pair}^{mult} \quad (4.35)$$

where ϵ_{pair}^{eID} is the e^+e^- pair reconstruction efficiency including the efficiency of all the electron identification cuts, ϵ_{pair}^{live} is the pair efficiency from the detector active area with respect to the ideal PHENIX detector acceptance, ϵ_{pair}^{ghost} is the ghost cut pair efficiency and ϵ_{pair}^{mult} is the multiplicity dependent efficiency loss described below in this subsection.

The product of $\epsilon_{pair}^{eID} \cdot \epsilon_{pair}^{live} \cdot \epsilon_{pair}^{ghost}$ is determined as follows. A cocktail is generated with the EXODUS event generator for the light mesons, and PYTHIA for the heavy flavor contributions (without smearing or filtering through the ideal PHENIX detector acceptance). The cocktail is passed through the detector simulation described in Section 4.5 and analyzed in the same way as data, including eID cuts, fiducial cuts and pair cuts. The resulting output is referred to as the PISA cocktail. The ratio of this PISA cocktail to the original cocktail gives $\epsilon_{pair}^{eID} \cdot \epsilon_{pair}^{live} \cdot \epsilon_{pair}^{ghost}$. This correction is derived in the two dimension mass - pair p_T space.

Similarly, by taking the ratio between the PISA cocktail and the cocktail generated in full azimuth and in one unit of rapidity gives the product $\epsilon_{pair}^{eID} \cdot \epsilon_{pair}^{live} \cdot \epsilon_{pair}^{ghost} \cdot \epsilon_{pair}^{geo}$.

In a high multiplicity environment, overlapping hits in each of the various detectors lead to a loss of efficiency. Such multiplicity dependent efficiency loss is estimated separately and is taken into account as an additional multiplicative factor to the efficiency correction derived using the PISA cocktail (See Eq. 4.35). The multiplicity dependent efficiency loss ϵ_{pair}^{mult} can have two reasons. The first reason is that the track reconstruction efficiency decreases with detector occupancy. This is clear by considering an event with infinite multiplicity. Since all the detector channels are fired, no track can be reconstructed. This loss is referred to as ϵ_{pair}^{embed} . The second reason is the eID step 1 discussed in Section 4.10.3. We erase the PMTs fired by background electron tracks. Therefore, if such an electron is close to a signal electron in the RICH, the associated PMTs of the signal electron are also erased. The probability for this to happen increases with multiplicity. This loss is referred to as ϵ_{pair}^{step1} . Using those efficiency losses, the ϵ_{pair}^{mult} is calculated as:

$$\epsilon_{pair}^{mult} = \epsilon_{pair}^{embed} \cdot \epsilon_{pair}^{step1} \quad (4.36)$$

The methods used to estimate the two factors are described below.

Efficiency loss due to detector occupancy ϵ_{pair}^{embed}

First, electrons and positrons from ϕ decays are passed through PISA. The simulated detector hits are added to a data file containing hits from a real Au+Au event. Then the new files containing the embedded e^\pm are run through the reconstruction software and analyzed in the same way as data including eID cuts, fiducial cuts and pair cuts. The embedding efficiency for single tracks $\epsilon_{single}^{embed}$ is calculated as

$$\epsilon_{single}^{embed} = \frac{\text{Number of reconstructed } e^\pm \text{ from embedded data}}{\text{Number of reconstructed } e^\pm \text{ from single track data}} \quad (4.37)$$

where the reconstructed particle from embedded data has most of its DC hits associated with hits from the simulated particle. The pair embedding efficiency is calculated as the square of the single track embedding efficiency, $\epsilon_{pair}^{embed} = (\epsilon_{single}^{embed})^2$. This is justified because the central arm is located after the magnetic field and tracks from a pair are well separated. Table 4.12 summarizes the ϵ_{pair}^{embed} and $\epsilon_{single}^{embed}$ with the eID cuts. The RICH step 1 is not applied to derive those numbers.

TABLE 4.12: Efficiency loss due to detector occupancy for the centrality bins used in the analysis.

	Centrality				
	0-10%	10-20%	20-40%	40-60%	60-92%
$\epsilon_{single}^{embed}$	0.72	0.81	0.87	0.93	0.97
ϵ_{pair}^{embed}	0.52	0.65	0.76	0.86	0.95

Efficiency loss due to eID step1 ϵ_{pair}^{step1}

The efficiency ϵ_{step1} is estimated using the yield of unlike-sign pairs below $20 \text{ MeV}/c^2$ in real data for each centrality bin. This mass region is dominated by Dalitz decays and γ conversions and provides a clean electron pair sample. The signal-to-background ratio is ~ 200 even for the most central events. The electrons from γ decays are not harmful for this study because the electrons are separated in the RICH. The ϵ_{pair}^{step1} is calculated as:

$$\epsilon_{pair}^{step1} = \frac{\text{Number of unlike-sign pairs below } 20\text{MeV}/c^2 \text{ with step1}}{\text{Number of unlike-sign pairs below } 20\text{MeV}/c^2 \text{ without step1}} \quad (4.38)$$

$\epsilon_{single}^{step1}$ is obtained by taking the square root of ϵ_{pair}^{step1} . Table 4.13 summarizes the $\epsilon_{single}^{step1}$ and ϵ_{pair}^{step1} values for each centrality bin.

TABLE 4.13: Efficiency loss due to the eID step 1 discussed in Section 4.10.3 for the centrality bins used in this analysis.

	Centrality				
	0-10%	10-20%	20-40%	40-60%	60-92%
$\epsilon_{single}^{step1}$	0.91	0.94	0.96	0.98	1.00
ϵ_{pair}^{step1}	0.85	0.88	0.93	0.97	1.00

The derived $\epsilon_{pair}^{eID} \cdot \epsilon_{pair}^{live} \cdot \epsilon_{pair}^{ghost} \cdot \epsilon_{pair}^{mult}$ is shown in Fig. 4.46 for all centrality bins.

The systematic uncertainty on the efficiency correction is estimated using the open Dalitz pair. (See Section 4.5 for the definition of the open Dalitz pair.) The open Dalitz pairs

are counted in data and in the PISA cocktail scaled by ($\epsilon_{pair}^{embed} \cdot \epsilon_{pair}^{step1}$) for two types of eID cuts. One is the analysis cuts used in the analysis and described in Section 4.10 and the other is the loose cuts applying only Step 0 and Step 1 without the HBD S/D cuts. The efficiencies of the analysis cuts relative to the loose cuts for data ($\varepsilon_{ana/loose}^{data}$) and MC ($\varepsilon_{ana/loose}^{MC}$) are defined as:

$$\varepsilon_{ana/loose}^{data} = \frac{N_{ana}^{data}}{N_{loose}^{data}} \quad (4.39)$$

$$\varepsilon_{ana/loose}^{MC} = \frac{N_{ana}^{MC}}{N_{loose}^{MC}} \quad (4.40)$$

where $N_{ana}^{data(MC)}$ and $N_{loose}^{data(MC)}$ are the number of open Dalitz pairs for the analysis cuts and loose cuts for data (PISA cocktail), respectively. These efficiencies vary between 0.2 and 0.5 from the most central to the most peripheral bin. The difference $|\varepsilon_{ana/loose}^{data} - \varepsilon_{ana/loose}^{MC}|$ is found to be less than 15% for all the centrality bins. This maximum value of 15% is assigned as systematic error of the efficiency correction independent of centrality.

The systematic uncertainty of the pair efficiency from the detector active area is estimated by counting the numbers of open Dalitz pairs in the east arm and the west arm and the ratio between them. The difference between data and PISA cocktail ratios is found to be 11% and this is assigned as the systematic error.

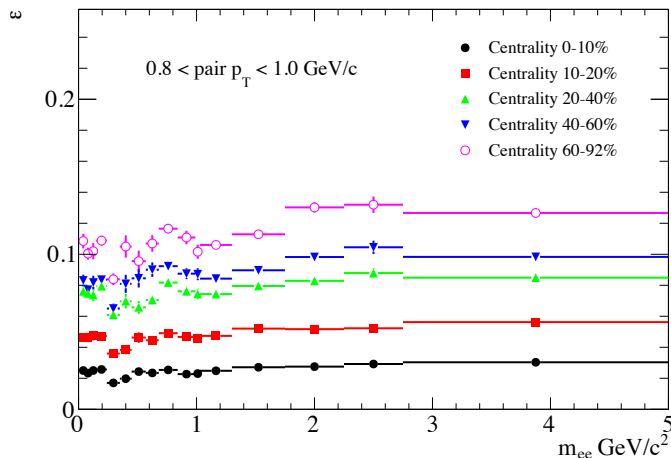


FIGURE 4.46: Acceptance and efficiency correction for the pair p_T range between 0.8 and 1.0 GeV/c for each centrality bin.

4.13.8 Bin shift correction

The data points of the p_T distributions of e^+e^- pairs are plotted at the center of the p_T bins. Therefore, a further correction has to be applied to take into account the difference

in the yield at the average p_T of the bin and its bin center. Given that the function $f(p_T)$ describes the spectrum, the corrected yield in a p_T bin [a, b] is calculated as follows:

$$\varepsilon_{bin} = \frac{\frac{1}{b-a} \int f(p_T) dp_T}{f(\frac{a+b}{2})} \quad (4.41)$$

$$\left. \frac{dN}{dp_T} \right|_{cor} = \frac{1}{\varepsilon_{bin}} \frac{dN}{dp_T} \quad (4.42)$$

The modified Hagedorn function is used as $f(p_T)$ in this analysis. An exponential function is also used and their difference is used as systematic error. The systematic error is estimated to be 5-10% depending on the bin width.

After applying the bin shift correction, dN/dp_T spectrum is converted to $(1/2\pi p_T) dN/dp_T$.

4.14 J/ψ yield

The data obtained in this analysis allow us to perform a study of the J/ψ yield and of the J/ψ nuclear modification factor. To extract the yield of J/ψ from the corrected spectra, the contributions from $c\bar{c}$ and $b\bar{b}$ need to be subtracted. These contributions are approximated with an exponential function and subtracted as follows:

1. Fit the corrected spectra to the sum of exponential and gaussian function. The mean of the gaussian function is fixed to be the PDG value of J/ψ mass.
2. Subtract the exponential function from the data points
3. Calculate the integral of the data points in the range 2.7-3.3 GeV/ c^2

The $c\bar{c}$ and $b\bar{b}$ contributions are also approximated by a first order polynomial function and subtracted. The difference in the results is taken as the systematic error of background subtraction instead of the one in Section 4.12.5. The value is estimated to be 10%.

4.15 Summary of systematic uncertainty

The following systematic errors are considered for the data:

- Background subtraction: The systematic errors are centrality and mass dependent as shown in Fig. 4.42. (See Section 4.12.5.)
- Efficiency correction (eID): 15% (See Section 4.13.7.)
- Efficiency correction (Active area): 11% (See Section 4.13.7.)
- J/ψ extraction: 10% (See Section 4.14.)
- Bin shift correction: 5-10% (See Section 4.13.8.)
- Minimum Bias Trigger efficiency: 3% (See Section 2.8.)

The quadratic sum of these components are assigned as the total systematic error.

The systematic error on the cocktail is described in Section 4.13.5.

Chapter 5

Results and discussion

This chapter presents and discusses the results of the analysis. The raw spectra shown in Section 4.12.5 is corrected for the reconstruction efficiency and acceptance as described in Section 4.13.7. The obtained invariant mass spectra and the acceptance corrected p_T spectra are presented in Section 5.1. Then, the obtained spectra are validated using the π^0 and J/ψ region as described in Section 5.2. The comparison of the acceptance corrected p_T spectra with the previous PHENIX measurement is shown in Section 5.3. After that, the spectra are compared to the hadronic cocktail in Section 5.4. For a quantitative comparison, we show the ratio data/cocktail vs centrality for the integrated yield in the low mass region and the intermediate mass region. In the end, the spectra are compared to several models of ρ meson shape modification, QGP radiation in Section 5.6.

5.1 Invariant mass spectra and acceptance corrected p_T spectra

Figure 5.1 shows the invariant mass spectra of e^+e^- pairs in the PHENIX acceptance for different centrality bins. The minimum bias spectrum obtained by combining the mass spectra of the five centrality bins is also shown in the figure.

Figures 5.2 and 5.3 show the transverse momentum spectra of dielectrons in different mass windows:

$$\frac{1}{2\pi p_T} \frac{dN}{dp_T dy} = \int_{m_1}^{m_2} \frac{1}{2\pi p_T} \frac{d^3 N}{dp_T dy dm_{ee}} dm_{ee} \quad (5.1)$$

where m_1 and m_2 are the lower and upper limits of the different mass slices. The spectra are truncated at low pair p_T due to the single track p_T cut of $0.3 \text{ GeV}/c^2$.

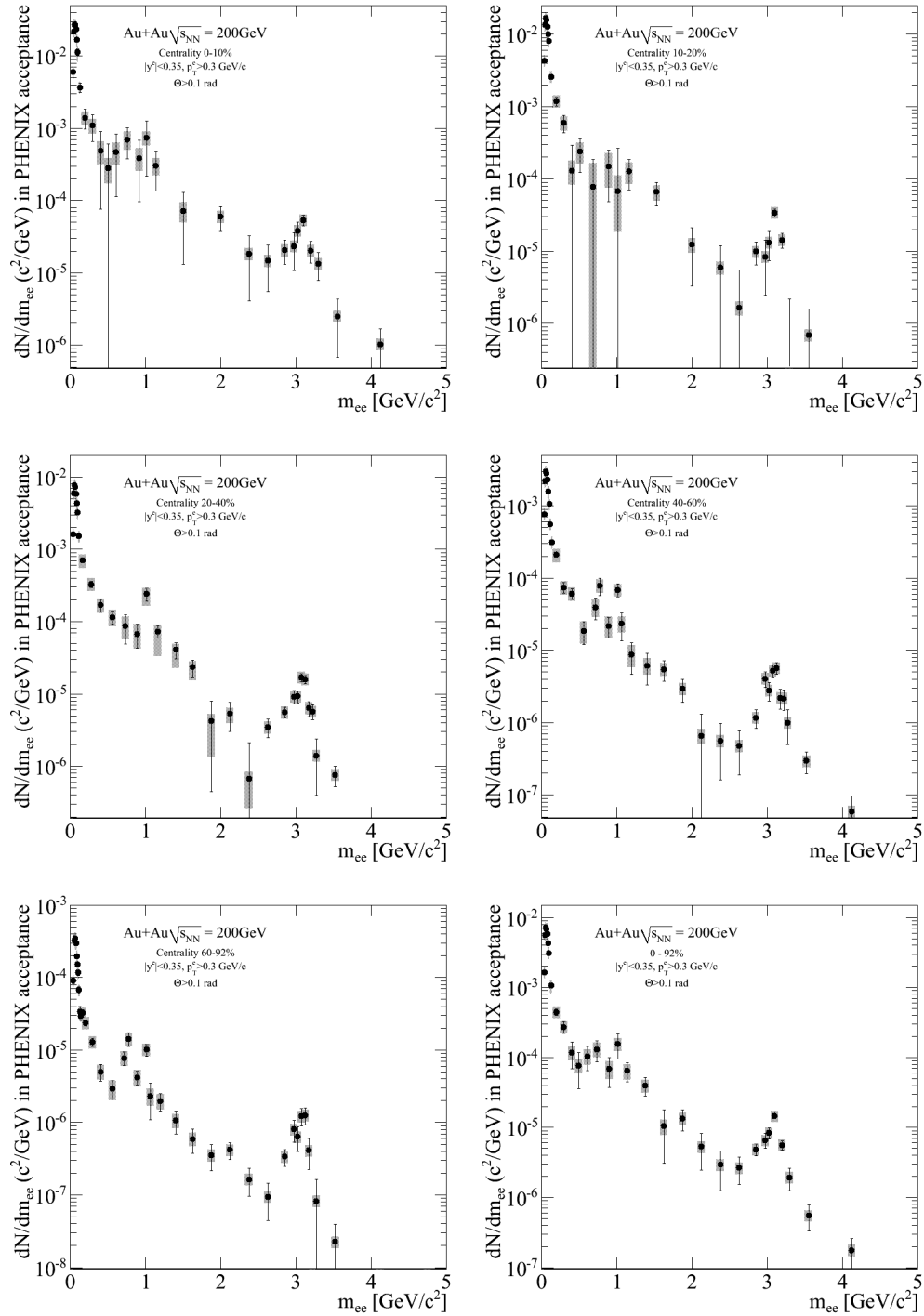


FIGURE 5.1: Invariant mass spectra of e^+e^- pairs in the PHENIX acceptance for different centrality bins. The invariant mass spectrum for the minimum bias events is also shown. Statistical and systematic errors are included.

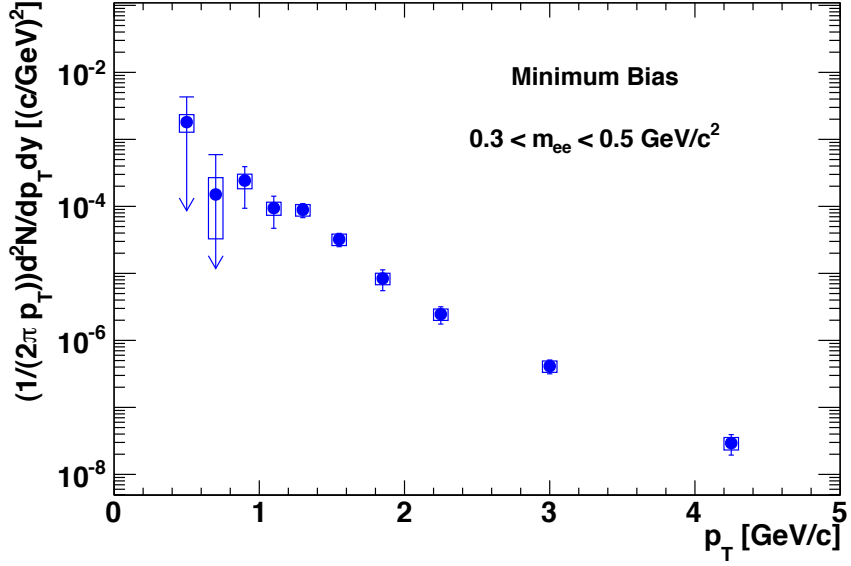


FIGURE 5.2: Acceptance corrected p_T spectra of e^+e^- pairs for $0.3 < m_{ee} < 0.5 \text{ GeV}/c^2$.

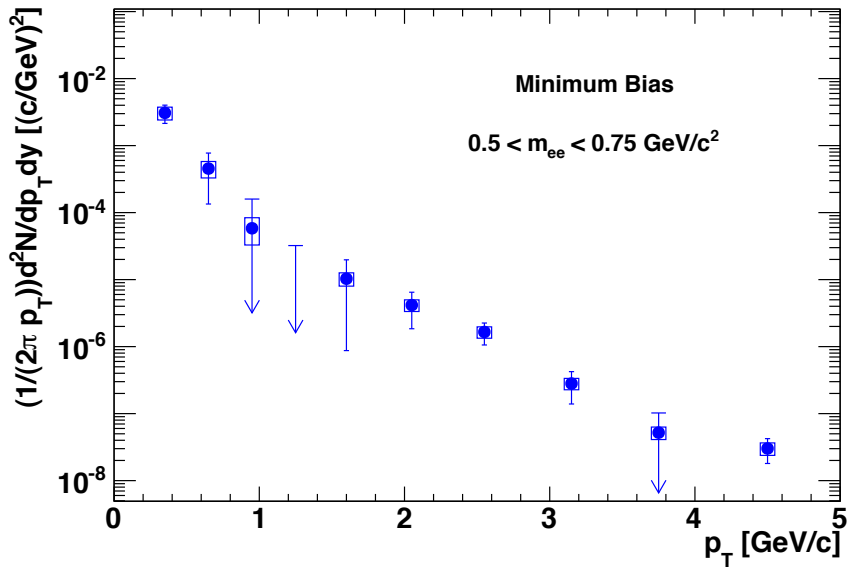


FIGURE 5.3: Acceptance corrected p_T spectra of e^+e^- pairs for $0.5 < m_{ee} < 0.75 \text{ GeV}/c^2$.

5.2 Control samples: π^0 and J/ψ region

Since the pion and J/ψ yield are well understood compared to the other sources, these mass regions provide control samples for the analysis procedure.

The ratio data/cocktail in the mass range $m_{ee} < 0.1 \text{ GeV}/c^2$ is shown as a function of N_{part} in Fig. 5.4. The ratio of the most peripheral bin is exactly at one because we are using this measurement for the normalization of the cocktail as described in Section 4.13. The ratios of the other centralities are consistent with one.

The nuclear modification factor R_{AA} of J/ψ is calculated using the extracted yield in Section 4.14. (See Eq 1.2 for the definition of R_{AA} .) The J/ψ yield in the mass window $m_{ee} = 2.7\text{-}3.3 \text{ GeV}/c^2$ in $p + p$ collisions is calculated using the J/ψ simulation used for the cocktail. Figure 5.5 shows the R_{AA} as a function of N_{part} in Run-10 and Run-4. The results are consistent with each other.

As a result, this analysis gives consistent results with the previous measurements in the two extreme mass windows. Therefore, the analysis procedure, mainly the reconstruction efficiency correction, is also validated in the mass window between the π^0 and J/ψ regions.

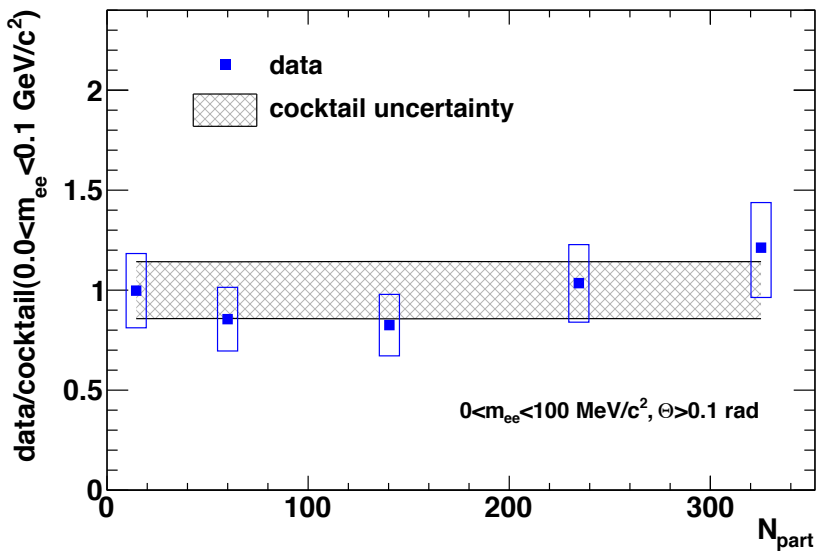


FIGURE 5.4: Data/cocktail ratio in the mass region $0.0\text{-}0.1 \text{ GeV}/c^2$. The shadowed band represents the systematic error on the cocktail.

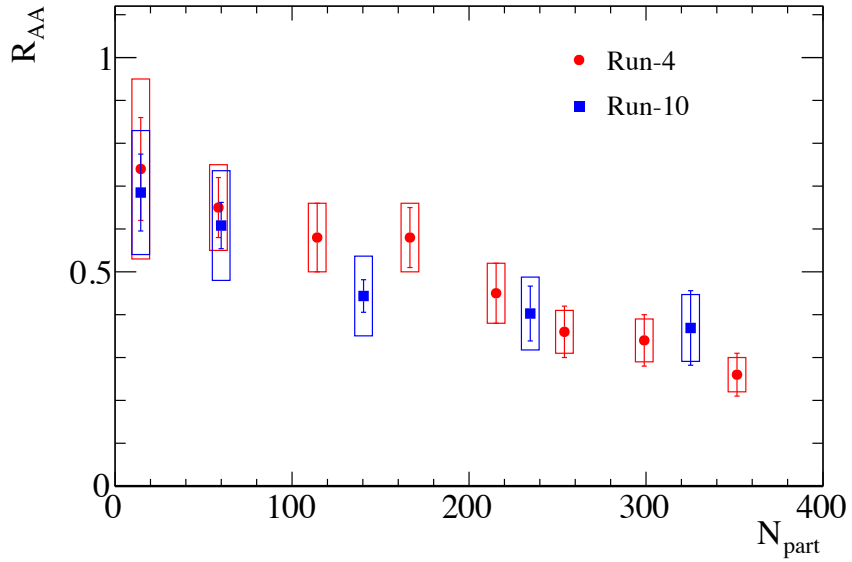


FIGURE 5.5: J/ψ R_{AA} as a function of N_{part} in Run-10 and Run-4 [52].

5.3 Comparison with PHENIX Run-4 data points

The invariant e^+e^- spectra obtained in this analysis and in Run-4 [35] are not directly comparable due to the different magnetic field and cut parameters. Therefore, those results are compared using the fully corrected pair p_T spectra in two mass windows: $0.3 < m_{ee} < 0.5$ and $0.5 < m_{ee} < 0.75$ GeV/c^2 . The comparisons are shown in Figs. 5.6 and 5.7. Some points around $p_T \sim 0$ are missing in Run-10 due to the stronger p_T^{single} cut used in this analysis: $p_T^{single} > 0.3$ GeV/c in this analysis and $p_T^{single} > 0.2$ GeV/c in Run-4 analysis. The stronger p_T^{single} cut in this analysis results in the smaller acceptance in small mass and pair p_T region. The Run-10 and Run-4 results are consistent with each other.

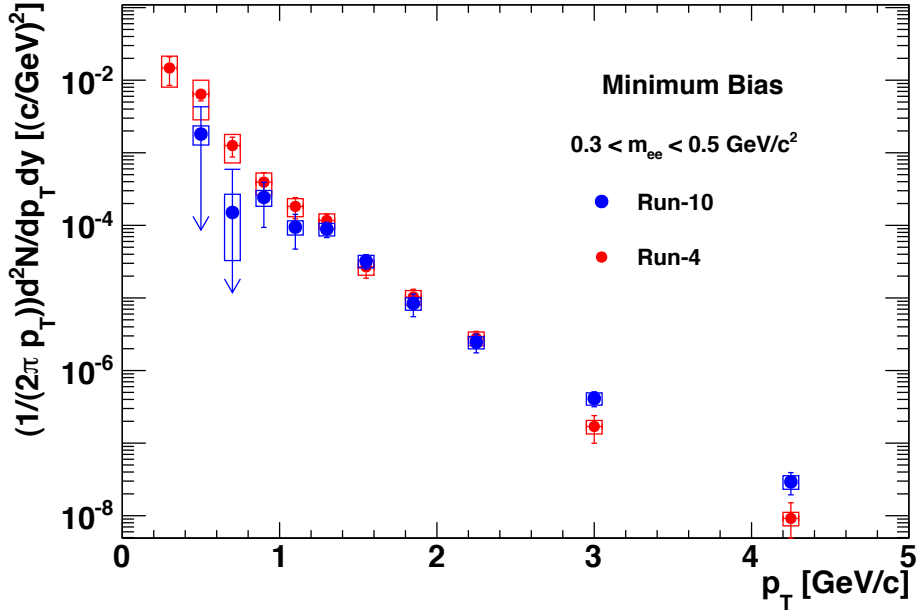


FIGURE 5.6: Acceptance corrected p_T spectra of e^+e^- pairs for $0.3 < m_{ee} < 0.5$ GeV/c^2 in Run-4 [35] and in the present analysis of Run-10.

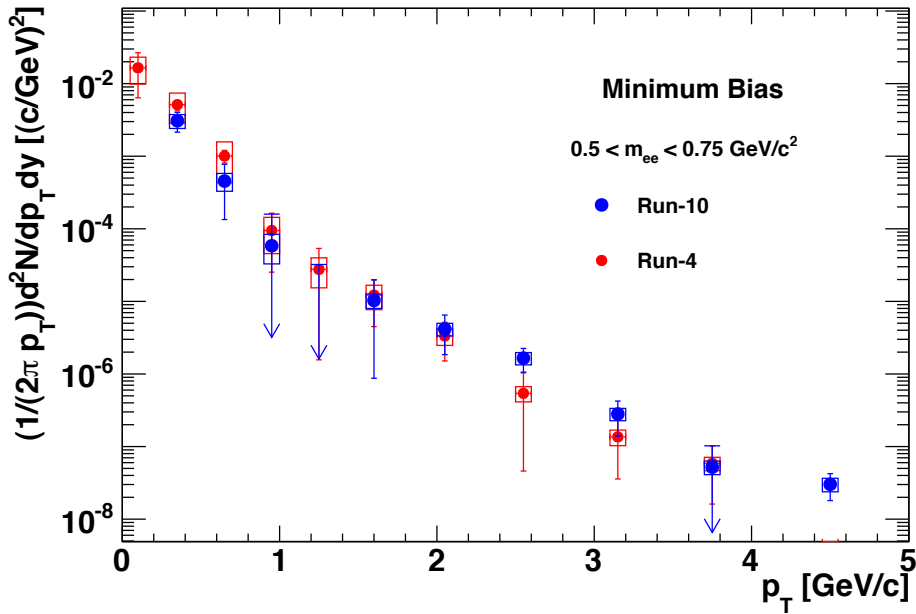


FIGURE 5.7: Acceptance corrected p_T spectra of e^+e^- pairs for $0.5 < m_{ee} < 0.75$ GeV/c^2 in Run-4 [35] and in the present analysis of Run-10.

5.4 Comparison with cocktail

5.4.1 Invariant mass spectra

Figure 5.8 shows the invariant mass spectra of e^+e^- pairs in the PHENIX acceptance for different centrality bins. The experimental results are compared to the expected yield from the cocktail of light hadron decays, correlated heavy flavor decays from MC@NLO and J/ψ decays as described in Section 4.13. Figure 5.9 shows the comparison for the minimum bias spectrum.

For a more quantitative comparison between data and the cocktail, we show in Figs. 5.11 and 5.12 the ratio data/cocktail vs N_{part} for the integrated yield in the low mass region ($0.15 < m_{ee} < 0.75 \text{ GeV}/c^2$) and in the intermediate mass region ($1.2 < m_{ee} < 2.8 \text{ GeV}/c^2$). In the low mass region, there is a hint of enhancement in the most central bin. Similarly, in the intermediate mass region, the ratios show a monotonic increase with centrality (about 60% from the most peripheral to the most central bin). However, in both mass regions, the error bars are too large for a definite statement and one can also argue that the ratios are consistent with one for all the centrality bins. To summarize, the medium modifications in the inclusive invariant mass spectrum are small compared to the contributions from hadronic decays.

In the previous section, we saw that the Run-10 measurement is consistent with the Run-4 measurement. This fact seems to be contradicting with their mass spectra, Fig. 5.9 for Run-10 and Fig. 5.10 for Run-4. In Fig. 5.10, a large enhancement is visible below ρ mass, whereas in Fig. 5.9, only a small enhancement is visible. The difference is due to their different acceptances, mostly due to the different single p_T cuts.

To understand the difference in their acceptances to the enhancement component, a Toy Monte Carlo simulation is performed as follows:

1. Determine the mass of a parent particle: m_0 . Its mass is uniformly distributed in each bin of 0.3-0.45, 0.45-0.55, 0.55-0.60, 0.60-0.65, 0.65-0.70 and 0.70-0.76 GeV/c^2 . The binning is chosen to be same as Fig 5.10.
2. Determine the p_T of a parent particle following the m_T distribution:

$$\frac{d^2N}{dm_T dy} \propto m_T \times e^{-\frac{m_T}{T_{eff}}} \quad (5.2)$$

where $m_T = \sqrt{m_0^2 + p_T^2}$ and $T_{eff} = 92 \text{ MeV}$ [35].

3. Decay the parent particle into e^+e^- pairs and pass the Run-10 and Run-4 acceptance filters.

4. Count the number of fully reconstructed parent particles in Run-10(N_{Run10}) and Run-4(N_{Run4}).

Figure 5.13 shows the N_{Run10}/N_{Run4} as a function of mass. Using the ratios, the enhanced yields, data-cocktail, in Fig. 5.10 are corrected to those of Run-10 acceptance. The corrected enhanced yields in two mass windows, $0.3\text{-}0.55 \text{ GeV}/c^2$ and $0.55\text{-}0.76 \text{ GeV}/c^2$, are shown in Table 5.1. The enhanced yields in Run-10 in those mass windows are also shown in the table. For this study, PYTHIA is used for $c\bar{c}$ contribution as was done in Run-4. The enhancement in Run-10 and Run-4 are consistent with each other.

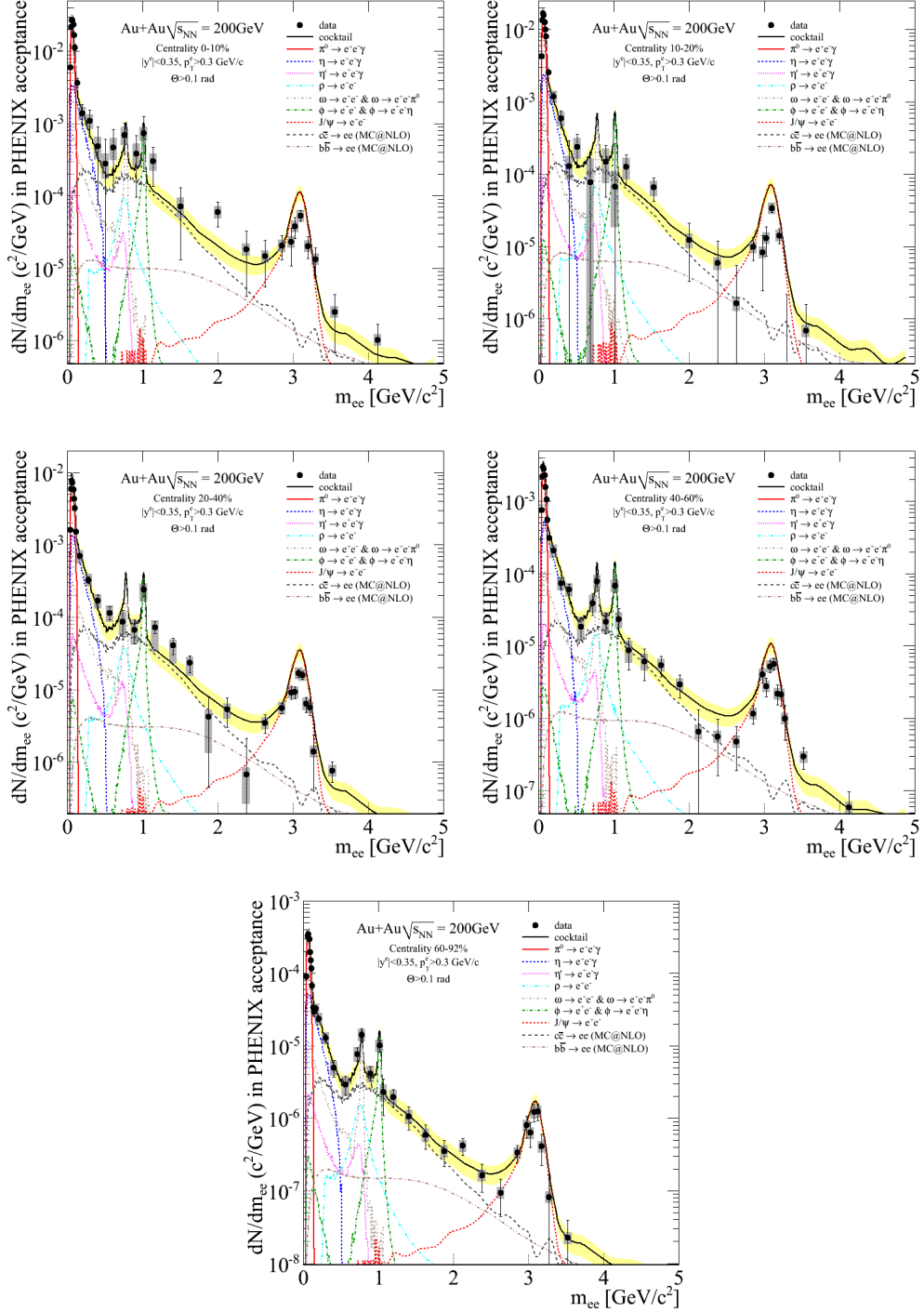


FIGURE 5.8: Invariant mass spectra of e^+e^- pairs in the PHENIX acceptance for different centrality bins. The experimental results are compared to the expected yield from the cocktail of light hadron decays, correlated heavy flavor decays and J/ψ decays.

Statistical and systematic errors both on data and the cocktail are included.

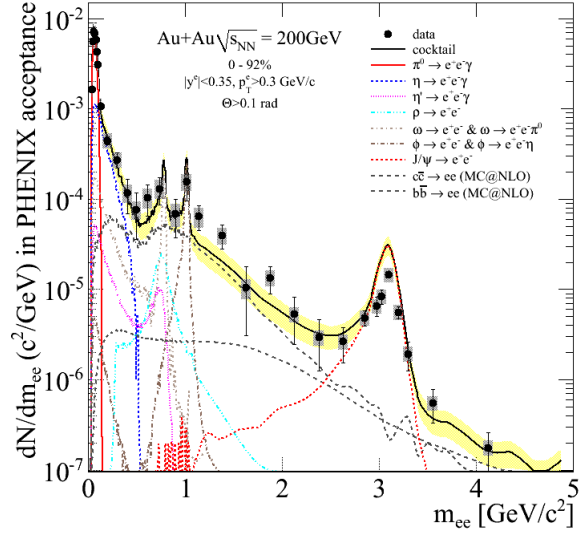


FIGURE 5.9: Invariant mass spectra of e^+e^- pairs in the PHENIX acceptance for minimum bias events. The experimental results are compared to the expected yield from the cocktail of light hadron decays, correlated heavy flavor decays and J/ψ decays.

Statistical and systematic errors both on data and the cocktail are included.

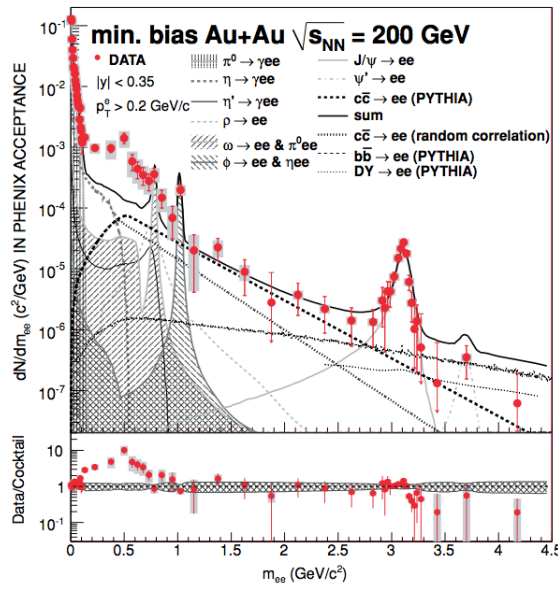


FIGURE 5.10: Invariant mass spectrum of e^+e^- pairs in the PHENIX acceptance in minimum-bias $Au + Au$ collisions compared to the Run-4 cocktail [35].

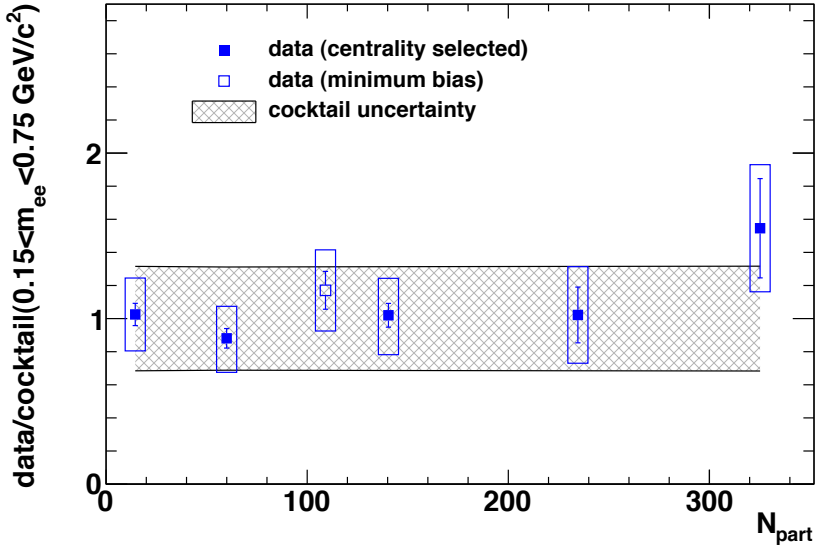


FIGURE 5.11: Data/cocktail ratio in the mass region $0.15 < m_{\text{ee}} < 0.75 \text{ GeV}/c^2$. The shadowed band represents the systematic error on cocktail.

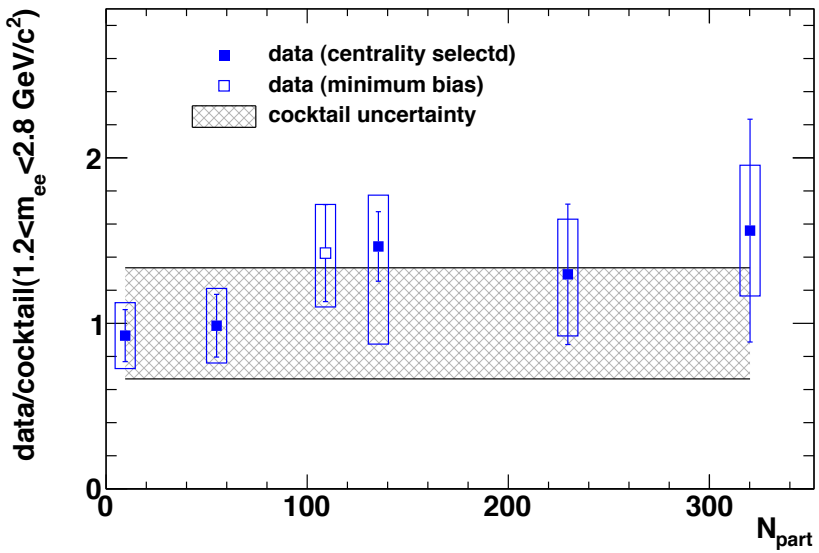


FIGURE 5.12: Data/cocktail ratio in the mass region $1.2 < m_{\text{ee}} < 2.8 \text{ GeV}/c^2$. The shadowed band represents the systematic error on the cocktail.

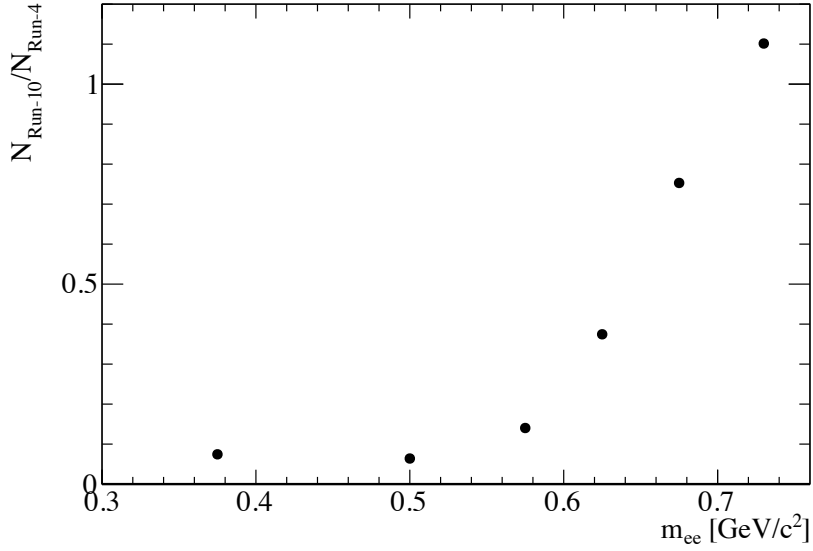


FIGURE 5.13: The ratio of the acceptances in Run-10 and Run-4 to the enhancement component observed in Run-4.

TABLE 5.1: The enhanced yields in Run-10 and Run-4 for the minimum bias events. The Run-4 yields are corrected to the yields in the Run-10 acceptance.

Mass [GeV/ c^2]	Corrected Run-4 [$\times 10^{-5}/\text{evt}$]	Run-10 [$\times 10^{-5}/\text{evt}$]
0.3-0.55	$1.7 \pm 0.2^{stat} \pm 0.6^{syst}$	$1.6 \pm 0.7^{stat} \pm 0.8^{syst}$
0.55-0.76	$2.8 \pm 0.6^{stat} \pm 1.8^{syst}$	$1.7 \pm 0.7^{stat} \pm 0.7^{syst}$

5.4.2 Acceptance corrected p_T spectra

In Figs. 5.14 and 5.15, the transverse momentum spectra of dielectrons in different mass regions are compared to the cocktail. In the both mass regions, the data points are higher than the cocktail at high p_T . This excess can be interpreted as the contributions from direct virtual photon as discussed in the next section. The first point in the Fig. 5.15 shows an excess from the cocktail($\sim 2 \sigma$), which is a possible signal of in-medium modifications of the low mass vector mesons or an anomalous enhancement observed in the previous PHENIX measurement.

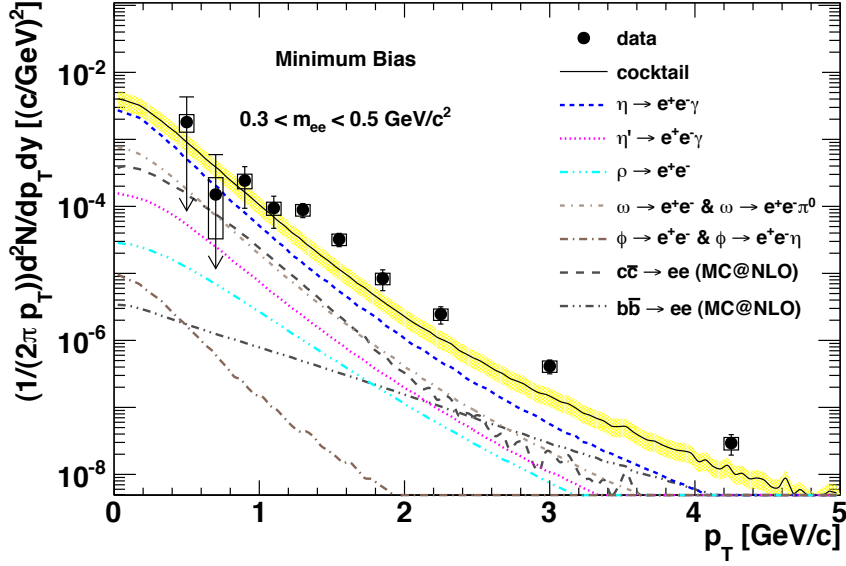


FIGURE 5.14: Acceptance corrected p_T spectra of e^+e^- pairs for $0.3 < m_{ee} < 0.5$ GeV/c^2 .

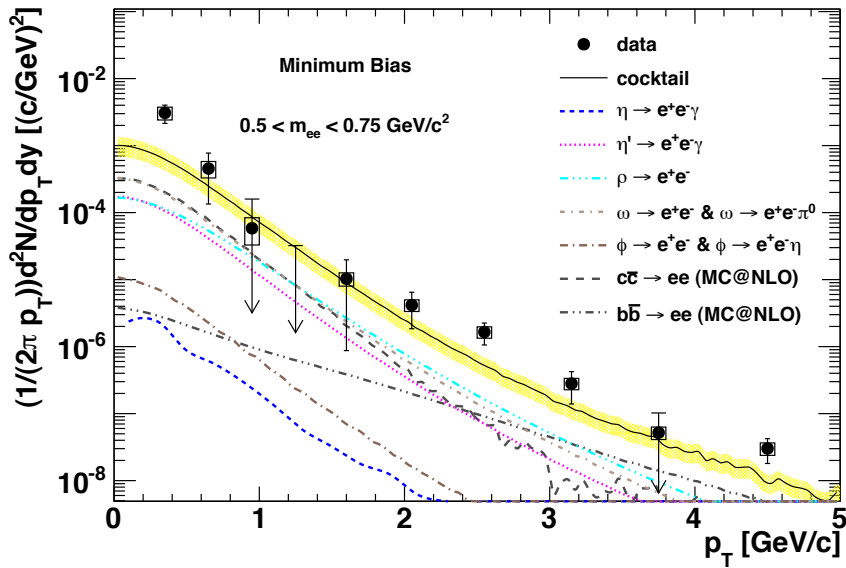


FIGURE 5.15: Acceptance corrected p_T spectra of e^+e^- pairs for $0.5 < m_{ee} < 0.75$ GeV/c^2 .

In Fig. 5.15, the enhancement from the cocktail grows rapidly at low p_T . To study the shape of this low p_T enhancement, Figure 5.16 shows the m_T distribution of the excess from the cocktail (ρ is excluded from the subtracted cocktail). Here, m_T is defined as $\sqrt{p_T^2 + m_0^2}$, where m_0 is the mean value of m_{ee} in the range $0.5 < m_{ee} < 0.75 \text{ GeV}/c^2$. The m_T distribution is fitted to the sum of two exponentials:

$$\frac{1}{2\pi m_T} \frac{dN}{dm_T dy} = N_1 e^{-\frac{m_T}{T_{low}}} + N_2 e^{-\frac{m_T}{T_{high}}} \quad (5.3)$$

where N_1 and N_2 are the normalization parameters and T_{low} and T_{high} are the effective temperatures of the low p_T and high p_T component. The derived effective temperature T_{low} is $70 \pm 40^{stat} \pm 20^{syst} \text{ MeV}$, which is consistent with $92.0 \pm 11.4^{stat} \pm 8.4^{syst} \text{ MeV}$ measured in the Run-4 measurement. These measured temperatures are very low compared to the effective temperatures of hadrons with similar masses. For example, kaon's effective temperature is larger than 200 MeV [105]. This low effective temperature is an outstanding feature of the low mass, low p_T enhancement.

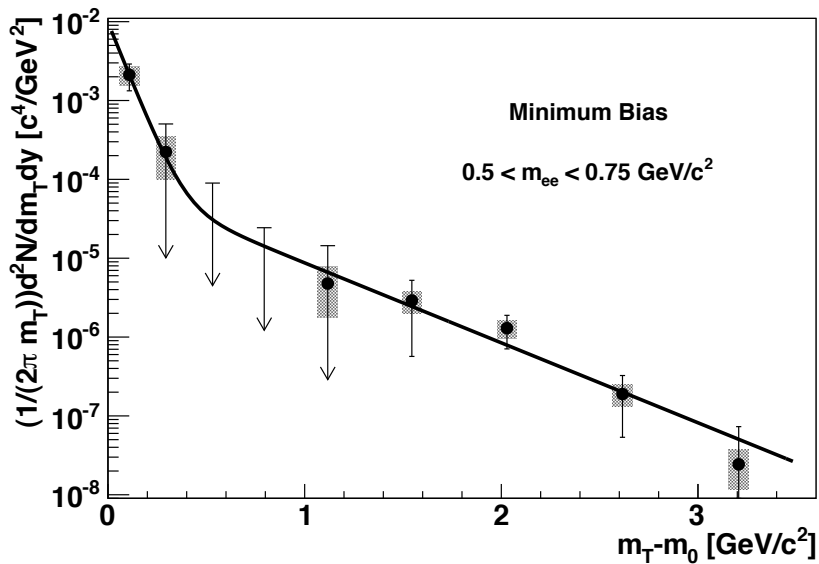


FIGURE 5.16: The m_T spectrum for the mass range $0.5 < m_{ee} < 0.75 \text{ GeV}/c^2$ after subtracting the hadronic cocktail without the ρ meson contribution. The fit to the sum of two exponentials is also shown.

5.5 Comparison with direct photon measurements

As shown in the previous section, data points are higher than the cocktail at high p_T in the low mass regions. This excess can be interpreted as the contribution from virtual photons ($\gamma^* \rightarrow e^+e^-$) associated with direct photon production.

Direct photons are the photons not originating from hadron decays. They can be classified into three categories:

1. Hard photons from initial hard scatterings
2. Thermal photons from QGP
3. Thermal photons from hadron gas

At high p_T , the photons from partonic origins, 1. and 2. in the classification above, are the dominant sources [106]. The leading-order Feynman diagrams of direct photon production from inelastic scattering of partons are $q\bar{q}$ annihilation and quark gluon Compton scattering.

The PHENIX measured the direct photon yield using e^+e^- pairs in the range $0.1 < m_{ee} < 0.3$ GeV/ c^2 and $p_T > 1.0$ GeV/ c [35]. In the limit of high p_T and low mass ($p_T \gg m_{ee}$), virtual photons are almost equivalent to real photons. The relation between real photon production and the associated e^+e^- production can be written as:

$$\frac{d^2N_{ee}}{dm_{ee}dp_T} \approx \frac{2\alpha}{3\pi} \frac{1}{m_{ee}} \frac{dN_\gamma}{dp_T} \quad (5.4)$$

where α is the fine structure constant, N_{ee} is the number of e^+e^- pairs and N_γ is the number of γ . The direct photon contribution estimated in the range $0.1 < m_{ee} < 0.3$ GeV/ c^2 is extrapolated to higher mass region using Eq. 5.4 and added to the cocktail as shown in Fig. 5.17 and 5.18. The sum of cocktail and direct photon yield describes the data at high p_T and the direct photon results of [35] is confirmed in this analysis. The data points start to deviate from the sum below ~ 1.5 GeV/ c^2 , probably because the assumption $p_T \gg m_{ee}$ does not hold true anymore in the region.

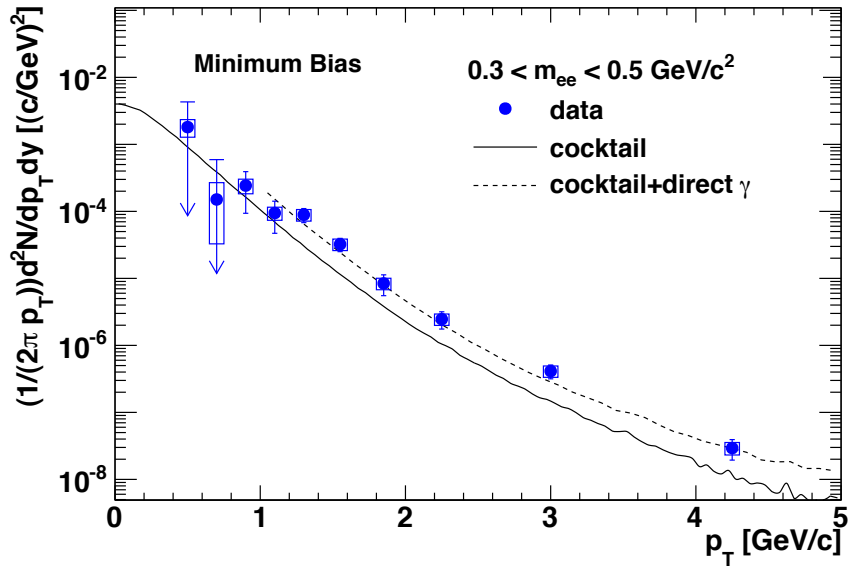


FIGURE 5.17: Acceptance corrected p_T spectra of e^+e^- pairs for $0.3 < m_{ee} < 0.5 \text{ GeV}/c^2$. The cocktail with the direct photon yield estimated in [35] is also shown in the figure.

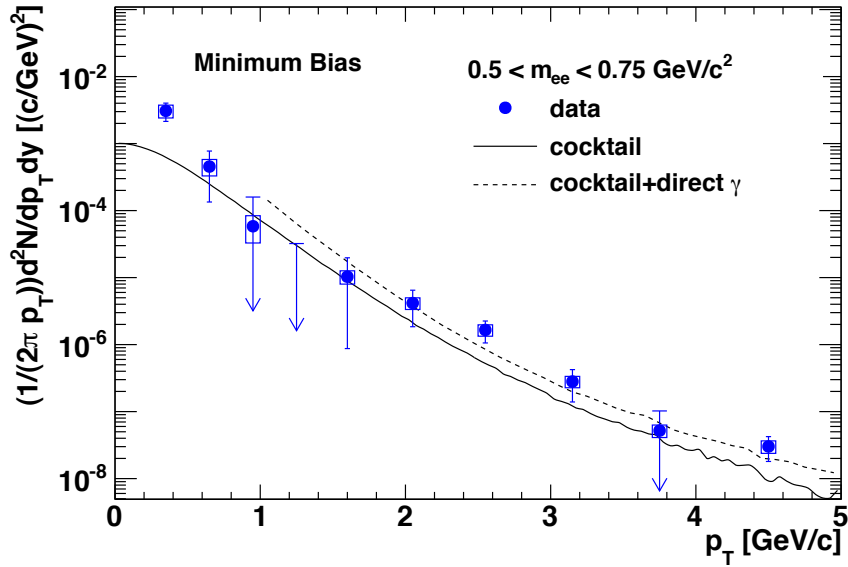


FIGURE 5.18: Acceptance corrected p_T spectra of e^+e^- pairs for $0.5 < m_{ee} < 0.75 \text{ GeV}/c^2$. The cocktail with the direct photon yield estimated in [35] is also shown in the figure.

5.6 Comparison with models

5.6.1 ρ modification

As shown in Fig. 5.15, there is an excess from the cocktail at low p_T . Therefore, the invariant mass spectrum in the p_T range 0-0.5 GeV/ c is compared to the models with in-medium modifications of the ρ meson.

There are several model calculations incorporating the dropping mass scenario and the broadening scenario of the ρ meson. Some of them are compared to the data:

1. Rapp and van Hees with broadening mass scenario or dropping mass scenario [35, 107, 108].
2. Dusling and Zahed with broadening mass scenario [35, 109].
3. Cassing and Bratkovskaya with broadening mass scenario and both broadening and dropping mass scenario [35, 110, 111].

The differences in e^+e^- yields in the various models are attributed to the differences in the in-medium spectral modifications, different durations of the fireball in the hadronic phase and different evolutions of the temperature as a function of time.

The contributions from those model calculations in the Run-4 acceptance is given in the ref [35]. They are corrected to the contributions in the Run-10 acceptance by taking the similar procedure as in Section 5.4. The m_T spectra given in the same reference for the mass range 0.3-0.75 GeV/ c^2 are assumed to be independent of the invariant mass with in the range. As an example, in-medium ρ meson contribution calculated by R. Rapp and H. van Hees is added to the cocktail (the contribution from ρ meson is excluded from the cocktail to avoid double counting) in Fig. 5.19. Table 5.2 summarizes the excess from the cocktail in each model calculation in the range $0.5 < m_{ee} < 0.75$ GeV/ c^2 , $0 < p_T < 0.5$ GeV/ c . The excess in the data is also shown in the table. Although the contributions from those models tends to be lower than the excess in data, the experimental uncertainties are too large for a definite statement.

Table 5.2 also shows the effective temperatures of the model calculations in the range $0.3 < m_{ee} < 0.75$ GeV/ c^2 , $0.05 < m_T - m_0 < 0.6$ GeV/ c^2 . All the models tend to overestimate the effective temperature of the excess in data.

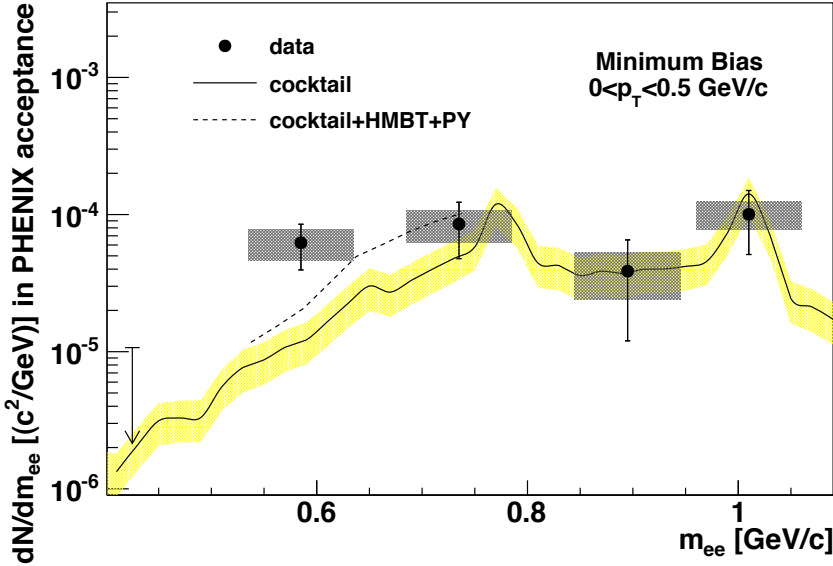


FIGURE 5.19: Invariant mass spectrum of e^+e^- pairs in the minimum bias collisions for the low p_T region, $0 < p_T < 0.5$ GeV/ c . The ρ meson contribution, including in-medium effects, calculated by R. Rapp and van Hees [35, 107, 108] is added to cocktail without the ρ and shown in the figure by the dashed line. The HMBT(Hadron Many Body Theory) refers to the broadening scenario and the PY refers to the partonic yield from $q\bar{q}$ annihilation.

TABLE 5.2: The excess from the cocktail in PHENIX acceptance calculated by the different models for the range $0.5 < m_{ee} < 0.75$ GeV/ c^2 and $0.0 < p_T < 0.5$ GeV/ c .
The excess in the data is also shown.

Model	Excess [$\times 10^{-5}$ /evt]	T_{eff} [GeV/ c^2]
Rapp (Broadening)	0.7	0.17
Rapp (Dropping)	0.6	0.17
Dusling (Broadening)	0.1	0.19
Cassing (Broadening)	0.5	0.18
Cassing (Broadening+Dropping)	0.6	0.15
Data	$1.6 \pm 0.5^{stat} \pm 0.6^{syst} \pm 0.2^{model}$	$0.07 \pm 0.04^{stat} \pm 0.02^{syst}$

5.6.2 QGP radiation

In this subsection, we compare the data with a theoretical model calculation and discuss the possible QGP radiation. The QGP radiation is calculated using the model by Dusling mentioned in the previous section for PHENIX Run-4 acceptance (magnetic field in the $++$ configuration) [35]. The yield in the Run-10 acceptance (magnetic field in the $+-$ configuration) is obtained by multiplying the yield by the ratio between the corresponding two cocktails, which takes into account the different acceptance in Run-4 and Run-10:

$$\text{Yield(Run - 10)} = \frac{\int_{1.2}^{2.8} dm_{ee} \text{ cocktail(Run - 10)}}{\int_{1.2}^{2.8} dm_{ee} \text{ cocktail(Run - 4)}} \cdot \text{Yield(Run - 4)} \quad (5.5)$$

where Yield(Run-10) and Yield(Run-4) are the predicted yield of the QGP radiation for $1.2 < m_{ee} < 2.8 \text{ GeV}/c^2$. The calculated yield is added to cocktail and then divided by the cocktail as shown in Table 5.3. The data/cocktail ratio is also shown in the table. The experimental uncertainties are too large and the data appears to be consistent with the model within the large experimental uncertainties.

The possible QGP radiation is almost comparable to the uncertainty in the $c\bar{c}$ contribution. Measurement of the QGP radiation also requires a thorough understanding of the $c\bar{c}$ correlation or a vertex detector to reject the electrons originating from charmed mesons.

TABLE 5.3: Thermal radiation calculations for $1.2 < m_{ee} < 2.8 \text{ GeV}/c^2$ are added to the cocktail and then divided by the cocktail. The data divided by cocktail is also shown.

Model	(model+cocktail)/cocktail
Dusling	1.3
Data	Data/cocktail
	$1.4 \pm 0.3^{stat} \pm 0.3^{syst} \pm 0.3^{model}$

Chapter 6

Conclusion and outlook

6.1 Conclusion

The Hadron Blind Detector (HBD) is a new Čerenkov detector consisting of a 50 cm long radiator operated with pure CF₄ and directly coupled to a triple Gas Electron Multiplier (GEM) photon detection element. The purpose of the HBD is to reject electrons coming from π^0 Dalitz decays and γ conversions, which are major background sources in electron measurements.

The HBD was installed in PHENIX for 2010 $Au + Au$ runs (Run-10) and successfully operated. This manuscript presented the results of the first di-electron measurement at mid-rapidity using the HBD in $Au + Au$ collisions at $\sqrt{s_{NN}} = 200$ GeV. As a result, the consistent results with the previous PHENIX measurement were obtained for all the mass regions. This fact demonstrates the proof-of-principle of the HBD.

The measured mass and p_T spectra were also compared to the cocktail of known hadronic sources and the possible spectral modifications were investigated. In the low mass, low p_T region ($p_T < 0.5$ GeV/c), an excess from the cocktail was observed. The excess was compared to several model calculations with the in-medium modifications of the ρ meson. All the models seemed to be insufficient to explain the excess in data, however, the experimental uncertainties were too large for a definite statement. In the low mass, high p_T region, we observed an excess consistent with the contribution from the virtual photon associated with direct photon production measured by PHENIX. In the intermediate mass region, the obtained yields were consistent with N_{coll} scaling of the open charm contribution. However, within the experimental uncertainties, the possibility of having the QGP radiation in the mass region was not ruled out.

6.2 Outlook

In the course of this analysis, several important things for future di-electron measurements were found. They are summarized below.

- Hadron rejection.

Hadron contamination results in unexpected correlations between particles and makes the understanding of the background shape difficult. In this thesis, the contamination was suppressed as low as 5%. Even with the small contamination, we had to consider the e - h correlation shown in Section 4.12.4. This correlation is not considered in the previous PHENIX analysis.

- Background electron rejection.

The idea of the HBD to reduce background electron sources is still a valid approach for a future di-electron measurement. However, for the purpose, we need to find a way to deal with the scintillation background.

One way is to use timing information. Since the scintillation is usually slow (order of ~ 100 ns decay time), with a timing resolution of 10 ns, the scintillation background can be suppressed by a factor of ~ 5 . Second way is to install a shade exploiting the fact that scintillation occurs uniformly in 4π whereas Čerenkov light is emitted in a narrow cone. This approach can reduces the scintillation background by a factor of ~ 3 . Third way is to change the radiator gas to the one that does not emit scintillation photons in the wavelength where CsI is sensitive, for example, CH₄. However, since the photon yield of CH₄ is relatively low ($\sim 1/5$ of CF₄), additional studies are needed to find the best radiator gas.

- Acceptance.

Since the enhancement observed by the previous PHENIX measurement has a very low effective temperature, the acceptance in the low mass, low p_T regions are important. In this analysis, the difference in the background condition led to the limited acceptance compared to the previous measurements. However, this can be improved by realizing the two previous bullets.

- Flow.

As shown in Section 4.12.1, the flow effect modifies the shape of the combinatorial background. This effect is not negligible in the mid-central events. The previous PHENIX measurement did not take the effect into account.

- Understanding of the open charm contribution.

After uninstalling the HBD from PHENIX in 2010, PHENIX has installed a vertex detector. The vertex detector enables the separation of the open charm contribution from other prompt sources. Their results are awaited.

Acknowledgements

First of all, I would like to express my gratitude to my supervisor, Prof. K. Ozawa for his comments and advice for this analysis. I learned many experimental techniques and physics from him.

I am grateful to Prof. I. Tserruya for giving me the chance to work with Weizmann group for this challenging analysis. His profound understanding of physics and analysis guided me at all stages of this analysis. I am obliged to Dr. I. Ravinovich for many useful discussions, encouragements and supports. I wish to thank Dr. M. Makek for many fruitful discussions, helps in this analysis and nice time we spent together inside and outside the office.

I also wish to thank Dr. D. Sharma for providing a nice company, encouragements and superb Indian food. I would like to express my appreciation to Dr. S. Tarafdar and Mr. P. Garg for our frequent outings for lunch/dinner/drinking. I am also thankful to Dr. Z. Citron and Prof. A. Milov for being so friendly and helpful.

I express my acknowledgements to all the collaborators of the PHENIX experiment. In particular, I would like to thank the members of the HBD group, Prof. A. Drees, Prof. T. K. Hemmick, Prof. B. V. Jacak, Dr. E. T. Atomssa, Ms. J. Sun and Mr. S. Rolnick for useful discussions and advice.

I am grateful to Dr. S. Yokkaichi and Dr. Y. Ikeda for their steady operation of CC-J at RIKEN. I am also grateful to Dr. P. Choukran for managing the PC-farm at Weizmann.

I am much obliged to the referees of this thesis, Prof. S. Shimoura, Prof. T. Hirano, Prof. H. Sakurai, Prof. J. Tanaka and Prof. K. Tokushuku, for their valuable comments and advice.

I would like to express my gratitude to the members of our group, Dr. T. Adachi, Mr. K. Utsunomiya, Mr. Y. Komatsu, Mr. S. Masumoto, Ms. A. Takagi, Mr. K. Kanno, Mr. W. Nakai, Mr. Y. Obara, Mr. T. Shibukawa and Ms. H. Murakami, for their friendships.

I express my appreciation to the CNS-PHENIX group, Prof. H. Hamagaki, Prof. T. Gunji, Dr. A. Aramaki, Dr. Y. Yamaguchi, Dr. A. Takahara and Dr. R. Akimoto, for their helps and supports, especially when I was at BNL.

I also wish to thank the present and past members of the NEX (Nuclear Physics Experiment) group, Prof. R. Hayano, Prof. H. Sakai, Prof. H. Sakurai, Prof. K. Yako, Prof. T. Suzuki, Prof. M. Niikura, Dr. M. Sasano, Dr. M. Sato, Dr. T. Nakao, Dr. D. Suzuki, Dr. H. Tatsuno, Dr. S. Noji, Dr. K. Miki, Dr. S. Itoh, Mr. Y. Fujiwara, Dr. N. Kobayashi, Dr. H. Shi, Mr. T. Hashimoto, Mr. T. Kobayashi, Mr. K. Todoroki, Mr. Z. Xu, Mr. T. Nishi, Mr. K. Okouchi, Mr. Y. Tanaka, Mr. Y. Murakami, Mr. H. Yamada, Mr. R. Taniuchi, Mr. K. Matsui, Mr. T. Miyazaki, Mr. S. Momiyama and Mr. Y. Watanabe, for their kindness.

I am also thankful to the people around the student office at KEK, Prof. N. Saito, Prof. T. Mibe, Prof. K. Ueno, Prof. Y. Fukao, Dr. H. Natori, Dr. M. Ohtani, Mr. T. Kakurai, Mr. S. Kanda, Mr. S. Nishimura, Mr. R. Kitamura, for their tender helps.

Last but not least, I would like to express my gratitudes to my families for their continuous supports and encouragements.

Appendix A

Non-standalone pattern recognition algorithm of HBD

A.1 Cluster size optimization

The cluster size of non-standalone algorithm is optimized to maximize the rejection of fake electrons while keeping high efficiency for the detection of genuine single electrons. The optimization is done using the charge distribution of a simulated single electron cluster embedded in 0-10% central $Au + Au$ events at $\sqrt{s_{NN}} = 62$ GeV, while the charge distribution of a fake cluster is obtained by randomly choosing pads in central $Au + Au$ data at $\sqrt{s_{NN}} = 62$ GeV.

The hexagonal pad is divided into 6 equilateral triangles and each of these is in turn divided into 16 small equilateral triangles of ~ 4 mm side as shown in Fig 3.15. When a track points to an hexagonal pad, four types of clusters are tested: (pad0 only), (pad0 \oplus pad1), (pad0 \oplus pad1 \oplus pad2) ,(pad0 \oplus pad1 \oplus pad3) where pad0 is the pad closest to the track projection point in the HBD and pad1, pad2 and pad3 are neighboring pads as shown in Fig. 3.15.

To determine the cluster size, we evaluate the electron efficiency when the number of backplane-conversion electrons is reduced to 10%. The optimization procedure is described below.

1. Determine the charge distribution of a fake cluster for each cluster size by randomly choosing readout pads in 0-10% central $Au + Au$ events at $\sqrt{s_{NN}} = 62$ GeV. Neighboring pads are chosen for 2 or 3 pad clusters, such as (pad0 \oplus pad1) configuration.

2. Determine the charge thresholds such that the fraction of events above the threshold is 10% .
3. Determine the charge distribution of genuine electron clusters. Electrons are generated by the decay of ϕ mesons with flat p_t distribution between 0 and 20 GeV/c. Since the simulation does not have the scintillation background of CF_4 , the electron is embedded in 0-10% central $Au + Au$ data at $\sqrt{s_{NN}} = 62$ GeV to obtain the real HBD response. We first embed the simulated electrons in the data and then subtract the underlying event in the same way as the real analysis.

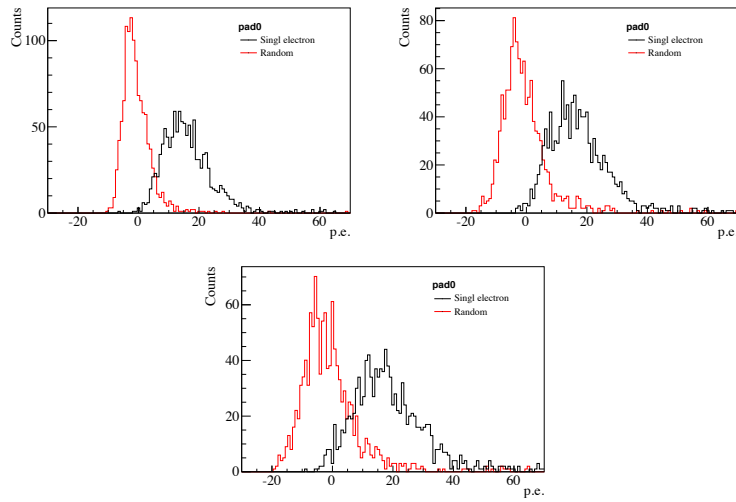


FIGURE A.1: Charge distribution of 1 pad (pad0), 2 pad (pad0 \oplus pad1) and 3 pad (pad0 \oplus pad1 \oplus pad2) clusters for genuine electrons (black) and fake electrons (red) pointing to the triangle 0 in Fig. 3.15.

The associated cluster charge distributions of single electrons and fake electrons when the tracks are pointing to the triangle 0 in Fig. 3.15 are shown in Fig. A.1.

4. Evaluate the electron efficiency for each cluster with the thresholds made in Step 2. The obtained efficiency is shown in Fig A.2. The algorithm uses the cluster size which gives the best efficiency in each triangle.

As a result, when the central arm track points to triangles 0-8, the cluster includes pad0 only, when it points to triangle 10-14, the cluster includes (pad0 \oplus pad1) and when it points to triangles 10 and 15, the cluster consists of (pad0 \oplus pad1 \oplus pad2) or (pad0 \oplus pad1 \oplus pad3), respectively.

The readout pads have several shapes as shown in Fig A.3. Most pads have an hexagonal shape, but there are also half hexagonal pads and slightly larger pentagonal pads along the edges of each detector module. Similar studies are performed for those pads to optimize the cluster size.

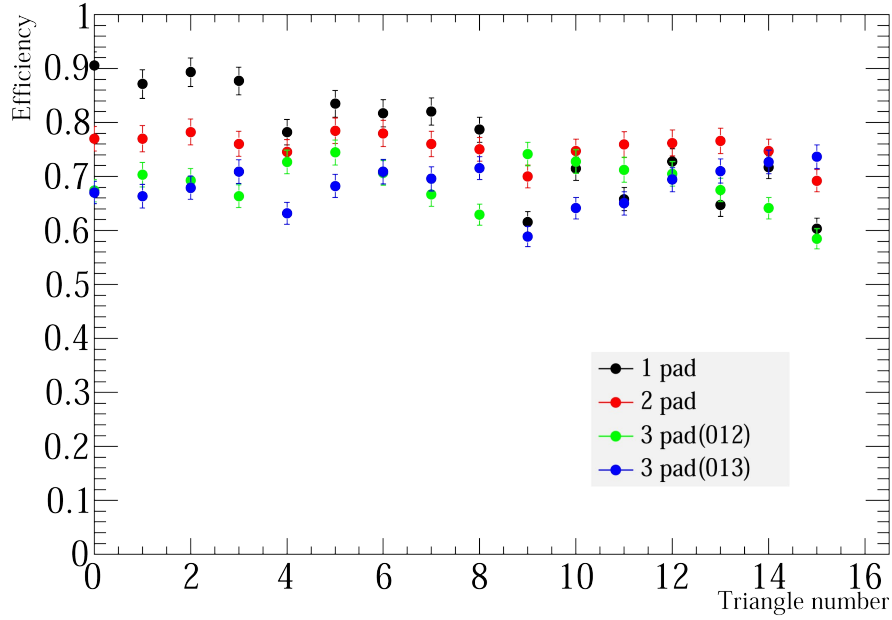


FIGURE A.2: Electron efficiency as a function of triangle number (Fig. 3.15) when 90 % of fake hits are rejected. The points with different colors show the efficiency of different cluster sizes.

A.2 Definition of hbdid variable

The hbdid variable is a normalized threshold to control the reduction of backplane-conversion electrons for all centralities, HBD modules and cluster sizes. The procedure to determine the variable is the following;

1. Determine charge thresholds to reduce the backplane-conversion electrons to 10% as a function of bbcq, HBD module and cluster size. As an example, The thresholds for 1 pad cluster in the east modules are shown in Fig. A.4.
2. To make the thresholds easier to handle, fit the thresholds as a function of bbcq to a straight line in the bbcq range 400-1900. The fitting is done for each cluster size and for each HBD module. These straight lines are used as thresholds for the full bbcq range in the further analysis. Note that, since the thresholds deviate from a straight line for small bbcq values, the thresholds calculated by the straight line reject more than 90% of the back plane conversion electrons.
3. Scale the thresholds by a constant scaling parameter, α , to define the thresholds needed to achieve a different rejection factor. ($\alpha = 0.1, 0.2, 0.3, 0.4, 0.5, 0.6, 0.7, 0.8, 0.9, 1.0, 1.1, 1.2, 1.3, 1.4, 1.5, 1.6, 1.7, 1.8, 1.9, 2.0, 2.1, 2.2, 2.3, 2.4, 2.5$)
4. For each track, compare its cluster charge Q with the 25 threshold charges Q_{th} determined in the previous step and find the maximum α value α_{max} that satisfies

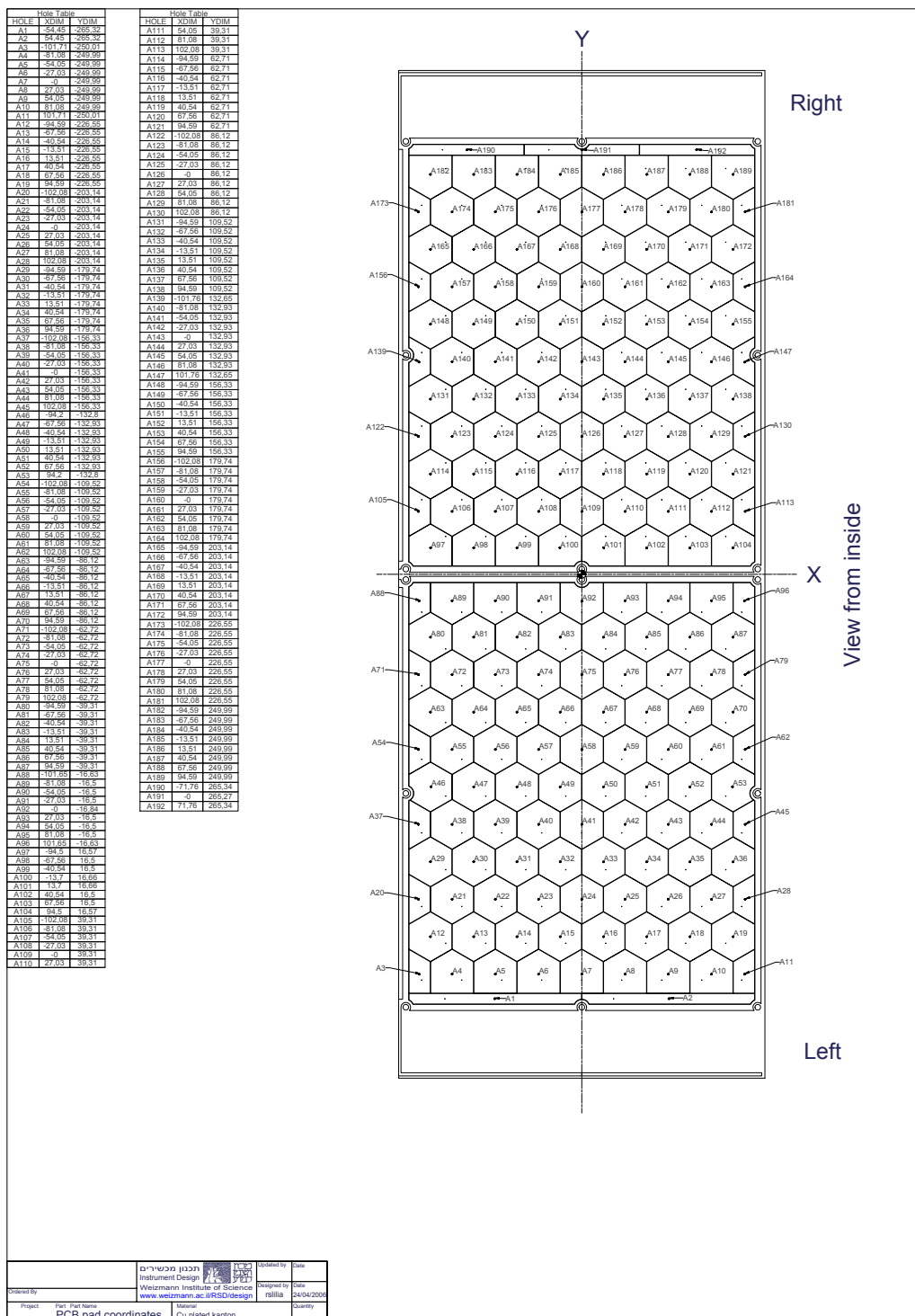


FIGURE A.3: Schematic drawing of the HBD readout plane.

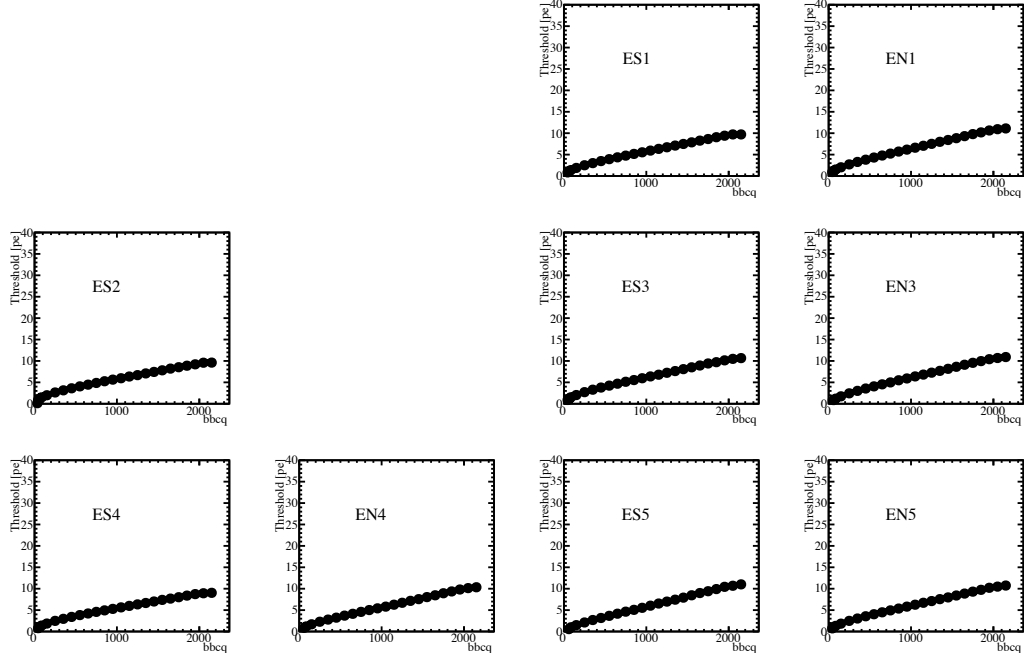


FIGURE A.4: Charge threshold of a cluster consisting of one hexagonal pad in each HBD module of the east arm at $\sqrt{s_{NN}} = 200$ GeV for a rejection of backplane conversion by a factor of 10.

the condition $Q > \alpha_{max} \times Q_{th}$. For example, if the cluster charge is 8.5 p.e. and the threshold determined in Step 2 is 10 p.e., then α_{max} is 0.8.

5. Assign to the track the value $hbdid = 10 \times \alpha_{max}$

The remaining fraction of backplane-conversion electrons and the electron efficiency are shown as function of $hbdid$ at $\sqrt{s_{NN}} = 200$ GeV in Fig. A.5. The figure shows that the inverse of $hbdid$ is a good approximation for the remaining fraction of backplane-conversion electrons in the range, $5 < hbdid < 20$. The electron efficiency is shown as a function of the electron p_T for the typical case of $hbdid \geq 10$ in Fig. A.6

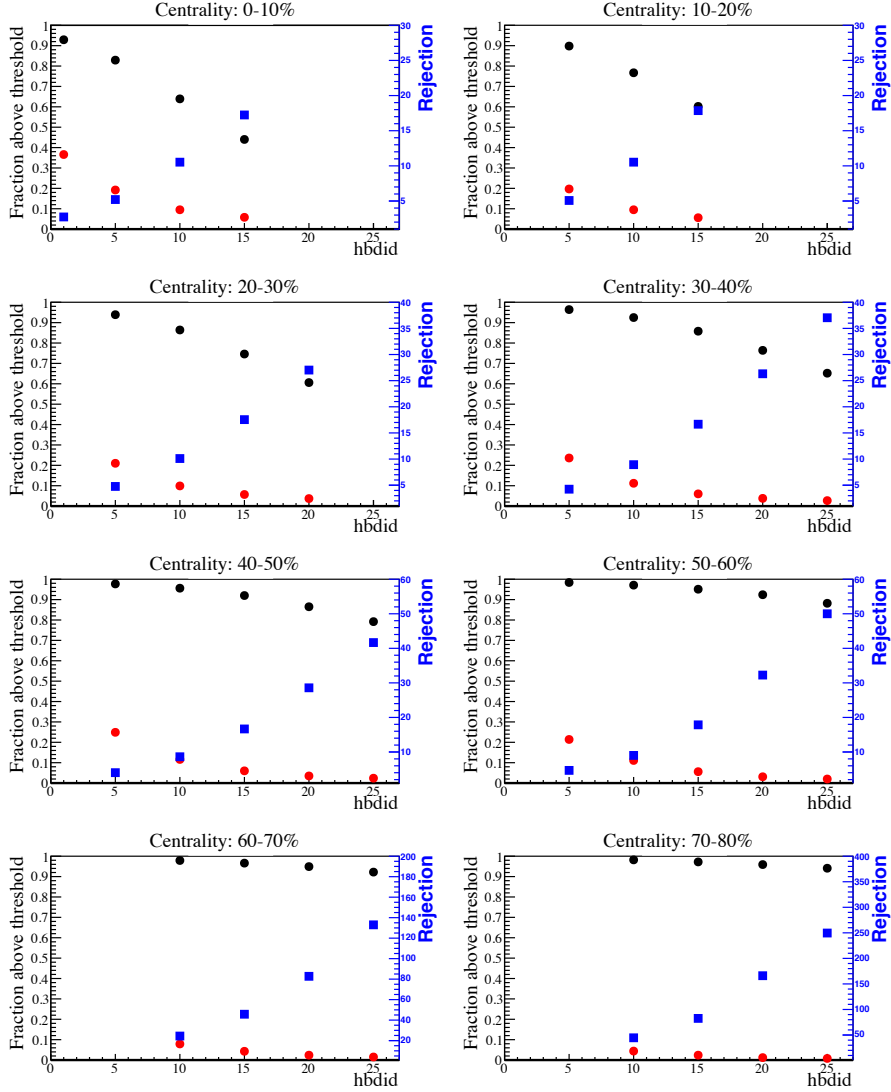


FIGURE A.5: Electron efficiency and the remaining fraction of backplane-conversion electrons as a function of hbdid. See the text for the definition of hbdid.

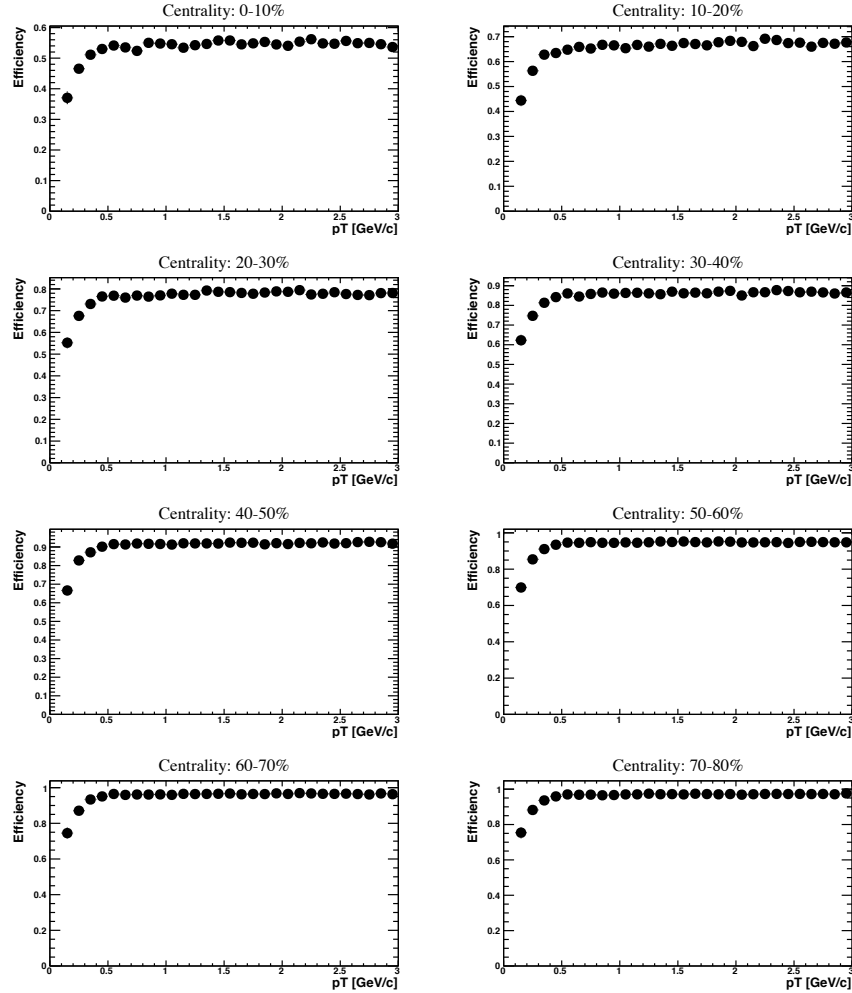


FIGURE A.6: Electron efficiency as a function of p_T for the case of $\text{hbdid} \geq 10$. See the text for the definition of hbdid .

Appendix B

DC fiducial cuts

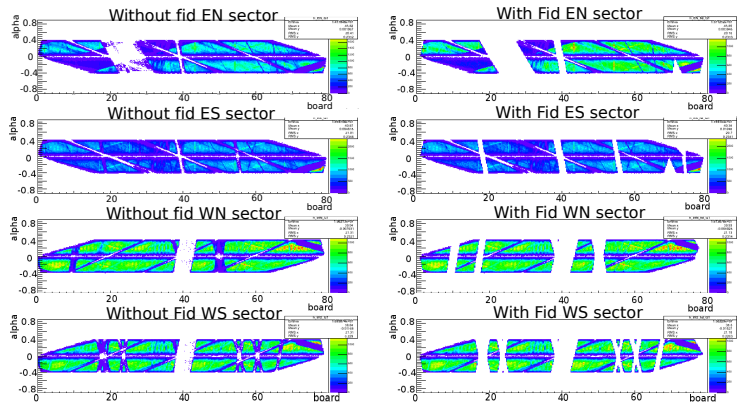


FIGURE B.1: α vs board number for e^\pm yield without fiducial cut (left column) and with fiducial cut (right column) for all the four sectors in Run Group 1.

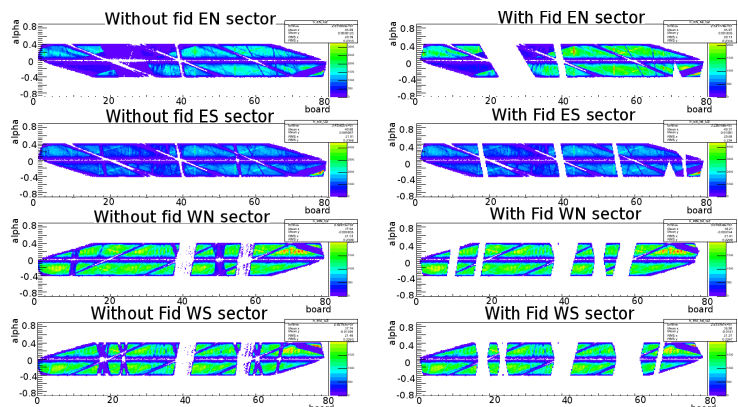


FIGURE B.2: α vs board number for e^\pm yield without fiducial cut (left column) and with fiducial cut (right column) for all the four sectors in Run Group 2.

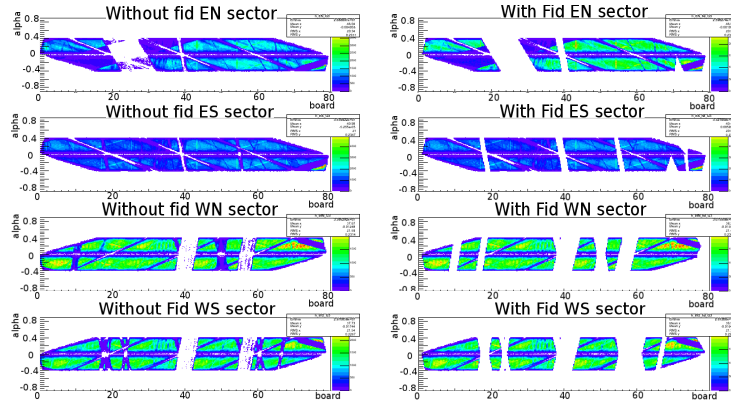


FIGURE B.3: α vs board number for e^\pm yield without fiducial cut (left column) and with fiducial cut(right column) for all the four sectors in Run Group 3.

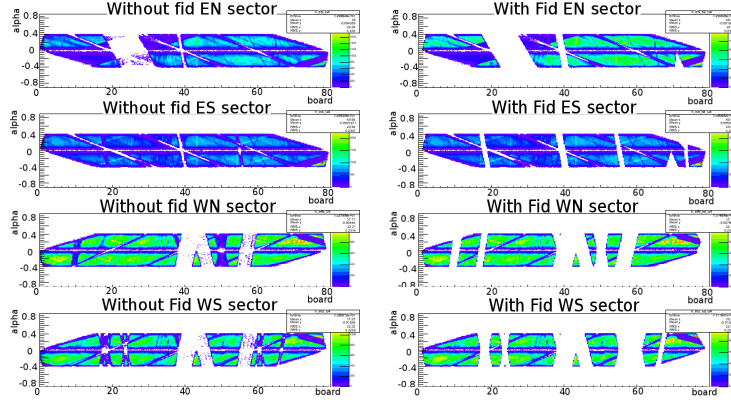


FIGURE B.4: α vs board number for e^\pm yield without fiducial cut (left column) and with fiducial cut(right column) for all the four sectors in Run Group 4.

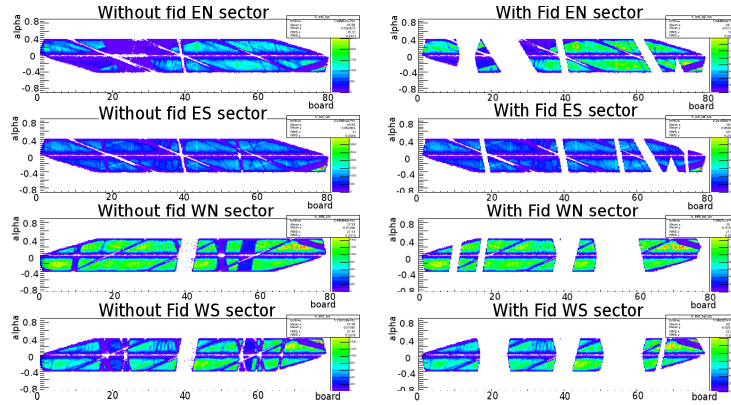


FIGURE B.5: α vs board number for e^\pm yield without fiducial cut (left column) and with fiducial cut(right column) for all the four sectors in Run Group 5.

Appendix C

Weighting factor to introduce “flow” into mixed background

Assume azimuthal distribution of a particle follows the following expression.

$$P(\phi - \Psi) = \epsilon(\phi)(1 + 2v_2 \cos 2(\phi - \Psi)) \quad (\text{C.1})$$

where ϕ is a particle emission angle in azimuth, Ψ is the reaction plane angle of the event and $\epsilon(\phi)$ is the detection efficiency of a spectrometer at ϕ .

First, calculate $\Delta\phi$ distribution of foreground pairs.

$$\begin{aligned} P_{FG}(\Delta\phi) &= \frac{1}{\pi} \int_{-\pi/2}^{\pi/2} d\Psi \int_{\phi_1 - \phi_2 = \Delta\phi} d\phi_1 d\phi_2 P(\phi_1 - \Psi) P(\phi_2 - \Psi) \\ &= \frac{1}{\pi} \int_{-\pi/2}^{\pi/2} d\Psi \int_{-\pi}^{\pi} d\phi_1 P(\phi_1 - \Psi) P(\phi_1 + \Delta\phi - \Psi) \\ &= \frac{1}{\pi} \int_{-\pi/2}^{\pi/2} d\Psi \int_{-\pi}^{\pi} d\phi_1 (1 + 2v_2 \cos 2(\phi_1 - \Psi))(1 + 2v_2 \cos 2(\phi_1 + \Delta\phi - \Psi)) \epsilon(\phi_1) \epsilon(\phi_1 + \Delta\phi) \\ &= \frac{1}{\pi} \int_{-\pi/2}^{\pi/2} d\Psi \int_{-\pi}^{\pi} d\phi_1 \underbrace{(\epsilon(\phi_1) \epsilon(\phi_2))}_{A} + \underbrace{2\epsilon(\phi_1) \epsilon(\phi_1 + \Delta\phi) v_2 \cos 2(\phi_1 - \Psi)}_{B} \\ &\quad + \underbrace{2\epsilon(\phi_1) \epsilon(\phi_1 + \Delta\phi) v_2 \cos 2(\phi_1 + \Delta\phi - \Psi)}_{C} \\ &\quad + \underbrace{4\epsilon(\phi_1) \epsilon(\phi_1 + \Delta\phi) v_2 v_2 \cos 2(\phi_1 - \Psi) \cos 2(\phi_1 + \Delta\phi - \Psi)}_{D} \end{aligned}$$

$$A = \int_{-\pi}^{\pi} d\phi_1 \epsilon(\phi_1) \epsilon(\phi_1 + \Delta\phi)$$

$$\begin{aligned} B &= \frac{1}{\pi} 2v_2 \int_{-\pi}^{\pi} d\phi_1 \epsilon(\phi_1) \epsilon(\phi_1 + \Delta\phi) \int_{-\pi/2}^{\pi/2} d\Psi \cos 2(\phi_1 - \Psi) \\ &= \frac{1}{\pi} 2v_2 \int_{-\pi}^{\pi} d\phi_1 \epsilon(\phi_1) \epsilon(\phi_1 + \Delta\phi) \left[-\frac{\sin 2(\phi_1 - \Psi)}{2} \right]_{\Psi=-\pi/2}^{\Psi=\pi/2} = 0 \end{aligned}$$

$$C = 0$$

$$\begin{aligned} D &= \frac{1}{\pi} 4v_2 v_2 \int_{-\pi}^{\pi} d\phi_1 \epsilon(\phi_1) \epsilon(\phi_1 + \Delta\phi) \int_{-\pi/2}^{\pi/2} d\Psi (\cos 2(\phi_1 - \Psi)) (\cos 2(\phi_1 - \Psi + \Delta\phi)) \\ &= \frac{1}{\pi} 4v_2 v_2 \cos 2\Delta\phi \int_{-\pi}^{\pi} d\phi_1 \epsilon(\phi_1) \epsilon(\phi_1 + \Delta\phi) \int_{-\pi/2}^{\pi/2} d\Psi \cos^2 2(\phi_1 - \Psi) \\ &- \frac{1}{\pi} 4v_2 v_2 \sin 2\Delta\phi \int_{-\pi}^{\pi} d\phi_1 \epsilon(\phi_1) \epsilon(\phi_1 + \Delta\phi) \int_{-\pi/2}^{\pi/2} d\Psi \sin 2(\phi_1 - \Psi) \cos 2(\phi_1 - \Psi) \\ &= \frac{1}{\pi} 4v_2 v_2 \cos 2\Delta\phi \int_{-\pi}^{\pi} d\phi_1 \epsilon(\phi_1) \epsilon(\phi_1 + \Delta\phi) \int_{-\pi/2}^{\pi/2} d\Psi \frac{\cos 4(\phi_1 - \Psi) + 1}{2} \\ &- \frac{1}{\pi} 4v_2 v_2 \sin 2\Delta\phi \int_{-\pi}^{\pi} d\phi_1 \epsilon(\phi_1) \epsilon(\phi_1 + \Delta\phi) \int_{-\pi/2}^{\pi/2} d\Psi \frac{\sin 4(\phi_1 - \Psi)}{2} \\ &= 2v_2 v_2 \cos 2\Delta\phi \int_{-\pi}^{\pi} d\phi_1 \epsilon(\phi_1) \epsilon(\phi_1 + \Delta\phi) \end{aligned}$$

Therefore,

$$P_{FG}(\Delta\phi) = \left(\int_{-\pi}^{\pi} d\phi_1 \epsilon(\phi_1) \epsilon(\phi_1 + \Delta\phi) \right) (1 + 2v_2 v_2 \cos 2\Delta\phi) \quad (\text{C.2})$$

Next, calculate $\Delta\phi$ distribution of mixed BG pairs produced without reaction plane binning.

$$\begin{aligned}
 P_{BG}(\Delta\phi) &= \frac{1}{\pi^2} \int_{-\pi/2}^{\pi/2} d\Psi_1 \int_{-\pi/2}^{\pi/2} d\Psi_2 \int_{\phi_1 - \phi_2 = \Delta\phi} d\phi_1 d\phi_2 P(\phi_1 - \Psi_1) P(\phi_2 - \Psi_2) \\
 &= \frac{1}{\pi^2} \int_{-\pi/2}^{\pi/2} d\Psi_1 \int_{-\pi/2}^{\pi/2} d\Psi_2 \int_{-\pi}^{\pi} d\phi_1 P(\phi_1 - \Psi_1) P(\phi_1 + \Delta\phi - \Psi_2) \\
 &= \frac{1}{\pi^2} \int_{-\pi/2}^{\pi/2} d\Psi_1 \int_{-\pi/2}^{\pi/2} d\Psi_2 \int_{-\pi}^{\pi} d\phi_1 (1 + 2v_2 \cos 2(\phi_1 - \Psi_1))(1 + 2v_2 \cos 2(\phi_1 + \Delta\phi - \Psi_2)) \\
 &\quad \epsilon(\phi_1) \epsilon(\phi_1 + \Delta\phi) \\
 &= \frac{1}{\pi^2} \int_{-\pi/2}^{\pi/2} d\Psi_1 \int_{-\pi/2}^{\pi/2} d\Psi_2 \int_{-\pi}^{\pi} d\phi_1 (\underbrace{\epsilon(\phi_1)\epsilon(\phi_2)}_E + \underbrace{2\epsilon(\phi_1)\epsilon(\phi_1 + \Delta\phi)v_2 \cos 2(\phi_1 - \Psi_1)}_F) \\
 &\quad + \underbrace{2\epsilon(\phi_1)\epsilon(\phi_1 + \Delta\phi)v_2 \cos 2(\phi_1 + \Delta\phi - \Psi_2)}_G \\
 &\quad + \underbrace{4\epsilon(\phi_1)\epsilon(\phi_1 + \Delta\phi)v_2 v_2 \cos 2(\phi_1 - \Psi_1) \cos 2(\phi_1 + \Delta\phi - \Psi_2)}_H
 \end{aligned}$$

$$E = \int_{-\pi}^{\pi} d\phi_1 \epsilon(\phi_1) \epsilon(\phi_1 + \Delta\phi)$$

$$\begin{aligned}
 F &= \frac{1}{\pi^2} 2\pi v_2 \int_{-\pi}^{\pi} d\phi_1 \epsilon(\phi_1) \epsilon(\phi_1 + \Delta\phi) \int_{-\pi/2}^{\pi/2} d\Psi_1 \cos 2(\phi_1 - \Psi_1) \\
 &= \frac{1}{\pi^2} 2\pi v_2 \int_{-\pi}^{\pi} d\phi_1 \epsilon(\phi_1) \epsilon(\phi_1 + \Delta\phi) \left[-\frac{\sin 2(\phi_1 - \Psi_1)}{2} \right]_{\Psi_1=-\pi/2}^{\Psi_1=\pi/2} = 0
 \end{aligned}$$

$$G = 0$$

$$\begin{aligned}
 H &= \frac{1}{\pi^2} 4v_2 v_2 \int_{-\pi}^{\pi} d\phi_1 \epsilon(\phi_1) \epsilon(\phi_1 + \Delta\phi) \int_{-\pi/2}^{\pi/2} d\Psi_1 \cos 2(\phi_1 - \Psi_1) \int_{-\pi/2}^{\pi/2} d\Psi_2 \cos 2(\phi_1 - \Psi_2 + \Delta\phi) \\
 &= 0
 \end{aligned}$$

Therefore,

$$P_{BG}(\Delta\phi) = \int_{-\pi}^{\pi} d\phi_1 \epsilon(\phi_1) \epsilon(\phi_1 + \Delta\phi) \tag{C.3}$$

The weighting factor to introduce the flow correlation into mixed BG pairs is the following.

$$w(\Delta\phi) = \frac{P_{FG}(\Delta\phi)}{P_{BG}(\Delta\phi)} \quad (\text{C.4})$$

$$= 1 + 2v_2 v_2 \cos 2\Delta\phi \quad (\text{C.5})$$

If pair cut efficiency $\epsilon_{pair}(\phi_1, \phi_2)$ is introduced, P_{FG} , P_{BG} and w change as follows.

$$\begin{aligned} P_{FG}(\Delta\phi) &= \left(\int_{-\pi}^{\pi} d\phi_1 \epsilon(\phi_1) \epsilon(\phi_1 + \Delta\phi) \epsilon_{pair}(\phi_1, \phi_1 + \Delta\phi) \right) (1 + 2v_2 v_2 \cos 2\Delta\phi) \\ P_{BG}(\Delta\phi) &= \int_{-\pi}^{\pi} d\phi_1 \epsilon(\phi_1) \epsilon(\phi_1 + \Delta\phi) \epsilon_{pair}(\phi_1, \phi_1 + \Delta\phi) \\ w(\Delta\phi) &= 1 + 2v_2 v_2 \cos 2\Delta\phi \end{aligned}$$

Applying pair cuts does not affect the weighting factor.

Bibliography

- [1] J. C. Collins and M. J. Perry, Phys. Rev. Lett. (1975).
- [2] N. Cabibbo and G. Parisi, Phys. Lett. B 59, 67 (1975).
- [3] S. A. Chin, Phys. Lett. B 78, 552 (1978).
- [4] E. V. Shuryak, Phys. Lett. B 78, 150 (1978).
- [5] F. Karsch, Nuclear Physics A 698, 199 (2002).
- [6] F. Karsch and E. Laermann, Physical Review D 50, 6954 (1994).
- [7] Y. Nambu, Phys. Rev. Lett. 4, 380 (1960).
- [8] Y. Nambu and G. Jona-Lasinio, Phys. Rev. 124, 246 (1961).
- [9] Y. Nambu and G. Jona-Lasinio, Phys. Rev. 122, 345 (1961).
- [10] T. Hatsuda and T. Kunihiro, Phys. Rept. 247, 221 (1994)
- [11] J. D. Bjorken, Phys. Rev. D 50, 2062 (1983).
- [12] E. Fermi, Prog. Theor. Phys. 5, 570 (1950).
- [13] Collective papers of L. D. Landau, ed. D. T. ter Haar New York: Gordon & Breach, p. 569 (1965).
- [14] L. P. Csernai, Introduction to Relativistic Heavy Ion collisions, New York: John Wiley & Sons (1994).
- [15] D. H. Rischke, Springer Lecture notes in Physics vol 516, 21 (1999).
- [16] K. Yagi, T. Hatsuda and Y. Miake, Quark-Gluon Plasma, Cambridge (2005).
- [17] P. F. Kolb, arxiv, nucl-th, 0304036 (2003).
- [18] Glauber, RJ. 1959. In Lectures in Theoretical Physics, ed. WE Brittin and LG Dunham, 1:315. New York: Interscience

- [19] I. Tserruya, arXiv nucl-ex, 0903.0415 (2009).
- [20] D. Sharma, Poster at Quark Matter 2012.
- [21] D. Sharma, PHENIX internal analysis note 1046.
- [22] R. S. Hayano and T. Hatsuda, Rev. Mod. Phys. 82, 2949 (2010).
- [23] R. D. Pisarski, Phys. Lett. B 110, 155 (1982).
- [24] G. Chanfray, R. Rapp, and J. Wambach, Phys. Rev. Lett. 76, 368 (1996).
- [25] R. Rapp, G. Chanfray, and J. Wambach, Nuclear Physics A 617, 472 (1997).
- [26] G. E. Brown and M. Rho, Phys. Rev. Lett. 66, 2720 (1991).
- [27] T. Hatsuda and S. H. Lee, Phys. Rev. C 46, R34 (1992).
- [28] R. D. Pisarski, Physical Review D 52, R3773 (1995).
- [29] G. Agakachiev et al., Phys. Rev. Lett. 75, 1272 (1995).
- [30] G. Agakivhiev et al., Eur. Phys. J. C 41, 475 (2005).
- [31] D. Adamová et al., Phys. Lett. B 666, 425 (2008).
- [32] R. Arnaldi et al., Eur. Phys. J. C 61, 711 (2009).
- [33] G. E. Brown and M. Rho, Phys. Rept. 363, 85 (2002).
- [34] R. Rapp, J.Wambach, Adv. Nucl. Phys, 25,1 (2000).
- [35] A. Adare et al., Phys. Rev. C 81, 034911 (2010)
- [36] J. Zhao, J.Phys.G 38, 124134 (2011).
- [37] F. Geurts, arXiv:1305.5447 (2013).
- [38] P. V. Ruuskanen, Nucl. Phys. A 544, 169 (1992).
- [39] A. L. S. Angelis et al, Eur. Phys. J. C 13, 433 (2000).
- [40] M. C. Abreu et al., Phys.Lett. B423, 207 (1998).
- [41] M. C. Abreu et al, The European Physical Journal C 14, 443 (2000).
- [42] M. C. Abreu et al., Phys. Lett. B 499, 85 (2001).
- [43] C.-Y. Wong and Z.-Q. Wang, Phys. Lett. B 367, 50 (1996).
- [44] Z. Lin and X.-N. Wang, Phys. Lett. B 444, 245 (1998).

- [45] G.-Q. Li and C. Gale, Phys. Rev. Lett. 81, 1572 (1998).
- [46] G.-Q. Li and C. Gale, Phys. Rev. C 58, 2914 (1998).
- [47] I. Kvasnikova, C. Gale, and D. Kumar Srivastava, Phys. Rev. C 65, 064903 (2002).
- [48] R. Rapp and E. Shuryak, Phys. Lett. B 473, 13 (2000).
- [49] K. Gallmeister, B. Kämpfer and O. P. Pavlenko, Phys. Lett. B 473, 20 (2000).
- [50] R. Arnaldi et al., Eur. Phys. J. C 59, 607 (2009).
- [51] T. Matsui and H. Satz, Phys.Lett. B178, 416 (1986).
- [52] A. Adare et al., Phys. Rev. Lett. 98, 232301 (2007).
- [53] L. Adamczyk et al., arXiv nucl-ex 1310.3563
- [54] M. Harrison, T. Ludlam, and S. Ozaki, Nucl. Instrum. Meth. A499, 235 (2003).
- [55] <http://www.rhichome.bnl.gov/RHIC/Runs>.
- [56] K. Adcox et al., Nucl. Instrum. Methods A499, 469 (2003).
- [57] H. Akikawa et.al., Nucl. Instr. and Methods A499, 537 (2003).
- [58] S. H. Aronson et al., Nucl. Instrum. Methods A499, 480 (2003).
- [59] M. Allenothers, Nucl. Instrum. Methods A499, 549 (2003).
- [60] K. Ikematsu et al., Nucl. Instrum. Methods A411, 238 (1998).
- [61] C. Adler et al., Nucl. Instrum. Methods A470, 488 (2001).
- [62] E. Richardson et al., Nucl. Instrum. Methods A636, 99 (2011).
- [63] A. M. Poskanzer and S. A. Voloshin, Phys. Rev. C 58, 1671 (1998).
- [64] S. Afanasiev et al., Phys. Rev. C 80, 024909 (2009).
- [65] V. G. Riabov, Nucl. Instrum. Methods A419, 363 (1998).
- [66] K. Adcox et al., Nucl. Instrum. Methods A499, 489 (2003).
- [67] K. Adcox et al., Nucl. Instrum. Methods A497, 263 (2003).
- [68] Y. Akiba et al., Nucl. Instrum. Methods A453, 279 (2000).
- [69] Y. Tanaka et al., Nucl. Instrum. Methods A455, 576 (2000).
- [70] M. Aizawa et al., Nucl. Instrum. Methods A499, 508 (2003).

- [71] L. Aphecetche et al., Nucl. Instrum. Methods A499, 521 (2003).
- [72] H. Fessler, P. Freund, J. Gebauer, J. M. Glas, K. P. Pretzl, P. Seyboth, J. Seyerlein, and J. C. Thevenin, Nucl. Instrum. Methods 228, 303 (1985).
- [73] Z. Fraenkel, B. Khachaturov, A. Kozlov, A. Milov, D. Mukhopadhyay, D. Pal, I. Ravinovich, I. Tserruya and S. Zhou, PHENIX Internal technical note 391 (2001).
- [74] W. Anderson et al., Nucl. Instrum. Methods A646, 35 (2011).
- [75] Z. Fraenkel et al., Nucl. Instrum. Methods A546, 466 (2005).
- [76] S. S. Adler et al., Nucl. Instrum. Methods A499, 560 (2003).
- [77] J. T. Mitchell et al., Nucl. Instrum. Methods A482, 491 (2002).
- [78] A. Chikianian et al., Nucl. Instrum. Methods A371, 480 (1996).
- [79] HADES experiment, Nucl. Instrum. Methods A221, 593 (1990).
- [80] S. Adler et al., Phys. Rev. C 71, 034908 (2005).
- [81] K. Adcox et al., Nucl. Phys. A 757, 184 (2005).
- [82] J. Adams et al., Nucl. Phys. A 757, 102 (2005).
- [83] B. B. Back et al., Nucl. Phys. A 757, 28 (2005).
- [84] I. Arsene et al., Nucl. Phys. A 757, 1 (2005).
- [85] J. Y. Ollitrault, Phys. Rev. D 46, 229 (1992).
- [86] C. Silva et al., PHENIX internal analysis note 666.
- [87] T. Sjöstrand et al., Comput. Phys. Commun. 135, 238 (2001)
- [88] X. -N. Wang and M. Gyulassy, Phys. Rev. D 44, 3501 (1991).
- [89] X. -N. Wang and M. Gyulassy, Phys. Rev. D 45, 844 (1992).
- [90] X. -N. Wang and M. Gyulassy, Phys. Rev. Lett. 68, 1480 (1992).
- [91] M. Gyulassy and X. -N. Wang, Comput. Phys. Commun. 83, 307 (1994).
- [92] A. Adare et al., Phys. Rev. Lett. 101, 232301 (2008).
- [93] S. S. Adler et al., Phys. Rev. C 69, 034910 (2004).
- [94] S. S. Adler et al., Phys. Rev. Lett. 91, 072301 (2003).
- [95] A. Adare et al., Phys. Rev. Lett. 101, 232301 (2008)

- [96] S. S. Adler and S. S. Kapoor, Phys. Rev. C 69, 034909 (2004).
- [97] A. Adare et al., Phys. Rev. C 84, 044905 (2011).
- [98] A. Adare et al., Phys. Rev. Lett. 98, 232301 (2007)
- [99] J. Kamin, PhD thesis at Stony Brook University
- [100] D. Sharma et al, "The cross section of $b\bar{b}$ production via di-electrons in d + Au collisions at $\sqrt{s_{NN}} = 200$ GeV" (in preparation)
- [101] S. Frixione and B. Webber, JHEP. 0206 029 (2002).
- [102] S. Frixione, P. Nason and B. Webber, JHEP. 0308 007 (2002).
- [103] G. Corcella and B. Webber, JHEP. 0101 010 (2001).
- [104] A. Adare et al., Phys. Rev. Lett. 97, 252002 (2006).
- [105] S. S. Adler et al., Phys. Rev. C 69, 034909 (2004).
- [106] S. Turbide, R. Rapp and C. Gale, Phys. Rev. C 69, 014903 (2004).
- [107] R. Rapp, Phys. Rev. C 63, 054907 (2001).
- [108] H. van Hees and R. Rapp, Nucl. Phys. A 806, 339 (2008).
- [109] K. Dusling, D. Teaney, and I. Zahed, Phys. Rev. C 75, 024908 (2007).
- [110] E. L. Bratkovskaya, W. Cassing, and O. Linnyk, Phys. Lett. B 670, 428 (2009).
- [111] E. L. Bratkovskaya and W. Cassing, Nucl. Phys. A 807, 214 (2008).